TUDelft

Delft University of Technology

Momentum Transport by Organised Shallow Convection

Savazzi, A.C.M.

DOI
10.4233/uuid:51ac9cd5-1ffc-4b13-ada1-f82714d4b531

Publication date
2025

Document Version
Final published version

Important note
To cite this publication, please use the final published version (if applicable).
Please check the document version above.

Momentum Transport by Organised Shallow Convection

Momentum Transport by Organised Shallow Convection

Dissertation

for the purpose of obtaining the degree of doctor
at Delft University of Technology
by the authority of the Rector Magnificus,
prof. dr. ir. T.H.J.J. van der Hagen,
chair of the Board for Doctorates
to be defended publicly on

Friday 6 June 2025 at 10:00 o'clock

by

Alessandro Carlo Maria SAVAZZI

This dissertation has been approved by the promotors.

Composition of the doctoral committee:

Rector Magnificus,   chairperson
Prof. dr. A. P. Siebesma,   Delft University of Technology, promotor
Dr. A. A. Nuijens,   Delft University of Technology, copromotor

Independent members:
Prof. dr. ir. F. Lopez-Dekker,   Delft University of Technology
Dr. C. Rio,   University of Toulouse / Meteo-France
Dr. L. Schlemmer,   Deutscher Wetterdienst
Prof. dr. J. Vilà-Guerau de Arellano, Wageningen University & Research

Other members:
Dr. P. Bechtold,   European Center for Medium-Range Weather Forecasts

To Nature,
Majestic and eternal,
Our harm scars us, not you.

Contents

Summary

Atmospheric shallow convection (SC) is characterised by cumulus clouds that extend between a few hundred meters and a few kilometres. These clouds are more than passive tracers of the air flow in which they are embedded. They play an active role in atmospheric dynamics and the climate system by redistributing moisture, temperature, and momentum in the troposphere.

Convective momentum transport (CMT) is important for the large-scale flow as it mixes the slow surface winds with the fast winds at aloft. This mechanism is important near the surface, where wind speed and direction determine the air coupling with the ocean, and it is important throughout the lower troposphere, as it modulates the flow of large-scale overturning circulations, such as the Hadley Cell. CMT is important for the climate system also through its role on the mesoscales: between a few kilometres and a few hundred of kilometres. This became clearer in recent years thanks to studies investigating the coupling between clouds and the mesoscale circulations around them. Mesoscale circulations are key to how clouds organise spatially, thus controlling the amount of energy they radiate back to space (cloud radiative effect).

Despite the importance for the climate and its future projections, the mechanisms underlying CMT by SC remain inadequately understood. Model simulations often failed to encompass the complexity of mesoscale processes, while accurate measurements of the winds have been difficult to attain. This thesis explores the role of CMT in realistic, organised and unorganised shallow cloud fields, using a hierarchical modelling approach and novel observational datasets. We investigate both the dependency of cloud organisation on CMT, and the uncertainties of modelling winds and CMT.

We focus on two recent field campaigns. 1. EUREC4A took place between January and February 2020 over the North Atlantic trade wind region, which provides perfect conditions for shallow cumuli. This campaign measured clouds and the wind flows on mesoscales. Notably, mesoscale circulations were measured thanks to an innovative technique of launching sondes from a plane while flying along a circle. 2. CMTRACE took place in September 2021 around Cabauw, The Netherlands. The Cabauw Experimental Site for Atmospheric Research features numerous instruments, including a 200 m meteorological tower, where winds are measured at high frequencies. During CMTRACE, a collocated wind lidar and cloud radar allowed, for the first time, to measure winds from the surface up to 2 km, with a frequency of about 1 minute (~500 m).

Our results show that CMT crucially influences wind speed and direction throughout the lower troposphere, it also controls cloud organisation and mesoscale circulations. CMT behaves differently to heat and moisture transport, with large compensating effect of positive and negative fluxes alternating in time and space, at different scales. Such

complexity of momentum transport is not well represented in current operational models, resulting in significant biases that extend from the surface into the cloud layer.

We quantify the wind bias of the ECMWF Integrated Forecasting System (IFS) during EU-REC4A, throughout the lower troposphere. Observations reveal an excessively pronounced diurnal cycle of the winds in the model, with too strong winds at night and too weak winds during the day. Without the mixing of sub-grid SC, the model worsen the wind prediction at cloud base while improving the wind prediction near the surface. Notably, the wind bias reduce after an improved representation of the equatorial deep convection, highlighting a complex coupling between the mesoscale and the large-scale.

We also focus on how the convective momentum flux is partitioned among scales. For this, we use the Dutch Atmospheric Large Eddy Simulation (DALES) model and simulate shallow convection at 100 m resolution over a 150×150 km^2 domain during EUREC4A. We improve the realism of the model setup compared to previous studies, and we simulate an extended period of time, spanning 9 days and capturing various environmental conditions. Momentum fluxes vary across scales with a dependency on cloud organisation. Organised cloud fields, with stronger convection, correspond to increased mesoscale contributions to momentum flux. These insights demonstrate that mesoscale circulations significantly influence cloud organisation, something that is not directly taken into account in current model formulations of sub-grid convection (parameterisations).

The role of shallow convection parameterisation (SCP) in kilometre-scale models is explored using the HARMONIE-AROME model. Experiments with inactive SCP produce stronger mesoscale circulations, altering cloud cover and wind profiles. The resolved-to-sub-grid flux partitioning in such scenarios also deviates from what shown by LES, emphasising the need for improved parameterisations informed by LES and high-resolution observations.

Finally, the thesis examines novel momentum flux observations from the CMTRACE campaign. These data confirm errors in IFS momentum flux parameterisation, particularly under active convection. The sub-grid fluxes near cloud base are overestimated and fail to represent the observed variability.

The findings outlined in this thesis hold important implications for advancing our understanding of CMT and its role in atmospheric dynamics. As numerical modelling and observational capabilities continue to evolve, a collaborative approach integrating large-scale observational campaigns, sophisticated LES setups, and mesoscale modelling experiments appears critical. Future efforts should prioritise experimental designs that bridge the gap between idealised simulations and real-world complexity.

Samenvatting

Ondiepe convectie in de atmosfeer (SC) wordt gekarakteriseerd door cumuluswolken die zich uitstrekken van enkele honderden meters tot een paar kilometer. Deze wolken zijn niet slechts passief aanwezig, maar spelen ook een actieve rol in de atmosfeer en het klimaatsysteem. Ze herverdelen vocht, temperatuur en momentum in de troposfeer.

Convectief impulsmomentumtransport (CMT) is belangrijk voor grootschalige luchtstroming omdat het de trage winden aan het oppervlak mengt met de snelle winden hoger in de atmosfeer. Dit mechanisme is belangrijk aan het oppervlak, waar windsnelheid en -richting de luchtkoppeling met de oceaan bepalen, en het is belangrijk in de hele lagere troposfeer, omdat het de stroming van grootschalige draaiende circulaties, zoals de Hadley-cel, beïnvloedt. Ook is CMT belangrijk voor het klimaatsysteem door de rol die het speelt op de mesoschaal: tussen enkele kilometers en een paar honderd kilometer. Dit werd de afgelopen jaren duidelijk dankzij studies die de koppeling tussen wolken en de mesoschaal circulaties daaromheen onderzochten. Mesoschaal circulaties zijn de sleutel tot hoe wolken zich ruimtelijk organiseren en zo de hoeveelheid energie bepalen die ze naar de ruimte terug stralen (stralingseffect van wolken).

Ondanks het belang voor het klimaat en de toekomstverwachtingen, blijven de mechanismen die ten grondslag liggen aan CMT door SC nog onvoldoende begrepen. De complexiteit van mesoschaal processen komt vaak niet tot zijn recht in modelsimulaties, en nauwkeurige metingen van de wind zijn moeilijk te verkrijgen. Deze dissertatie onderzoekt de rol van CMT in realistische, georganiseerde en ongeorganiseerde ondiepe wolkenvelden, met behulp van een combinatie van modellen en nieuwe meetgegevens. We onderzoeken zowel de relatie tussen de organisatie van wolken en CMT, als de onzekerheden van het modelleren van winden en CMT.

We focussen op twee recente veldcampagnes. 1. EUREC4A vond plaats tussen januari en februari 2020 boven het Noord-Atlantische passaatwindgebied, dat perfecte omstandigheden biedt voor ondiepe cumuluswolken. Bij deze campagne werden wolken en de windstromen op mesoschaal gemeten, met name de mesoschaalcirculaties dankzij een innovatieve techniek waarbij sondes vanuit een vliegtuig worden gelanceerd in een cirkelvlucht. 2. CMTRACE vond plaats in september 2021 bij Cabauw, in Nederland. De Cabauw Experimental Site for Atmospheric Research heeft veel verschillende instrumenten, waaronder een 200 m hoge meteorologische toren, waar met een hoge frequentie wind wordt gemeten. Tijdens CMTRACE maakten een gekoppelde windlidar en wolkenradar het voor het eerst mogelijk om winden te meten vanaf de grond tot 2 km hoogte, met een frequentie van ongeveer 1 minuut (500 m).

Onze resultaten tonen aan dat CMT een cruciale invloed heeft op de windsnelheid en -richting in de lagere troposfeer en ook de organisatie van wolken en mesoschaalcirculaties

controleert. CMT gedraagt zich anders dan warmte- en vochttransport, met een groot compensatie-effect van positieve en negatieve fluxen die elkaar afwisselen in tijd en ruimte, op verschillende schalen. De complexiteit van CMT wordt niet goed weergegeven in de huidige operationele modellen, wat resulteert in significante afwijkingen vanaf het oppervlak tot in de wolkenlaag.

We kwantificeren de afwijking in de wind van het ECMWF Integrated Forecasting System (IFS) tijdens EUREC4A, in de hele lagere troposfeer. Uit de waarnemingen blijkt een te uitgesproken dagcyclus van de wind in het model, met te sterke wind 's nachts en te zwakke wind overdag. Zonder de menging van subgrid SC verslechtert het model de windvoorspelling aan de onderkant van de wolken, terwijl de voorspelling van de wind aan het oppervlak verbetert. Met name de afwijking van de wind neemt af na een verbeterde weergave van de equatoriale diepe convectie, wat een complexe koppeling tussen de mesoschaal en de grote schaal benadrukt.

Daarnaast richten we ons op de verdeling van de CMT over de verschillende schalen. Hiervoor gebruiken we het Dutch Atmospheric Large Eddy Simulation (DALES) model en simuleren we ondiepe convectie met een resolutie van 100 m over een domein van 150×150 km^2 tijdens EUREC4A. We verbeteren het model door de CMT te verdelen over de verschillende schalen. Georganiseerde wolkenvelden, met sterkere convectie, corresponderen met verhoogde mesoschaal bijdragen aan de impulsmomentumtransport.

De rol van de parameterisatie van ondiepe convectie (SCP) in kilometerschaalmodellen wordt onderzocht met behulp van het HARMONIE-AROME model. Uit experimenten met inactieve SCP komen sterke circulaties op mesoschaal, waardoor de bewolking en windprofielen veranderen. Experimenten met inactief SCP produceren sterkere mesoschaal circulaties, waarbij de bewolking en windprofielen veranderen. Ook de verdeling tussen de "resolved-to-sub-grid" flux in zulke scenario's verschilt van wat de LES laat zien. Dit benadrukt de noodzaak van betere parameterisaties op basis van LES en hoge-resolutie observaties.

Ten slotte worden in dit proefschrift nieuwe CMT waarnemingen van de CMTRACE-campagne onderzocht. Deze data bevestigen fouten in de IFS- parametrisering van de CMT, vooral bij actieve convectie. De sub-grid fluxen rond de wolkenbasis worden overschat en geven de geobserveerde variabiliteit niet weer.

De bevindingen in dit proefschrift hebben belangrijke implicaties voor ons begrip van CMT en de rol daarvan in de dynamica van de atmosfeer. Aangezien numerieke modellering en observatiemogelijkheden zich blijven ontwikkelen, is een gezamenlijke benadering van grootschalige observatiecampagnes, geavanceerde LES-opstellingen en mesoschaal-modelleringsexperimenten essentieel. In de toekomst zou prioriteit moeten worden gegeven aan experimentele ontwerpen die de kloof overbruggen tussen geïdealiseerde simulaties en de daadwerkelijke complexiteit.

1

1

INTRODUCTION

"Se non siete curiosi, lasciate perdere."
Achille Castiglioni

1

1.1 ATMOSPHERIC SHALLOW CONVECTION

Imagine a pot of water on the stove. As the water at the bottom warms up, it becomes less dense and rises, while the rest of the fluid makes way and sinks to replace the void. This bulk motion of the fluid is called convection and exhibits typical eddies.
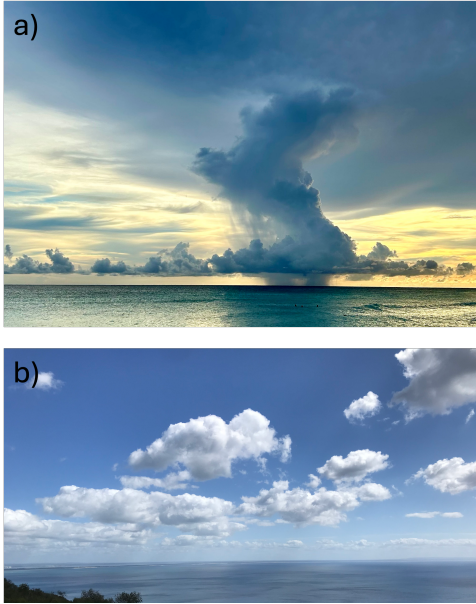
Figure 1.1: Examples of convective clouds. In a) a deep convective cloud reaches the top of the troposphere. This cloud produces rain, while the shallow cumuli around do so less frequently. In b) is a field of non precipitating shallow cumuli.

Convection is driven by buoyancy (defined in the intermezzo) as warmer, less dense fluid rises, and cooler, denser fluid sinks under the influence of gravity. When the Earth's surface is heated by the sun, the lower layer of the atmosphere warms up, generating the same buoyant convection as in the pot of water. Similar to bubbles in the boiling water, convective clouds (or cumuli) help visualise the narrow updraft regions of convective eddies, while the descending motion is usually slower and occurs over larger clear-sky regions.

In the atmosphere, convection transports heat, moisture and momentum (defined in the intermezzo) vertically, actively shaping the thermodynamic and dynamic structure of the (lower) troposphere. Surface buoyancy, which provides the initial vertical "kick" for convection, determines how high a warm air parcel can rise. However, the atmosphere's vertical structure can include layers where temperature increases sharply, reducing the air density. These "inversion layers", such as the tropopause, act as a lid, capping the upward motion of convection.

Deep convective clouds (Figure 1.1 a), typical of the warm and moist equatorial regions, can reach the top of the troposphere, at about 10 km. Shallow convective clouds (Figure 1.1 b) are not as vigorous and are usually confined to the lower 2 km. Dry convection refers to smaller convective eddies confined to the sub-cloud layer, where no condensation occurs.

We define atmospheric shallow convection as a multi-scale process because it can be characterised at multiple spatial scales. Individual shallow cumuli have a horizontal size between a few kilometres and a few tens of kilometres (meso-γ scales), although the updraft region can be less than 1 km wide (sub-meso scales). Furthermore, shallow convection can form coherent patterns on scales between a few tens of kilometres and a few hundreds of kilometres (meso-β scales), as shown later in Figure 1.2.

1

Buoyancy
Let us define an air parcel as an imaginary volume of air that is small enough so that it is approximately uniform and it can move without mixing dynamic and thermodynamic properties with the surrounding air. An air parcel is positively buoyant, thus rises, if its density is lower than the surrounding air, while it is negatively buoyant and sinks if its density is higher than the surrounding air. From the ideal gas law we know that the density of an air parcel depends on its temperature and water content, where moist air is less dense than dry air. The variable virtual temperature T_v is a corrected temperature that represents the temperature a dry air parcel would need to have to match the density of a given moist air parcel. Virtual temperature is defined as:

$$T_v \approx T(1 + 0.61 q_v), \tag{1.1}$$

where q_v is the water vapour content. The buoyancy force is proportional to the difference in virtual temperature between an air parcel and its surroundings.

On its ascent in the troposphere an air parcel undergoes adiabatic expansion as the surrounding air pressure decreases with height. This process cools the parcel and thus reduces its buoyancy. Some air parcels have enough initial buoyancy to reach the so called lifting condensation level (LCL). At the LCL the air parcel has cooled so much that the water vapour carried by the rising parcel condenses and forms a cloud. Condensation heats the parcel, which increases its buoyancy. Parcels rising with similar surface conditions, in terms of temperature and humidity, start condensing at a similar height, explaining the typical flat base of cumulus clouds.

Momentum
Momentum is a vector quantity carried by any moving particle, and it is defined as the product of its mass m and velocity $\mathbf{u}$. This vector is often split into three components on a geographic coordinate system: one associated with the vertical velocity w, and two for the horizontal velocity components u and v, respectively the east-to-west (zonal) and south-to-north (meridional) wind component.

1.2 Importance for the climate system

Shallow cumuli populate many areas of the world across seasons. In The Netherlands, for example, they are often seen during the spring and summer months, associated with fair weather. Shallow cumuli are particularly abundant above the subtropical oceans, between the 10°-30° latitude bands. In these regions, called the trades or trade-wind regions, the warm ocean surface and the gently subsiding motion of the Hadley Cell (Hadley, 1735) maintain favourable conditions, with enough heat and moisture rising from the surface, and a strong trade-wind inversion at the top (Nuijens et al., 2009). The trade winds blow near the surface from north-east to south-west, as part of the converging branch of the Hadley Cell. For centuries, sailors relied on these easterly winds for navigation, giving rise to the term "trades". The North Atlantic trade winds, for example, conveniently blow from the coasts of Europe to Central America and the Caribbeans.

The mixing effect of shallow convection (SC) is critical for climate. By transporting mo-

1

mentum, SC helps regulate the low-level winds that are part of the larger-scale Hadley circulation. This is particularly important for air-sea interaction, because near-surface winds influence fluxes across the air-sea interface, and waves. Shallow convective momentum transport (CMT) also influences mesoscale circulations. These affect the climate by controlling cloud organisation and the cloud radiative effect.

1.2.1 Impact on the large-scale and the surface winds

CMT has long been recognised as a key process for the development of mesoscale and global circulations (Schneider and Lindzen, 1976). Stevens (1979) was among the first to suggest representing the transport of momentum by (unresolved) cumulus clouds in global models. Their analysis revealed a significant residual imbalance in the large-scale momentum budget, characterised by a substantial missing frictional term near the surface and a missing acceleration term in the upper cloud layer. In 2007, Hogan and Pauley reported that accounting for CMT significantly improves the forecast of tropical cyclones. It is now well established that CMT is crucial for the representation of winds, at least near the surface (Richter and Rasch, 2008; Sandu et al., 2020). Despite this, there is still a fundamental lack of understanding around CMT (Badlan et al., 2017).

The role of CMT in regulating surface wind stress and air-sea coupling was explained by Chelton et al. (2001). However, the influence of CMT is not confined to the surface layer; it also modulates the mean climate by redistributing momentum vertically within the atmosphere (Wu et al., 2007). For example, Lin et al. (2008) showed how shallow CMT regulates the wind profiles of the trades, where it reduces the strength of a so called "low-level jet": a local wind maximum around cloud base (Larson et al., 2019).

Convective momentum transport is also intrinsically linked to the turning of the wind with height (Nuijens et al., 2022). This sets weak synoptic-scale vertical motion (Ekman pumping), hence regulating how quickly a low-pressure system fills up (Sandu et al., 2013). More vigorous and organised shallow convection is associated with veering of the wind away from the direction of the pressure gradient, thus reducing convergence on the scale of the Intertropical Convergence Zone (ITCZ) (Nuijens et al., 2022). Without accurately representing these effects, models may fail to capture the realistic evolution of low-pressure systems.

1.2.2 Cloud feedback

Owing to their abundance and ubiquitous geographical extent, small changes in the characteristics of shallow cumuli, in response to a warmer climate, can significantly alter the Earth's system. Any response to a perturbation of the climate system —such as an increase in temperature— is referred to as climate feedback (Bony and Dufresne, 2005; IPCC, 2023). Climate feedback can either intensify or dampen the initial change, making them extremely important to understand and represent in models.

The cloud feedback has been at the centre of research for decades because of its uncertain effect on the earth's climate (Charney et al., 1979; Schneider et al., 2017). In particular, Bony and Dufresne (2005) identify marine subtropical low clouds at the heart of tropical cloud feedback uncertainties. Trade cumuli, for example, cool the planet by reflecting short-wave

solar radiation back to space (Hartmann et al., 1992) while, given their proximity to the surface, have little effect in trapping longwave radiation from Earth. Other than their radiative effect, trade cumuli affect the climate through vertical transport of heat, moisture, and momentum, which mix the lower troposphere. As such, they are not solely markers of convection, but they influence and shape the circulations in which they are embedded (Hwang and Frierson, 2013; Slingo and Slingo, 1988).

Models show an average positive trade-cumulus feedback of 0.5 W m^{-2} K^{-1}, while recent observational evidences show a lower feedback for these clouds (Myers et al., 2021; Vogel et al., 2022). On one hand, models suggest that enhanced cumulus mixing in a warmer climate would dry the lower troposphere, decreasing low-level cloudiness and amplifying positive climate feedback (Vial et al., 2016, 2017). On other hand, recent observations suggest that increased cumulus mixing would invigorate mesoscale circulations, transporting moisture into updraft regions and promoting cloud formation (Vogel et al., 2022). More trade cumuli would then reduce the climate feedback (Brient et al., 2016).

A key uncertainty in this cloud-circulation coupling, or ”mesoscale motion control”, lies in the way convection is spatially organised. Cloud organisation, in particular, refers to the spatial arrangement of clouds. This can range from random distributions to structured patterns, often shaped by interactions between convection, radiation, and dynamics. How will the cloud patterns evolve in response to a warmer climate? And how will such changes be reflected on the circulations and thus on the cloud feedback?

1.2.3 MESOSCALE ORGANISATION

Bony et al. (2015) pointed at convective aggregation as one of the four most pressing scientific puzzles to solve for better understanding the climate system. Wing and Emanuel (2014) showed that any change in convective organisation with a warmer climate can introduce important feedbacks. In fact, model simulations suggest that when convection is more aggregated the atmosphere is drier, clearer, and more efficient at radiating heat to space (Bretherton et al., 2005). Roode et al. (2004) suggested that the development of mesoscale structures, in fields of low-level clouds, is an inherent feature of buoyancy-driven convection. These structures introduce significant fluctuations in moisture, temperature, and horizontal wind fields, making their representation in models essential.

Evidences of clusters in fields of shallow cumuli date back many decades to aircraft observations (Malkus and Riehl, 1964) or to the first images from weather satellites (Agee, 1987). More recently, Nuijens et al. (2014) quantified the distribution and variability of trade-wind clouds suggesting that these are most variable at the mesoscale. Nuijens and Siebesma (2019) recognised the importance of mesoscale organisation in shallow convection for understanding the cloud radiative effect.

There are numerous existing metrics to quantify cloud organisation, most of these rely on projecting the cloud field onto a two-dimensional horizontal plane (Janssens et al., 2021). The simplest metrics include the fractional area covered by clouds (cloud cover) and the mean cloud size. More sophisticated metrics compare the cloud field to a reference field of randomly distributed clouds (Tompkins and Semie, 2017) or incorporate information about the size and proximity of convective elements (Retsch et al., 2020).

A recent subjective, yet interpretable, classification, attempts at providing evocative names for mesoscale trade-cumulus patterns. Based on satellite images, above the North Atlantic trade-wind region, Stevens et al. (2020) identify four patterns:

Sugar: "Dusting of very fine-scale clouds with small vertical extension and little evidence of organisation." (1.2a)

Gravel: "Cloud fields patterned along meso-β (20 to 100 km) lines or arcs defining cells with intermediate granularity, and brighter cloud elements (as compared to Sugar), but with little evidence of accompanying stratiform cloud anvils." (1.2b)

Flowers: "Irregularly shaped meso-β (20 to 200 km) scale stratiform cloud features, often with higher reflectivity cores, and appearing in quasi-regular spaced bunches (hence the plural) with individual features well separated from one another by regions devoid of clouds."(1.2c)

Fish: "Meso-α scale (200 to 2,000 km) skeletal networks (often fishbone-like) of clouds separated from each other, or from other cloud forms, by well-defined cloud-free areas and sometimes accompanied by a stratiform cloud shield." (1.2d)
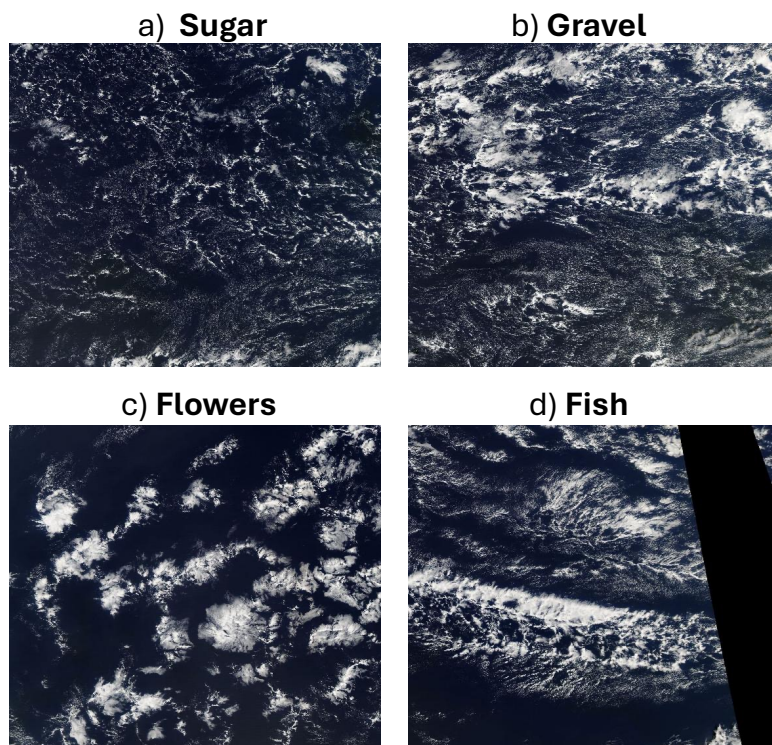
Figure 1.2: Cloud fields over the North Atlantic ocean featuring four patterns. a) Sugar - on 12 December 2015, b) Gravel - on 12 December 2016, c) Flowers - on 7 January 2010, d) Fish - on 10 February 2013. The images show the "true color" product by the MODIS instrument onboard the Aqua satellite. Each figure extend from 10° N to 20° N and from 48° W to 58° W.

This classification in four patterns aids in conceptualising shallow cumuli as collective

structures capable of organising and interacting with their environment on mesoscales. Although simple and somewhat arbitrary, this framework marked a significant advance in analysing the organisation of shallow cumuli and understanding their variability (Beucher et al., 2022; Dauhut et al., 2023; Schulz et al., 2021; Vial et al., 2021).

While observing the spatial organisation of clouds is relatively simple, observing the organisation of the wind flow around clouds is extremely more challenging. With recent measurements from the field campaign EUREC4A (see section 1.4.1), George et al. (2023) first observed structures in the mesoscale wind flow of the trades, raising further questions on the coupling between shallow clouds and mesoscale circulations.

1.3 Modelling shallow convection

The idea of modelling the atmosphere to predict its evolution began with the pioneering work of the British mathematician and physicist Lewis Fry Richardson in the early 20th century. In 1922, Richardson introduced the concept of using hydrostatic variation of Bjerknes's primitive equations to simulate weather patterns. However, the attempt was ultimately unsuccessful due to the unbalanced initial state of the atmosphere and the lack of computational resources. It was not until the development of computers in the mid-20th century that numerical weather prediction (NWP) became feasible, transforming atmospheric modelling into a cornerstone of modern meteorology.

Atmospheric motion is governed by the laws of thermodynamics, gas, and fluid mechanics. The so-called primitive equations describe the three fundamental physical relations of conservation of energy, conservation of mass, and conservation of momentum (via the Navier-Stokes equations). Any modern weather model uses a set of simplified equations to evolve the humidity and temperature scalar fields, and the flow velocity vector field through time. For computation, these equations are discretised on a three-dimensional grid and each grid box is described by averaged variables. This truncation requires that all sub-grid scales are either neglected or approximated by parameterisations. Parameterisations are simplified statistical relationships between the resolved variables and the unresolved sub-grid processes (see section 1.3.2).

A turbulent flow, such as that in a convective atmosphere, exhibits fluctuations spanning a continuous spectrum of spatial and temporal scales. Even with high-frequency observations or high-resolution models, a turbulent flow will always include frequencies beyond what can be measured or resolved. For this reason, it is useful to express variables (*e.g.* humidity, temperature, and momentum) as the sum of a mean, denoted by an overbar, and a fluctuation relative to the mean, denoted by a prime symbol. This approach, known as Reynolds decomposition, is mathematically represented as follows for the wind vector $\mathbf{u}$:

$$\mathbf{u} = \overline{\mathbf{u}} + \mathbf{u}'. \tag{1.2}$$

The scale at which the atmospheric flow is decomposed into mean $\overline{\mathbf{u}}$ and anomaly $\mathbf{u}'$ is strongly dependent on the situation: for example, the size of the studied region, or the size of a model grid box. After neglecting any viscous stress and applying the Reynolds

1

decomposition, the primitive equation for horizontal winds (conservation of momentum) reads:

$$\begin{cases} \frac{\partial \overline{u}}{\partial t} + \overline{u}\frac{\partial \overline{u}}{\partial x} + \overline{v}\frac{\partial \overline{u}}{\partial y} + \overline{w}\frac{\partial \overline{u}}{\partial z} = +f\overline{v} - \frac{1}{\rho}\frac{\partial \overline{P}}{\partial x} - \frac{\partial \overline{u'w'}}{\partial z}, \\ \frac{\partial \overline{v}}{\partial t} + \overline{u}\frac{\partial \overline{v}}{\partial x} + \overline{v}\frac{\partial \overline{v}}{\partial y} + \overline{w}\frac{\partial \overline{v}}{\partial z} = -f\overline{u} - \frac{1}{\rho}\frac{\partial \overline{P}}{\partial y} - \frac{\partial \overline{v'w'}}{\partial z}, \end{cases} \quad (1.3)$$

where the first term on the lhs represents the storage of momentum or tendency, and the other three terms on the lhs together represent advection. On the rhs, f is the Coriolis parameter and its term describes the influence of the Earth's rotation. The second term on the rhs describes the pressure gradient force, where ρ is the density of moist air. The last term on the rhs is the divergence of the turbulent momentum flux, which represents the influence of Reynolds' stress (or fluctuations) on the mean motion.

The last term of equation 1.3 is particularly studied in atmospheric modelling because it can be used to include all unresolved processes at scales smaller than the model resolution, for example the transport by convection. Convection is often treated as a turbulent process superimposed on the mean flow. Consequently, atmospheric convection generates a vertical flux of horizontal momentum which can be expressed in the form of a Reynolds stress as:

$$\rho\overline{u'w'}, \qquad \rho\overline{v'w'}, \quad (1.4)$$

where the terms $\overline{u'w'}$ and $\overline{v'w'}$ represent the covariances of the vertical wind component with the zonal and meridional wind components, respectively. This turbulent flux within a mean flow, whereby the mean is indicated by the overbar, which represents the transfer of a quantity per unit area per unit time, is expressed in kinematic units by dividing by the density of moist air. The momentum fluxes in kinematic units ($\overline{u'w'}$ and $\overline{v'w'}$) are thus expressed in $m^2 s^{-2}$.

1.3.1 Types of atmospheric models

The ever increasing computational capabilities allow for finer and finer grids, meaning that there are less unresolved eddies to be parameterised. The first global models operated with horizontal grid spacing of several hundreds of kilometres (Bengtsson et al., 1982; Phillips, 1956). In recent years, global simulations at resolutions of a few kilometres became possible (Stevens et al., 2019), but computational costs remain a significant limitation to numerical weather prediction.

An effective approach to overcome this limitation and to model the multitude of scales of atmospheric flow is to use different models tailored to specific problems. Very high-resolution simulations are too expensive to be run globally, but they are feasible with a limited domain and short time range, while global simulations can be run at a coarser resolution with less detail. This multitude of tools with different levels of detail boosted rapid understanding of a wide range of atmospheric processes. We can classify three types of models based on the scales they aim to represent:

1. **Hydrostatic models** assume that the vertical pressure gradient is balanced by gravity, an approximation that simplifies the governing equations by neglecting vertical

accelerations. This makes them computationally efficient and suitable for simulating large-scale atmospheric phenomena, such as global circulation and synoptic-scale weather patterns, typically at resolutions coarser than 10 km. These models are widely used for climate simulations and medium- to long-range weather forecasting. However, they are not suitable for resolving vertical accelerations associated with convection or small-scale turbulence. Figure 1.3 a) shows the global cloud field on 26 November 2024 simulated with the Integrated Forecasting System (IFS) with 9 km grid spacing.

2. **Mesoscale models**, also referred to as storm-resolving models, are designed to simulate the atmospheric phenomena on scales ranging from a few kilometres to hundreds of kilometres. These include thunderstorms and clustered convective systems. Unlike hydrostatic models, they include the effects of vertical accelerations by solving the full set of governing equations without assuming hydrostatic balance. This allows them to accurately capture the vertical motions and processes critical to storm dynamics and convective activity. Mesoscale models are widely used for high-resolution weather forecasting and research into regional atmospheric processes. The outer domain in Figure 1.3 b) shows a cloud field simulated with the mesoscale model HARMONIE-AROME with 2.5 km grid spacing.

3. **Large Eddy Simulations (LES)** are models with grid spacing smaller than 1 km, specifically useful to study turbulence and small-scale atmospheric processes. LES directly resolve large turbulent eddies while parameterising the smaller eddies with a 3D scheme. While 1D schemes, used in hydrostatic and mesoscale models, assume that turbulence is predominantly driven by vertical mixing, 3D turbulent schemes represent turbulence in all three spatial dimensions. LES provide a much finer understanding of atmospheric dynamics at a local or micro scale. In studies of convective boundary layers they have been typically used with grid spacing ranging from a few tens to a few hundreds of metres. Until recently, such resolutions would only allow for domains smaller than 100 x 100 km^2. The orange domain in Figure 1.3 b) spans 150 x 150 km^2 and shows a cloud field simulated with 100 m grid spacing by the Dutch Atmospheric Large Eddy Simulation (DALES).

Simulations with a limited domain require assumptions about the boundary flow, which limit a holistic view of the system. With periodic-boundary conditions the domain "wraps around" and the flow re-enters the domain from the opposite side to where it leaves. In this case, large-scale forcing can be imposed on the domain as a bulk external force that represents the large-scale atmospheric dynamics. With open-boundary conditions the flow enters and leaves the boundaries as imposed by a "parent" model in which the limited area model is embedded. In this case, the large-scale forcing is directly passed at the boundaries together with any mesoscale system resolved by the parent model. The reverse feedback, from the limited area model to the parent model, remains challenging to implement, although some workarounds exist (Moeng et al., 2007).

Any discretisation of the atmospheric flow implies assumptions on the separation of scales. There is always a process that occurs at the scale of the model resolution. This "grey zone" problem is a challenge intrinsic to discretising the atmosphere. In the grey zone a

1

process is not fully resolved nor fully sub-grid, challenging its representation (Honnert, 2019; Wyngaard, 2004). Several studies have tried to identify the range of scales where shallow convection occurs (Dorrestijn et al., 2013; Nuijens et al., 2014), while others have tried to partition the process between resolved and unresolved components for model resolutions within the grey zone (Gerard, 2007; Honnert et al., 2011; Yu and Lee, 2010).

With the recent computational improvements, the resolutions and domains of the different models often overlap, so that km-scale storm-resolving models are run globally and LES can cover tens of thousands of km^2. This brings new opportunities to study the interaction between the sub-meso scales and the global scale, though the smaller convection and the turbulence require a level of detail that is still far from possible with the latest global km-scale models.

Many of the assumptions in the models' formulation are resolution-dependent. This means that there are challenges in adapting the parameterisations to run at different resolutions and across various domains from those for which they were originally designed. For the new generation of models three difficult question need to be addressed: 1. When is shallow convection fully resolved? 2. How should we handle resolutions that only partly resolve shallow convection? 3. What sub-grid processes become relevant as model resolution increases?

Figure 1.3: In panel a) is the cloud field as simulated with the hydrostatic global model Integrated Forecasting System (IFS) for 26 November 2024. In panel b) is the cloud filed simulated by the mesoscale model HARMONIE-AROME (outer domain) for 3 February 2020. The inner orange domain in panel b) shows the cloud field simulated by the Dutch Atmospheric Large Eddy Simulation (DALES) for the same day.

1.3.2 Parameterising shallow convection

The grid sizes of global and regional models are generally larger than individual convective updrafts and downdrafts, but fine enough to resolve some mesoscale convective structures. It is common for models to split the sub-grid turbulent flux of a general variable ϕ into a local, diffuse contribution and a non-local –buoyancy driven– contribution. Local diffusive mixing is parameterised with a turbulence or eddy-diffusivity (ED) scheme, while the non local transport is parameterised in the convection (C) schemes. For the flux $\overline{\phi' w'}$, this partition reads:

1

$$\overline{\phi'w'} = \overline{\phi'w'}^{ED} + \overline{\phi'w'}^{C}. \tag{1.5}$$

The eddy-diffusivity scheme simply dissipates the local gradient of ϕ along the vertical dimension z. The turbulent flux is thus written as:

$$\overline{\phi'w'}^{ED} = -K\frac{\partial\overline{\phi}}{\partial z}, \tag{1.6}$$

where K is the eddy-diffusivity.

Convection schemes are often divided into shallow and deep convection schemes and are intended for larger scale, intermittent vertical motions driven by buoyancy and latent heat release, leading to cloud and precipitation formation. Before 1969, convection parameterisations were simple adjustments to a moist adiabat: oversaturated air is cooled back to its saturated profile and the excess moisture removed through precipitation. In 1969, Akio Arakawa introduced a new cumulus convection parameterisation for the general circulation model developed at the University of California, Los Angeles. Along the lines of this convective parameterisation, Ooyama (1971) firstly formulated the mass-flux approach, which was further improved by Arakawa and Schubert (1974).

The mass-flux approach assumes that a fraction a_c of a model's grid box is covered by cumulus clouds or "convective plumes" with properties that are different from the environment. The fractional area a_c must be much smaller than the total grid box area, and the physical variables associated with each plume are only functions of height, meaning that a plume is horizontally homogeneous (top-hat approximation).

With the above approximations, the turbulent flux carried by sub-grid convection is written as:

$$\overline{\phi'w'}^{C} = a_c(w_c - \overline{w})(\phi_c - \overline{\phi}), \tag{1.7}$$

where the subscript c indicates a cloud property, a_c is the area fraction covered by convection and w_c the vertical velocity inside the convection. Introducing the mass flux term $M_c = \rho a_c(w_c - \overline{w})$, equation 1.7 can be rewritten as:

$$\rho\overline{\phi'w'}^{C} = M_c(\phi_c - \overline{\phi}), \tag{1.8}$$

where only M_c and ϕ_c need to be estimated to have an estimate of the sub-grid flux.

The mass-flux approach is resolution dependent and neglects the role of organisation (Redelsperger, 1997). Furthermore, the same parameterisation is applied to the transport of momentum as well as the transport of temperature and humidity, despite the differences between vector and scalar quantities (see section 1.3.3). Convective transport of horizontal momentum ($\phi = [u,v]$) is less understood and studied than the convective transport of temperature and humidity. Among the reasons for this lack of study are the difficulties in measuring winds (see section 1.4), and in modelling realistic mesoscale flows.

1

1.3.3 Momentum transport

Accurate prediction of mesoscale winds (for cloud organisation) and sub-mesoscale winds (for wind energy) is increasingly relevant, and the representation of unresolved components of the momentum budget (convection, turbulence, gravity waves) require scrutiny. Models are hampered by inadequate formulations of such process (Brown, 1999; Kershaw and Gregory, 1997; Zhang and Cho, 1991). Zhu (2015) investigated the extent to which momentum flux can be represented by a mass-flux approach. Using LES, they identify four shortcomings:

1. The top-hat approximation is overly simplistic for the distribution of momentum in the cloud layer.

2. Large coherent eddies are less efficient in transporting momentum compared to smaller shear-driven eddies.

3. The in-cloud pressure gradient is important for the momentum budget since horizontal momentum is not conserved in adiabatic motion.

4. The structure of horizontal momentum is highly variable even within the same climate regime.

Despite the similarities in the budget equations with scalar quantities like heat and moisture, momentum is a vector and a non-conservative quantity during mass transport. For example, momentum is exchanged with the environment through pressure perturbations and drag. As the atmosphere becomes more convective and organised, the momentum transport becomes increasingly inefficient compared to scalars (Li and Bou-Zeid, 2011). Unlike heat and moisture transports, reliable estimates of convective momentum transport are difficult to obtain (e.g. Carr and Bretherton, 2001; Tung and Yanai, 2002a,b; Wu and Yanai, 1994). Consequently, the development and evaluation of CMT parameterisation has been a challenging problem for a long time, despite some new parameterisations have been proposed (Lappen and Randall, 2001).

Turbulent fluxes of heat tend to be positive as buoyancy makes warm anomalies ($T_v' > 0$) go upward ($w' > 0$) and cold anomalies ($T_v' < 0$) go downward ($w' < 0$). The same is not true for momentum where an upward displacement of air ($w' > 0$) can carry horizontal winds that are stronger or weaker than average. Furthermore, the sign depends on the direction of the mean wind so that $u' > 0$ indicates zonal winds stronger than average if the mean zonal wind is negative (east-to-west), but it indicates zonal winds weaker than average if the mean zonal wind is positive (west-to-east).

Momentum transport is often thought of as a "down-gradient" diffusive process, meaning that it acts to reduce the vertical wind gradient, or shear. This involves slow winds near the surface being carried upwards, where they slow down the faster winds aloft. Conversely, the downward branch of an eddy transports faster winds from higher levels downwards, increasing surface wind speeds. In 1983, LeMone observed that the vertical transport of horizontal momentum can be against the vertical momentum gradient. This "counter-gradient" transport implies a strengthening of the wind shear contrary to what a down-gradient diffusive model would predict.

Counter-gradient transport of momentum can happen when the wind profile has a local maximum or minimum (Larson et al., 2019). Convection is a non-local process that can transports momentum from distant atmospheric layers against the local gradient. In the trades, for example, winds strengthen from the surface to around cloud base, but they weaken aloft. This means that an air parcel, lifted from the slow moving surface layer to above the local wind jet at cloud base, can enhance the already existing wind gradient above cloud base.

Down-gradient and counter-gradient momentum transport are also intrinsically linked to the mesoscale organisation of convective systems (Grant et al., 2020; Moncrieff, 1981, 2019). Less organised convection decelerates environmental flow, whereby CMT is down-gradient, reducing vertical shear of horizontal wind. However, organised convection, such as squall lines, can generate an in-cloud horizontal pressure gradient that acts to accelerate the environmental flow and enhance vertical shear (Tung and Yanai, 2002b).

The sign of momentum transport by organised eddies propagating in a shear flow is a fundamental property of their tilt relative to the shear vector (Moncrieff, 1992). In Figure 1.4 is an eastward moving system under positive environmental shear. The up-shear-tilted eddy (a) carries negative momentum flux, while the down-shear-tilted eddy (b) carries positive momentum flux. For an eastward moving system with positive wind shear, a negative momentum flux (a) is down-gradient, while a positive momentum flux (b) is counter-gradient.
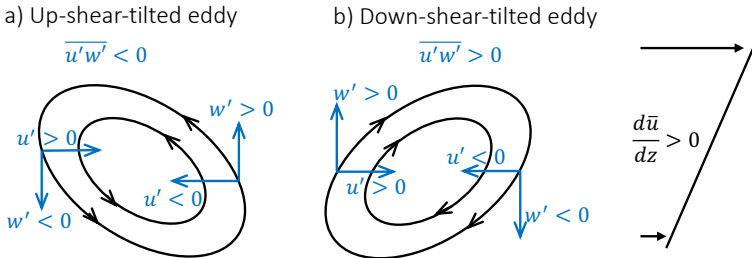
Figure 1.4: Schematic diagram of a) upshear-tilted and b) downshear-tilted organised eddies in a positively sheared flow associated with negative and positive momentum fluxes respectively. Adapted from Moncrieff (1992)

Despite these and other early milestones (LeMone et al., 1984; LeMone and Moncrieff, 1994; LeMone and Pennell, 1976), the structure and role of momentum flux in different cloud fields remains unclear. A major challenge lies in understanding how CMT is related to cloud spatial organisation. This topic only began to receive attention in studies of low-level clouds, such as stratocumuli and shallow cumuli, in the early 2000s (Carr and Bretherton, 2001), when advances in modelling allowed exploration at finer scales.

Schlemmer et al. (2017) combined idealised LES and global model experiments to highlight the importance of small scale turbulence for the momentum budget, even in the cloud layer. Helfer et al. (2021) made a further step in investigating the frictional effect of shallow CMT through more realistic LES experiments. They found that resolved advection and unresolved turbulent stresses together decelerate the easterly trade winds in a layer extending from

1

the surface to about 2 km, thereby balancing the two other key components of the mean momentum budget: the pressure gradient and Coriolis forces. Mesoscale motions appeared particularly important between 500 and 800 m (in the upper half of the well-mixed layer) whereas at 1 km (in the lower cloud layer at the level of a wind jet) unresolved turbulent stresses played a larger role.

These results, highlighting the importance of mesoscale flow, might still be limited and sensitive to the size of the domain, which spanned only 50 x 50 km^2. Dixit et al. (2021) showed how periodic boundary conditions and limited domain sizes can dampen the mesoscale circulations and counter-gradient momentum transport. With a significantly larger domain (100 x 100 km^2), Saggiorato et al. (2020) showed the richness of wind structures under a field of shallow cumuli. This evidence has led us to appreciate that a shallow convective atmosphere is much more complex and rich than it was ever simulated or measured, with circulations on scales between 100 m and 100 km. In light of current high resolution model developments, it is instrumental to gain more observational perspective on CMT.

1.4 Observational perspectives on wind-cloud relationships

The Barbados Oceanographic and Meteorological Experiment (BOMEX; Holland and Rasmusson (1973)) was among the first to provide measurements of mass, energy, and momentum budgets at the synoptic scale over the tropical ocean. This campaign, and the related model intercomparison by Siebesma et al. (2003), shifted our understanding of how tropical boundary layers function, and what sets the momentum budget. Brümmer et al. (1974) showed that models were missing a frictional component compared to what observed in BOMEX. This large residual in the momentum budget motivated the hypothesis that vertical momentum transport involves more than just diffusive turbulence, and could be attributed to organised convective motion. Even though it unlocked great understating of trade cumuli, BOMEX did not measure the meso- and sub-meso scales, and it provided a limited picture of the trades, as the field campaign was in a period populated mostly by non-precipitating, unorganised shallow cumuli.

The widespread presence of rain and its coupling with the winds and the cloud (*e.g.* through cold pools) became possible and evident thanks to the "Rain in shallow Cumulus over the Ocean (RICO)" campaign (Rauber et al., 2007), which focused on measuring cloud microphysics in the trades. With data from RICO, Nuijens et al. (2009) showed how stronger winds are associated with stronger precipitation. Their hypothesis was that stronger winds drive stronger surface fluxes, which moisten the cloud layer (Nuijens and Stevens, 2012). However, the coupling between winds and rain, or between winds and convection, is more intricate, where convection itself can affect the winds through the driving circulations or cold pool gust fronts. The work done in this thesis is motivated by this recent awareness and it is enabled by novel measurement of the winds in complex cloud atmospheres, from the EUREC4A (section 1.4.1) and the CMTRACE (section 1.4.2) field campaigns.

1

1.4.1 EUREC4A

The EUREC4A field campaign was conducted over the North Atlantic between 12 January and 23 February 2020 (Stevens et al., 2021). It is an international initiative that constitutes a key study in support of the World Climate Research Programme's Grand Science Challenge on Clouds, Circulation and Climate Sensitivity. The aim is to advance understanding of the interplay between clouds, convection and circulation and their role in climate change. More than 40 partner institutions were involved, with four research aircraft, four research vessels, ground measurement stations, and satellite remote sensing all contributing to the campaign.
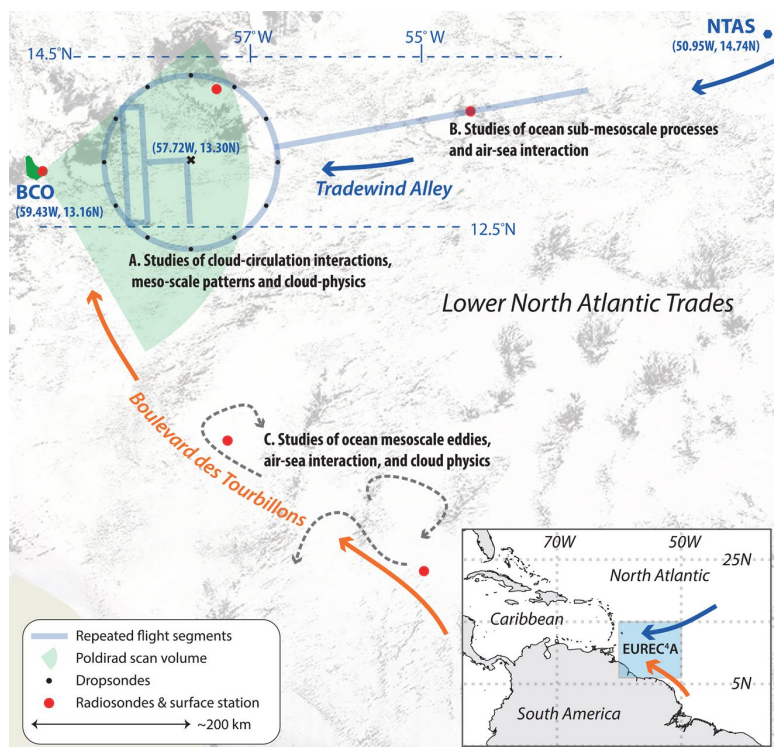
Figure 1.5: Sketch of the EUREC4A study area Stevens et al. (2021). The Tradewind Alley (study area B) is a zonally oriented band following the direction of the trades between the Northwest Tropical Atlantic Station (NTAS) and the Barbados Cloud Observatory (BCO). The "EUREC4A-Circle" (study area A) is defined by the circular airborne sounding array centred at 13.3N, 57.7W. The background shows a negative of the cloud field taken from the 5 February 2020 MODIS-Terra (ca. 14:30 UTC) overpass.

Figure 1.5 shows the study area, off the coast of Barbados, and offers a quick-look of the measurement strategy, characterised by circular flights. For the campaign, a total of 2500 balloon and parachute borne soundings (dropsondes) of the atmosphere were used. In particular, the novelty of launching multiple dropsondes along a circle with diameter of 220 km, allowed to measure the mesoscale flow on scale of the circle (George et al., 2021a). Measurements from EUREC4A have been the first to illuminate the climatic role of

mesoscale circulations and are helping to assess their influence on crucial climate processes such as cloud-circulation coupling and convective momentum transport.

1.4.2 CMTRACE

The CMTRACE (tracing convective momentum transport in complex cloudy atmospheres) project organised three field campaigns with the aim of measuring high frequency wind profiles in the sub-cloud and cloud layer of complex convective boundary layers. The campaigns measured various cloud regimes, including non-precipitating shallow cumulus clouds, deep convective clouds and stratiform clouds. The measurements took place at the Cabauw Experimental Site for Atmospheric Research (CESAR) in The Netherlands, which features a 213-m high meteorological tower and a wide range of advanced ground-based remote-sensing facilities (Figure 1.6).
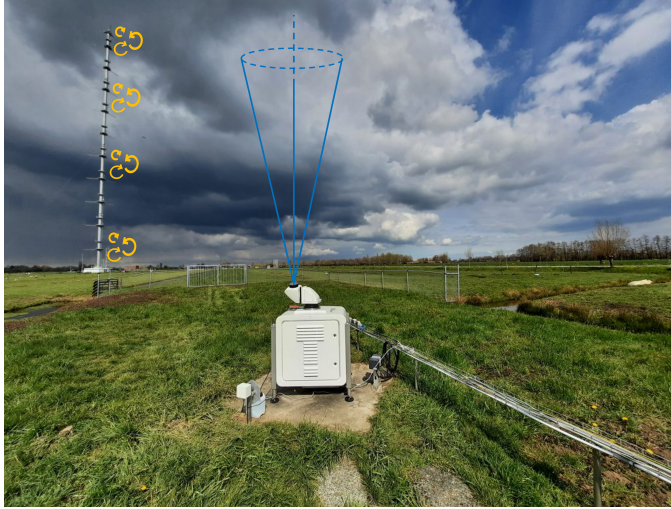
Figure 1.6: Picture of the Cabauw site featuring the tower on the left and a wind lidar (Vaisala WindCube 200s) in the middle. The yellow arrows depict turbulence measured by sonic anemometers at 5 m, 60 m, 100 m, and 180 m. The blue lines help visualise the scanning technique of the lidar, which draws an upside down cone and before pointing in the vertical direction.

The CMTRACE campaigns use collocated wind lidar and radar measurements with a novel scanning technique to measure the three wind components. This innovative setup takes advantage of the synergy of using wind lidars to retrieve wind profiles in the boundary layer and cloud radars to retrieve wind in the cloud layer. The first campaign, in September 2021, deployed one wind cube lidar and two radars, where the lidar would perform every ~ 1 min a scan to retrieve horizontal winds, followed by a vertical measurement to retrieve vertical velocity (see blue lines in Figure 1.6). During the second campaign (May and June 2022) and third campaign (summer 2023), an additional wind lidar allowed to have one instrument always vertically pointing, and the second instrument always scanning, further increasing the resolution. Dias Neto et al. (2023) show the success of the experimental setup and point at possible applications of the CMTRACE dataset, which range from model

validation, to the analysis of scales accompanying diverse cloud fields, process studies of momentum transport, and transport of scalars (e.g. air pollution).

1.5 Aim and outline

The representation of unresolved momentum transport by shallow convection can impact both the short-term local winds and the general circulation of the atmosphere. As shown in the previous sections, the current understanding of CMT is largely based on idealised simulations of limited cloud cases that broadly oversimplify nature. In nature, complex cloud fields are the rule rather than the exception, motivating the following question:

How does CMT influence and depend on organised shallow cumulus fields?

Answering this question, this thesis aims to advance the understanding of shallow convective momentum transport (CMT) in real weather conditions, and explore the implication for numerical weather prediction models. We build on the hypothesis that mesoscale circulations and shallow cloud organisation are linked to CMT, and that they play a non-negligible role in setting wind profiles. New model experiments, combined with new ground-based remote sensing observations, are exploited to trace CMT in realistic atmospheres in which mesoscale flows are prominent. With this, we try to realistically account for atmospheric complexity and investigate the mesoscale contribution to momentum fluxes.

We use an hierarchy of models, combining the strength of LES, mesoscale models, and hydrostatic models. The Dutch Atmospheric Large Eddy Simulation (DALES) allows us to simulate convective processes down to the scale of 100 m, still maintaining a large domain of 150 x 150 km^2, and accounting for realistic boundary conditions taken from the mesoscale model HARMONIE-AROME. The latter model, operated by the Royal Netherlands Meteorological Institute (KNMI), is extensively used in this thesis. With a resolution of 2.5 km, it is also employed to analyse the response of kilometre-scale modelling to different formulations of the shallow convection scheme. Finally, the Integrated Forecasting System (IFS) of the European Centre for Medium-Range Weather Forecasts (ECMWF) completes the hierarchy, with a resolution of 9 km and global coverage.

We complement the simulations with novel observations of the atmospheric flow at the mesoscale. The EUREC4A and CMTRACE field campaigns provide state of the art measurements to tackle the fundamental challenge of identifying mechanisms key to CMT and determining the importance of CMT in comparison to other (drag) processes. EUREC4A is exploited to understand the cloud-circulation coupling and the response of the cloud field to CMT. CMTRACE provides great information on the scales at which momentum is transported and allows for a direct evaluation of the parameterised momentum flux in IFS.

The content of this thesis is organised so that each chapter addresses a specific aspect of the overarching goal.

1. **Relationship between CMT and shallow organised convection.**

   (a) How are different scales contributing to momentum fluxes in organised and unorganised cloud fields? (Chapter 3)

1

(b) How does low-level cloudiness, including its organisation and accompanying mesoscale circulations, depend on parameterised transport of heat, moisture, and momentum by shallow convection? (Chapter 4)

2. **Uncertainties in parameterised CMT and winds.**

(a) What is the role of subgrid momentum transport on the IFS wind bias? (Chapter 2)

(b) Does the current parameterisation of sub-grid CMT in IFS adequately represent nature? (Chapter 5)

In **Chapter 2**, we take a fresh look at the lower-tropospheric winds bias under shallow convective regimes for one of the most well established global models: the Integrated Forecasting System (IFS) of the European Centre for Medium-Range Weather Forecast (ECMWF). With unique measurements from the EUREC4A field campaign, we investigate the origin of this bias and we explain the role of parameterised shallow CMT on the mean winds.

In **Chapter 3**, we design and perform an high-resolution simulation of EUREC4A, which helps reveal how different scales contribute to momentum fluxes in the boundary layer. The novelty of our LES experiment is the large size of the domain (150 x 150 km^2) and the realistic boundary conditions. This chapter sheds light on the link between cloud organisation and the scales of shallow cumulus mixing. This chapter highlights limits of the way CMT is currently parameterised in coarser resolution models.

Within the context of EUREC4A, in **Chapter 4**, we use a storm permitting model with three different configurations of the shallow cumulus parameterisation. This allows to evaluate the mesoscale cloud representation of kilometre-scale models and its dependency on the shallow cumulus parameterisation. The chapter characterises and explains the influence of parameterised CMT and shallow convection on the cloud circulation coupling.

In **Chapter 5**, we complement what we learned in the previous chapters about CMT over the tropical Atlantic. This chapter provides an evaluation of the sub-grid momentum fluxes in IFS over land at mid-latitudes. Simulations of the CMTRACE field campaign with IFS highlight conceptual limits of the current parameterisation and allow to extend the conclusions of previous chapters from tropical ocean to mid-latitude land.

Finally, **Chapter 6** provides the main conclusions of this thesis, an outlook on the most pressing remaining questions around CMT, and recommendations for further studies.

2

THE REPRESENTATION OF THE TRADE WINDS IN ECMWF FORECASTS AND REANALYSES DURING EUREC^{4}A

This chapter is published as:

The characterization of systematic forecast errors in lower-tropospheric winds is an essential component of model improvement. This paper is motivated by a global, longstanding, surface bias in the operational medium-range weather forecasts produced with the Integrated Forecasting System (IFS) of the European Centre for Medium-Range Weather Forecasts (ECMWF). Over the tropical oceans, excessive easterly flow is found. A similar bias is found in the western North Atlantic trades, where the EUREC4A field campaign provides an unprecedented wealth of measurements. We analyse the wind bias in the IFS and ERA5 reanalysis throughout the entire lower troposphere during EUREC4A. The wind bias varies greatly from day to day, resulting in RMSE's up to 2.5 m s^{-1}, with a mean wind speed bias up to -1 m s^{-1} near and above the trade-inversion in the forecasts and up to -0.5 m s^{-1} in reanalyses. These biases are insensitive to the assimilation of sondes. The modeled zonal and meridional wind exhibit a too strong diurnal cycle, leading to a weak wind speed bias everywhere up to 5 km during daytime, but a too strong wind speed bias below 2 km at nighttime. Removing momentum transport by shallow convection reduces the wind bias near the surface but leads to stronger easterly near cloud base. The update in moist physics in the newest IFS cycle (cycle 47r3) reduces the meridional wind bias especially at daytime. Below 1 km, modelled friction due to unresolved physical processes appears too strong, but is (partially) compensated by the dynamics, making this a challenging coupled problem.

2.1 Introduction

Accurate wind predictions are vital for renewable wind energy generation, which has experienced substantial growth in the last decade (Foley et al., 2012). An improvement in the representation of horizontal winds is also necessary for a stepwise change in the realism of climate projections, as they redistribute energy, moisture and momentum, and can drive cloud patterns (Bony et al., 2015).

Motivated by this need to improve the representation of winds in weather and climate models, we take a fresh look at one of the most systematic and longstanding biases in forecasts of near-surface weather, i.e. the biases in lower-tropospheric winds (Brown et al., 2006, 2005; Hollingsworth, 1994; Sandu et al., 2013).

The characterization of systematic forecast errors in tropospheric winds over the ocean, and the understanding of their causes, is largely limited by the availability of observations of the wind profile. Apart from island radiosonde launches and near-surface measurements from buoys, there are no regular wind profiling observations over the oceans, including the tropical Atlantic Ocean (Brown et al., 2005). Only the Aeolus satellite mission provides since 2019 (Rennie et al., 2021; Stoffelen et al., 2005) a global coverage of tropospheric winds, but with a footprint on the order of 100 km, a vertical resolution on the order of 500 m, and systematic errors of ~2 m s^{-1} (Witschas et al., 2020), its resolution and accuracy is hardly sufficient to evaluate the forecast wind biases in the lower troposphere.

ASCAT scatterometer provides near-surface measurements of the winds at a resolution of about 25 km with random errors of ~0.7 m s^{-1} per component. ASCAT measurements have been used to evaluate at a global scale the medium-range forecasts and ranalyses produced with the Integrated Forecasting System (IFS) of the European Centre for Medium-Range Weather Forecasts (ECMWF) (Sandu et al., 2020). The 10-m wind speeds over the oceans were shown to be biased by up to 0.5 m s^{-1} compared to ASCAT scatterometer observations in the ECMWF reanalyses: ERA-Interim, where ASCAT data are not assimilated, (Dee et al., 2011) and ERA5, where ASCAT data are assimilated, (Belmonte Rivas and Stoffelen, 2019; Hersbach et al., 2020). In particular the reanalyses show excessive mean easterlies and too weak mean meridional winds in the trade region (Belmonte Rivas and Stoffelen, 2019). These biases may seem small, but they can introduce a large bias in the wind stress, which is a function of the wind speed squared. Such a wind stress bias could result in significant errors in ocean-atmosphere coupling and climate prediction (Chelton and Freilich, 2005).

Belmonte Rivas and Stoffelen (2019) also demonstrated that errors in the mean surface wind speed and direction in ERA-INTERIM and ERA5 are accompanied by errors in the transient component of the winds, defined as root mean square of the departure from the mean. The reanalyses underestimate the variability of the transient wind, which could be due to a misrepresentation of the mesoscale convective variability, and wind shear, as previously suggested by Houchi et al. (2010).

Although successive changes to the ECMWF Integrated Forecasting System (IFS) reduced the near-surface wind error over the oceans throughout the years, its typical global signature remains (Sandu et al., 2020). Sandu et al. (2020) analysed in more detail the wind profile forecast errors over the trade-winds region east of Barbados, on which we also focus in this

2

study. They showed that the model analysis (initial condition of the forecasts) is uncertain in the lowest part of the troposphere, particularly in the cloud layer, where it is most poorly constrained by observations. The IFS wind errors develop in the first 12 hours of the forecast and do not grow significantly until day five. Excessive zonal surface winds are not a widespread characteristic of day 5 forecasts, as is the case in short-range forecasts. This suggests that the cause of the bias lies in processes that act on fast time scales. Sandu et al. (2020) also explored the influence of convective momentum transport (CMT) by the abundant shallow convection in this region and showed that it plays an important role in communicating wind biases that are present at cloud levels towards the surface, hinting that the biases may be established at levels above the surface layer.

Here we exploit a unique opportunity offered through the EUREC4A field campaign (Stevens et al., 2021) to assess wind biases in medium-range forecasts and reanalyses produced with the IFS, not only at the surface but throughout the lower troposphere. Between January and February 2020 the EUREC4A field campaign took place in the oceanic trade-winds region east of Barbados, where no in-situ observations are regularly made. EUREC4A is among the largest observational field campaigns of the coupled atmosphere-ocean system and it provided benchmark measurements for a new generation of models and scientific discoveries. The duration of the campaign and the large communal effort resulted in an unprecedentedly comprehensive record of tropospheric winds in the trades. In particular, during EUREC4A more than 1200 dropsondes, 800 radiosondes and a total of six wind lidars were deployed (Stevens et al., 2021), allowing a detailed study of the vertical structure of the winds and circulations in the boundary layer.

For the EUREC4A period we show (Figure 2.1) global maps of the surface wind bias with respect to ASCAT as in Sandu et al. (2020). As already suggested by Sandu et al. (2020), the surface bias near Barbados is representative of the entire trade region and during the campaign the bias is consistent with the average for the winter time. On average, the zonal component is overestimated and the meridional component is underestimated.

Some aspects of the systematic error in surface winds from weather models have been described in the literature, for instance the insufficient mesoscale variability in the extratropics (Gille, 2005), the lack of small-scale features relevant for sea surface temperature (SST) gradient effects (Chelton et al., 2004; Risien and Chelton, 2008) and the generally excessive zonal winds (Belmonte Rivas and Stoffelen, 2019; Chaudhuri et al., 2013; Sandu et al., 2020). In the northern hemisphere there is a clear veering of the forecasted surface wind direction with respect to observations leading to a smaller wind turning angle between the forecasted surface wind and the forecasted geostrophic wind than that seen in observations (Sandu et al., 2020).

In this study we focus on the representation of the vertical profile of winds during EUREC4A in operational forecasts and the ERA5 reanalyses produced with the ECMWF IFS. Our objectives are to:

   a) Combine various wind profiling observations to investigate the temporal variability of the wind bias in the operational ECMWF high-resolution deterministic short range forecasts (approximately 9km at the Equator).
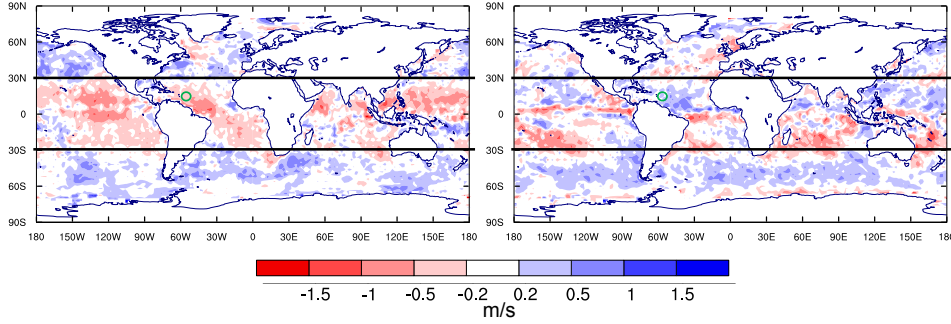
Figure 2.1: Surface wind bias with respect to ASCAT in the ECMWF operational deterministic forecasts, for the months of January and February 2020. The green circles include the study area of EUREC4A. The left and right panels refer to the zonal and meridional wind components respectively.

b) Evaluate the differences in the bias of the analyses and reanalyses, compared to the bias of the forecasts.

c) Assess the extent to which the assimilation of observations gathered during EUREC4A helped improve the analyses and forecasts performed with the IFS.

d) Explore the origin of the wind bias through the use of additional model sensitivity experiments.

After a description of the data (section 2.2) and of the methods used to derive and compare statistics of the wind profiles (section 2.3), we present a description of the observed wind profiles during EUREC4A (section 2.4). In section 2.5 we look at modelled winds and answer the following questions: What is the vertical distribution of the wind bias in forecasts and reanalyses produced with the IFS? How much are the analyses constrained by the assimilation of radio- and dropsondes during EUREC4A? What is the temporal variability of the wind bias? In section 2.6 we then evaluate the influence of model physics, in particular the role of convection and turbulence representation. Our results are summarised and discussed in section 2.7.

2.2 DATA

Within EUREC4A, a region of intensive measurements was defined, it is situated in the trade-winds region near the western end of the 'Tradewind Alley', an extended corridor across the Atlantic (see Figure 1 in Stevens et al. (2021)) with its downwind terminus defined by the Barbados Cloud Observatory (BCO). We adopt this region as the domain of our study (Figure 2.2), more precisely we cover an area of about 350 km x 350 km, between 55.8W and 59.25W and between 11.4N and 14.7N. Our study samples 29 days during the boreal winter, from the 18th of January 2020 to the 15th of February 2020. During the boreal winter

the Inter-Tropical Convergence Zone (ITCZ) is typically located at lower latitudes, and the area east of Barbados experiences undisturbed trade-winds from an east to northeast direction, with prevalence of cumulus clouds confined to the lower troposphere, moderate large-scale subsidence and an inversion around 800 hPa (Brueck et al., 2015; Nuijens et al., 2014; Stevens et al., 2016).

Several observational datasets, such as dropsondes, radiosondes and a ship-borne wind lidar system, are used to evaluate the forecasts and (re)analyses produced with ECMWF IFS.

2.2.1 Observations
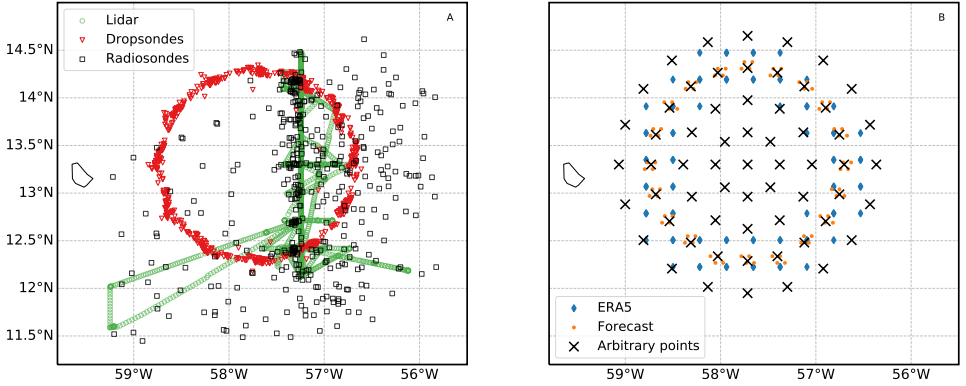
Figure 2.2: Overview of the spatial coverage of different datasets. Left panel illustrates the observational datasets: 3169 lidar measurements from the Meteor research vessel (green circles), 444 radiosondes from research vessels (black squares), 799 dropsondes from JOANNE (red triangles). Right panel illustrates the points in which profiles were retrieved from IFS forecasts and (re)analyses. Model grid points are shown only for the second most external ring: see text for an explanation of different modelling datasets and resolutions.

JOANNE

We use EUREC4A dropsonde measurements from the Joint dropsonde Observations of the Atmosphere in tropical North atlaNtic meso-scale Environments (JOANNE) dataset (George et al., 2021b). Level-3 of this dataset is made available with a homogenised vertical resolution of 10 m. The primary strategy of the EUREC4A dropsondes launches was to sample atmospheric profiles along a ~222 km diameter circle centred at 13.3°N, 57.7°W. Following Stevens et al. (2021), we call this as the EUREC4A-circle. The majority of the dropsondes over the EUREC4A-circle were launched from the German high altitude and long-range research aircraft HALO, a few complementary flights being also performed by the American WP-3D Orion research aircraft. Typically, a flight over the EUREC4A-circle took one hour and 12 dropsondes were launched per circle, although the number of profiles per circle is often less than 12 due to either instrument or operator errors. An overview of the circles and corresponding dropsondes is outlined in George et al. (2021b). For our study, we use sounding profiles from 799 dropsondes (see red dots in Figure 2.2) launched from 73 EUREC4A-circles spread over 13 days between the 18th of January 2020 and the 15th of February 2020. In this study, we refer to the days with dropsonde measurements as

flight-days, and we use flight-hours for the hours with dropsonde measurements within the flight-days. We produce one mean dropsonde profile for each flight-circle. Figure 2.3 schematically represents the temporal availability of JOANNE and of the other EUREC4A datasets used in this study. Black stripes indicate hours sampled in the corresponding dataset.

Radiosondes

Radiosondes considered in this study were launched from four research vessels (RV) over the northwestern tropical Atlantic eastward of Barbados: two German research vessels, Maria S. Merian (Merian) and Meteor; a French research vessel, L'Atalante (Atalante); and a United States research vessel, Ronald H. Brown (Ron Brown). The Meteor operated between 12.5°N and 14.5°N along the 57.25°W meridian. The Ron Brown measured air-masses along the Tradewind Alley, while the Merian and Atalante vessels mainly sailed southward of Barbados (see Figure 1 in Stevens et al. (2021)). Most radiosondes recorded information both in the ascent and descent sections, with descending radiosondes falling by parachute for all platforms except for the Ron Brown.

This study makes use of 444 radiosondes (258 in ascending mode and 186 in descending mode) within the study domain defined above, as documented in Stephan et al. (2021). We use Level-2 of this dataset which is made available with a vertical resolution of 10 m. Each black square in Figure 2.2 (left) refers to a radiosonde either in ascending or descending mode. Radiosondes drifting outside of the area of interest are considered only when inside the domain, and radiosondes launched outside and drifting inside the domain are also considered only where relevant.

There are about 2 radiosondes per hour and we produce one averaged wind profile every three hours to represent the entire domain. The radiosondes provide a regular and comprehensive dataset during all days of the study, as it can be seen in Figure 2.3.

WindCube Long-range Wind Lidar

A Leosphere long-range Windcube (WLS70) on board of the Meteor research vessel performed measurements at 20 different height levels, every 100 m between 100 m and 2000 m. The WLS70 device has a sampling rate of approximately 6 s and measures the line-of-sight radial velocity successively at four azimuthal positions along a cone angle of 14.7°, thus every 360° scan takes around 24 s.

The radial velocities are corrected for ship motions using a simplified correction methodology using an internal GPS system of an accompanying short-range WLS7 WIndCube, which uses a combination of an xSEns MTi-G attitude and heading reference sensor (AHRS) and a Trimble SPS361 satellite compass. The simple motion correction applied to the LOS velocities takes into account the translational ship motions and the yaw information, as explained in Wolken-Möhlmann et al. (2014) and Gottschall et al. (2018). The pitch and roll information is not used, since according to previous studies (Wolken-Möhlmann et al., 2014), the effect of these tilt motions are less relevant for relatively stable platforms. After corrections, the wind vector is retrieved and the data is averaged to 1 hourly values.

The left panel of Figure 2.2 shows for each 10 minutes, in green, the location of the RV Meteor carrying the WindCube. Figure 2.3 shows that wind profiles from lidar measurements are available continuously from the 25th of January to the 15th of February.
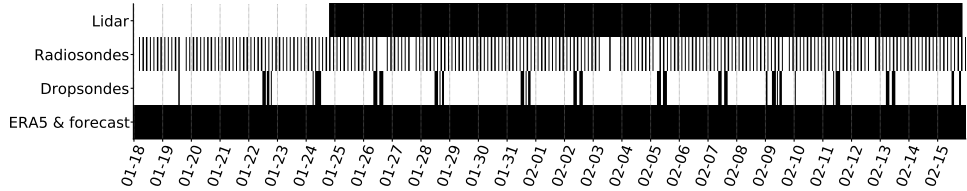

Figure 2.3: Overview of the temporal coverage of different observational datasets from EUREC4A which are used in this study. A black stripe indicates the availability of data for the corresponding hour.

2.2.2 Modelling datasets
The modelling datasets comprise the operational (at the time of the campaign) deterministic high-resolution (9km) forecasts, the ERA5 reanalysis (Hersbach et al., 2020), and several experiments at coarser resolution. The modelling data are on hybrid vertical coordinates which give about 20 m resolution near the surface and ~300 m resolution at 5 km. For each of these datasets, model output was extracted at the nearest four neighbours of 61 points placed concentrically around the centre of EUREC4A-circle. Each group of four points was then used to interpolate the model values to the locations of the 61 arbitrary points using an inverse distance weighting method. This method is applied to reduce to a minimum the already marginal impact of different spatial resolutions on the results of this study. The location of these 61 arbitrary points is shown on the right panel of Figure 2.2 with black crosses. They are chosen to represent the mean state of the study area, with particular attention to the the EUREC4A-circle, which coincides with the second most external ring of points.

Forecast
For the operational ECMWF deterministic ten-days forecasts (cycle 47r2) the extracted model grid points for the EUREC4A-circle are marked in orange in Figure 2.2 B. For clarity, we avoid showing the rest of the extracted model grid points. We extract hourly output for day two of the forecasts (a leadtime of 24 to 48 hours) and hereafter we will refer to this simply as forecast. We focus on these short-range forecasts after Sandu et al. (2020) showed that over this trade-winds region the errors in wind profiles develop in the first 12 hours of the forecast and do not grow significantly until day five.

ERA5
The fifth generation ECMWF global reanalysis (ERA5) produced for the Copernicus Climate Change Service is widely used for model evaluation, and often it is used as a proxy for observations. Similar to the operational analysis, ERA5 is produced with ECMWF IFS by optimally combining short-range forecasts and observations through data assimilation (as it is done to create the analysis, or initial condition of the forecasts). While operational analyses are not consistent in time because of regular upgrades to the forecasting system, reanalyses are produced with an unique version of the forecasting system. This leads to

a consistent time series which allows one to monitor environmental changes. ERA5 is produced with the IFS model cycle 41r2, at a resolution of approximately 32 km, and covers the period 1950 to present (Hersbach et al., 2020).

Here we exploit EUREC4A observations to evaluate the quality of the wind profiles also in the ERA5 reanalysis. The extraction points for ERA5 corresponding to the EUREC4A-circle are shown in blue in Figure 2.2 B. In the sections below we focus on the wind profiles from ERA5, rather than from the operational analysis, because the differences in wind profiles over the EUREC4A region between the operational analysis and ERA5 are marginal (not shown) but ERA5 is available hourly, whereas the operational analysis is available 6 hourly. The choice of using ERA5 is also motivated by its widespread use in the literature as a reference and truth.

Sensitivity Experiments

EUREC4A drop- and radio- sondes are assimilated in ERA5, which may lead to an underestimation of the bias calculated with respect to these measurements. Sentic et al. (2022) recently analysed the impact of dropsondes on the ECMWF IFS analysis and found overall small differences. For our case, we similarly, investigate to what extent the IFS reanalysis is close to reality because local observations are assimilated. To answer this question, several sensitivity experiments were performed at 40 km resolution and outputs saved every 3 hours for the forecasts and every 6 hours for the analyses.

First, a control analysis (CTRL_an) and corresponding ten-days control forecasts (CTRL_fc) initialized from it were performed at this resolution. Second, so-called data denial experiments were performed in which measurements made during EUREC4A are not assimilated when creating the initial conditions of the forecasts. These experiments consist of: (a) an analysis experiment in which the EUREC4A dropsondes are not assimilated, and corresponding ten-days forecasts (Exp1_an, Exp1_fc); (b) an analysis experiment where neither EUREC4A dropsondes nor radiosondes are assimilated, and corresponding ten-days forecasts (Exp2_an, Exp2_fc).

Another pair of experiments allow us to explore the origin of the IFS wind bias. We performed an analysis experiment, and corresponding ten-days forecasts, where shallow convective momentum transport is switched off (Exp3_an, Exp3_fc). In the IFS cumulus convection is parametrized with a bulk mass-flux scheme which was originally described in Tiedtke (1989). Clouds are represented by a single pair of entraining/detraining plumes which describes updraught and downdraught processes. Convection is classified as shallow when the cloud top is below 200 hPa, deep otherwise. This distinction is only necessary for the closure and the specification of the entrainment rates that are a factor of two larger for shallow convection (Bechtold et al., 2020).

Lastly, an experiment is performed with the most recent IFS cycle (47r3), which was not yet operational at the time of the campaign. This is used to investigate the role of the model physics in determining the wind bias, particularly the deep convection away from Barbados. For all the above mentioned sensitivity experiments forecasts were initialized daily at 00UTC from the corresponding analysis.

2.3 Methods

Mean wind profiles are derived using the datasets described above. The differences between the modelled and observed winds are quantified by computing at all timestamps the instantaneous model error ($\Theta_{mod} - \Theta_{obs}$) and subsequently defining the mean model bias and the root mean square error (RMSE) as:

$$\text{Bias} = \overline{\Theta_{\text{mod}} - \Theta_{\text{obs}}}, \tag{2.1}$$

$$\text{RMSE} = \sqrt{\overline{(\Theta_{mod} - \Theta_{obs})^2}}, \tag{2.2}$$

where the overbar represents the arithmetic mean and Θ is any modeled (*mod*) or observed (*obs*) variable.

While the RMSE measures model accuracy independent of the sign of the error, the model bias takes into account the sign of the errors and can be used to study the distribution of the error. The skewness of the error distribution is important for the bias: large errors that are normally distributed result in large values of RMSE, but a bias that is approximately zero. Otherwise said positive and negative errors can compensate each other and result in a nearly zero mean bias.

All profiles are interpolated to a grid of 50 m vertical resolution between 0.15 km and 5 km for simplicity. The mean sub-cloud layer top (630 m) and the mean inversion height (2260 m) are calculated from the JOANNE dataset. The sub-cloud layer top is defined as the height at which relative humidity maximise below 1 km. The inversion height is defined as the altitude below 6 km at which the Brunt–Väisälä frequency squared (N^2) is maximum. The wind vectors are decomposed into zonal (u) and meridional (v) components and analysed at different hours of the day using hourly and 3-hourly composites. While the modelling datasets directly provide vectorial wind components, the observations measure scalar quantities such as wind speed (wspd) and wind direction. In this study we retrieve the corresponding meridional and zonal components for each radiosonde and dropsonde and for each of the 10 minute lidar winds, thus before computing any mean.

While model outputs uniformly sample the entire domain at each time step, observations only sample one location at the time. To partially account for these differences in the data sets, we sample the model output to match the sampling of the respective observational dataset when we derive the forecast and (re)analysis errors. For example, when we compare to the radiosondes, we average the model profiles for the 61 points and over 3-hourly intervals, assuming that the launch locations over three hours are sufficiently dispersed to provide a good representation of the entire domain. When we compare to the dropsondes, we average only the model points extracted along the EUREC4A-circle at the hour during which the circle was flown. In the case of the wind lidar, we use only the closest extraction point to the instrument when computing the model errors. When the model is simultaneously compared to multiple observational datasets (e.g. in Figure 2.5 A-C and in Figure 2.7 A-C), we show the model mean obtained from all the 61 points and with the temporal resolution available for the model output.
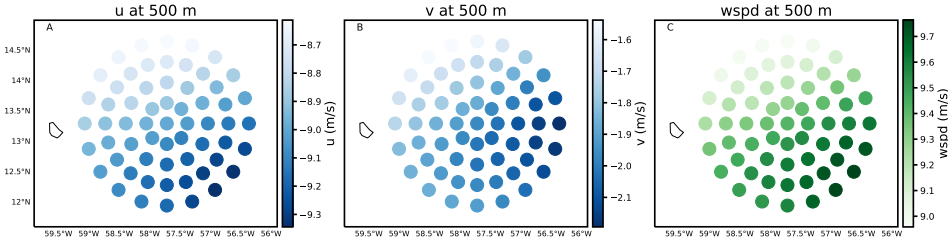
Figure 2.4: Spatial variability of wind components (zonal u, meridional v, and wind speed wspd) at 500 m derived from ERA5 for the whole period and at all hours.

Figure 2.4 helps quantifying the spatial variability of winds in the study area and motivates our choice of the spatial matching between observations and the model output. It shows that there is a NW to SE gradient in wind, whereby the south-east region of the domain experiences winds about 0.5 m s^{-1} stronger than the average of the domain. The lidar samples this region more frequently than the north-west area where weaker winds prevail. Thus, we expect the wind-lidar winds to generally be stronger.

2.4 Observed Winds during EUREC4A

2.4.1 Wind profile and synoptic variability

EUREC4A was characterised by on average low-level north-easterly winds, as shown in Figure 2.5 (A, B), which includes both observations (in black the radiosondes and in green the lidar) and models (in blue). The JOANNE dropsonde dataset is not shown, because of the limited number of flight-days and because JOANNE does not sample all hours of the day. We will show in section 2.5.3 that on flight hours dropsondes and radiosondes only disagree for the zonal component in the cloud layer (630 - 2260 m). Note that the lidar measured stronger winds in the sub-cloud layer, while deployed in a region where winds were stronger (section 2.3).

The mean wind speed (panel C) is about 9 m s^{-1} at 150 m, it slightly increases in the lower 800 m and sharply reduces to 6 m s^{-1} in the cloud layer, between 1 km and 2 km. The zonal component is the largest contributor to the total wind speed, which typically peaks near cloud base and decreases aloft, establishing a so-called backward sheared wind profile. This structure was documented in earlier field studies (Brümmer et al., 1974; Riehl et al., 1951) and more recently using the BCO climatology alongside ERA-Interim (Brueck et al., 2015). A recent study using north-Atlantic wide Large Eddy Simulations with ICON (hindcasts performed for the pre-EUREC4A NARVAL campaign period) suggests that the local maximum in zonal wind near cloud base results from efficient turbulent diffusion in the sub-cloud layer, but little if any cumulus friction at cloud base (Helfer et al., 2021). In the cloud layer counter-gradient momentum transport is found, which suggests that moist convection tend to enhance and not reduce the vertical wind shear above $\approx$ 1 km (Dixit

2
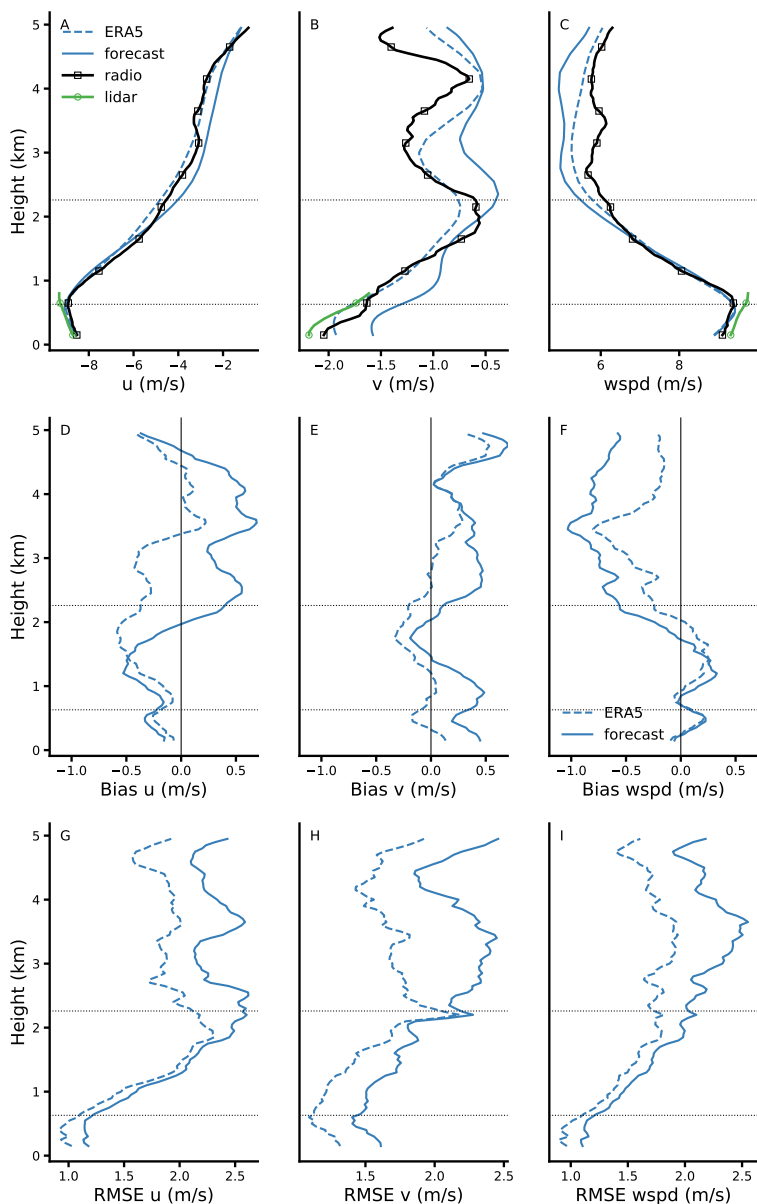
Figure 2.5: Mean profiles of zonal wind (A, D, G), meridional wind (B, E, H) and wind speed (C, F, I) during EUREC4A. In the top row (A, B, C) are monthly profiles retrieved from lidar (green circles), radiosondes (black squares), ERA5 reanalysis (dashed blue), and day 2 forecast (solid blue). The middle (D, E, F) and bottom (G, H, I) rows show the monthly biases, and root mean square error, of the forecast and ERA5 with respect to radiosondes. The horizontal dotted lines indicate the mean sub-cloud layer top and inversion height.

et al., 2021; Larson et al., 2019).

The mean meridional wind maximizes closer to the surface with wind speeds of about -2 m s^{-1}, and it decreases in magnitude (negative numbers) to -0.5 m s^{-1} at 2 km.

Although the trade-winds are generally steadier than midlatitude flows, they still exhibit significant synoptic variability. Figure 2.6 shows the observed winds (zonal and meridional wind and wind speed) at 3-hourly resolution derived from the radiosondes. Winds were relatively weak with strong backward shear during the final two weeks of January 2020, transitioning to a period with stronger winds and weaker shear during the first week of February 2020, and the campaign ended with several days with strong winds and strong backward shear.
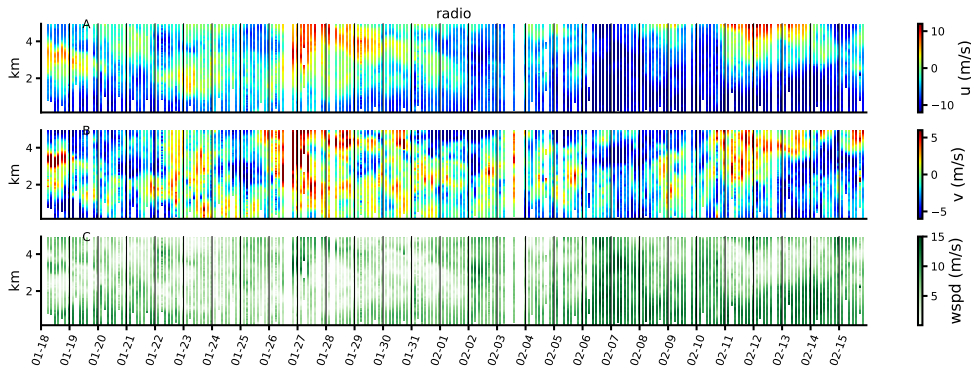
Figure 2.6: Time series of 3-hourly zonal wind (top), meridional wind (middle) and wind speed (bottom) from radiosondes, averaged over the whole domain.

2.4.2 Wind Diurnality
An important highlight of EUREC4A, although not novel, is the presence of pronounced diurnality in both convection and the winds. Figure 2.7 A-C plots hourly and 3-hourly wind composites averaged over the layer between 0.15 km and 0.75 km from the lidar data (green) and the radiosondes (black). A diurnal cycle is present with the weakest wind speeds during the day and the strongest winds at night. The amplitude of the observed diurnal cycle is about 1 m s^{-1} in both the meridional and zonal component.

The diurnal wind variations are not fully understood, but Ueyama and Deser (2008) showed that over the tropical Pacific such variations agree very well with pressure-derived wind diurnality, suggesting that the pressure gradient force plays a dominant role in setting the diurnality, next to a possible role for boundary layer stability and/or diurnality in moist convection. We will return to this in section 2.6, where we present the diurnality in the large-scale pressure gradient as part of the observed and modeled momentum budget.
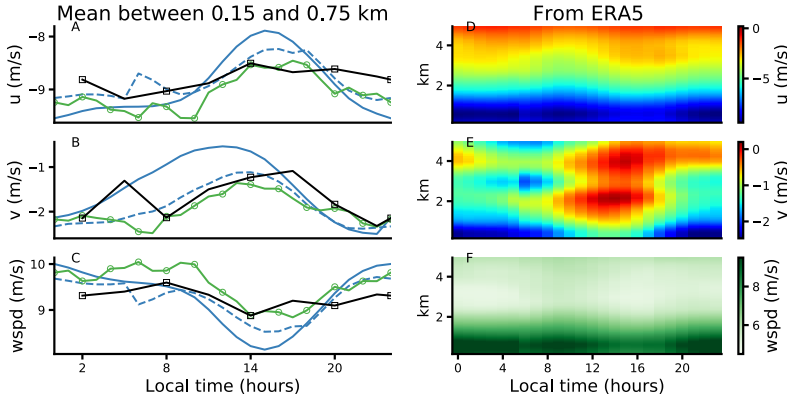
Figure 2.7: Diurnal cycle of zonal wind (A, D), meridional wind (B, E) and wind speed (C, F). The left column refers to the layer between 0.15 km and 0.75 km with values from radiosondes (black squares), lidar (green circles), ERA5 (dashed blue) and forecast (solid blue). The right column refers to multiple levels from surface to 5 km with values from ERA5 only.

2.5 MODELLED WINDS

2.5.1 MEAN BIAS

The EUREC4A mean zonal wind profile in Figure 2.5 is captured well by ERA5 (blue dashed line) and the forecast (solid blue line), particularly below 2km, but the forecast especially suggests weaker meridional winds at all heights and in particular near 0.15 km and 3 km. A bias in the wind direction, where winds are veered with respect to the observations, has long known to be present in the model, see also Sandu et al. (2020), and the comparison of ERA5 and surface scatterometer winds in (Belmonte Rivas and Stoffelen, 2019). Less appreciated is that the wind bias (see also the actual bias with respect to the radiosondes in Figure 2.5 D-F) is larger above the boundary layer, while it is small ($\sim$0.1 m s^{-1}) below roughly 2 km (near the trade-inversion).

However, the mean bias is not a good representation of the errors made on shorter time scales. The panels G, H, and I in Figure 2.5 show that the RMSE between the forecast/ERA5 and radiosondes is as large as 1 m s^{-1} at 250 m and 2.5 m s^{-1} between 3 km and 4 km, for all components. Figure 2.8 shows - as a function of height - the mean, the quartiles (Q1,Q2,Q3), and the first to last percentiles of the forecast errors at individual times (top row). The interquartile range of errors can be up to ± 1 m/s, while the first and last percentiles range from ± 4 m s^{-1}. The errors are fairly normally distributed, and as such the mean bias can be small.

With the data available here, the spatial distribution of the model bias can only be addressed with dropsondes on the HALO-circle, thus for few days. Instead, we show the difference between the forecast and ERA5 for all 61 extraction points and investigate the spatial variability of this difference for the entire period (Figure 2.8 D-F). Compared to the temporal

variability, the errors made at individual locations within the circle are far more similar and at least an order of magnitude smaller, ranging from ± 0.4 m s^{-1}.
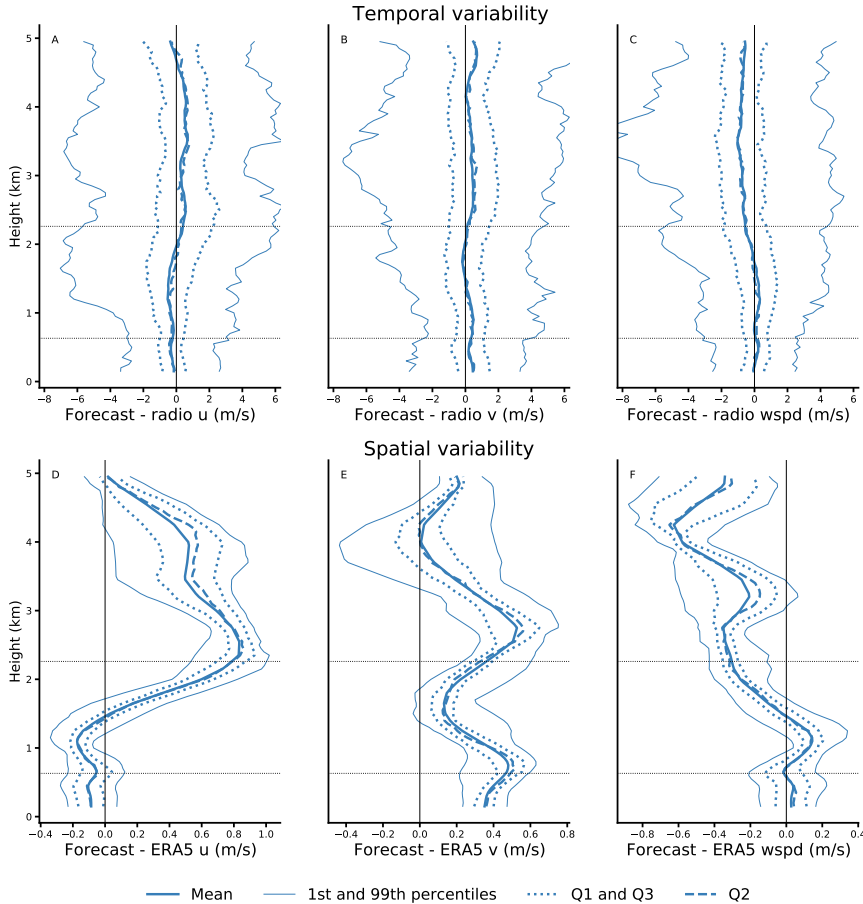
Figure 2.8: Statistical distribution over time of the forecast error with respect to the radiosondes for all levels up to 5km (A-C). Statistical spatial distribution for the 61 extraction point of the difference between forecast and ERA5 (D-F).

As expected, the bias and RSME of ERA5 is smaller than that of the forecast. The radiosondes and dropsondes launched during EUREC4A were used in the data assimilation process of ERA5. The following section investigates to what extent the assimilation of these observations has influenced the performance of the analysis and the forecast.

2.5.2 Influence of Sounding Assimilation

We performed extractions from the IFS analysis and forecast of a control experiment (CTRL_an, CTRL_fc), of an experiment without assimilating dropsondes (Exp1_an, Exp1_fc), and an experiment without assimilating dropsondes nor radiosondes (Exp2_an, Exp2_fc).

For each of the mentioned experiments the monthly mean bias and RMSE is calculated over all hours of the day, with respect to the radiosondes, as done in Figure 2.5 D-I. The results are shown in Figure 2.9, where the dashed lines refer to the analyses and the solid lines to the forecasts.
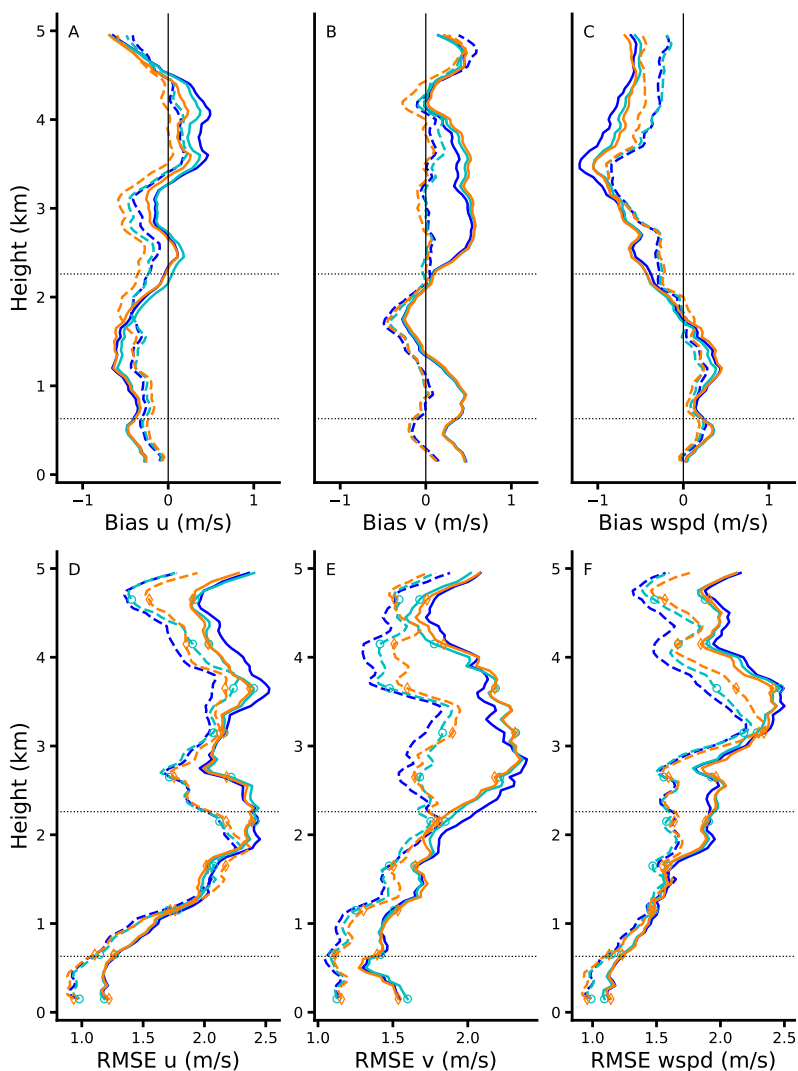
Figure 2.9: Monthly mean IFS bias (A, B, C) and root mean square error (D, E, F) against radiosondes as in Figure 2.5 (D-I), forecasts are in solid and analyses in dashed. In the control experiment (blue) both dropsondes and radiosondes from EUREC4A are assimilated. In the first experiment (cyan) dropsondes are excluded from the assimilation. In the second experiment (orange) neither dropsondes nor radiosondes are assimilated.

Evidently, all analysis and forecast experiments remain considerably close to the corre-

sponding control experiment (blue lines): the differences are everywhere small, and almost non-existent below 2 km. The sign, shape and magnitude of the profiles in Figure 2.9 confirm the results described in previous sections (e.g. see Figure 2.5) and support the idea that the mean wind bias does not increase with coarser model runs (40 km spatial resolution and 3 hours temporal resolution of the model output). This also suggests that assimilating the local soundings does not alleviate the existing biases.

That the analysed wind profile error does not change much in any of the denial experiments, does not necessarily mean that the observations have not played a role in constraining the wind profiles, because typically, when one observing system is withdrawn from the data assimilation system, the analysis is constrained through other observing systems Sandu et al. (2020).

The variability in the (sign of) the errors is explored next, and also shown to critically depend on the time of the day.

2.5.3 Temporal structure of the bias

Do certain days during EUREC4A have systematically larger wind errors? The sign and magnitude of the 3-hourly biases are relatively similar in the first and second half of the EUREC4A period, with positive and negative values of up to 2 m s^{-1} in both the zonal and the meridional wind components that sometimes just last a few hours and sometimes last for several days. The 3-hourly forecast bias with respect to radiosondes shows a similar results but with larger values (not shown).
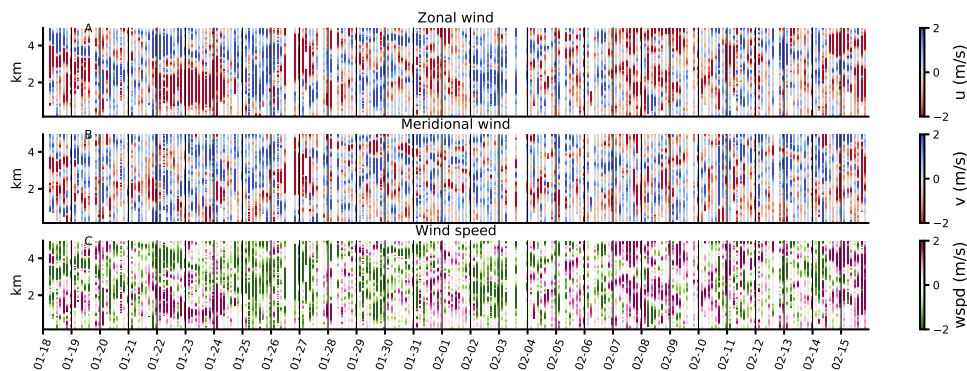
Figure 2.10: Difference between ERA5 and radiosonde wind profiles averaged over the whole domain and over 3-hourly intervals. From top to bottom: zonal, meridional winds and wind speed.

A more systematic bias is seen in the the diurnal cycle of winds, which was already hinted at in Figure 2.7. The wind diurnality is significantly overestimated by the forecast with an amplitude almost twice that of the observations. At 15 LT the zonal wind bias is largest: the forecast underestimates the magnitude of the zonal wind component by 1 m s^{-1} with respect to both lidar and radiosondes measurements. Instead, in the late night and early morning the forecast biases are most pronounced in the meridional wind (Figure 2.7 B):

the forecast is out of phase exaggerating and anticipating the morning weakening of the meridional wind.

ERA5 is notably better at capturing the amplitude and phase of the diurnal cycle in the meridional component, despite the fact that the assimilation of local drop- and radio- sondes is not important for reducing the bias (section 2.5.2). The origin of the diurnality in winds is not fully understood. Above 2 km, the zonal and total wind speed variations (Figure 2.7 D-F) suggest a semi-diurnal cycle of the zonal winds, with weakest winds in the first few hours of the day and around 16 LT. Such a semi-diurnal cycle in zonal winds (and diurnal cycle in meridional winds) has been found over the tropical oceans in earlier studies (Dai and Deser, 1999; Ueyama and Deser, 2008) and linked to semi-diurnal atmospheric thermal tides generated by the absorption of solar radiation by ozone in the stratosphere and water vapor in the troposphere. These tides travel downward and affect sea level pressure, whose tidal amplitudes appear mostly semi-diurnal.
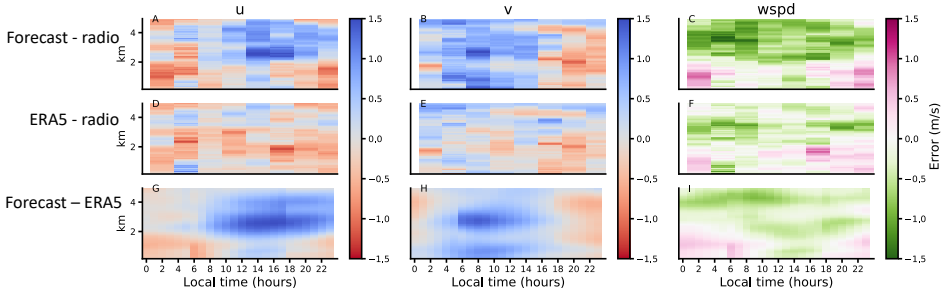
Figure 2.11: Diurnal cycle of the forecast bias with respect to radiosondes (top row), the ERA5 bias with respect to radiosondes (middle row), and the forecast bias with respect to ERA5 (bottom row). From left to right, columns refers to the biases in zonal wind, meridional wind and wind speed. Blue regions are related to a positive bias (e.g. too weak negative zonal wind), red regions are related to a negative bias (e.g. too weak wind speed).

Figure 2.11 quantifies the mean model bias as a function of height and time of day with respect to radiosondes (A-C and D-F), while Figure 2.12 shows the mean bias during flight hours (A-C), during daytime (between 10 LT and 16 LT) and nighttime (between 22 LT and 4 LT). These figures reveal that a too strong easterly wind in the IFS during nighttime (as found near the surface in Figure 2.7) is present throughout the lower 2 km of the atmosphere. During daytime and during flight hours (which are predominantly during daytime), the meridional wind component contributes most to the weak wind speed bias in the forecasts below 2 km. Too weak easterly wind are seen also above 2 km, where both meridional and zonal winds are underestimated (Figure 2.11 and 2.12).

ERA5 performs much better than the forecast at all hours of the day. Nevertheless the pattern in the right most panels (wind speed) suggests that the reanalysis only reduces the magnitude of the bias, without eliminating the fundamental causes of an overestimated diurnal wind cycle below 1 km. At nighttime the forecast is close to ERA5, while at daytime the forecast and ERA5 differ considerably (more than 1 m s^{-1} at 2.5 km for both the zonal
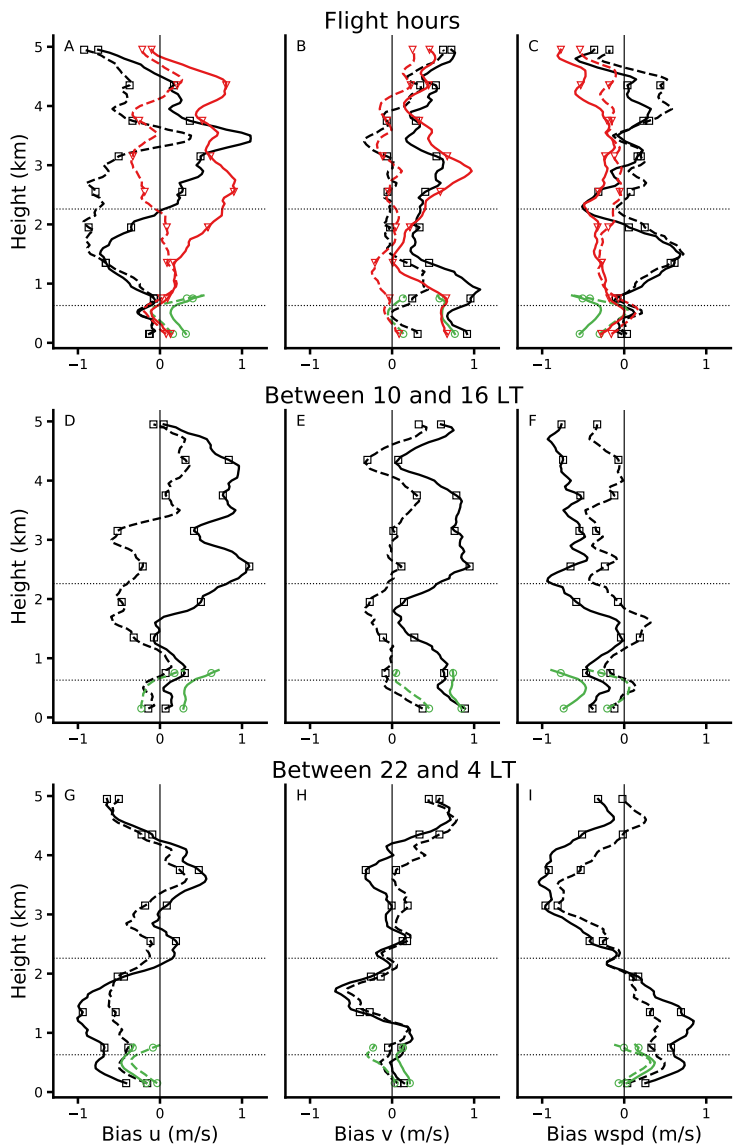
Figure 2.12: Mean model bias (forecast in solid and ERA5 in dashed) during flight hours (top row) and during the whole EUREC4A campaign, measured separately for daytime between 10 and 16 LT (middle row), and for nighttime between 22 and 4 LT (bottom row). The bias is calculated with respect to radiosondes (black squares), lidar measurements (green circles), and dropsondes (red triangles). From left to right the columns refer to the bias in the zonal wind (*u*), meridional wind (*v*), and wind speed.

and meridional components). This can be traced back to what is seen in Figure 2.7, where both the forecast and reanalysis overestimate the amplitude of the diurnal cycle, but only ERA5 captures the phase of the cycle.

From Figure 2.12 A-C we can also infer that the dropsondes and radiosondes agree fairly well, apart for the zonal wind in the cloud layer. Here, at about 1.5 km, the radiosondes show zonal winds ~1 m s^{-1} stronger than the dropsondes. These differences may be due to differences between the descending and ascending radiosondes. Descending radiosondes tend to show stronger winds above 1.5 km. Excluding the 186 descending radiosondes produces a better agreement with the dropsondes above 2 km (not shown). However, around 1 km the descending radiosondes match the dropsondes considerably better than the ascending radiosondes. We also notice that the number of operating dropsondes reduces at lower altitudes.

2.6 The role of parameterized moist convection

Previous sections highlighted that a wind speed bias exists throughout the lower troposphere and not just near the surface. To address the role of shallow moist convection in setting the bias, this section compares the modeled momentum budget with the observed momentum budget during EUREC4A and discusses a sensitivity experiment that removes momentum transport by shallow convection, which already has a profound effect on the circulation. Rather than turning off shallow convection entirely, which would lead to a substantial different structure of the trade-wind layer, the control run can be compared to the latest IFS model cycle 47r3, which has a different representation of moist physics.

2.6.1 Observed versus modeled momentum budget

In Figure 2.13 the mean tendencies in the momentum budget are compared against the mean momentum tendencies derived from the JOANNE dataset (section 2.2.1). Panel A and B represents the average over all flight hours during all flight days, while the daytime and nighttime tendencies over all EUREC4A days and just for the model are shown in panels C, D respectively E, F. In the observations (solid lines) and in the IFS (dashed lines), the advection, pressure gradient and Coriolis force are combined into a "dynamical" forcing that acts on the scale of the circle (~200 km). In the model, the so-called "frictional force" is comprised of parameterized convective and turbulent momentum transport. In the observations, it is derived as the residual in the momentum budget and interpreted as the vertical eddy flux divergence established by turbulent flows within the circle (including small-scale turbulence, convection and mesoscale circulations) (Nuijens et al., 2022). Horizontal and vertical advection of the mean wind are combined and on average an order of magnitude smaller than the other budget terms (not shown), so that the momentum balance is predominantly a balance between the pressure gradient force, a Coriolis force and friction.

Because most flight hours took place in the early morning, the observed and modeled tendencies are most comparable to the daytime tendencies between 8 and 14 LT (Figures 2.13 C, D). During this time the dynamical forcing is about half that of the forcing experienced at night (Figure 2.13 E, F). This diurnality in pressure gradients is not fully understood, but
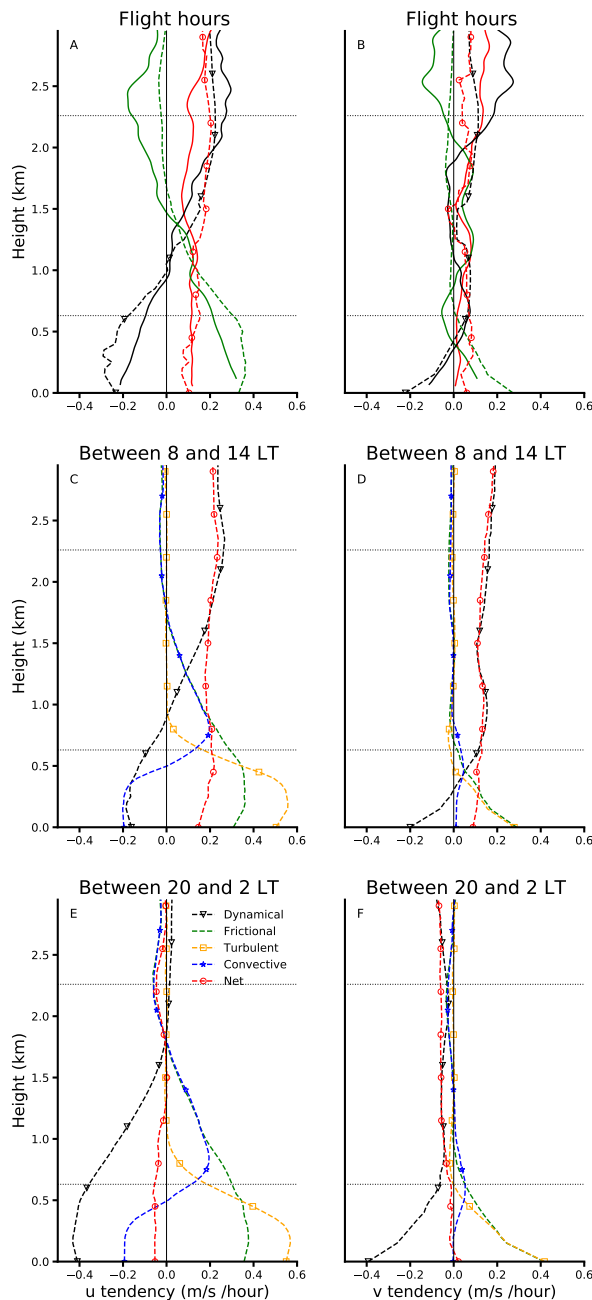
Figure 2.13: Components of the momentum budget retrieved from the dropsondes (solid) and the forecast (dashed). The net tendency (red circles) balances the dynamical force (black triangles) and the frictional force (green). The latter is split into turbulent and convective for the forecast. The top row refers to days and hours sampled by the dropsondes (flight hours). The middle row refers to the hours between 8 and 14 LT during all EUREC4A days. The bottom row refers to the hours 20 to 2 LT during all EUREC4A days.

may be linked to a diurnality in remote deep convection *e.g.*, deep convection in the ITCZ peaks in the early morning, while deep convection over the South American continent peaks in the afternoon (Wood et al., 2009).

There is remarkable agreement between the general structure and magnitude of the tendencies in the observations and the IFS in the boundary layer, providing confidence in the method used to estimate the budget from observations, as well as in the ability of the IFS to reproduce the different processes at play. There is a non-negligible positive net tendency in the zonal direction (red), in agreement with a slow-down of the easterly wind in the morning and afternoon, which is preceded by a reduction in the large-scale dynamical forcing (black lines in Figures 2.13 C and E).

Compared to the observations, the IFS has larger dynamical and frictional tendencies in the zonal component in the sub-cloud layer up to ~0.75 km (Figure2.13 A), where the observations suggest a gradual weakening of these tendencies with height. Because the turbulent friction and the large-scale pressure gradients are coupled through the circulation, it is hard to disentangle which error is driving which. In the meridional component the model and observations agree on the dynamical forcing driving northerly winds below 500 m, but the IFS overestimates the frictional force.

Between 1.5 and 3 km the frictional force is near zero in the IFS, but the observations suggest a layer with negative frictional force (i.e., an acceleration of the easterly flow) that is near cumulus tops. As such there is a larger net deceleration of easterly winds in the IFS, consistent with the finding that the IFS has a slow zonal wind bias at those heights during flight hours (Figure 2.12, top row). In the meridional component, the IFS appears to overestimate friction in the sub-cloud layer and underestimate friction above ~ 500 m, where the observations suggest that small frictional effects are present (between 1 and 2 km). An acceleration of northerly winds in the observations is seen above 2 km.

2.6.2 Shallow convective momentum transport

In previous work, the role of convectively-driven circulations and variability has been suggested to play a role in the long-standing near-surface wind bias over subtropical oceans (Belmonte Rivas and Stoffelen, 2019; Sandu et al., 2020). We cannot disentangle the role of convection versus turbulence in the observed tendencies, and therefore not test whether the IFS has either too little or too much (cumulus) friction at different levels (the above-mentioned simulations are targeting these open questions).

However, in the IFS we can turn off shallow convective momentum transport (CMT) to study which aspects of the wind bias are sensitive to the process. CMT acts to mix winds between the surface and the cloud layer. If the wind speed increases with height, as is typically true for the sub-cloud layer, this would result in an increase of wind speed near the surface and a decrease in wind speed in the cloud layer, the latter being the so-called "cumulus friction" effect. Without shallow CMT, the subcloud layer shear is expected to be enhanced. Figure 2.14 compares simulations without shallow CMT, Exp3_an and Exp3_fc in black dashed and solid lines with circles, to the same control experiment as in section 2.5.2 (CTRL_an, CTRL_fc, in dashed and solid blue). It confirms that shallow CMT acts to strengthen winds near the surface and weaken easterly winds in the cloud layer. Without

shallow CMT, the bias near the surface disappears, but the bias around 1 km gets much larger. At this level, especially at night, too strong easterly winds develop (Figure 2.14 D-F). This highlights the role of shallow convection in partially just communicating wind biases from the lower cloud layer to the surface.

Above 2 km, there is little difference between the black lines (Exp3_an and Exp3_fc) and the blue lines (CTRL_an and CTRL_fc) (Figure 2.14). At these height levels, convective tendencies in the IFS are small or negligible (Figure 2.13 C-F) and the weak wind speed bias, evident in both the zonal and meridional components, remains.
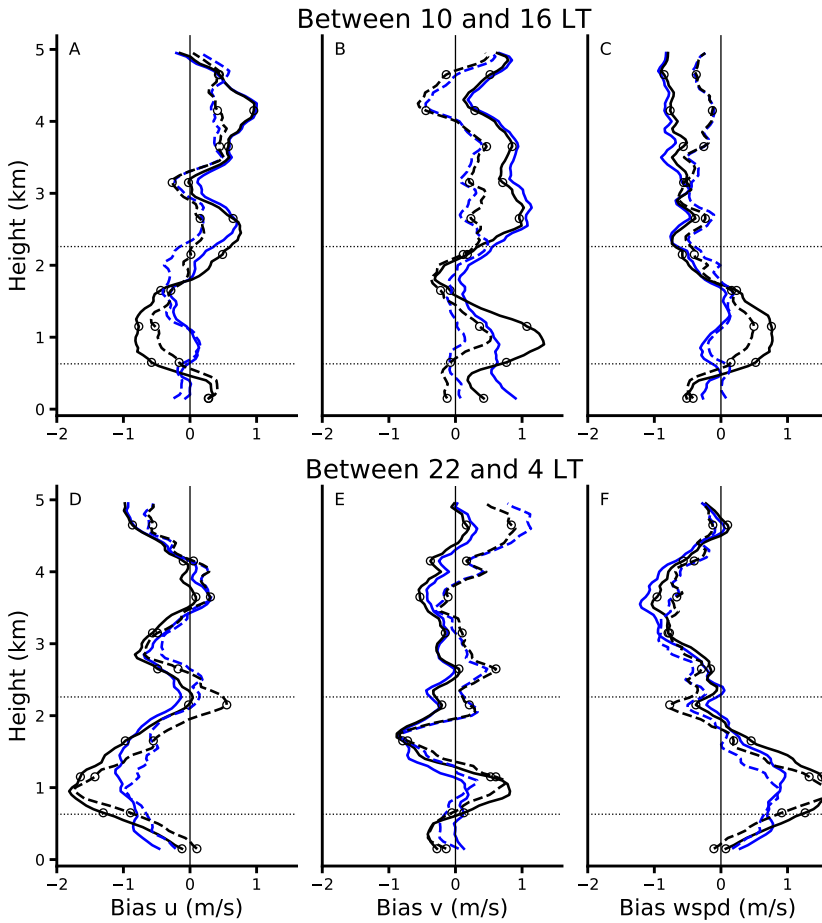
Figure 2.14: Mean IFS bias (forecast in solid and analysis in dashed) during EUREC4A with respect to radiosondes. Blue refers to the control experiment while black circles to the experiment with convective momentum transport turned off (Exp3). Top and bottom row respectively for bias between 10 and 16 LT and between 22 and 4 LT.

2

2.6.3 New moist physics

In this section we compare a model experiment with the most recent IFS cycle (47r3) (Forbes et al., 2021) to the forecast of cycle 47r2 used here, which was operational at the time of the field campaign. In the 47r3 cycle the main revisions concern the parametrization of deep convection, especially the representation of propagating mesoscale convective systems and their diurnal cycle (Bechtold et al., 2020). The coupling between convection and dynamics is improved by adding a tendency from the dynamics to the mass flux closure, namely the total (vertical and horizontal) advective moisture tendency. Insufficient night-time convection over land has been identified as a major shortcoming in IFS forecasts of convective activity (Becker et al., 2021; Forbes et al., 2021). Comparing the two cycles thus reflects changes in the wind bias that are more likely to be caused by changes in remote convection and subsequent changes in circulation patterns, than by changes in local convection.

The red lines in Figure 2.15 indicate that the mean wind bias with respect to radiosondes is largely reduced during daytime and above 2 km. The solid blue lines refer to the operational forecast while the dashed blue lines refer to ERA5. We present separate panels for the EUREC4A mean over all hours of the day (A-C), for daytime (D-F), and for nighttime (G-I). The upgraded model improves the wind forecast everywhere except for a slight deterioration of the zonal component below 1.5 km during daytime and above 2 km during nighttime.

Although the overall mean wind profiles are similar for the two model versions (see first row in Figure 2.15), there is a remarkable reduction of the daytime meridional wind bias (see panel E). With the upgraded model, the forecast becomes closer to the observations and to ERA5 at all levels. This suggests that the IFS wind bias is, at least in part, related to remote deep convection.

2
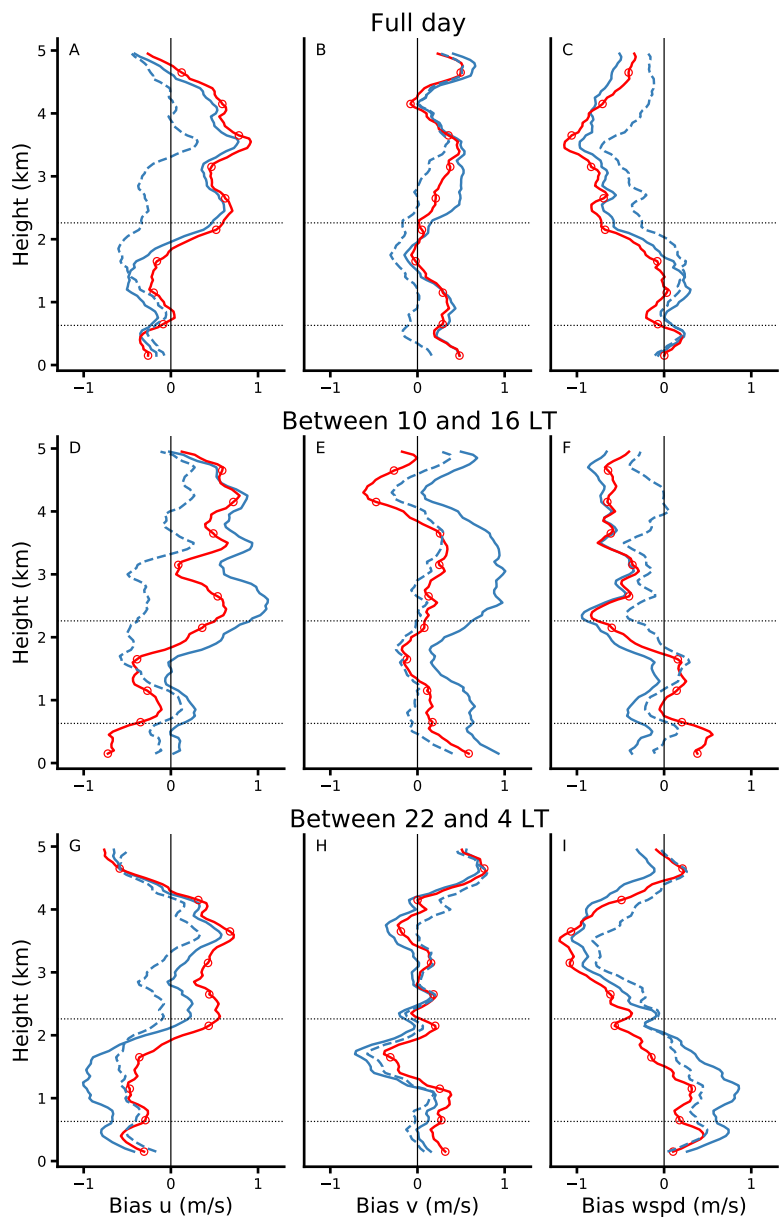
Figure 2.15: Mean model bias for ERA5 (dashed blue), the operational forecast (solid blue), and a forecast with the new model cycle 47r3 (red circles). The bias is shown separately for all hours of the day (top), for daytime between 10 and 16 LT (middle row), and for nighttime between 22 and 4 LT (bottom row). The bias is calculated with respect to radiosondes. From left to right the columns refer to the bias in the zonal wind (*u*), meridional wind (*v*), and wind speed.

2.7 Discussion and Conclusions

In this study we exploited multiple measurements from the EUREC4A field campaign to assess the lower tropospheric wind bias in the operational forecasts and ERA5 reanalyses performed with the Integrated Forecasting System (IFS) of the European Centre for Medium-Range Weather Forecast (ECMWF). We focused on a 350 km x 350 km domain in the trade-winds region eastward of Barbados and investigated wind profiles extending up to 5 km height during a month-long period during boreal winter. To the authors' knowledge, this is the first time that observational vertical profiles of wind fields are available over ocean for such an extended period of time and from various instruments.

Our analysis shows that the structure and variability of the trade-winds are reasonably reproduced in the IFS, although there are biases both at the surface and throughout the troposphere, with the largest values of the bias near and above the mean trade-inversion (~ 2.3km). In a monthly average the forecast underestimates the meridional wind component by about 0.5 m s^{-1} in the layers below 1 km and between 2.5 and 4 km. The zonal wind component is also about 0.5 m s^{-1} too weak between 2.5 and 4 km, while it is slightly overestimated below 1 km, in line with the known near-surface excessive easterly flow of the IFS (Belmonte Rivas and Stoffelen, 2019). The RMSE of the forecasts is larger: it increases with height from 1 m s^{-1} near the surface to 2.5 m s^{-1} near 3.5 km in all wind components. The RMSE is independent of the sign of the error and thus also measures positive and negative random errors that can otherwise compensate. As expected, the wind bias is smaller in ERA5 with the RMSE peaking at about 2 m s^{-1}. An analysis of the impact of the assimilation of the EUREC4A soundings shows that the IFS (re)analysis and forecasts are not very sensitive to the assimilation of local wind information in these undisturbed trade-winds conditions, and are apparently well constrained through large-scale dynamics and other observing systems.

The wind bias in the sub-cloud layer is not constant throughout the day, but exhibits a diurnal cycle just like the wind speed itself (Vial et al., 2019), which is weakest during the day, at 14 LT (~9 m s^{-1}) and strongest at midnight (~10 m s^{-1}). This diurnality is overestimated by the IFS, with too weak winds during the day and too strong winds during the night, particularly in the forecasts.

The wind biases are consistent with biases in the momentum tendencies through a direct comparison of the tendencies with observed tendencies. Momentum tendencies in the model are confined to the lowest 1.5 km in the zonal direction, where the parameterized friction appears too large, compensated by larger than observed dynamical forcing, while it is missing a net acceleration of winds at levels above 2 km. In the meridional direction, the model overestimates the friction below cloud base (~500 m) and misses tendency aloft, which is not well understood.

Using ICON-LEM hindcast runs over the North Atlantic corresponding to the NARVAL flight campaigns Dixit et al. (2021) and Helfer et al. (2021) show that the cumulus friction effect is rather small at cloud base and in the cloud layer, and more friction takes place in the upper mixed layer due to sub-cloud layer overturning (coherent dry convective circulations). Ten days of EUREC4A large-eddy simulation hindcasts are currently being

investigated to shed more light on the relative contribution of dry and moist convection and different scales to the momentum budget.

Previous studies have suggested that missing convective variability may be the cause of the near-surface wind bias (Belmonte Rivas and Stoffelen, 2019). Removing momentum transport by shallow convection altogether reduces the wind bias near the surface, but a strong easterly wind bias near cloud base develops. The wind biases above 2 km in both the zonal and meridional wind remain. This suggests that convective momentum transport may be too active in mixing too strong easterly momentum towards the surface, and/or that there is a missing source of friction near cloud base.

A comparison with the latest IFS release (cycle 47r3), which has most significantly updates in tropical deep convection, shows that the meridional wind bias (and to a lesser extent the zonal wind bias) are notably reduced at daytime. This suggests that equatorial deep convection may contribute to the bias by influencing large-scale pressure gradients. Unraveling the causes of the bias remains challenging because small-scale physics and large-scale dynamics are closely coupled. At the moment, large domain LES hindcasts for EUREC4A are analyzed to disentangle which processes and what scales critically influence the momentum budget.

DATA AVAILABILITY

The observational data used in this publication was gathered in the EUREC4A field campaign. We used version 1.0.0 of the JOANNE dataset which is publicly available (https://doi.org/10.25326/221). The version 2.0.0 of the radiosondes dataset is publicly available at https://doi.org/10.25326/62 . The WindCube lidar dataset is publicly available (https://eurec4a.aeris-data.fr/).

The data for the sensitivity experiments performed with the IFS used in this study are available at the following DOIs. CTRL_an: https://doi.org/10.21957/4vgx-3f28 , CTRL_fc: https://doi.org/10.21957/240p-1k07 , Exp1_an: https://doi.org/10.21957/zfxz-3h02 , Exp1_fc: https://doi.org/10.21957/nv0f-pr71 , Exp2_an: https://doi.org/10.21957/7zx9-6084 , Exp2_fc: https://doi.org/10.21957/mgrt-pp74 , Exp3_an: https://doi.org/10.21957/2t2w-wy02 , Exp3_fc: https://doi.org/10.21957/af7h-bf97 .

ERA5 was produced by ECMWF as part of implementing the Copernicus Climate Change Service on behalf of the European Union and is made publicly available through the Copernicus Data Store (DOI: 10.24381/cds.bd0915c6).

3

MOMENTUM TRANSPORT IN ORGANIZED SHALLOW CUMULUS CONVECTION

This study investigates momentum transport in shallow cumulus clouds as simulated with the Dutch Atmospheric Large Eddy Simulation (DALES) for a 150 x 150-km^2 domain east of Barbados during nine days of EUREC4A. DALES is initialized and forced with the mesoscale weather model HARMONIE-AROME and subjectively reproduces observed cloud patterns. This study examines the evolution of momentum transport, which scales contribute to it, and how they modulate the trade-winds. Daily-mean momentum flux profiles show down-gradient zonal momentum transport in the sub-cloud layer, which turns counter-gradient in the cloud layer. The meridional momentum transport is non-trivial, with mostly down-gradient transport throughout the trade-wind layer except near the top of the surface layer and near cloud tops. Substantial spatial and temporal heterogeneity in momentum flux is observed with much stronger tendencies imposed in areas of organised convection. The study finds that while scales <2 km dominate momentum flux at 200 m in unorganized fields, sub-mesoscales $\mathcal{O}$(2-20 km) carry up to 50% of the zonal momentum flux in the cloud layer in organised fields. For the meridional momentum flux, this fraction is even larger near the surface and in the sub-cloud layer. The scale-dependence of the momentum flux is not explained by changes in convective or boundary layer depth. Instead, the results suggest the importance of spatial heterogeneity, increasing horizontal length scales, and counter-gradient transport in the presence of organised convection.

3.1 INTRODUCTION

Shallow cumulus clouds cover vast areas over the tropical and subtropical oceans. They influence the atmosphere through their effect on the humidity and temperature distribution (Neggers et al., 2007; Tiedtke, 1989), and through their modulation of the radiation budget (Bony et al., 2020a). Shallow convection precipitates and organises frequently, which may matter for the energy budget and the momentum budget in ways that are not well understood. In recent years, mesoscale organisation has drawn increased attention from the community. The main focus has been on describing and explaining mesoscale patterns in clouds. Studies have also emphasised the presence of cold pools and gustiness at times of significant precipitation (Vial et al., 2019; Vogel et al., 2021; Zuidema et al., 2017) and the ubiquity of shallow mesoscale overturning circulations (SMOCs) on scales of 10 - 100 km (George et al., 2021a).

This study focuses on momentum transport in shallow cumulus fields with different mesoscale organisation. Convective momentum transport by shallow cumulus (shallow CMT in short) has been studied primarily in the context of idealised cloud cases, such as BOMEX Brown (1999); Larson et al. (2019) and RICO (Schlemmer et al., 2017), which do not represent the widely varying cloud and wind fields observed in nature. It has hardly been evaluated to what extent such realistic and complex cloud fields further complicate known issues with representing momentum fluxes in models. In general, common approaches to model turbulent and convective fluxes require scrutiny, as model grid spacings are approaching the scales of convection.

The mass-flux approach is commonly used for convective transport of heat and moisture, and also often of momentum. CMT parameterisations of deep convection (e.g. Kershaw and Gregory (1997)) combine the convective mass-flux with an empirical relationship that relates the cross-updraught pressure gradient to the large-scale vertical wind shear, while others (Schneider and Lindzen, 1976) assume the updraft or downdraft have horizontally uniform properties. In the context of deep convection, Badlan et al. (2017) shows how these schemes are not able to represent the transport associated with organised mesoscale circulations, as they neglect an important mesoscale pressure gradient term in the momentum budget. Models handle the transport of momentum by shallow convection in ways that are not readily documented. A variety of approaches appear in place, that include transport in the cloud layer by a mass flux scheme, an eddy-diffusivity mass flux (EDMF) approach, which also includes a dry mass flux of momentum in the sub-cloud layer, or higher-order turbulence schemes, which include prognostic equations for the variance and fluxes.

Larson et al. (2019), and also Helfer et al. (2021) and Dixit et al. (2021) highlight the complex layered structure of wind and momentum flux in typical shallow convective boundary layers, whereby the zonal wind establishes a jet or local maximum near cloud base. This implies that buoyant updrafts can carry slower momentum originating from the surface upward through cloud base into the lower cloud layer, which results in counter-gradient transport: an enhancement of the vertical gradient of the wind. To model the significant transport that results from smaller dry plumes (sub-cloud layer overturning), an eddy-diffusivity approach in the sub-cloud layer alone would not be sufficient. In the cloud layer, the environmental wind decreases with height, so that the momentum deficit in those

updrafts will turn into a momentum excess somewhere in the cloud layer, above which the transport becomes down-gradient again.

Already demonstrated by (Brown, 1999; Schlemmer et al., 2017), the mass flux approach underestimates momentum fluxes in the cloud layer to a greater degree than it underestimates moisture and heat fluxes. Part of the missing flux is attributed to environmental velocity fluctuations that may be produced through pressure perturbations created by cloud cores. Compared to BOMEX simulations in Larson et al. (2019), the counter-gradient transport layer is notably more pronounced and deeper in double-nested LES with time-varying forcing run with ICON on 100 x 100 km^2 domains (based on the NARVAL campaigns) (Dixit et al., 2021; Helfer et al., 2021). In the ICON-LES hindcasts, a varying large-scale forcing and the use of open-boundaries likely favoured the development of a larger variety of (deeper) shallow convective systems with more pronounced horizontal circulations. Dixit et al. (2021) analyzed the budget of the momentum flux in these simulations, which revealed that the dominant mechanism acts through a subtle balance between the flux generation through nonhydrostatic buoyancy residue and the horizontal circulations triggered by the associated pressure gradients. These mechanisms produce significant positive, counter-gradient momentum flux that counteracts the negative flux production through shear-driven turbulent diffusion near cloud tops. In the smaller 25 x 25 km^2 BOMEX simulations of Larson et al. (2019) the buoyancy production term and turbulent advection terms are important.

Following these recent studies, the simulations we carry out here to study momentum transport have realistically varying large-scale forcings and use a domain much larger than that of previous LES studies. Our study focuses on the first nine days of February 2020 during the EUREC4A campaign (Stevens et al., 2021),that we simulated with the Dutch Atmospheric Large Eddy Simulations (DALES, Heus et al. (2010)) on a 150 x 150-km^2 domain forced with large scale dynamical tendencies from the regional weather model HARMONIE-AROME (Bengtsson et al., 2017; de Rooy et al., 2022).

The EUREC4A campaign provided observational estimates of large-scale wind and pressure gradients as well as large-scale divergence (subsidence) through circular dropsonde arrays - a dataset named JOANNE (George et al., 2021b). Nuijens et al. (2022) used the JOANNE dataset to derive the momentum budget of the trades and showed that into February, as the trade-winds strengthened and the cloud field organised into gravel and flower structures, the effect of different flows on the wind may change substantially. For instance, as the winds strengthened, the derived observed amount of vertical divergence of momentum flux appeared to accelerate winds in the upper cloud layer. The in-situ turbulent momentum fluxes measured by different aircraft vehicles also suggested that horizontal gradients of momentum flux can be large across 20-km flight legs, suggesting that horizontal homogeneity is a poor assumption, and horizontal flux divergence may not be neglected.

Our objectives are three-fold: 1) reveal which scales are contributing to momentum fluxes throughout the boundary layer, 2) study changes in the scale contribution as the cloud field organises; and 3) study the impact of different scales of momentum transport on the vertical flux divergence. With that, the simulations may provide insight into what the observed momentum budget during EUREC4A appears to suggest: that in organised

shallow convection, just as in deep convection, (sub)mesoscale flows $\mathcal{O}$ 2-100 km play a non-negligible role in the momentum budget.

The paper is structured as follows: Section 3.2 introduces the experimental design (3.2.1 3.2.2, 3.2.3, 3.2.4), and it explains a filtering method that is used to partition the flux into different contributing scales (3.2.5). The results first describe the simulated wind and cloud field, along with the momentum fluxes (Section 3.3). Section 3.4 shows the temporal evolution of the momentum flux (3.4.1), the spatial scales that contribute to the flux (3.4.2 and 3.4.3), and how this varies with precipitation and degree of organisation (3.4.4). In Section 3.5 we explain the influence of mesoscale flows in (un)organised cloud fields. The discussion and conclusions are given in Section 3.6.

3.2 Experimental design

3.2.1 EUREC4A

The EUREC4A field campaign took place in the oceanic trade-winds region east of Barbados, between January and February 2020. EUREC4A is among the largest observational field campaigns of the coupled atmosphere-ocean system, providing benchmark measurements for a new generation of models and scientific discoveries. EUREC4A aims at advancing understanding of the interplay between trade-wind clouds, convection and circulation and their role in climate change. EUREC4A also includes a modeling component that consists of a model intercomparison (MIP) case for LES and Storm Resolving Models (SRMs). Among the goals of this intercomparison are: 1) assessing the simulation capability of the observed shallow cloud mesoscale organisation over the subtropical ocean, and 2) understanding the underlying dynamical processes leading to the mesoscale organisational patterns. The simulations presented in this study, run from 2 February to 10 February 2020, which are interesting days because of the range of cloud patterns observed during a transition from weaker to stronger trade-winds. These simulations have largely been used to establish the framework and the set up of the EUREC4A-MIP. While the intercomparison case uses large-scale forcing derived from ERA5, this study derives its forcing from the regional weather model HARMONIE-AROME. The latter allows a comparison between the parameterized physical tendencies from the regional model with the resolved physical tendencies of the LES, as described below.

3.2.2 HARMONIE-AROME

In this paper we use version cy43 of the numerical weather prediction model HARMONIE-AROME. A general overview of HARMONIE-AROME cy40 can be found in (Bengtsson et al., 2017). Most modifications in the physics from model version cy40 to cy43, as well as a comprehensive description of the most relevant parameterisations, namely the cloud, turbulence, and convection scheme, are presented in de Rooy et al. (2022). The total turbulent fluxes are parameterised using the eddy-diffusivity mass flux (EDMF) framework which facilitates a unified description of the turbulent transport in the dry convective boundary layer (Siebesma et al., 2007) and the cloud-topped boundary layer (Rio and Hourdin, 2008; Soares et al., 2004). In such an approach the total turbulent transport is described by a small-scale, diffusive part and a larger-scale transport by organised updrafts.

Diffusive, smaller-scale turbulent transport is described by the TKE turbulence scheme HARATU (HArmonie with RAcmo TUrbulence) as described in Lenderink and Holtslag (2004). The shallow convection scheme, as described by de Rooy et al. (2022), utilises a mass flux approach in which dry and moist updrafts are distinguished (Neggers, 2009). The variables treated in the shallow convective scheme are temperature, humidity, and momentum. This means that the CMT is simply the mass flux times the excess of the updraft u or v. The only difference with scalar variables concerns the initialisation of the updraft properties at the lowest model level. Temperature and humidity have an initial excess over the environmental values scaled by the surface fluxes, whereas u and v have the same values for the updraft and the environment. As the updraft rises, the environment changes and entrainment dilutes the updraft, together determining the excess of the updraft in both scalars and momentum at higher levels.

HARMONIE-AROME (from hereon HARMONIE) is used with a grid spacing of 2.5 km in an area of 3200 x 2025 km^2 centred around Barbados. HARMONIE runs in a free (climate) mode starting on Jan-1st and is forced with ERA5. In climate mode, HARMONIE is not reinitialised every 24 hours, which limits the effect of biases inherited from the forcing model. However, HARMONIE receives lateral boundary fields from ERA5 every hour. With this setup the model is allowed to develop its own synoptic systems which we assume to be plausible although we recognise they are different from the real, observed meteorological conditions.

3.2.3 DALES

As described in Heus et al. (2010), DALES is a community-based model and it is freely available. In this study we use DALES version 4.3. Under anelastic approximation, the model solves filtered prognostic equations in finite volumes. The model uses doubly periodic boundary conditions on the domain sides, no-slip condition at the bottom and a sponge layer at the top. Advection is done using a 5th order central difference scheme (Wicker and Skamarock, 2002). Sub-filter scale fluxes are modeled through an eddy diffusivity approach, following Deardorff (1980). Monin-Obukhov similarity theory is applied for the computation of the surface fluxes for heat, moisture, and momentum at the bottom boundary of the model. For condensation a traditional adjustment scheme is used, and a 2-moment scheme (Khairoutdinov and Kogan, 2000) is used for rain, while in the cloud microphysics a constant cloud droplet number concentration of 50 cm^{-3} is prescribed.

The EUREC4A simulations are run on a domain of 150 x 150 km^2, centered at 13.3 N,-57.7 E, which covers an area of intensive measurements eastward of Barbados. 1512 horizontal grid points are used in both x and y directions, corresponding to a grid spacing of about 100 m. The vertical grid is stretched with the following exponential function: $dz_i = 20(1 + 0.012)^i$, where dz is the grid spacing, and i is the level. This gives a dz of 20 m near the surface and about 55 m at 3 km. The domain extends up to 8 km, with a sponge layer occupying the upper one-third of its levels. Above this simulated domain lies a horizontally homogeneous layer with prescribed profiles of pressure, temperature, humidity, and ozone. These so-called background profiles serve as inputs for a rapid radiation transfer model. DALES is run in a climate mode without re-initialisation, whereby the first four hours are disregarded as spin-up. This mode allows aggregated cloud fields and mesoscale circulations to evolve

over multiple days.

3.2.4 Large scale forcing

The regional weather model HARMONIE provides the initial conditions, SST, and large scale dynamical forcing (tendencies) of momentum, temperature and humidity to DALES. At the surface the sea surface temperature (SST) is prescribed daily, and the roughness length is kept constant at 10^{-5} m. This means that our results exclude the effect of a diurnality in SST (not captured by HARMONIE).

Throughout the layers, the large scale forcing is applied as one dynamical tendency that includes both vertical and horizontal advective tendencies as well as the large-scale pressure-gradient and Coriolis force (for momentum). The tendency equation (here for the zonal wind u) can be split into two parts as follows:

$$\frac{\partial \overline{u}}{\partial t} = \left(\frac{\partial \overline{u}}{\partial t}\right)_{\text{forcing}} + \left(\frac{\partial \overline{u}}{\partial t}\right)_{\text{DALES}} \quad , \tag{3.1}$$

where the overbar defines the spatial average over a horizontal slab of the DALES domain. The two terms on the rhs represent respectively 1) the large-scale forcing from HARMONIE, and 2) the tendencies calculated by DALES for scales smaller than the computational domain. The large-scale forcing includes:

$$\left(\frac{\partial \overline{u}}{\partial t}\right)_{\text{forcing}} = -\overline{\mathbf{v}} \cdot \nabla u + \frac{\partial \overline{p}}{\rho \partial x} + f \overline{v} + \mathcal{F}_{nudge} \quad , \tag{3.2}$$

where ρ is the reference density, $\mathbf{v} = (u, v, w)$ is the wind vector, $\overline{\mathbf{v}} \cdot \nabla u$ represents the horizontal and vertical advection of momentum, $\frac{\partial \overline{p}}{\rho \partial x}$ is the pressure gradient term, $f \overline{v}$ is the Coriolis force, and $\mathcal{F}_{nudge}$ is the tendency introduced by the nudging to the HARMONIE profiles. All terms in equation (3.2) are calculated hourly on a 300 x 300-km^2 subdomain of HARMONIE, which encompasses the DALES domain. These forcing and profiles are then spatially averaged and imposed uniformly to DALES. The relatively weak nudging is applied separately on an hourly basis with a timescale that changes with height: above 3 km it is 6 hours, at 2.5 km it is 28 hours, and it becomes increasingly negligible at lower levels.

The second term on the rhs of equation (3.1) is the turbulent momentum flux divergence term as calculated by DALES:

$$\left(\frac{\partial \overline{u}}{\partial t}\right)_{\text{DALES}} = -\frac{1}{\rho} \frac{\partial}{\partial z} \rho \overline{u'w'} \quad , \tag{3.3}$$

The horizontal flux divergence is omitted because of the periodic boundary conditions. In section 3.5 we make use of the Boussinesq approximation to drop density dependencies and rewrite equation (3.3) as:

$$\left(\frac{\partial \overline{u}}{\partial t}\right)_{\text{DALES}} = -\frac{\partial}{\partial z} \overline{u'w'} \quad . \tag{3.4}$$

3.2.5 Sub-filter and up-filter partitioning of turbulent fluxes

To evaluate the contribution of different scales to momentum transport, we apply Reynolds decomposition and obtain momentum fluctuations with respect to the horizontal domain average on 3D fields that are low-pass filtered with different filter sizes. This effectively partitions the total flux into a sub-grid and a resolved component (see also Honnert et al. (2011) and Dorrestijn et al. (2013)) .

The low-pass spectral filter uses a two dimensional Fourier transform and a cut-off frequency in Fourier space (see Appendix 1 in Honnert (2019) for other procedures), and returns all fluctuations occurring at the sub-filter scales. Small filter sizes correspond to high wave-numbers. The smallest possible filter has the size of a grid-box and returns no fluctuations, indicating that all variance is carried at scales larger than the specific size (up-filter). To obtain Figures 3.6 and 3.9, the partitioning is done repetitively at 40 different filter sizes, from 100 m to 150 km, to uniformly cover the range of scales in the domain (or spectrum of wave-numbers in the Fourier space). The partitioning can be described with the following set of equations:

$$
\begin{aligned}
u' &= u'_{SF} + u'_{UF} \quad , \\
w' &= w'_{SF} + w'_{UF} \quad ,
\end{aligned}
\tag{3.5}
$$

where u' and w' indicate the fluctuations with respect to the horizontal slab average, and the subscripts SF and UF refer to the sub- and up- filter scales, respectively. The turbulent momentum flux averaged over the DALES domain can be written as

$$
\begin{aligned}
\overline{u'w'} &= \overline{(u'_{SF} + u'_{UF})(w'_{SF} + w'_{UF})} \\
&= \overline{u'_{SF}w'_{SF}} + \overline{u'_{UF}w'_{UF}} + \overline{u'_{SF}w'_{UF}} + \overline{u'_{UF}w'_{SF}} \quad ,
\end{aligned}
\tag{3.6}
$$

which simplifies to

$$
\overline{u'w'} = \overline{u'_{SF}w'_{SF}} + \overline{u'_{UF}w'_{UF}} \quad ,
\tag{3.7}
$$

because high- and low-pass filtered functions with the same cutoff wave number are orthogonal (Frisch, 1995). In equation (3.7) the first term on the rhs is the flux carried at scales smaller than the size of the filter, the second term is the flux carried at scales larger than the size of the filter.

Within the 150 x 150-km^2 DALES domain sub-mesoscale and mesoscale flows are present and in this study we consider the contribution of all of these to what would be a Reynolds averaged flux over an area representative of the current resolution of global climate models (50 - 100 km). Current generation weather models are often in the so called grey-zone of convection as they use a grid mesh far less than ~ 50 km and thus explicitly resolve some mesoscale flows. The contribution of scales and a discussion on which flux needs to be parameterised will follow in sections 3.4 and 3.6.

3.3 Simulated and observed atmospheric conditions

The nine days of EUREC4A simulations between 2 February and 10 February were characterised by a significant evolution in winds and cloud patterns. It was chosen specifically to simulate the somewhat deeper and more vigorous trade-wind convection that develop as

winds strengthen. Figure 3.1A shows a time series of the domain-averaged cloud fraction in DALES, along with the temporal evolution of the rain rate (solid red line in A), and the surface zonal and meridional wind (B and C) from DALES, HARMONIE, ERA5 and from the HALO dropsondes and RV Meteor radiosondes. Along with the time series, the simulated liquid water path (LWP) in Figure 3.2 shows the model's ability to reproduce different cloud patterns on different days, which have been identified from GOES satellite imagery as *Flowers* on 2 February, *Sugar* on 6 February, and *Gravel* on 7 and 9 February (Schulz, 2022).

3
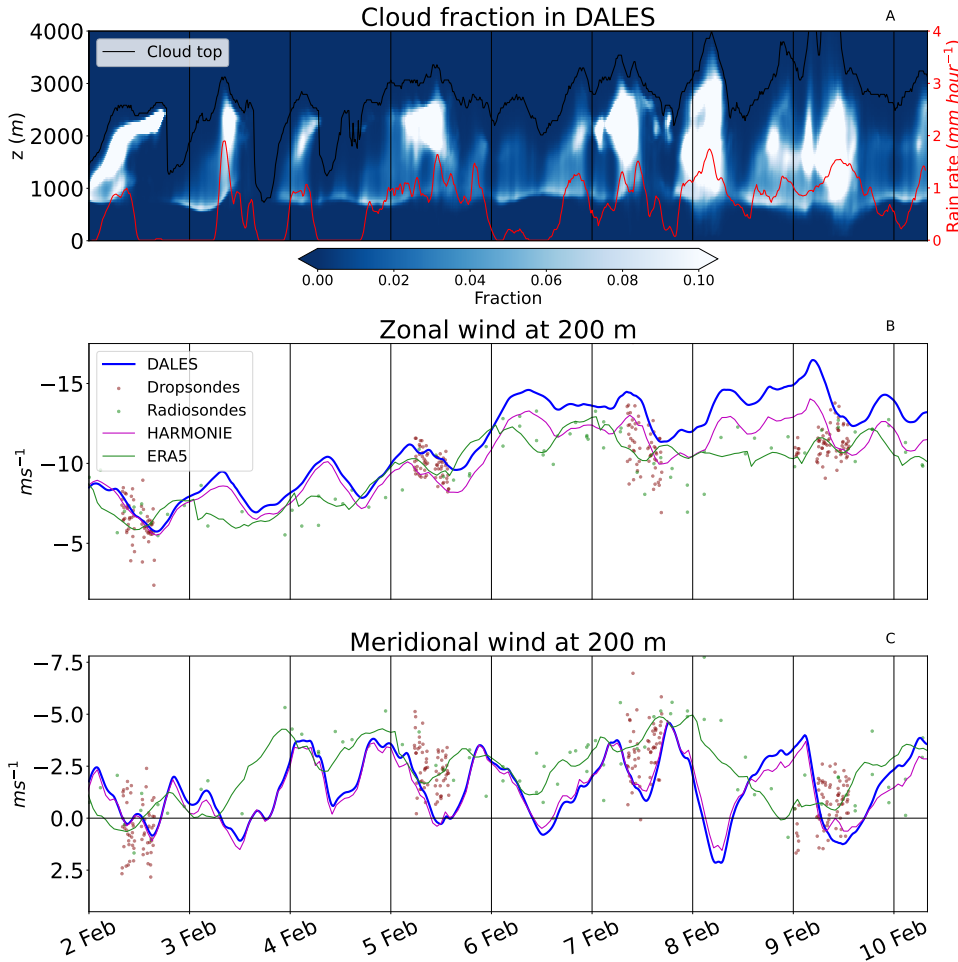
Figure 3.1: Time series of simulated quantities, where every vertical black line is at 0000 LT. In panel A are the mean cloud fraction and precipitation rate from DALES. In panel B and C is the zonal (B) and meridional (C) wind at 200 m, where we also included HARMONIE (magenta), ERA5 (green), and observations (dots).

The black line in Figure 3.1A indicates the cloud top height, which is defined as the level where the averaged liquid specific humidity becomes negligible ($ql < 0.0001 g \, kg^{-1}$), above

the level where *ql* maximises. Precipitating shallow clouds reach up to 2.5 or 3 km on most days. Despite being over ocean, the cloud top oscillates significantly, ranging from about 1 km to almost 4 km. The variability reflects the diurnality, with deepening cloud trends during the morning hours, and a general deepening of the cloud layer over the 9 days as surface wind speeds increased.
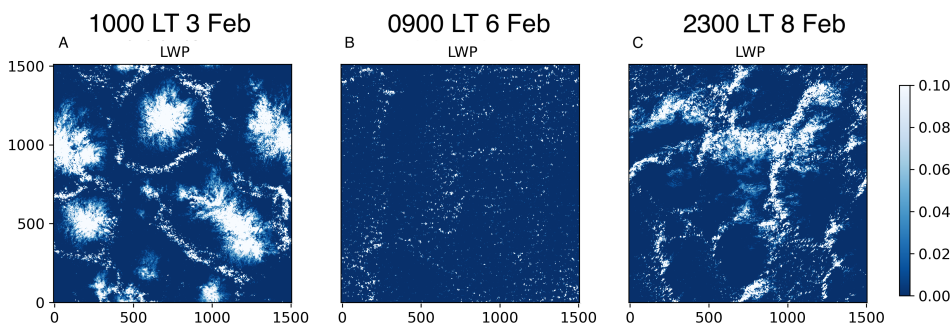
Figure 3.2: Examples of simulated fields of liquid water path (LWP). The time corresponds to 1000 LT 3 Feb (A), 0900 LT 6 Feb (B), 2300 LT 8 Feb (C).

On 2 February, after 0800 LT, a persistent thin layer of clouds between 2 and 2.5 km appears, which is typical of the stratiform anvil associated with flowers. The flower patterns and associated cold pools are still present on 3 February, as seen in the LWP field in Figure 3.2A. The anvil can persist, as in this case, after the convective area of the cloud has dissipated by rain. On 6 February, the cloud fraction is relatively low, but constant throughout the day and with a maximum near cloud base and a cloud top near 2 km. On this day, DALES shows unorganised sugar clouds (see Figure 3.2B) with almost zero rain-rate (red line) at the surface. This is in line with the observations. Gravel patterns are also clearly reproduced in our simulation on 8 and 9 February (see Figure 3.2C). On these days, the cloud layer deepens and large cold-pools develop, but the cloud patterns are less regular or symmetric as in the flower case of Figure 3.2A.

The diurnality in the clouds and precipitation is evident, with the deepest and rainiest clouds around 0700 local time (LT). A diurnality in cloudiness and wind is supported by observations, although less strong than in HARMONIE and DALES. Vial et al. (2019, 2021) found two populations of cumuli with different diurnality: 1) non-precipitating very shallow cumuli that develop during the day and maximise around sunset; and 2) deeper precipitating cumuli with stratiform cloud layers below the trade inversion that develop during the night and maximise before sunrise. The deeper ones dominate the diurnality of the total cloud cover.

The diurnality in surface winds has been argued as one of the possible drivers of the diurnality in clouds, besides differences in radiative heating rates between day and night. Strongest winds occur at 0600 LT, shortly before the peak in precipitation and cloud cover. The simulated winds evolve in a similar way as the radiosonde and dropsonde winds, but biases increase in the last four days, which is not unexpected given that the simulations

are not reinitialized at midnight. During the final days, the surface sensible heat flux (not shown) is also larger in DALES than observed. Differences with ERA5 and the observations are expected in such climate runs. The excessive diurnal cycle, which DALES inherits from HARMONIE, is a known problem and it should be discussed in a separate article, as diurnality is not the focus of this study. From Figure 3.1 emerges that DALES and HARMONIE are in good agreement with each other. After 6 February the strong large-scale forcing in the zonal component challenge the double periodic boundary conditions resulting in winds that are stronger in DALES than in HARMONIE. We assume that these somewhat stronger winds are still probable in the trade region.
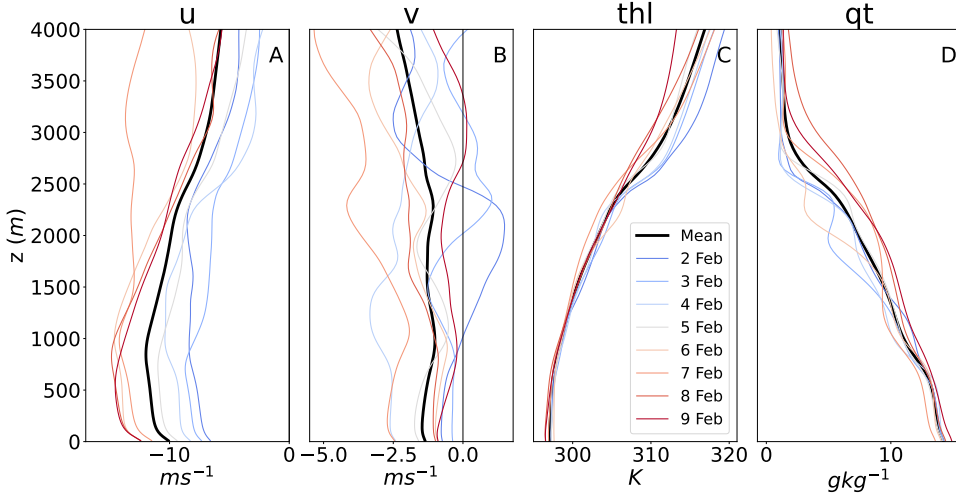
Figure 3.3: Domain averaged profiles. Black is the mean over the entire dataset, and each coloured line refers to a single day. Panel A displays the zonal wind, panel B the meridional wind, panel C the liquid potential temperature (thl) and, panel D the total specific humidity (qt).

Daily mean profiles of the simulated winds and thermodynamic structure are shown in Figure 3.3. The days with strong zonal winds near the surface (the second half of the simulated days, 6 to 10 February, in orange / red in Figure 3.3A and B) tend to have larger shear in the cloud layer, except for 7 February, which exhibits a deep layer of strong easterlies. The meridional winds are more variable but overall negative (northerly winds). On the first few days (blue) the inversion is well pronounced around 2500 m, and capped by a relatively warm and dry free troposphere. In contrast, on the last few days (red lines) the inversion is less evident and the profiles indicate heat and moisture mixing across a deeper layer, in line with the presence of deeper and more vigorous convection.

3.4 Characteristics of the momentum flux

3.4.1 Mean momentum flux profiles

The daily-mean total (resolved plus unresolved) zonal momentum flux profiles in DALES (Figure 3.4A) are typically positive near the surface and turn negative between 1 and 1.5 km (above cloud base). A positive momentum flux up to 1 km is consistent with local

turbulence: for an easterly flow ($\overline{u} < 0$), upward ($w' > 0$) motions generate positive zonal wind anomalies ($u' > 0$), while downward motions ($w' < 0$) generate negative zonal wind anomalies ($u' < 0$). As the evolution of the flux in Figure 3.4B shows, the near-surface zonal momentum flux almost doubles in the last four days, in line with the strengthening of the easterly surface wind, and the height at which the flux turns negative increases. Large values of momentum above 2 km are found more frequently during the final days of simulation and correspond to increases in cloud top height (shown as a black line).

As seen in Figure 3.3A, the zonal wind shear becomes positive around 1 km ($\frac{du}{dz} > 0$), whereas the zonal momentum flux remains positive up until ~ 1.3km ($\overline{u'w'} > 0$). This implies a layer where, in a simple K-diffusion model, the turbulent diffusivity parameter K is negative, denoting counter-gradient momentum transport.

The meridional momentum flux (Figure 3.4C, D) is smaller compared to the zonal momentum flux. It is positive at the surface and negative between 200 m and 1200 m on most days. The sign of the meridional momentum flux is less trivial to interpret because, at times, the meridional wind can turn southerly (positive), as seen in Figure 3.1C. Negative fluxes near the surface are associated with hours of southerly winds, typically occurring during daytime. The largest values of meridional momentum flux are inside the cloud layer on days with stronger convection (last four days).
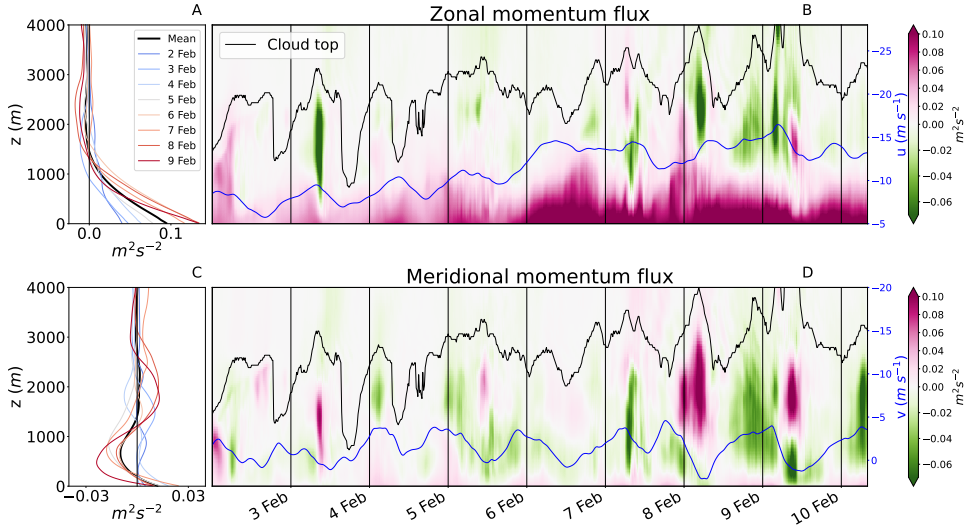
Figure 3.4: Zonal (A, B) and meridional (C,D) momentum flux profiles, shown as daily averages (A, C) and as contours of 15-minutes averages (B,D). The black line in panels B and D marks the cloud top height (h_b), while the blue lines indicate the surface zonal and meridional momentum.

In Figures 3.4 B and D convective events range from few hours (e.g., 3 February) to more than 5 hours (e.g., 8 February) and go hand in hand with strong momentum fluxes in the cloud layer. These strong variations are not always evident from the daily-mean profiles. Even more pronounced is the spatial heterogeneity in the momentum flux across the domain, which we present next.

3.4.2 Spatial heterogeneity

Figure 3.5 shows a snapshot of the momentum flux at 200 m on 1000 LT 3 February (the flower case of Figure 3.2A). Panel A and B show, respectively, the total zonal and meridional flux. The sub-filter flux (for a filter $\Delta x = 2.5$ km) is in panels C and D, whereas the up-filter flux is in panel E and F.
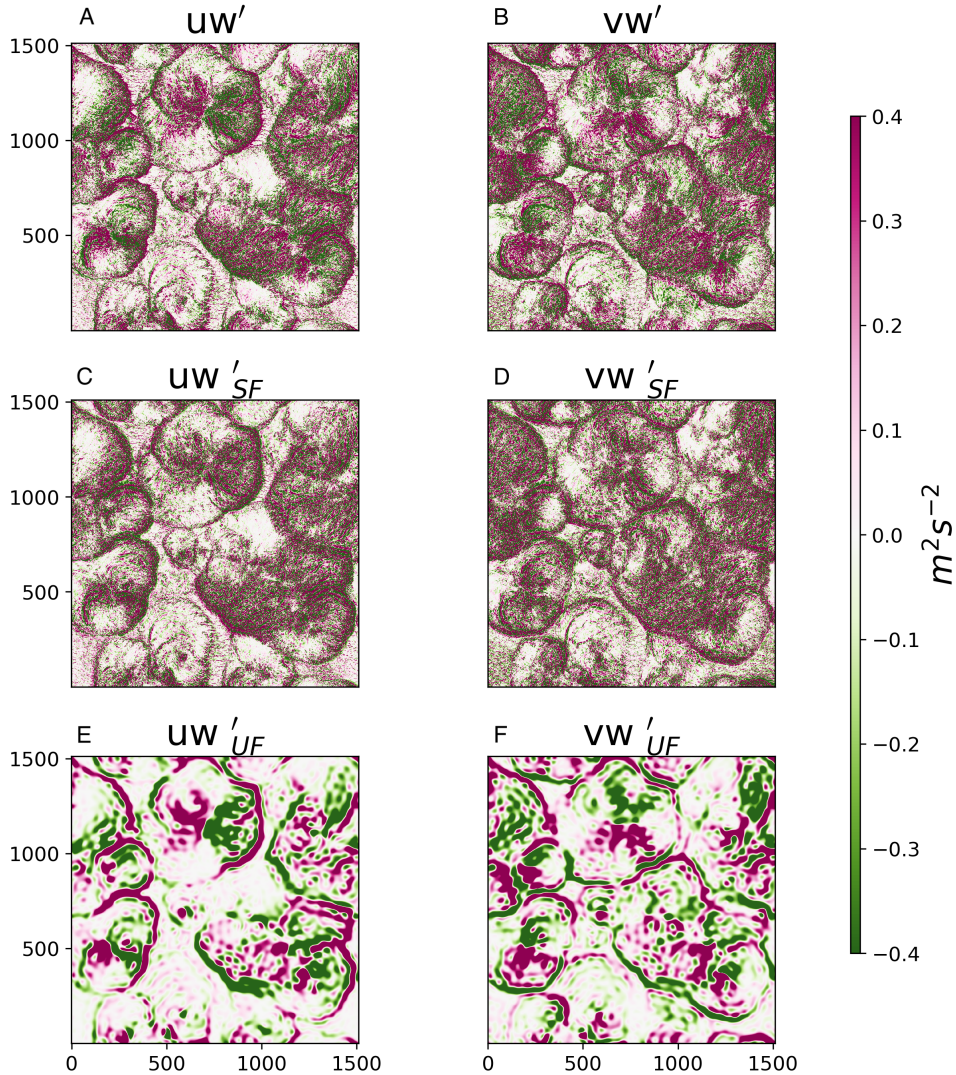
Figure 3.5: Instantaneous fields at 200 m on 1000 LT 3 Feb for resolved zonal (left) and meridional (right) momentum fluxes from DALES. In panels A and B is the total resolved flux: $\overline{u'w'} = 0.037\ m^2 s^{-2}$, $\overline{v'w'} = 0.018\ m^2 s^{-2}$. In panels C and D is the sub-filter resolved flux for $\Delta x = 2.5 km$: $\overline{u'_{SF}w'_{SF}} = 0.024\ m^2 s^{-2}$, $\overline{v'_{SF}w'_{SF}} = 0.01\ m^2 s^{-2}$. In panel E and F is the up-filter resolved flux: $\overline{u'_{UF}w'_{UF}} = 0.013\ m^2 s^{-2}$, $\overline{v'_{UF}w'_{UF}} = 0.009\ m^2 s^{-2}$.

The total (resolved plus sub-grid) zonal flux is 0.037 $m^2 s^{-2}$, of which 65% (0.024 $m^2 s^{-2}$) is carried by scales smaller than 2.5 km and 35% (0.013 $m^2 s^{-2}$) by larger scales, even near the top of the surface layer. The total meridional flux $\overline{v'w'}$ is 0.0178 $m^2 s^{-2}$, of which 52% is carried by scales smaller than 2.5 km ($\overline{v'_{SF} w'_{SF}} = 0.0092 \ m^2 s^{-2}$), and 48% by scales larger than 2.5 km ($\overline{v'_{UF} w'_{UF}} = 0.0086 \ m^2 s^{-2}$). Because of the large spatial heterogeneity in the sign of the flux, domain-averaged fluxes suggest much smaller momentum flux than there is on a more local scale.

Below the flowers, Figure 3.5 captures several large cold pools, which appear as circles of diverging wind with a diameter of about 50 km. The combination of positive and negative signs in the horizontal wind anomalies divides the cold pool into four parts. Upwind, the momentum flux is positive at the edge and negative between the edge and the centre of the structure; downwind, the momentum flux is negative at the edge, and positive between the edge and the centre. These mesoscale structures are clear in the up-filter flux fields of Figure 3.5E, F and are partly visible also at the sub-filter scales (Figure 3.5C, D). To generalize beyond this one scene, the next sextion analyzes the scales responsible for momentum transport using all available statistics.

3.4.3 Scales of momentum transport
The relative contribution of different scales to the total momentum flux is shown in Figure 3.6. This essentially shows the change of the sub-filter component as a function of increasing filter size, here for the momentum fluxes simulated in the middle of the cloud layer, as it displays the largest variability. The y-axis is normalised by the total flux in the domain. Panels A and B show the zonal momentum flux ($\overline{u'_{SF} w'_{SF}}$) and panel C, D show the meridional momentum flux ($\overline{v'_{SF} w'_{SF}}$). Following Honnert et al. (2011) in Figure 3.6A, C a dimensionless x-axis is created by scaling the size of the filter with the height of the sub-cloud plus cloud layer (h_b). The vertical black line marks the mesh at which the filter size Δx equals h_b. This height varies in time, which explains why the lines begin and end at different points on the x axis. In panels B, D the flux partition is plotted against the size of the filter only and the vertical line marks $\Delta x = 2$ km. Hereafter we refer to the mesoscale as all scales between 2 km and 150 km, thus the meso-gamma and part of the meso-beta scales. As the dimensionless mesh size and the filter size increase, the contribution of the sub-filter scale also increases. Ultimately, 100% of the flux is carried by the sub-filter scale when the filter is as large as the domain. The y-axis value at the smallest filter size represents the percentage of the total flux carried by the unresolved scales ($\Delta x < 100$ m). Each curve refers to the median for an 8-hour interval and the colours refer to the different days, as in Figure 3.3.

The observed spread in scale contribution in the cloud layer is large: at $\Delta x = 2$ km, the sub-filter momentum flux (Figure 3.6B, D) varies from less than 20% to almost 100% of the total flux. In both directions, scales can contribute negatively to the total momentum flux, making the curves in Figure 3.6 non-monotonic, in line with Zhu (2015). This is because thermally driven plumes or cells do not necessarily possess similar horizontal momentum, whereas they often have similar thermodynamic properties. Furthermore, mesoscale flows associated with organised shallow convection and heating contrasts on even larger scales are introduced. The mesoscales contribute more to $\overline{v'w'}$ than to $\overline{u'w'}$, suggesting that
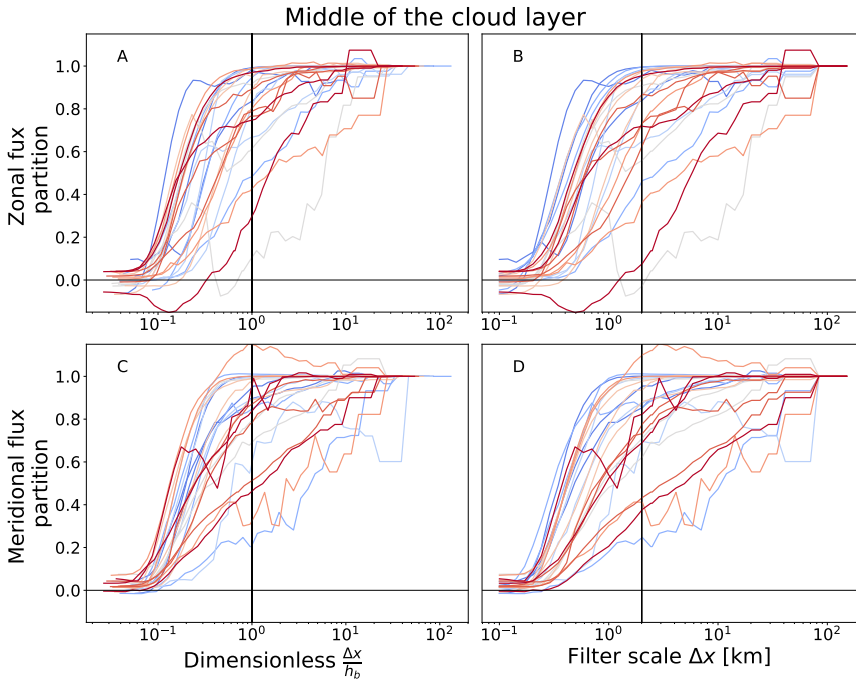
Figure 3.6: Partition of the sub-filter zonal (A, B) and meridional (C, D) momentum flux as a function of the dimensionless mesh $\frac{\Delta x}{h_b}$ (A, C) and of the dimensional filter size Δx (B, D). All panels refer to an horizontal cross section in the middle of the cloud layer. The vertical black lines denotes $\frac{\Delta x}{h_b} = 1$ and $\Delta x = 2$ km. Each curve is the median of an 8-hour interval identified by the colours: from blue at the beginning of the simulation to red at the end of the simulation.

circulations induced by coherent convective structures are more important for transporting meridional momentum than zonal momentum. This is even more evident at lower heights in the boundary layer (as we will see in the next section).

In contrast to Honnert et al. (2011), after rescaling with the cloud top height, the individual lines do not collapse onto a single curve, which would universally describe the partitioning of the momentum flux as a function of a well-defined vertical scale. Whereas the method proposed by Honnert et al. (2011) might work for thermodynamic variables in a clear boundary layer or for simple non precipitating cases, it fails to capture the momentum flux partitioning in organised, precipitating shallow cumulus convection. Cloud top height, or alternatively the boundary layer height, only captures the vertical growth of a convective system, but is clearly not always correlated with the dominant horizontal length scales, which play an important role in organised cloud fields (Janssens et al., 2021).

The contribution of mesoscales to the momentum fluxes depends strongly on the specific day considered. Figure 3.7 shows the temporal evolution of the contribution of the sub-filter component at $\Delta x = 2$ km. The data is grouped into 8-hour intervals, where each interval includes 16 cross-sections of flux, whose spread is shown as a box plot. The median,

corresponding to the value at the vertical black line in Figure 3.6B, D, is indicated with a red line. While on some days for the zonal component (Figure 3.7A), the majority of the data suggests a contribution of the sub-filter scales between 60% and 90%, with relatively small spread, other days suggest a significant increase in the contribution of mesoscales, shown as a reduction of the sub-filter contribution. For instance, on 3 February, the winds are slow and large coherent convective structures develop into flowers that dissipate again after a few hours. The smallest variability is on 6 February, where the scales smaller than 2 km consistently carry around 90% of the total flux: $\frac{u'_{SF} w'_{SF}}{u' w'}$ and $\frac{v'_{SF} w'_{SF}}{v' w'} \approx 0.9$. On this day the winds are strong, and only small thermals form, resulting in a persistent sugar-type field (see Figure 3.2B). Next, we investigate whether convective organisation can explain the shape of the curves in Figure 3.6.
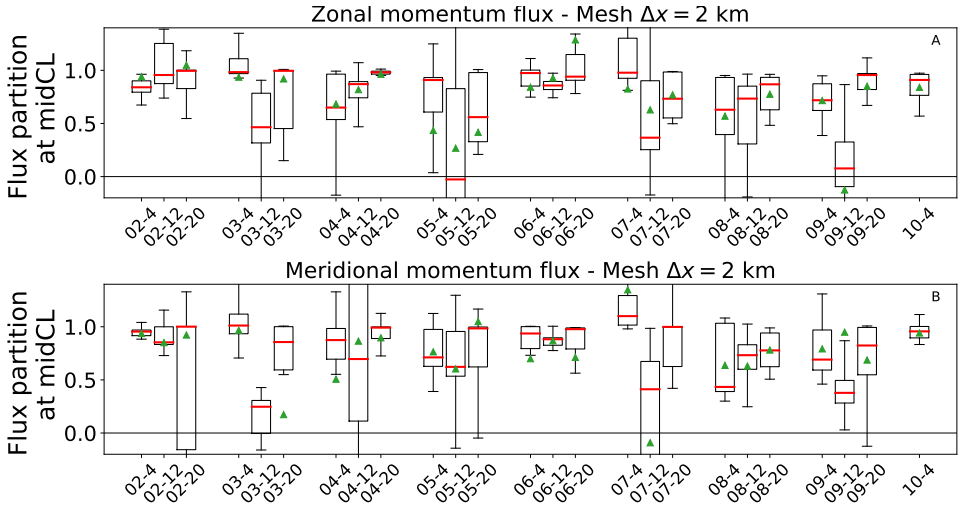
Figure 3.7: Distribution of the sub-filter zonal (A) and meridional (B) momentum flux in the middle of the cloud layer, for a filter $\Delta x = 2$ km. Each box-plot refers to a 8-hour interval, thus includes 16 values. The x-labels tell the day and central hour of the interval (e.g. 02-04 is 0004 LT 2 Feb), the green triangles indicate the mean.

3.4.4 Influence of precipitation and organisation

Spatial organisation is quantified using the widely used metric I_{org} applied to fields of LWP (Weger et al., 1992). I_{org} ranges between 0 and 1. A value of 0.5 indicates that objects (clouds) are randomly distribute in space, higher values indicate a clustered and organised field, whereas lower values indicate a regularly distributed field. Using a LWP mask means that anvils and non-convecting clouds are seen as cloudy objects, possibly overestimating the degree to which dynamically active clouds map onto the momentum fluxes. The different colours in Figure 3.8A represent three groups of I_{org}: Group 1 (yellow) corresponds to the lower quartile of I_{org} values, Group 3 (green) is the upper quartile, and Group 2 (blue) includes the remainder. The analysis gives similar results when creating groups defined by rain rate, but in line with Radtke et al. (2022), the two indices have some differences: I_{org} can be high on the first two days although precipitation (and total momentum fluxes in Figure 3.4) are moderate.
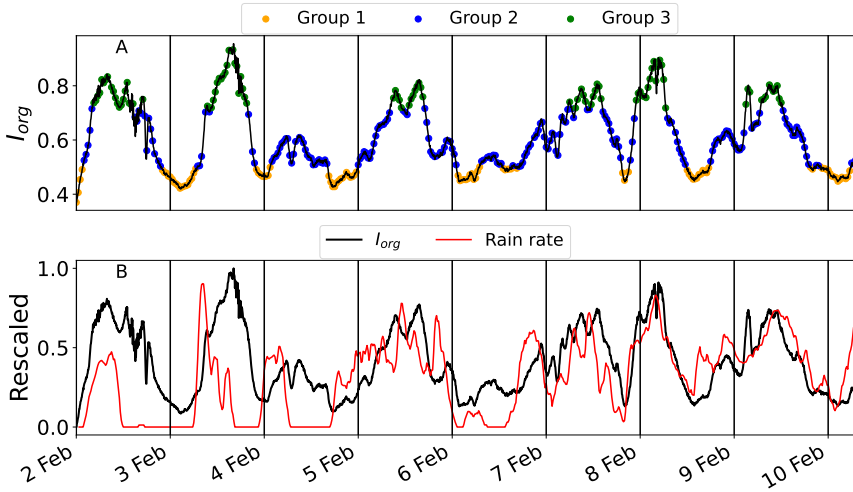
Figure 3.8: Time series of I_{org} as a 1.5 hours rolling average (A). Values in the lower quartile are in yellow (Group 1), values in the upper quartile are in green (Group 3), the remaining values are in blue (Group 2). In panel B are I_{org} (black) and surface rain-rate (red) as a 1.5 hours rolling average and rescaled between 0 and 1.

Precipitation is shown to precede organisation on the first few days of the simulation, which may be typical of flower structures, where anvils persist long after rain events have killed the source of convection. Differently, with gravel and mixed cloud structures (e.g., on 8 February) precipitation and organisation tend to have local peaks at the same time. Figure 3.8 is also informative concerning the observed diurnal cycle of shallow convection in the trades (Radtke et al., 2022; Vial et al., 2019). The early morning typically brings more vigorous convection, which is reflected into peaks of rain-rate and I_{org} around 1000 LT. Lowest rain rates are in the evening, and unorganised fields typically occur around 0000 LT.

Hereafter we analyse the flux partitioning as a function of scale for the three groups identified with I_{org}. Figure 3.9 shows results for three heights: 200 m (A,B), at cloud base (C,D), and in the middle of the cloud layer (E,F), as was shown before. Group 1 (yellow lines) tends to capture scenes where the small scales are the most active and the sub-filter scales dominate over 90% of the total flux for $\Delta x = 2$ at all levels. In Group 3 (green lines) on the other hand only 70-80% of the flux is carried by scales smaller than 2 km in the cloud layer. The different spread (smallest in Group 1 and the largest in Group 3) is partly explained by the different range of I_{org} values in the two groups. In Group 1 I_{org} ranges between 0.37 and 0.5, whereas in Group 3 I_{org} ranges between 0.72 and 0.96.

The separation of the data by I_{org} thus helps explain the spread in scale behaviour seen in Figure 3.6, with more mesoscale contribution to the flux higher up in the boundary layer than near the surface. However, for the meridional momentum flux, the mesoscales already have an imprint near the surface, because the meridional wind and thus meridional wind stresses are comparably small. Instead, for the zonal momentum flux, large small-scale

3
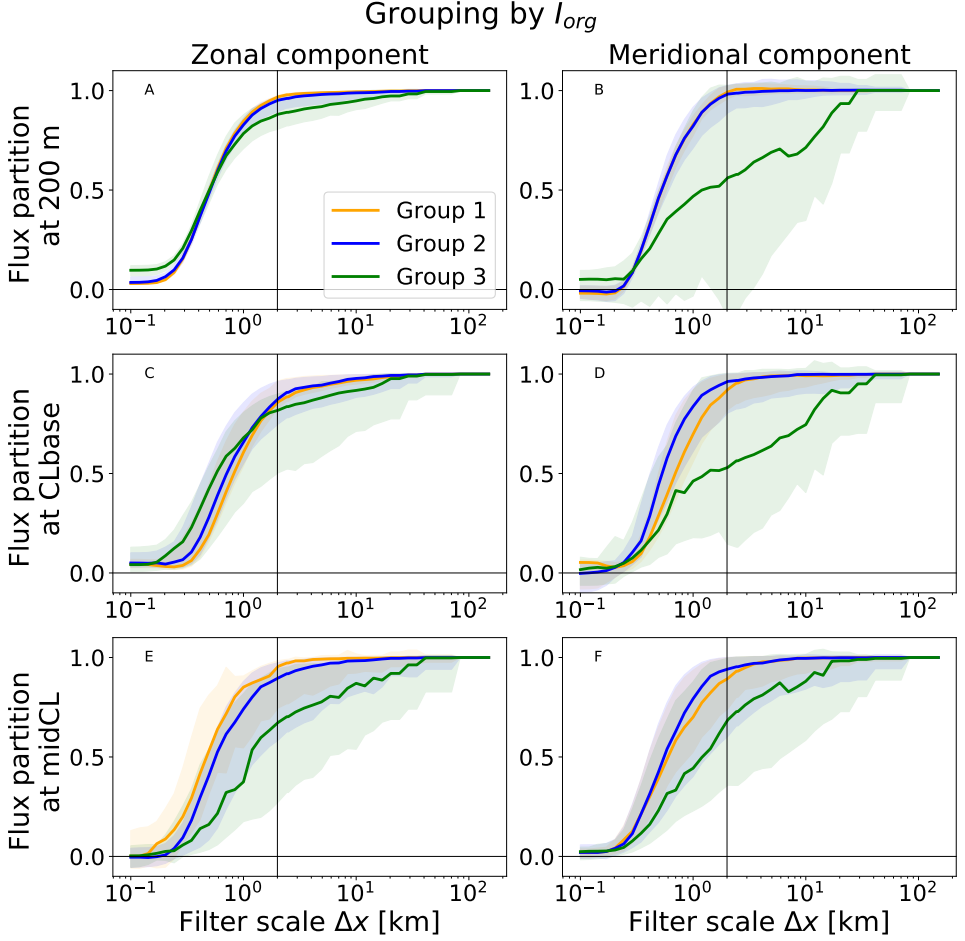
Figure 3.9: Partition of the sub-filter momentum flux as a function of the filter size Δx. The vertical black line denotes $\Delta x = 2.5$km, and each row refers to a different height: 200m (panels A, B), cloud base (C,D), the middle of the cloud layer (E,F). Each colour refers to one of the groups based on I_{org}. Group 1 is in yellow, Group 2 is in blue, and Group 3 is in green. See the text for a description of the groups.

turbulent stresses due to stronger zonal winds at the surface still lead to a dominance of smaller scales.

The scale behaviour of the heat and moisture flux is shown in the appendix. Much like the meridional momentum flux, these thermodynamic variables have a large imprint of mesoscales near the surface for groups 2 and 3 (see appendix 3A). In the cloud layer, heat and moisture tend to be carried vertically at smaller scales than momentum, although with small differences, especially in Group 2.

3.5 Role of (organised) convective momentum transport

From section 3.4 we can infer that, for scales of 1-10 km, there is not a clear, constant separation between scales in carrying momentum transport. In the following, we will use the definition of mesoscales and a filter size of 2 km to study how momentum transport on scales smaller and larger than 2 km influences the momentum budget by means of its vertical flux divergence. This is done for the unorganised and organised groups: sections 3.5.1 and 3.5.2 respectively.

3.5.1 Momentum flux divergence in unorganised shallow convection

The mean zonal wind shear in the lowest I_{org} group is negative below 1 km and positive above (Figure 3.10A), with a pronounced wind jet just above cloud base. Near the surface, the total resolved zonal momentum flux (solid green in 3.10 B) is larger than the average shown in Figure 3.4. The counter-gradient transport layer (marked in red on the y-axis) is small between 1 and 1.5 km.

The (northerly) meridional wind also has a small local maximum at the top of the surface layer and then decreases up to 2.5 km (3.10 D). The small local maximum implies a narrow layer of counter-gradient momentum transport up to 300 m, while everywhere above 300 m, the meridional momentum flux is negative, sustaining down-gradient momentum transport in the cloud layer. The up-filter flux (brown line) maximizes around cloud base and its relative contribution is small both in the zonal and meridional direction. In other words, at all heights, scales smaller than 2 km (sub-filter) carry the majority of the momentum flux.

The vertical divergence of the momentum flux (3.10 C and F) indicates an acceleration where $-\frac{\partial}{\partial z}\overline{u'w'} < 0$, because of the negative sign of the zonal wind. Scales smaller than 2 km decelerate the zonal wind at all heights, but least so near cloud base, as shown in Dixit et al. (2021); Helfer et al. (2020). Meridional winds are decelerated below cloud base, while they accelerate in a layer above cloud base. The up-filter zonal momentum flux (brown line) is symmetric around cloud base and introduces a deceleration. The positive sign of the up-filter flux can be explained by the tilting of the coherent overturning cells that are responsible for this transport. According to Moncrieff (1992) momentum transport by organised eddies propagating in a shear flow is a fundamental property of their tilt relative to the shear vector. Hence, these coherent cells must be tilted in the direction of the shear vector (du/dz): downshear (to the west) when defined as the zonal wind at cloud top minus
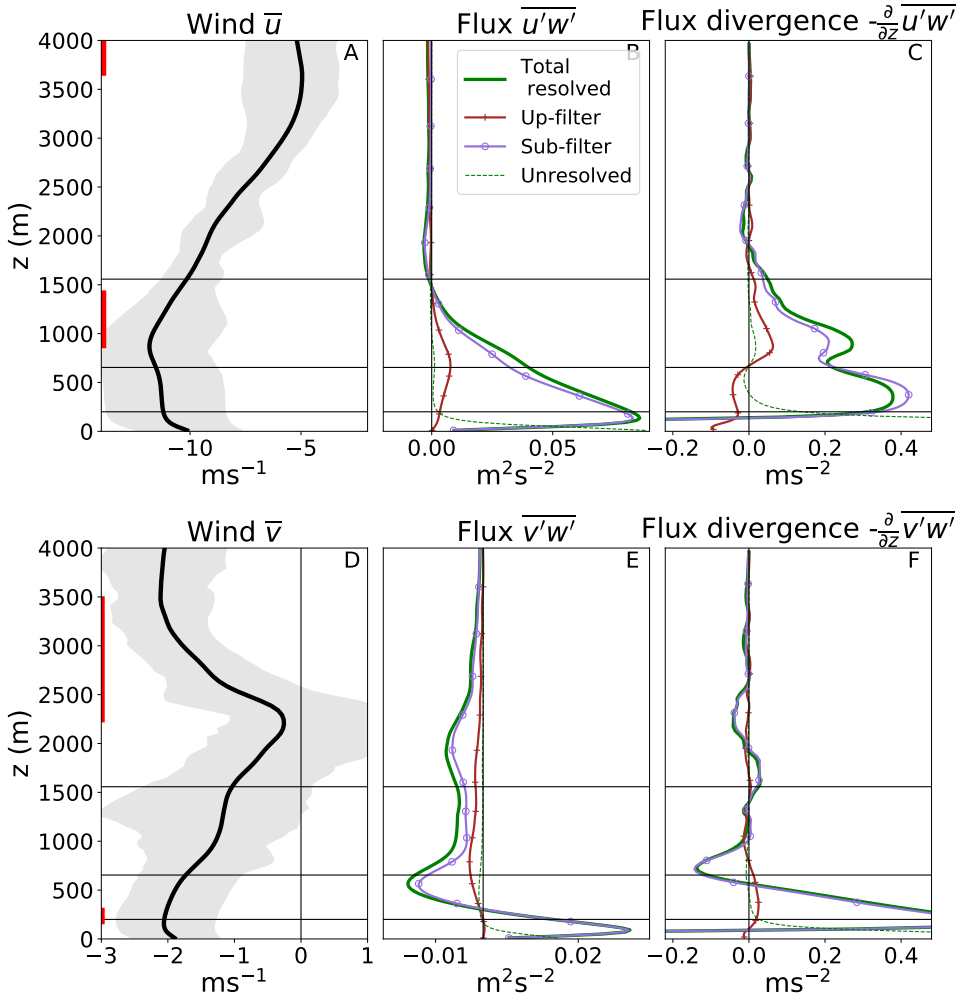
Figure 3.10: Vertical profiles for unorganised cases (Group 1). Mean zonal and meridional wind and interquartile range (A, D). Mean zonal and meridional flux partitioned with a filter of 2 km (B,E). Mean zonal and meridional eddy momentum flux divergence (C,F). The black horizontal lines mark the mean cloud top, mean cloud base, and 200 m. The red vertical lines indicate levels of counter-gradient momentum transport.

the zonal wind at 200 m. In that case, the upward ($w' > 0$) branches of these cells move to the west ($u' > 0$), leading to $u'w' > 0$. With transport maximizing near cloud base, the flow below is experiencing a net acceleration that opposes the friction imposed by turbulence and convection, while in the cloud layer, it contributes to a 'cumulus friction'. Vertically integrated, the meso-scale momentum flux tendency is zero, which means that mesoscale circulations merely rearrange momentum.

3.5.2 Organised convective momentum transport

In Group 3 of large I_{org}, up-filter scales carry more than 50% of the momentum flux everywhere above cloud base (Figure 3.11B, E). The mean cloud top of this group is few hundred meters higher than in unorganised cases, but one should consider that convection often extends above this mean value (Figure 3.4), as suggested by the negative zonal fluxes above 2 km. As such, the layer with non-zero momentum flux is deeper in this group.
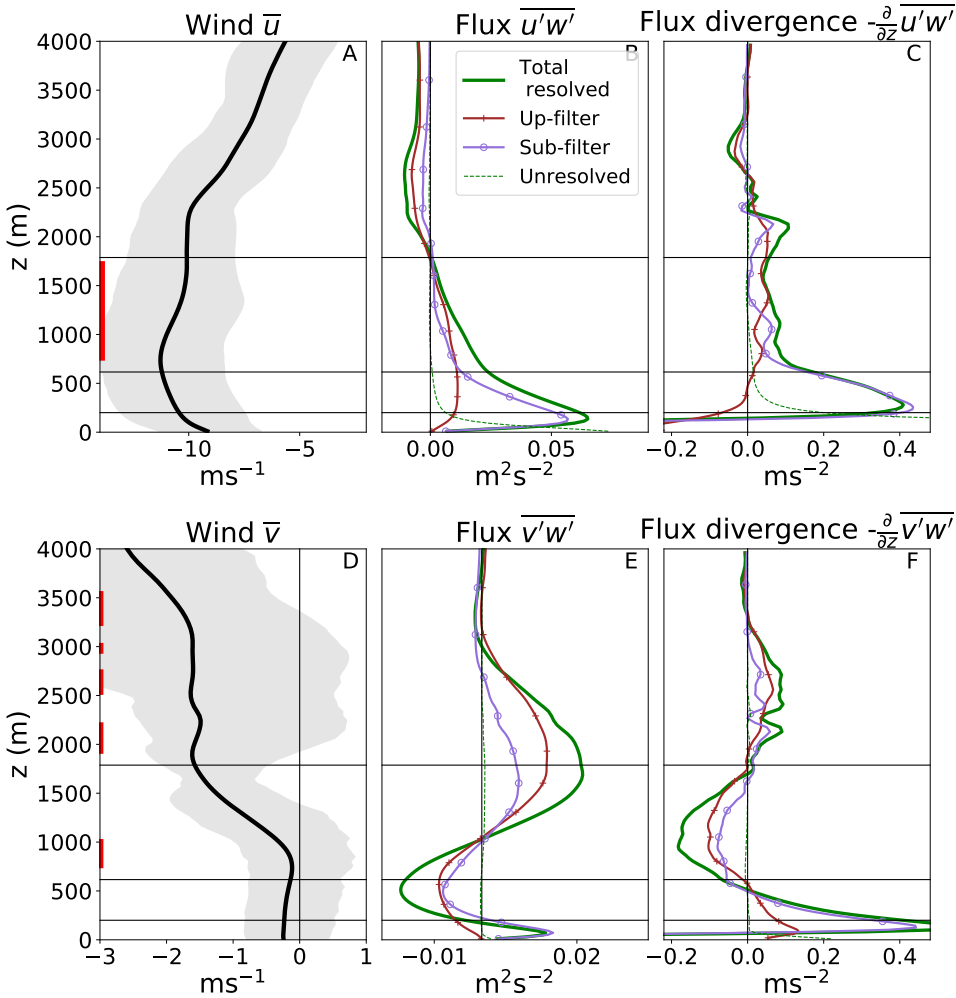
Figure 3.11: Vertical profiles for organised cases (Group 3). Mean zonal and meridional wind and interquartile range (A, D). Mean zonal and meridional flux partitioned with a filter of 2 km (B,E). Mean zonal and meridional eddy momentum flux divergence (C,F). The black horizontal lines mark the mean cloud top, mean cloud base, and 200 m. The red vertical lines indicate levels of counter-gradient momentum transport.

The wind profiles are notably different from the unorganised cases, with weaker winds near the surface and much smaller meridional winds in the sub-cloud layer. Above 1 km the

zonal winds are well mixed with little vertical shear and a deep layer of counter-gradient transport. The meridional winds are negatively sheared and a thin layer of counter-gradient transport appears also in the meridional component between 800 m and 1 km.

In the lower cloud layer the sign of the up-filter zonal momentum flux is positive, which means that the coherent or mesoscale overturning cells are tilted down-shear, but they become tilted up-shear above 2 km, and momentum fluxes there turn negative. Apparently, the mesoscale cold pool structures near the surface do not generate much up-filter momentum flux there when averaged over the domain, which must be because the diverging and converging branches of cold pools are symmetric and of opposite sign (see Figure 3.5).

In the meridional direction, the mesoscale flux is negative below 1 km, which implies a strong tilting up-shear despite the near-zero mean shear that is present. The deceleration (positive flux divergence) that is a result of this may help contribute to the profile of meridional wind. In the cloud layer, both sub-filter and up-filter fluxes are positive, which implies an even stronger tilting upshear against the shear that prevails in the background wind. The results suggest that the more organised convection has a pronounced role in setting the meridional wind profile.

3.5.3 Coherent, mesoscale circulations across cloud patterns

Here we illustrate the flow associated with the up-filter momentum flux in different cloud patterns. We examine the flower case on 1000 LT 3 February, which falls in group 3 with an I_{org} value of 0.7 and is depicted in Figure 3.2A. Figure 3.12 shows two vertical cross sections taken at 119.1 km on the y axis and at 69.5 km on the x axis, representing the decaying phase of a convective system, which started a few hours earlier from a cluster of shallow convective plumes. Those plumes lead to the accumulation of liquid water that spreads around 2 km (the anvil), and which will become thinner and detached from the convective activity of the boundary layer, but persist for about another hour before dissipating. Rain occurs during the evolution of this system and contributes to its dissipation. The colours represent the zonal respectively meridional wind anomaly, while the streamlines are calculated for up-filter wind anomalies corresponding to a filter scale of 15 km. They are coloured magenta when they are associated with a positive momentum flux, and green for a negative momentum flux.

The wind anomalies highlight a large cold pool which is symmetrical in the meridional direction but expands more to the west in the zonal direction, influenced by the easterly winds. Winds propagate radially from the centre with opposite sign in the anomaly vector and pushing the front. This symmetry explains why cold pools carry momentum fluxes of opposite sign at the two sides of their axis of symmetry (also visible in Figure 3.5E, F). The streamlines show the presence of two circulations that expand well beyond the size of the anvil. In both the zonal and meridional direction, Figure 3.12 shows two eddies spanning 30 to 40 km on both sides of the system. The streamlines move upward into the flower, but the horizontal wind anomaly is only positive in the part of the anvil expanding upstream. For weak background wind and a perfectly symmetric anvil one could expect net zero momentum transport at the anvil level. Nevertheless, the asymmetry of the anvil in the zonal direction (Figure 3.12B) produces a strong easterly wind anomaly, large negative
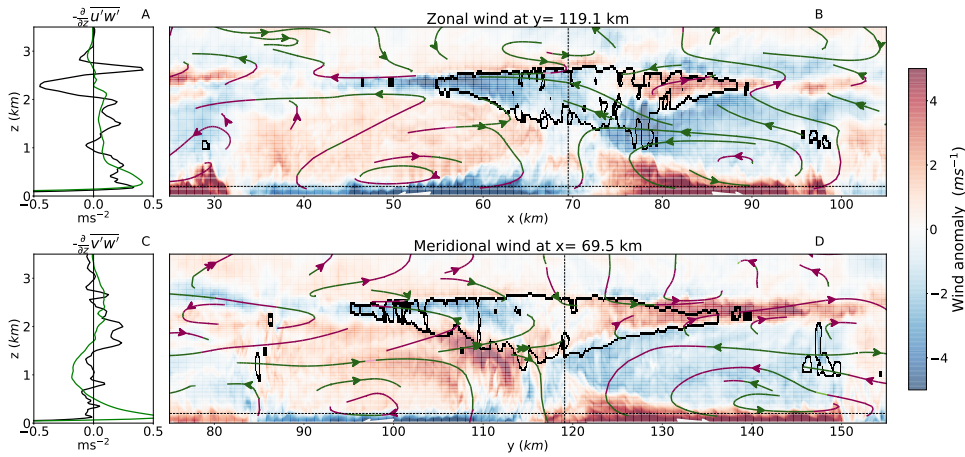
Figure 3.12: Mean flux divergence profiles (A, C) and vertical cross sections of the flower case on 1000 LT 3 February. The green profiles in A and C are (as in Figure 3.11C, F) the mean of Group 3. The black lines are the slab average for the scene. In panels B and D the contours indicate wind anomaly and the streamlines are the filtered velocity vectors for a filter scale of 15 km. Red streamlines refer to positive momentum flux and green to negative momentum flux.

momentum fluxes, and as a result, leads to a net acceleration of the easterly flow at the specific time of this flower (black profile in A).

These mesoscale circulations accompanying shallow cloud clusters (titled SMOCS, (George et al., 2021a)) can expand horizontally for twice the size of the visible anvil and determine the sign and intensity of the domain mean momentum flux. This flower case is a good example of a situation where vertical length scales (e.g. cloud top height) are not indicative of the size of the eddies nor the scales at which momentum transport occurs.

3.6 Discussion and Conclusions

This study analyses momentum transport from unorganised and non-precipitating to organised and precipitating shallow-convection in simulations on large-domains (150 x 150 km^2) subjected to varying large-scale flow. Its goals are to: 1) reveal which scales are contributing to momentum fluxes throughout the boundary layer, 2) study changes in the scale contribution as the cloud field organises; and 3) study the impact of different scales of momentum transport on the vertical flux divergence.

We simulated 9 days of the EUREC4A campaign with DALES using a horizontal grid spacing of about 100 m, forced with large-scale tendencies from the regional model HARMONIE-AROME. Both DALES and HARMONIE were run in a climate mode, allowing cloud fields and mesoscale circulations to evolve over multiple days with a wide variety of synoptic conditions. Although the study is not free of limitations, especially with respect to the periodic boundary conditions of DALES, the large spatial domain and the 9-day temporal extent allow us to assess the variability of momentum transport in more complex cloud fields subjected to various dynamical tendencies.

Our results reveal that the momentum flux profile averaged over a large domain is not representative of the flux profile found at individual locations, as the fluxes vary significantly in space and time and even change sign. This variability is observed on sub-mesoscales and mesoscales, with local flux values up to ten times larger than the domain average. The dominant scales contributing to momentum transport in the cloud layer are notably larger than the dominant scales in the sub-cloud layer. In the cloud layer scales larger than 2 km contribute between 1% and 80% to the total momentum flux, with large temporal variability that can be explained by the degree of cloud organisation. As the cloud field organises, the contribution of mesoscales to the flux increases. This is true for both the zonal and meridional momentum flux in the cloud layer. For example, when $I_{org} > 0.7$, scales larger than 2 km can contribute to more than 50% of the zonal momentum flux everywhere above cloud base. The meridional momentum flux has even a larger contribution of mesoscales at 200 m and at cloud base, suggesting that horizontal circulations are favoured in the cross-wind direction.

The mesoscale contribution to heat and moisture fluxes also increases with the degree of organisation (see appendix). Mesoscale flux contributions to especially the heat flux are much larger in the subcloud layer and near the surface than for momentum, because near the surface turbulent wind stresses dominate. However, in the cloud layer the contribution of mesoscales to heat and moisture fluxes is generally smaller or comparable to momentum fluxes. Evidently, horizontal circulations and mesoscale wind inhomogeneity can have scales much larger than the size of a single cloud. The presence of mesoscale circulations with scales on the order of hundreds of kilometers have been observed by George et al. (2021a) during EUREC4A and have been called shallow mesoscale overturning circulations (SMOCS). SMOCS are hypothesised to be internally driven by convection, whose heating anomalies drive ascent that helps aggregate moisture into already moist areas and drives the growth of convective areas to mesoscales (Bretherton and Blossey, 2017; Janssens et al., 2022).

The spread in simulated momentum fluxes throughout the nine day of simulation does not reduce significantly after re-scaling the scale contributions to the flux with the cloud top height. In other words, shallow CMT in complex cloudy atmospheres is, just like deep convection, strongly dependent on accompanying circulations that have scales several times the boundary layer depth. Principally, such circulations should be resolved by models with grid spacing small enough to resolve cloud clusters with length scales of a few kilometers. Thus, the part of the flux that is driven by pressure-gradients does not need to be included (anymore) in a mass-flux representation of cloud layer momentum fluxes. To distinguish between momentum transport that should be resolved or parameterized, a vertical length scale can not be used as, instead, done in current approaches towards scale-adaptive parameterisations of the momentum flux (e.g., Honnert (2019)). As the definition of organisation is debatable and may be problematic to account for in current models, precipitation might be a good proxy (of organisation) for a first step towards better scale-adaptive parameterisation.

Several questions remain open in the understanding of mesoscale momentum flux in shallow convective regions. For example, its feedback on the large scale. Also, the role of current shallow convective parameterisations on SMOCS and cloud organisation remains largely

unexplored, although it is crucial for the improvement of numerical weather predictions. With open boundary conditions, and larger domains, the EUREC4A-MIP will provide coordinated sets of LESs and SRMs to evaluate momentum fluxes in more realistic setups.

DATA AVAILABILITY

The LES data used in this study are publicly available at the following DOI: https://doi.org/10.4121/014e83eb-a5ea-469a-9e6b-980e38bdf197.v1

APPENDIX TO CHAPTER 3

3.A SCALES OF HEAT AND MOISTURE TRANSPORT

Figure 3.13 shows the relative contribution of different scales to the total moisture (red) and heat (brown) flux, together with the zonal (blue) and meridional (green) fluxes. Each column refers to one of the groups based on I_{org} and described in session 3.4.4, whereas each row refers to one height: 200 m, cloud base, and the middle of the cloud layer.
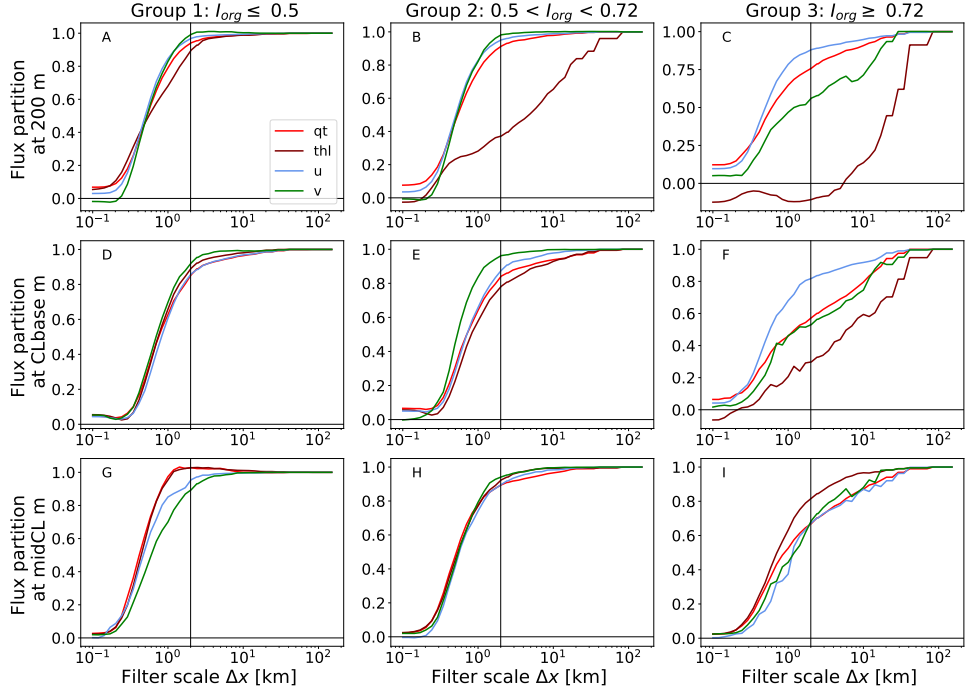
Figure 3.13: Partition of the sub-filter moisture (red), heat (brown), zonal momentum (blue) , and meridional momentum (green) fluxes as a function of the filter scales Δx. The vertical black line denotes $\Delta x = 2$, and each row refers to a different height: 200m (panels A, B, C), cloud base (D,E,F), the middle of the cloud layer (G,H,I). Each column refers to one of the groups based on I_{org}: Group 1 (A,D,G), Group 2 (B,E,H), and Group 3 (C,F,I).

Similar to momentum, I_{org} controls the partitioning of the total heat and moisture fluxes into the various scales. Nevertheless, the shapes of these curves have significant differences, reflecting differences in the processes involved. Shear can be an important driver of momentum flux, while buoyancy is more important for temperature and humidity, which are not influenced by shear (Zhu, 2015). At 200 m, especially for Group 1 and Group 2, the curves of momentum flux grow more rapidly than moisture and heat fluxes. The scales involved for momentum are confined between 0.2 and 2 km. At this height the effect of cold pool is very visible when they occur. Cold pools are more present in organised fields (Group 2 and Group 3) and they introduce significant contribution of scales larger than 2 km. At 200 m the heat flux (brown) is most dominantly influenced by cold pool dynamics.

At cloud base and in the cloud layer at 1.5 km shear is less strong than at 200 m. Instead

buoyancy becomes the dominant process for the transport of all variables. In the cloud layer heat and moisture fluxes are carried more efficiently by the sub-mesoscales. For unorganised cases (Group 1), scales smaller than 1 km carry about 20% more heat and moisture fluxes than momentum fluxes.

Under well organised conditions (Group 3), mesoscale circulations are important for all fluxes as shown by the growth of the curves in panel I. Here the curves suggest that the heat flux is the least effected by these circulations.

3

4

THE INFLUENCE OF PARAMETERISED SHALLOW CONVECTION ON TRADE-WIND CLOUDS AND CIRCULATIONS IN THE HARMONIE-AROME MESOSCALE MODEL

4

4

Mesoscale numerical weather prediction models currently operate at kilometre-scale and even sub-kilometre-scale resolutions. Although shallow cumulus convection is partly resolved at these resolutions, it is still common to use a shallow cumulus parameterisation (SCP). Within the context of the EUREC4A model intercomparison project, we evaluate how the modelled mesoscale cloud field in the trades responds to parameterised or explicit shallow convection in the mesoscale model HARMONIE-AROME. We simulate a region of 3200 x 2025 km^2 east of Barbados using a grid spacing of 2.5 km for a two month period (1 January to 29 February, 2020). We compare three configurations of HARMONIE-AROME: 1) one with an active SCP (control), 2) one without parameterised momentum transport by shallow convection, and 3) one with an inactive SCP. The experiments produce different responses in the cloud field that are not incremental. With the SCP inactive, the model produces a warmer lower troposphere with many smaller but deeper clouds that precipitate more. Along with stronger resolved eddy kinetic energy, wider and stronger shallow meridional overturning circulations develop. In the configuration without parameterised momentum transport by shallow convection, the eddy-diffusivity scheme effectively takes over the missing transport in the sub-cloud layer up to ~ 800 m. Above that level, horizontal wind variance increases as the total momentum flux decreases, enhancing eddy kinetic energy at scales of 2.5 km and larger. In contrast to the configuration with an inactive SCP, cloud top heights hardly deepen, but stratiform cloudiness below the inversion and mean cloud size increase.

4.1 INTRODUCTION

Shallow cumulus clouds are widespread over tropical and subtropical oceans and small changes in their radiative effect, primarily through low cloud amount, have an important impact on modelled equilibrium climate sensitivity (ECS) (Bony et al., 2020a; Schneider et al., 2017). In climate models, the vertical transport of momentum, heat and moisture by parameterised shallow convection has a strong control on low cloud amount and hence ECS (Vial et al., 2017). Recent observational evidence suggests that models might overestimate parameterised shallow convective transport and miss an important control on cloud amount, namely that of mesoscale circulations (Vogel et al., 2022). While in high-climate-sensitivity models lower-tropospheric mixing by shallow convection has a strong influence on (reducing) cloud-base cloudiness (Sherwood et al., 2014), observations show that mesoscale motions have an equally important but opposite influence on lower-tropospheric humidity, whereby increased mesoscale overturning does not desiccate cloudiness (Vogel et al., 2022).

Current shallow convection parameterisations (SCPs) (Schlemmer et al., 2017) have been designed for models with a mesh $\mathcal{O}$(10-50 km) and rely, among others, on the assumption that resolved (large scale) circulations and unresolved (turbulent) eddies are sufficiently distinct at these resolutions (Dorrestijn et al., 2013; Yu and Lee, 2010). However, in the past decades the mesh of mesoscale models has approached $\mathcal{O}$(1km), at which scale current SCPs may no longer be valid and produce excessive fluxes (Honnert et al., 2011). Still, completely turning off the SCP at 1 kilometre resolution, as often suggested in the literature (Bryan et al., 2003; Craig and Dornbrack, 2008; Petch et al., 2002), may not be appropriate when shallow convection is not fully resolved at that scale.

Wyngaard (2004) uses the term "terra incognita" , while others have denoted sub-kilometre to km-scale resolutions as the "grey zone" of shallow convection (Honnert, 2019; Lancz et al., 2018), for which a few SCPs have been adjusted. Arakawa et al. (2011) suggest to follows a multi-scale modelling framework, with explicit representation of moist convection. Alternatively, they suggest to eliminate the assumption of small fractional area covered by convective clouds and then apply the parameterisation to finer horizontal resolutions. Based on idealised large eddy simulations, Boutle et al. (2014) propose to suppress the non-local turbulence in the grey zone with a coefficient proportional to the ratio of grid mesh to boundary layer depth. Brast et al. (2018) test the scale adaptivity of mass-flux models, and Lancz et al. (2018) introduce a new closure for the SCP in which the initialisation of the parameterised mass-flux depends on the horizontal resolution.

The debate on modelling shallow convection across the grey zone is ongoing, with one of the main challenges stemming from the wide range of scales involved in shallow convection organised on mesoscales. Atkinson and Wu Zhang (1996) describe the horizontal length scale of typical mesoscale shallow convection as ranging from a few kilometres to a few tens of kilometres. The rich mesoscale structure in cloud-topped boundary layers, such as cloud bands (LeMone et al., 1984; Malkus and Riehl, 1964) or cellular convection (Agee et al., 1973) has been recognised for decades. Meanwhile, the ubiquity of patterns in scattered shallow clouds (Bony et al., 2020b; Rasp et al., 2020; Stevens et al., 2020) and their relationship to mesoscale circulations in the atmosphere (George et al., 2023) has received stronger focus more recently. This is partly because it may be critical to understanding precipitation

(Radtke et al., 2022) and the radiative budget (Bony et al., 2020a).

In this study, we aim to investigate how low-level cloudiness, including its organisation and accompanying mesoscale circulations, depend on parameterised (sub-grid) transport of heat, moisture, and momentum by shallow convection. We use a mesoscale or storm-resolving model with a horizontal grid spacing of 2.5 km on a domain of 200 km x 200 km to answer: How does shallow convective transport influence trade-wind cloudiness and mesoscale circulations in simulations where shallow convection is either fully parameterised or (partially) resolved? Our study uses the High Resolution Local Area Modelling - Aire Limitee Adaptation dynamique Developpement InterNational (HIRLAM-ALADIN) Research on Mesoscale Operational NWP In Europe - Applications of Research to Operations at Mesoscale (HARMONIE-AROME) model. With this model we focus on the model intercomparison project (MIP) associated with EUREC4A (Stevens et al., 2021), an observational campaign that focused on trade-wind convection east of Barbados, following seminal field studies of this cloud regime (Holland and Rasmusson, 1973; Rauber et al., 2007).

Some of the goals of the EUREC4A-MIP are to assess the simulation capability of the observed shallow cloud mesoscale organisation over the subtropical ocean, and understand the underlying dynamical processes leading to mesoscale organisational patterns. Our study specifically focuses on characterising and explaining the differences between three model setups: i) an experiment with fully parameterised transport of heat, moisture and momentum by shallow convection (control), ii) an experiment without parameterised momentum transport by shallow convection, and iii) an experiment without any transport by parameterised shallow convection (turning off the SCP altogether).

Our paper is organised as follows: section 4.2 introduces the HARMONIE-AROME model and explains the parameterisation of shallow convection in it. Section 4.3 introduces the experimental design with a description of the different model experiments (section 4.3.1), the observational data (section 4.3.2), and the tools used for the analysis (section 4.3.3). We then compare modelled and observed time series (section 4.4.1) and mean profiles (section 4.4.2) of key atmospheric quantities, before analysing the impact of the SCP on cloud statistics (section 4.5), on parameterised and resolved fluxes (section 4.6), and on circulations (section 4.7). In section 4.8 we discuss the relation between changes in cloudiness and circulation. The conclusions are given in section 4.9.

4.2 HARMONIE-AROME

Bengtsson et al. (2017) provide a general description of the numerical weather prediction model HARMONIE-AROME (HARMONIE hereafter) version cy40. Here we use the more recent version cy43. The relevant modifications in the physics in cy43 compared to cy40 are presented by de Rooy et al. (2022), together with a comprehensive description of the statistical cloud scheme, the (bulk) mass-flux convection scheme, and the turbulent kinetic energy (TKE) turbulence scheme (or eddy diffusivity scheme). HARMONIE uses the eddy-diffusivity mass-flux (EDMF) framework which facilitates a unified description of the turbulent transport in the dry convective boundary layer (Siebesma et al., 2007) and the cloud-topped boundary (Rio and Hourdin, 2008; Soares et al., 2004). This is a widely

applied framework, which has often been extended for a unified representation of sub-grid scale turbulence and convection. For example, Tan et al. (2018) propose an extended EDMF scheme with explicit time-dependence and memory of sub-grid-scale variables, while Suselj et al. (2019a,b) propose a multiplume EDMF where all plumes are initialised at the surface. Here we shortly review the formulation of parameterised transport and clouds in HARMONIE.

4.2.1 PARAMETERISED TRANSPORT

The momentum budget for the zonal wind component u can be written as:

$$\frac{\partial \overline{u}}{\partial t} = -\overline{\mathbf{u}} \cdot \nabla \overline{u} - \frac{1}{\rho} \frac{\partial \overline{p}}{\partial x} + f\overline{v} - \frac{1}{\rho} \frac{\partial \overline{(w'u')}_{\text{sbg}}}{\partial z}, \tag{4.1}$$

where the overline represents a grid box mean, $\mathbf{u}$ is the wind vector, p is the atmospheric pressure, ρ the air density, f the Coriolis parameter, v is the meridional wind component, and $\overline{(w'u')}_{\text{sbg}}$ is the sub-grid zonal momentum flux. The sub-grid flux is divided into that carried by shallow convection (SC) and by turbulent transport modelled by the eddy diffusivity (ED) scheme:

$$\overline{(w'u')}_{\text{sbg}} = \overline{w'u'}^{\text{SC}} + \overline{w'u'}^{\text{ED}}. \tag{4.2}$$

The first term on the rhs represents the non-local flux carried by the largest coherent (dry and moist) turbulent eddies, while the second term on the rhs represents the flux carried by the smaller scale turbulent eddies. A similar separation is applied for fluxes of liquid potential temperature θ_l (heat), total specific humidity q_t (moisture), and meridional wind v (meridional momentum).

The SC parameterisation in HARMONIE (de Rooy et al., 2022), hereafter referred to as the SCP, applies a dual updraft mass-flux (MF) approach (Neggers, 2009) and can be written as:

$$\rho \overline{w'\phi'}^{\text{SC}} \approx M_{\text{dry}}(\phi_{\text{u,dry}} - \overline{\phi}) + M_{\text{moist}}(\phi_{\text{u,moist}} - \overline{\phi}), \tag{4.3}$$

where $\phi = [\theta_l, q_t, u, v]$ is a generic variable, M_{dry} and M_{moist} are the convective mass fluxes of the dry and moist updraft respectively. The updraft profiles $\phi_{\text{u},i}$ ($i \in [\text{dry, moist}]$) are determined by an entraining plume model.

The fractional entrainment of the dry updraft and the moist updraft in the sub-cloud are build on the formulation of Siebesma et al. (2007). These formulations depend on height (z) and the inversion height. The fractional entrainment formulation of the moist updraft in the cloud layer is connected to the formulation of the moist updraft in the sub-cloud layer and decreases proportionally to z^{-1}. Finally, the detrainment in the cloud layer is formulated according to de Rooy and Siebesma (2008). Both entrainment and detrainment formulations are described in detail in de Rooy et al. (2022) and are supported by numerous LES studies (Boing et al., 2012; de Rooy et al., 2013; Jonker et al., 2006).

The SC scheme distinguishes between two different convective boundary layer regimes: dry convective boundary layers, with only a dry updraft, and cloud-topped boundary

layers, with a dry and a moist updraft. In the formulation of the mass-flux approach, the treatment of momentum differs from that of scalar variables only in the initialisation of the updraft properties at the lowest model level, whereby temperature and humidity are given a small excess value compared to the environment that is scaled by the surface fluxes, while u and v do not.

The small-scale turbulence parameterisation can be written as:

$$\overline{w'\phi'}^{\text{ED}} \approx -K\frac{\partial \overline{\phi}}{\partial z}, \tag{4.4}$$

where K is the eddy diffusivity. This is the ED component of the EDMF framework.

In this study we always consider both the dry- and moist- mass flux components together. In the experiments without the SCP, we omit all mass-flux contributions (dry + moist) and leave only the ED scheme active as a sub-grid transport process (see section 4.3.1 for a description of the different experiments).

4.2.2 PARAMETERISED CLOUDS AND PRECIPITATION

Low clouds are parameterised with a statistical cloud scheme (Bougeault, 1981; Sommeria and Deardorff, 1977). In such an approach, cloud cover and liquid water content are derived from estimates of the sub-grid variance of q_t and θ_l. In the literature, several approaches exist to estimate these sub-grid variance (Bechtold et al., 1995; Golaz et al., 2002). De Rooy et al. 2022 describe the statistical cloud scheme as applied in HARMONIE. Both the ED and SC fluxes contribute to the sub-grid variance but in HARMONIE we apply an additional term with the characteristics of a relative humidity scheme (de Rooy and Siebesma, 2010). This means that, in the absence of convection and no noticeable amount of turbulent activity, the variance is still different from zero. The role of this extra variance term is to account for the effect of surface heterogeneity, horizontal large-scale advection, mesoscale circulations, and gravity waves.

Precipitation above the surface is determined by the microphysics within the grid box, while at the surface there can be a sub-grid contribution from the SC scheme. The sub-grid precipitation calculated in the updraft of the SC scheme is added only to the surface precipitation and not transferred to the grid box at the corresponding model level. This means that the sub-grid precipitation from the SC scheme cannot help in the development of mesoscale circulations (e.g. by evaporation). Turning off the SCP effectively removes a (small) source of surface precipitation and a source of sub-grid variance for q_t and θ_l. The latter leads the cloud scheme to more easily produce fully cloudy or cloud free grid boxes, with less intermediate states.

4.3 THE SETTING

4.3.1 EXPERIMENTS

We use HARMONIE to simulate an area of 3200 x 2025 km^2 over the North Atlantic trade-wind region with a horizontal grid spacing of 2.5 km. The analysis domain spans 200 x 200 km^2 centred at 13.28 N and 57.76 W, a key region in EUREC4A studies (Savazzi et al., 2024, 2022). HARMONIE receives lateral boundary fields from ERA5 (Hersbach et al., 2020) every

hour and the SST is updated every 24 hours. The runs are performed in a free (climate) mode for two months, from 1 January to 29 February, 2020. In climate mode, HARMONIE is initialised only once at 1 January, which limits the effects of biases inherited from the forcing model. With this setup there are no discontinuities in the time series. The model can more freely develop its dynamics in response to varying large-scale forcing.

The two months of simulation allow us to address the response of clouds and convection across a wide range of conditions and different mesoscale organisation, during a period for which extensive observations are available. The model physics respond very quickly to changes in dynamical forcing, and that forcing generally changes substantially on sub-daily and intra-daily time scales, such that differences do not build up over time. As our results in section 4.4.1 will show, the response of cloudiness to parameterised convection can be very different from day to day, depending on the large-scale forcing that may make the environment more conducive to (explicitly) resolving convection.

We perform three experiments with different representation of $\overline{w'\phi'}^{SC}$ under convective conditions:

1. A control run with the operational setup as used in (Savazzi et al., 2024):

$$\text{Control:} \quad \overline{w'\phi'}^{SC} \neq 0 \quad \text{with } \phi = [\theta_l, q_t, u, v], \tag{4.5}$$

   where both the SC (dry+moist MF) and the ED scheme are active.

2. A run without SCP (dry+moist MF) for horizontal momentum, whereby the SCP remains active for heat and moisture:

$$\text{UV-OFF:} \quad \overline{w'\phi'}^{SC} \neq 0 \quad \text{with } \phi = [\theta_l, q_t],$$
$$\overline{w'u'}^{SC} = 0 \quad \overline{w'v'}^{SC} = 0. \tag{4.6}$$

3. A run where the SCP (dry+moist MF) is turned off completely:

$$\text{SC-OFF:} \quad \overline{w'\phi'}^{SC} = 0 \quad \text{with } \phi = [\theta_l, q_t, u, v] \tag{4.7}$$

The ED scheme and the cloud scheme remain active in all simulations; thus the model can respond to the removal of mass-flux transport by adjusting both the resolved and sub-grid ED transport.

4.3.2 Observations
We use the following observations to evaluate the realism of the model experiments:

1. Images from GOES16 (NOAA, 2020), the first of the Geostationary Operational Environmental Satellite R (GOES-R) series. Spaceborne instruments have proven useful in assessing cloud patterns in the trades (Bony et al., 2020a; Schulz, 2022), despite challenges in detecting shallow cumuli because of their small footprint and low optical depth, and overlying mid- and high-level clouds (Marchand et al., 2010; Zhao and Di Girolamo, 2006). From GOES16, we use channel 13 of the Advanced

Baseline Imager (ABI), which provides brightness temperature at a spatial resolution of 2 km. We extract 1140 images of the analysis domain with a temporal resolution of 1 hour, which are regridded to 2.5 km to match the resolution of HARMONIE. We define a marine low-cloud mask using measurements with a brightness temperature between 270 K and 292 K. Cloud top height (CTH) is derived assuming a constant dry adiabatic lapse rate of 10 K km^{-1} up to 700 m and a moist adiabatic lapse rate of 6.5 K km^{-1} aloft. These numbers allow us to include somewhat deeper clouds than in Bony et al. (2020a), which used 280 K and 290 K as thresholds.

2. Radiosondes from the Barbados Cloud Observatory (BCO) (Stephan et al., 2021). More than 300 radiosondes were launched at 13.1 N and 59.3 W during EUREC4A, between 16 January and 17 February. The interval between consecutive launches varies between two and three hours.

3. The JOANNE (Joint dropsonde Observations of the Atmosphere in tropical North atlaNtic mesoscale Environments) dataset (George et al., 2021b). We use Level 3 of this dataset, which comprises around 1000 dropsondes launched from the high-altitude and long-range research aircraft HALO during EUREC4A, between 19 January and 15 February, along a ~220 km diameter circle centred at 13.3 N, 57.7 W.

4.3.3 Tools

The cloud fields are analysed using organisation metrics define by Janssens et al. (2021). For GOES16 the cloud mask is defined in section 4.3.2; while for HARMONIE, any grid box in the lower 4 km with a cloud fraction larger than 0.5 is considered cloudy. A number of organisation metrics require further explanation:

1. Cloud size is determined by the square root of its area, projected onto the surface. In other words, cloud size is the length of one side of a square that has the same area as the cloud object.

2. Cloud cover (CC) is the fractional area covered by clouds projected onto the surface plane. In this study we consider cloudy grid cells only up to 4 km.

3. Open sky is the fraction covered by the largest possible rectangle placed in the domain without touching any cloud, and is thus a measure of the cloud-free area.

4. Orientation is a dimensionless quantity between 0 and 1, with 0 denoting that clouds have no preferential direction of orientation and 1 denoting that all clouds are oriented in one direction.

We also apply the organisation metrics to the flow field. We identify shallow mesoscale overturning circulations (SMOCs) as in George et al. (2023). These are regions where the sub-cloud (0-600 m) and the cloud layers (900-1500 m) exhibit mesoscale horizontal divergence D with the opposite sign. The sign of the divergence in the sub-cloud layer ($D_{sc} = \frac{\partial u}{\partial x} + \frac{\partial v}{\partial y}$) reveals mesoscale ascent ($D_{sc} < 0$) or mesoscale subsidence ($D_{sc} > 0$).

After smoothing the fields of D to 20 km (see Savazzi et al. (2024) for the filtering method) we only consider grid boxes where $|D|$ is greater than $\pm\ 10^{-6}s^{-1}$. This is a fairly small

threshold compared to the values of the $\mathcal{D}$ dipole ($\mathcal{D}'$) found in the domain (shown later in section 4.7). We define the following metrics:

1. The $\mathcal{D}$ dipole ($\mathcal{D}'$) strength (or SMOC strength) is the difference between the cloud layer and the sub-cloud layer divergence ($\mathcal{D}' = \mathcal{D}_c - \mathcal{D}_{sc}$).

2. SMOC coverage, similar to CC, is the fractional area covered by SMOCs.

3. Aspect ratio is the non-dimensional ratio between (horizontal) SMOC size and its vertical extent, where the size is defined as for the cloud objects, while the vertical extent is the height of maximum divergence when $\mathcal{D}_{sc} < 0$ and minimum divergence when $\mathcal{D}_{sc} > 0$.

In our analysis of the mesoscale circulations we also apply Reynolds decomposition and identify fluctuations ϕ'_{res} of a generic variable ϕ at the 2.5 km grid resolution with respect to the slab average $\langle \phi \rangle$ taken over the 200 x 200 km^2 analysis domain. This allows to distinguish between parameterised sub-grid fluxes $(\overline{\phi'w'})_{sbg}$ and resolved fluxes $(\overline{\phi'w'})_{res}$. The total turbulent flux in the domain is thus defined as:

$$(\overline{\phi'w'})_{total} = (\overline{\phi'w'})_{sbg} + (\overline{\phi'w'})_{res} \tag{4.8}$$

We drop the subscript for the variances of the fluctuations ϕ'_{res} at scales larger than 2.5 km, thus $\overline{\phi'^2}_{res} = \sigma_\phi^2$.

Wind variances at scales larger than 2.5 km (σ_u^2, σ_v^2, σ_w^2) can be combined to define the eddy kinetic energy (EKE), as a proxy of mesoscale variability and intensity of resolved eddies:

$$EKE = \frac{1}{2}(\sigma_u^2 + \sigma_v^2 + \sigma_w^2). \tag{4.9}$$

Following Salesky et al. (2017) we also define the EKE anisotropy as the ratio $\sigma_w^2/(\sigma_u^2 + \sigma_v^2)$, which helps indicate the relative importance of buoyancy and shear production of vertical and horizontal wind variance.

4.4 Characteristics of the simulated period

4.4.1 Time series

The temporal variability in cloudiness driven by different mesoscale and synoptic conditions is rich in the trades (Nuijens et al., 2014; Vogel et al., 2022). Compared to dropsonde measurements (the JOANNE dataset collected during EUREC4A), all three HARMONIE experiments reasonably capture the evolution of the wind speed in the lower 200 m, plotted as a 24-hour rolling average in Figure 4.1 d). While the left panel of Figure 4.1 shows the temporal evolution of selected quantities, the box charts in the right panel show their distribution over the two months. The triangles indicate the mean, the boxes indicate the interquartile range, and the whiskers indicate the extremes.

Satellite observations from GOES16 (orange in panel e) show that the domain mean cloud top height is also in the right ballpark, although with more pronounced variability in the model. In the first half of January and first half of February, the modelled clouds deepen more than what observed. When the winds weaken in the second half of January the

4
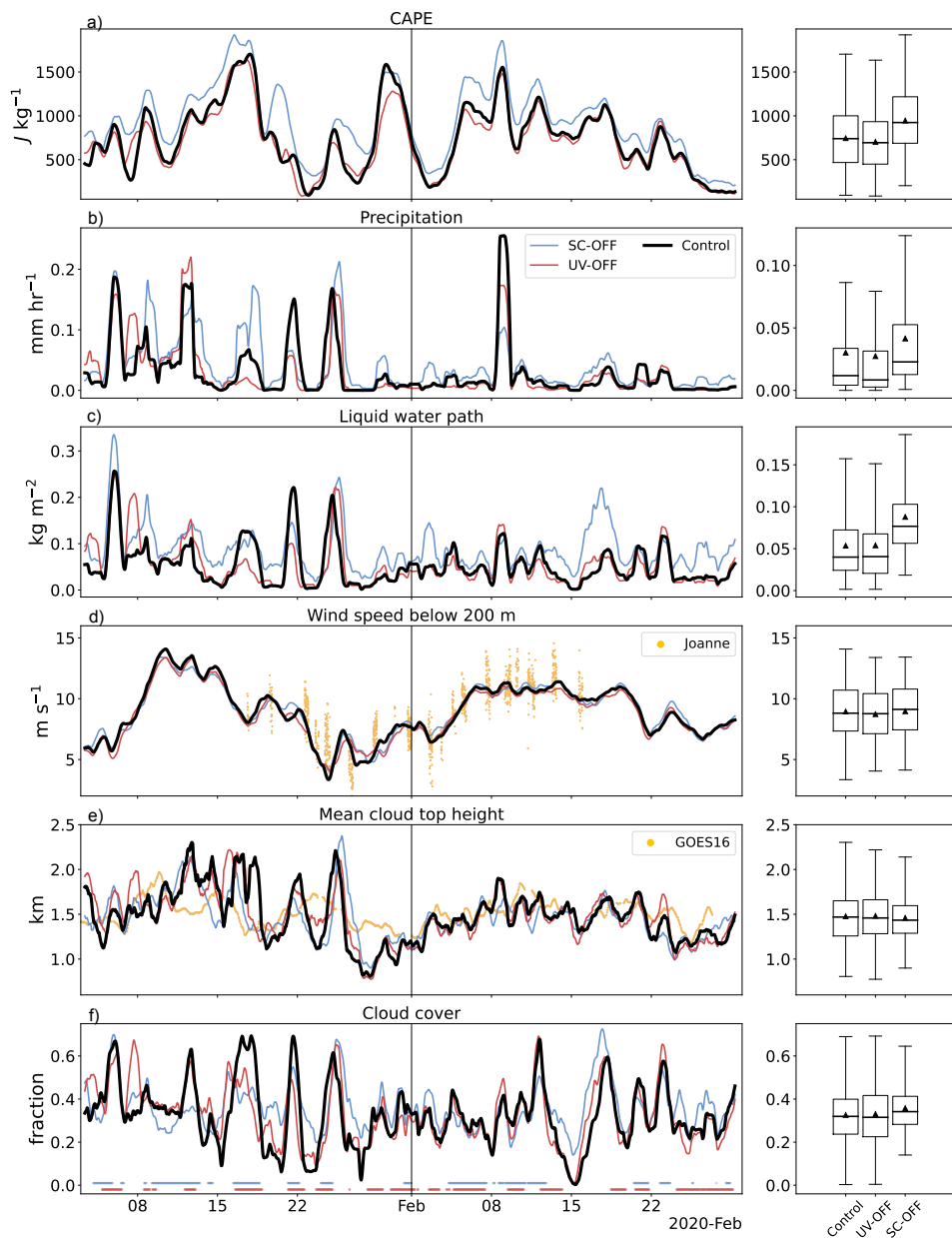
Figure 4.1: Temporal evolution (left column) and distribution (right column) of a) convective available potential temperature CAPE, b) surface precipitation, c) liquid water path LWP, d) mean wind speed of the lower 200 m, e) mean cloud top height CTH, f) cloud cover CC below 4 km. The time series are shown as 24-hour rolling averages. The dots at the bottom of panel f) mark times where $CC_{UV-OFF} < CC_{control}$ (red), and $CC_{SC-OFF} < CC_{control}$ (blue). Black is for the control, red for UV-OFF, and blue for SC-OFF. The orange dots indicate dropsonde measurements from JOANNE in panel d) and satellite measurements from GOES16 in panel e).

modelled cloud field oscillates between deeper clouds with large CC (panel f), and shallower cloud tops with low CC, while GOES16 shows a more constant mean CTH of about 1.5 km.

The mean CC is surprisingly similar among the three experiments, as seen in the box chart of panel f), although the distribution narrows for the SC-OFF experiment. However, on a daily basis, differences in CC between the experiments as large as 20% are not unusual, and they are both positive and negative, explaining why differences are small in the mean. In the time series, we use coloured dots at the bottom of panel f) to highlight hours where CC in SC-OFF is smaller than the control (blue dots), and where CC in UV-OFF is smaller than the control (red dots). About 40% of the time, $CC_{SC-OFF} < CC_{control}$, whereas $CC_{UV-OFF} < CC_{control}$ about 49% of the time. We will make use of this distinction later in section 4.5 when we describe how this relates to changes in cloud organisation and wind speed.

The evolution of mean CTH and CC in HARMONIE is not strictly tied to the convective available potential energy (CAPE), which is shown in Figure 4.1 a). For example, the peak in CAPE captured by all experiments at the end of January is not associated with any rapid increase in mean CTH nor in CC. Nevertheless, CAPE in SC-OFF is about 250 J kg^{-1} higher on average, suggesting that the absence of SC helps build up instability that would otherwise be quickly removed. Panels b) and c) further indicate more mean precipitation and higher liquid water path (LWP) in SC-OFF.

4.4.2 Mean profiles

The mean thermodynamic and dynamic profiles of the control experiment, along with the interquartile range to indicate the variability, are shown in Figure 4.2 as black lines and shaded areas. The profiles of specific humidity q_t (panel a) and liquid potential temperature θ_l (panel b) show a relatively well-mixed boundary layer reaching 600 m, with a weak trade-inversion in θ_l between 2 and 2.5 km. The warm, moist surface layer and a strong easterly breeze (~10 m s^{-1} in panel c) establish the typical environment of trade-wind shallow cumulus convection (Nuijens et al., 2014). Near cloud base, between 700 m and 800 m, the zonal wind u has a local maximum, or low-level wind jet (Larson et al., 2019). The meridional wind is weaker than the zonal wind with values around -2 ± 1 m s^{-1} below 600 m, and -1 ± 1 m s^{-1} above.

Figure 4.2 also shows the mean differences of UV-OFF (red), SC-OFF (blue), and the BCO soundings (orange) with respect to the control. The dashed orange line in panel a) and b) shows that the control is about 1 g kg^{-1} too dry in the lower 500 m and 1 K too cold in the lower 1 km compared to the BCO soundings, a bias that is inherited from ERA5 (not shown). In SC-OFF, the profile of q_t improves with respect to the observations in the lower few hundred meters and above 1.5 km, because the difference between SC-OFF and the control (dashed blue) has the same sign as the difference between the BCO soundings and the control. Still, SC-OFF is too dry around cloud base and too moist at cloud top (2.5 km).

In SC-OFF, the profiles of q_t and θ_l are better vertically-mixed in the cloud layer: drier and warmer than the control around 1 km, and moister and colder than the control at 2.5 km. This suggests that non-local transport of heat and moisture from the lower to the upper cloud layer is more efficient when done by resolved eddies in SC-OFF than by the parameterisation in the control. In contrast, without SCP the sub-cloud layer humidity
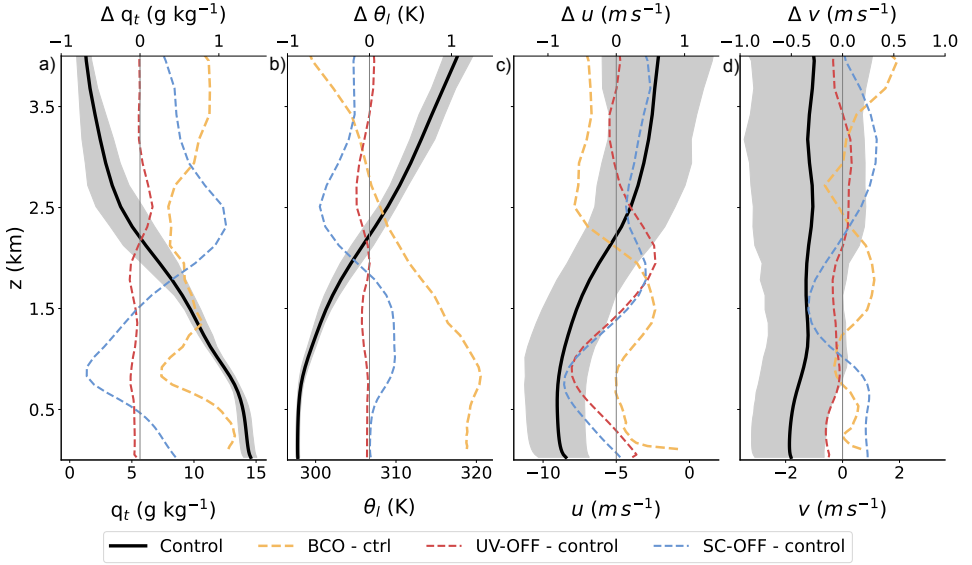
Figure 4.2: Mean profiles of a) specific humidity q_t, b) liquid potential temperature θ_l, c) zonal u, and d) meridional u wind. The bottom x-axes display the mean (solid black) and interquartile range (shading) of the control experiment. The top x-axes display the mean difference of the observations and other experiments to the control: observations (BCO) - control (orange), UV-OFF - control (red), SC-OFF - control (blue).

becomes less well-mixed, highlighting the importance of the sub-grid transport by dry MF. The removal of parameterised momentum transport by SC (UV-OFF) has a negligible effect on the mean thermodynamic profiles. From Figure 4.2 a), the main difference between UV-OFF and the control run is a somewhat moister layer near 2.5 km in UV-OFF (dashed red line), which relates to enhanced cloudiness at this level, which we return to below.

In terms of the horizontal wind profiles (Figure 4.2 c,d), SC-OFF and UV-OFF have more wind shear on average than the control. Momentum transport by the SCP acts to mix winds across the boundary layer *e.g.*, by transporting zonal momentum from the surface upwards into the cloud layer. The result is less shear throughout the lower troposphere when the SCP is active, with reduced zonal wind jet at 700 m and stronger winds between 1.5 km and 2.5 km. A comparison between the orange line and the blue and red lines in panel c) reveals that the zonal wind jet that develops without parameterised momentum trasnport by SC is too strong and the wind shear becomes too large compared to the observations. Sandu et al. (2020) showed a similar effect of parameterised shallow convective mixing for the ECMWF-IFS (ECMWF, 2024) at 40 km resolution. They observed that the zonal wind jet developing without momentum transport by SCP in the ECMWF-IFS is too strong compared to observations and reanalysis, although the lack of mixing reduces the surface bias (Savazzi et al., 2022).

The largest effect on the zonal wind comes from the removal of parameterised momentum transport by the SCP. Further removing the parameterised transport of heat and moisture in SC-OFF does not significantly change the zonal wind. This is not the case for the meridional

wind, which weakens in SC-OFF, producing a veering of the wind and a weaker meridional component, while the surface winds in UV-OFF turn southward, acquiring a stronger meridional component. These differences in the mean winds do not directly translate into different mesoscale circulations (which we describe in section 4.7), but help understand how parameterised shallow convection modulates the large scale flow feeding into the ITCZ. Overall, we find that HARMONIE reproduces observed zonal and meridional wind profiles better in the control, which highlights that sub-grid momentum transport by SC is non-negligible.
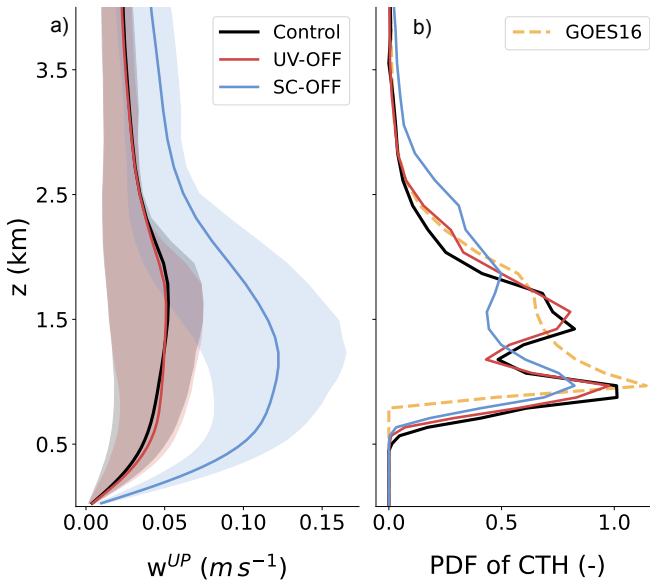
Figure 4.3: Profiles of a) resolved updraft w^{UP}, and d) normalised histogram (or PDF) of cloud top height CTH averaged over two months. w^{UP} is the positive resolved vertical velocity w when there is a cloud somewhere in the column. In a) the solid lines indicate the mean, while the shadings indicate the interquartile range. Black is for the control, red for UV-OFF, blue for SC-OFF, and orange for the observations (GOES16).

In SC-OFF the model produces more resolved convection as a way to compensate for the missing parameterised SC fluxes, while in UV-OFF the resolved fluxes remain similar to the control. We will return to the flux transport and its partition between resolved and parameterised, in section 4.6.1. Here we first analyse the differences in convective activity through profiles of vertical velocity. Figure 4.3 a) shows the mean and interquartile range for the variable w^{UP} as a proxy for resolved updraft strength. We define w^{UP} as the positive resolved vertical velocity w sampled in columns with at least one cloudy grid box at any level. In SC-OFF, w^{UP} is twice that of the control (and of UV-OFF) throughout the cloud layer, with mean values of ~ 0.12 m s^{-1} at 1 km.

Stronger resolved vertical velocity drives deeper clouds as shown by the normalised probability density function (PDF) of CTH in Figure 4.3 b). For all datasets, this distribution peaks just above cloud base, at ~ 800 m, and below the inversion, at ~ 2 km. Deeper clouds

in SC-OFF are associated with a higher probability of finding clouds above 2 km. Below the trade-inversion, here near 2 km, stratiform outflow layers, very similar to anvils found near the tops of deep cumulus, are common (Nuijens et al., 2014). SC-OFF produces less of these layers here, in line with previous studies that have found that the deepening of the cloud layer leads to reduced inversion strength and less stratiform cloudiness (Vogel et al., 2020).

Without parameterised momentum transport by SC (UV-OFF), w^{UP} does not change markedly (panel a), and neither does the overall distribution of CTH. However, as we will show in the next section, UV-OFF does on many days have a tendency to produce enhanced stratiform cloudiness and larger mean cloud sizes.

4.5 CLOUD STATISTICS

In the simulated period various cloud patterns were simulated in HARMONIE. Quantifying these is important to validate the model's performance across the grey-zone. Figure 4.4 a) and b) show two snapshots of CTH from GOES16. On 13 January at 12:00 LT (a) the cloud field is relatively unorganised with small clouds scattered throughout the domain, while on 13 February at 12:00 LT (b) the cloud field is highly organised with two large objects elongated in the south-west to north-east direction. Figure 4.4 c) quantifies the organisation of the cloud fields through orientation (y-axis) and open sky (x-axis), which have been introduced in section 4.3.3. 13 January at 12:00 LT and 13 February at 12:00 LT are marked in the phase space with green crosses, which show that the clouds in panel b) have a stronger preferential orientation than clouds in panel a), and they allow for a larger cloud free area between object. All other images from GOES16 are represented by the orange dots and suggest that the relationship between orientation and open sky is not linear. Nevertheless, when clouds are aligned in a preferential direction (high orientation) there are larger patches of clear sky (high open sky).

In Figure 4.4 c) we compare the statistical distribution of orientation and open sky for the HARMONIE experiments, where the control is in black, UV-OFF is in red, and SC-OFF is in blue. For these, we use probability density functions (univariate in the external panels) and box charts (bivariate in the phase space), instead of scatter-plots. For each dataset the box charts intersect at the mean. SC-OFF tends to have cloud fields similar to panel a), while the control and UV-OFF show more frequent cloud fields similar to panel b), with distributions of orientation and open sky comparable to GOES16 (orange).

This purely geometrical evaluation shows that SC-OFF produces different organisation patterns than the observation and other experiments. Smaller values of open sky, with relatively similar cloud cover (see section 4.4.1), indicate a more "spotty" cloud field, where clouds are smaller and more homogeneously distributed. Images from GOES16, the control, and UV-OFF instead reveal a wider distribution of open sky with a mean around 0.4. For GOES16, the lower tail of the distribution is shifted to larger values, because small clouds are difficult to see from space. The orientation of projected clouds is less preferential in SC-OFF, with a mean orientation < 0.6, compared to ~0.7 from GOES16. This indicates clouds that are too symmetric (round) in SC-OFF, which may be a result of stronger updrafts reaching higher, rather than becoming negatively buoyant near the inversion and producing
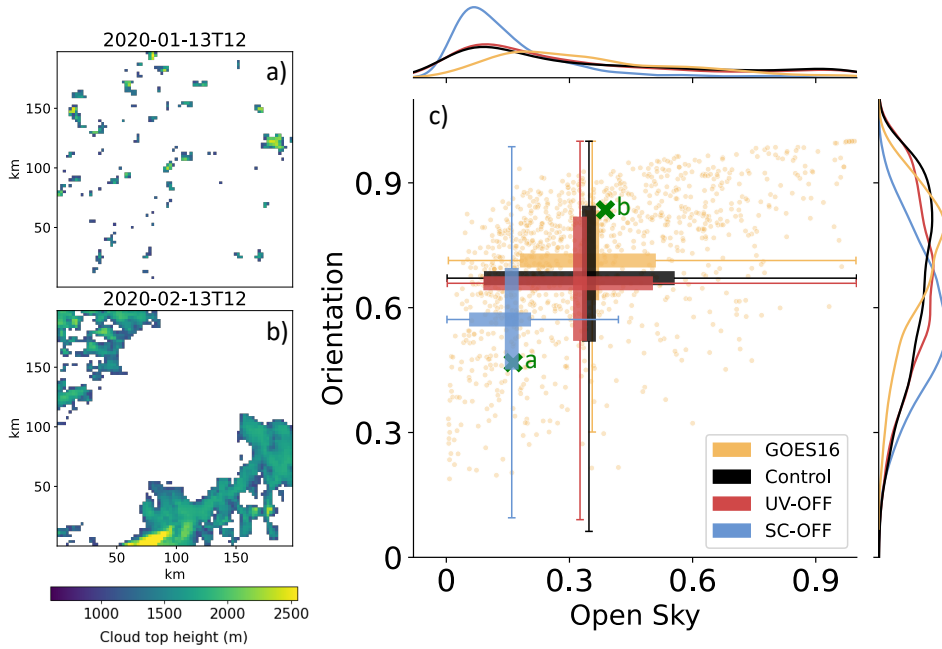
Figure 4.4: Snapshots of cloud top height (CTH) from GOES16 on (a) 13 January at 12:00 LT, and (b) 13 February at 12:00. In panel c) is the phase space for the cloud metrics orientation (y-axis) and open sky (x-axis), where the instances in a) and b) are marked with green crosses. The orange dots refer to all other GOES16 images. The distributions are shown also as probability density functions (lines) and box charts for GOES16 (orange), the control (black), UV-OFF (red), and SC-OFF (blue). For each dataset the box charts indicate interquartile range and extremes, and they cross at the mean.

spreading stratiform outflow.

The difference in convective activity modulates cloudiness in a non-trivial way. Cloud cover (CC), can be split into a contribution from grid columns with clouds below 1 km and a residual contribution from grid columns that are cloudy above 1 km, without any cloud underneath. Stratiform cloud anvils are an important contributor to the latter (Nuijens et al., 2014). In Figure 4.5, this partition shows important differences among the three experiments, which are not evident from the total CC in Figure 4.1 f).

Compared to the control, SC-OFF shows increased CC near cloud base, from 0.1 to 0.15. Above 1 km, the mean contribution remains similar to the control, but the distribution indicates a smaller maximum, suggesting that SC-OFF produces less stratiform outflow than the control. Clouds respond in the opposite manner in UV-OFF, with marginally smaller CC near cloud base, but more CC aloft, indicating more frequent stratiform outflow.

In Figure 4.6 we use total CC (below and above 1 km) to divide the time series into subsets of hours in which responses can be very different than the mean. Each experiment is compared to the control for those subsets during which CC is larger than the control (solid)

Figure 4.5: Contribution to total cloud cover from layers below (left side) and above (right side) 1 km. Black is for the control, red for UV-OFF, and blue for SC-OFF. Box limits indicate the range of the central 50% of the data (interquartile), with a central line marking the median. The triangle indicates the mean, and the whiskers capture the range of the remaining data.

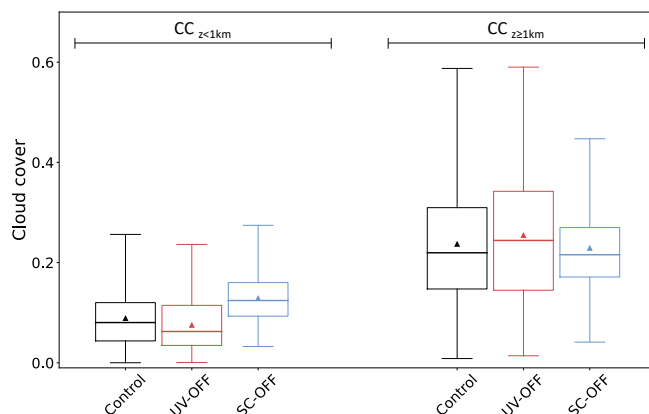or smaller than the control (dashed). Cloud cover (e,f) combines information on the number of clouds (a,b) and their size (c,d) (defined in section 4.3.3).

Clouds are equally numerous in UV-OFF and in the control (a). The mean size of the projected clouds, which is strongly influenced by the presence of stratiform outflows, determines the differences in CC between UV-OFF and the control: larger clouds increase CC, while smaller clouds decrease CC. This translates to a clear negative correlation between CC (e) and open sky (g), meaning that open sky reduces as clouds become larger.

This relationship between CC and open sky changes in SC-OFF. In SC-OFF the distribution of all cloud metrics is narrower compared to UV-OFF and the control, except for CTH. Clouds are always more numerous in SC-OFF, but they are smaller. SC-OFF produces fewer stratiform outflows, and the larger number of clouds in SC-OFF is not always enough to compensate, so that CC decreases. Comparing the solid blue and black box charts draws the picture that more clouds in SC-OFF, despite being smaller, help make larger cloud cover, except when the control experiment makes stratiform anvils, as evident from the increase in mean cloud size (dashed black in panel d).

Figure 4.6 i) and l) reveal changes in the depth of convection by means of CTH. The CTH statistics are very similar for UV-OFF and the control (panel i), while SC-OFF (panel l) has a wider distribution of CTHs, ranging from below 1 km to above 2.5 km, when $CC_{SC\text{-}OFF} > CC_{control}$, and even up to 3 km when $CC_{SC\text{-}OFF} < CC_{control}$. This highlights the connection between resolved updraft strength and total (low) cloud cover, as described in Vogel et al. (2020). When convection gets stronger, there is less detrainment below the inversion (at about 2 km), and less stratiform cloud, which has a large contribution to total cloud cover.

Space-borne observations over the western North Atlantic reveal that trade-wind clouds
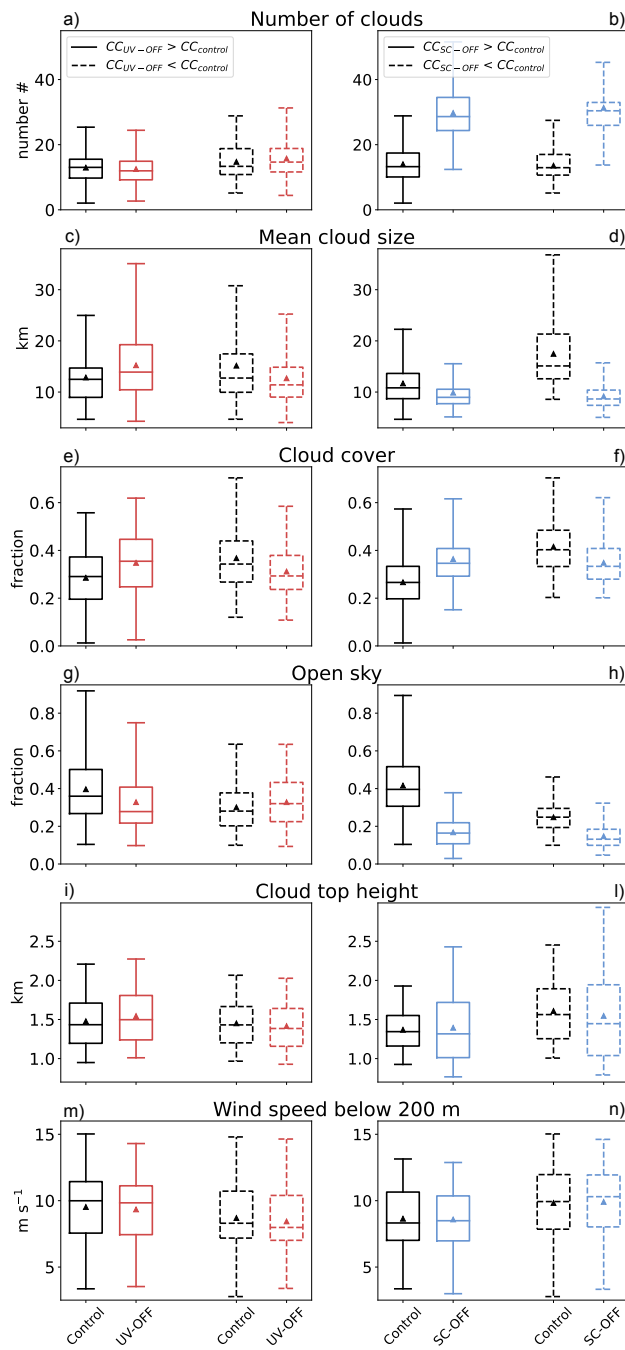
Figure 4.6: Distribution of key cloud metrics (a to l) and surface-layer wind speed (m, n) grouped by instances where $CC_{UV\text{-}OFF} > CC_{control}$ (left panels, solid lines), $CC_{UV\text{-}OFF} < CC_{control}$ (left panels, dashed lines), $CC_{SC\text{-}OFF} > CC_{control}$ (right panels, solid lines), and $CC_{SC\text{-}OFF} < CC_{control}$ (right panels, dashed lines).

favour specific mesoscale patterns under specific environmental conditions (Bony et al., 2020a). Isolated smaller cumulus clouds (*sugar*) are favoured in more unstable boundary layers and weak winds. This environment promotes frequent updrafts, but weak winds and smaller surface fluxes generally make for a drier environment and raise the lifting condensation level. In these conditions, the SC-OFF experiment tends to produce more CC (near cloud base) than the control by promoting stronger updrafts, see Figure 4.6 n).

Precipitating cumulus convection with cold pools (*gravel*) and with stratiform outflows (*flowers*) are favoured in more stable boundary layers and strong winds. This environment promotes moistening of the boundary layer and larger cloud clusters, but a more stable lower troposphere prevents clouds from deepening, and detrainment promotes stratiform outflow. In these conditions, UV-OFF promotes larger changes in stratiform cloudiness (Figure 4.6m).

4.6 Impact on fluxes and variances

Without dry and moist MF contributions to transport, the eddy diffusivity (ED) scheme and the resolved dynamics will carry all the flux (section 4.2.1). In SC-OFF, all fluxes (moisture, heat, and momentum) change in response to the missing MF, while in UV-OFF only the momentum fluxes need to adjust (although other indirect effects might cause secondary adjustments to the heat and moisture fluxes). In Figure 4.7 we investigate how HARMONIE partitions the total fluxes between parameterised and resolved fluxes, and how these change in the three experiments.

In the top row of Figure 4.7 (a, b, c, d) we show the parameterised fluxes $(\overline{\phi'w'})_{\mathrm{sbg}}$, comprising the MF contribution (dotted lines, where active) and the ED contribution (dashed lines). Panels e, f, g, h on the bottom row display the resolved fluxes $(\overline{\phi'w'})_{\mathrm{res}}$ as dashed lines, and the total fluxes $(\overline{\phi'w'})_{\mathrm{total}}$ as solid lines. The sub-grid fluxes of moisture and heat from UV-OFF were not saved and thus not shown, but given the unchanged thermodynamic structure in UV-OFF compared to the control, we anticipate that these fluxes are very similar to the control.

The SCP (dotted black in panels a to d) introduces fluxes that are largest in the cloud layer and reduce to zero at the surface and at 2.5 km, above the cloud layer. The ED scheme (dashed in panels a to d) introduces fluxes that are largest near the surface. Focusing on the parameterised moisture flux (panel a), we see that the ED component increases across all heights when the SCP is turned off. At the surface this goes from 0.02 g kg^{-1} m s^{-1} in the control to 0.03 g kg^{-1} m s^{-1} in SC-OFF, compensating for the absence of the SCP, as the dashed blue line is closest to the combined ED and MF components in the control (solid black). At other levels below 2.5 km, however, the increase in ED flux is insufficient, with the combined ED and MF in the control being more than double the ED flux in SC-OFF (dashed blue).

The combined ED + MF zonal momentum flux (solid black in panel c) has a profile that can be represented well by the ED approach alone: large, positive near the surface and reducing to zero above cloud base, around 1 km. In this case, removing the parameterised momentum transport by SC causes the ED component to increase, producing a similar parameterised flux in SC-OFF and UV-OFF as in the control (solid black), but only in the
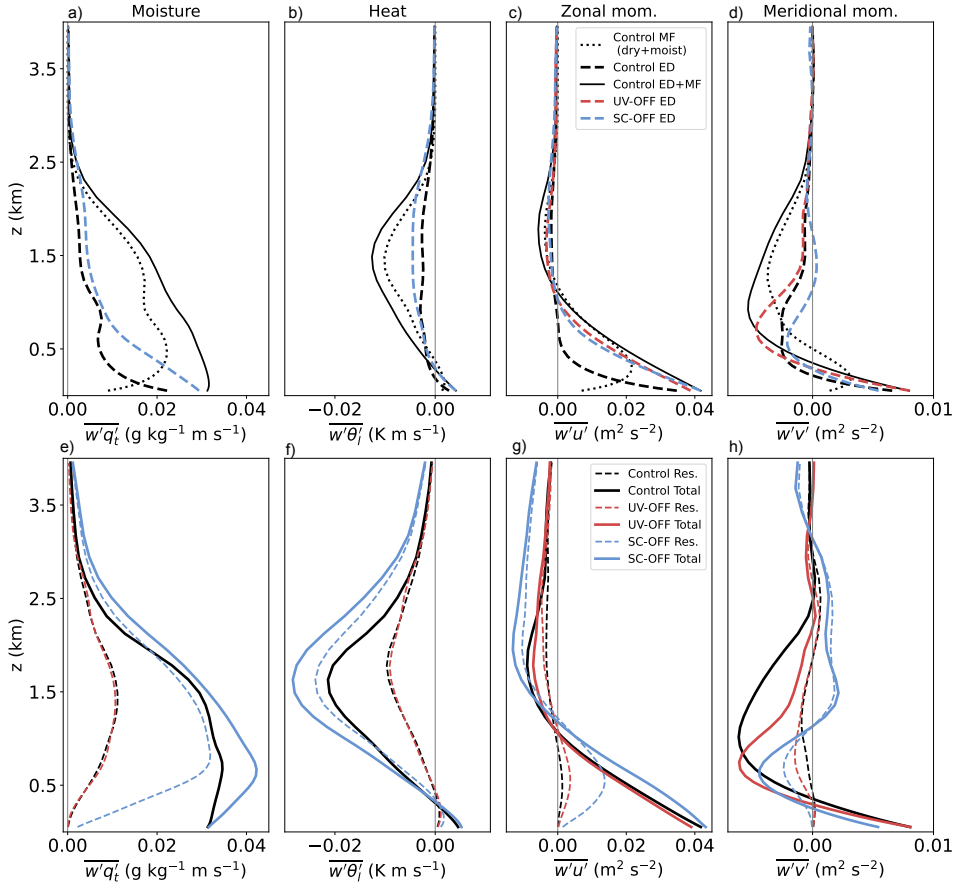
Figure 4.7: Mean in space and time of the flux profiles for moisture (a, e), heat (b, f), zonal momentum (c, g), and meridional momentum (d, h). On the top row (a, b, c, d) the parameterised flux (solid) is divided into the SC scheme (dotted), which includes dry and moist MF, and the ED scheme (dashed). The SC scheme is turned on in the control (black), and turned off in SC-OFF (blue). On the bottom row (e, f, g, h) is the resolved flux (dashed) and the total flux (solid), which is the sum of the parameterised and resolved fluxes.

sub-cloud layer. Compared to the control, the parameterised zonal as well as the meridional momentum flux in SC-OFF and UV-OFF is substantially weaker near cloud base and in the cloud layer up to 2 km, which helps explain the larger wind shear and stronger zonal wind jet that develops in these experiments (Figure 4.2c,d).

The resolved transport also adjusts, as shown by the dashed lines in Figure 4.7 (e to h). This adjustment, combined with adjustments in MF and ED fluxes, set the heat, moisture and momentum tendencies and thus the mean profiles (see Figure 4.2). The resolved moisture flux (panel e) in SC-OFF increases from about 0.01 g kg^{-1} m s^{-1} to 0.03 g kg^{-1} m s^{-1} at 1 km compared to the control, and the resolved heat flux increases from about -0.01 K m s^{-1} to -0.03 K m s^{-1} at 1.5 km. The resolved momentum fluxes in UV-OFF (dashed red in bottom row) increase primarily in the cloud layer, but while this brings the total zonal momentum flux from UV-OFF (solid red in panel g) very close to the control (solid black), the total meridional momentum flux is less in UV-OFF compared to the control. This helps explain, as we show in the next section, that resolved momentum variance increases in UV-OFF in the presence of weaker sub-grid momentum fluxes.

In SC-OFF, the combination of increased ED and resolved fluxes produce a total flux (solid lines in panels e to h) that exceeds the fluxes of moisture, heat, and zonal momentum in the control. Notably, in this configuration, the resolved flux alone can surpass the total flux in the control. As we show next, the enhanced resolved heat and moisture transport can drive stronger mesoscale circulations, in line with Janssens et al. (2022).

4.6.1 Eddy kinetic energy

Spatial variability in the trade-winds is known to be rich from both observations (George et al., 2023; Vogel et al., 2022) and simulations (Savazzi et al., 2024). Presumably, a change in the total heat, moisture and momentum fluxes and in the character of clouds brings about a change in resolved circulations on mesoscales. With a 2.5 km grid spacing, resolved circulations are somewhat artificial, as individual updrafts and the effect of cold pools cannot be captured (Kurowski et al., 2024; Lamaakel and Matheou, 2022). Despite this constraint, we use the resolved eddy kinetic energy (EKE), defined in section 4.3.3 to measure wind fluctuations (u'_{res}, v'_{res}, w'_{res}) at scales larger than 2.5 km. This can indicate to what extent the flow field is gaining or losing energy in response to stronger convection in SC-OFF and less sub-grid momentum flux, at least in the cloud layer, in UV-OFF.

Figure 4.8 a) shows the mean profile and interquartile range of EKE for each experiment and reveals that EKE in the cloud layer increases in UV-OFF and further increases in the sub-cloud layer as well when SC becomes resolved in SC-OFF. Figure 4.8 b) shows EKE as a function of spatial scale, which is computed by progressively coarsening the wind field and computing the EKE for all mesh sizes between 2.5 km and 200 km. The contribution of each scale is shown as a percentage to the total EKE at 1 km, just above cloud base. This contribution is largest at the smallest spatial scales, declining quickly beyond 2.5 km to 50 km. The decline is largest for SC-OFF, in which 50% of the total resolved EKE is carried at scales less than 50 km, compared to 35% and 40% in the control and UV-OFF, respectively. Of the three experiments, UV-OFF has the largest contribution of scales between ~25 and 100 km, and more EKE in the cloud layer compared to the control.
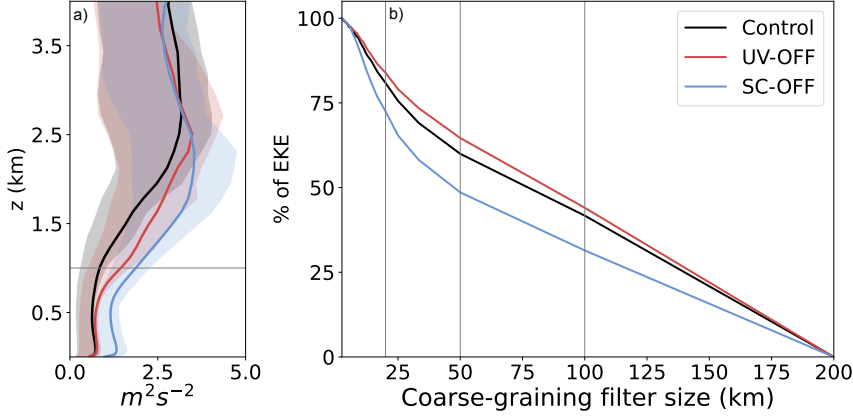
Figure 4.8: Eddy kinetic energy (EKE) as a proxy of mesoscale wind variability. Panel a) shows the mean profile and interquartile range (shaded) of EKE, without any coarsening. Panel b) shows the percentage of EKE at 1 km height (indicated by the horizontal grey line in panel a) for progressively coarser filter sizes. The vertical grey lines indicate filters of 20 km, 50 km, and 100 km. Black is for the control, red for UV-OFF, and blue for SC-OFF.
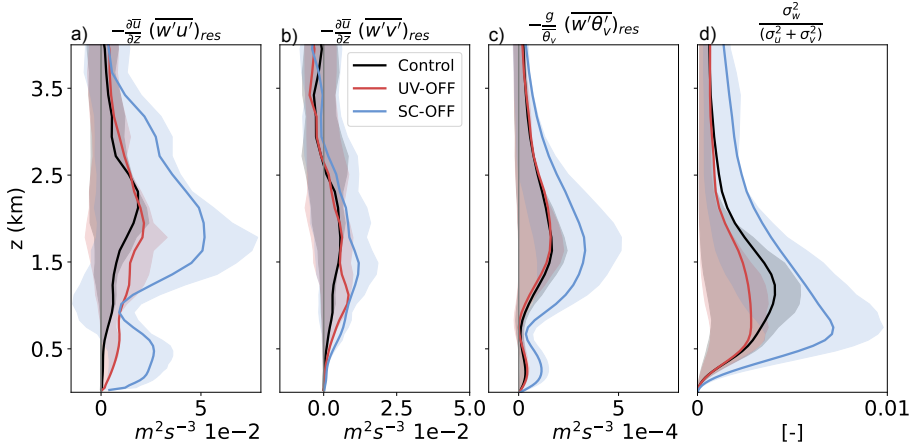
Figure 4.9: Source (or sink) terms of eddy kinetic energy EKE: a) zonal shear production $-\frac{\partial \overline{u}}{\partial z}(\overline{w'u'})_{res}$, b) meridional shear production $-\frac{\partial \overline{v}}{\partial z}(\overline{w'v'})_{res}$, and c) buoyancy production $\frac{g}{\overline{\theta}_v}(\overline{w'\theta'_v})_{res}$. In panel d) is the non-dimensional term $\sigma_w^2/(\sigma_u^2+\sigma_v^2)$, which quantifies EKE anisotropy. The fluxes and the variances ($\sigma_u^2, \sigma_v^2, \sigma_w^2$) refer to scales larger than 2.5 km.

In SC-OFF both shear and buoyancy production of EKE increase in the sub-cloud layer, as shown in Figure 4.9a), b), and c). The shear production terms are defined as $-\frac{\partial \overline{u}}{\partial z}(\overline{w'u'})_{\text{res}}$ (a) and $-\frac{\partial \overline{v}}{\partial z}(\overline{w'v'})_{\text{res}}$ (b), the buoyancy production term is defined as $\frac{g}{\theta_v}(\overline{w'\theta_v'})_{\text{res}}$ (c). The buoyancy production term is overall two orders of magnitude smaller than the shear production. Zonal shear production of EKE is the largest term for all experiments, with a peak around 2 km near the inversion, where wind shear and resolved momentum fluxes (Figure 4.7 g) peak.

In SC-OFF (blue) zonal shear production of EKE is, on average, twice as large due to stronger w'_{res}, except near 1 km, where a local wind maximum leads to small shear $\frac{\partial \overline{u}}{\partial z} \approx 0$ (see Figure 4.2 c). The meridional shear production of EKE is also larger than the control for both SC-OFF and UV-OFF, peaking near 1.5 km in SC-OFF and just above 1 km in UV-OFF. In other words, parameterised momentum transport by SC in the control is effective at diffusing EKE that is established in the cloud layer on mesoscales.

EKE production is anisotropic, with buoyancy production occurring only in the vertical component w. The EKE anisotropy, expressed as $\sigma_w^2/(\sigma_u^2 + \sigma_v^2)$ in Figure 4.9d (section 4.3.3) helps quantify the relatively importance of buoyancy versus shear (Salesky et al., 2017). The EKE anisotropy is largest in the cloud layer, and it increases from the control to the SC-OFF experiment, suggesting a relative larger increase in buoyancy production compared to shear production. The response is opposite in UV-OFF (red), where the mean EKE anisotropy decreases in the cloud layer compared to the control. This is explained by more shear production (panels a and b) and almost equal buoyancy production (panel c) to the control.

4.7 MESOSCALE CIRCULATIONS

Following George et al. (2023), we introduced a definition of mesoscale overturning circulations (SMOCs) in section 4.3.3, which are regions where the sub-cloud and the cloud layers exhibit mesoscale horizontal divergence $\mathcal{D}$ with the opposite sign. The $\mathcal{D}$ dipole ($\mathcal{D}'$) is positive when mesoscale ascent leads to divergence in the cloud layer and convergence in the sub-cloud layer, and vice-versa, negative for mesoscale subsidence.

Figure 4.10 shows SMOCs coloured by $\mathcal{D}'$ so that positive values (magenta) indicate convergence in the sub-cloud layer, and negative values (green) indicate divergence in the sub-cloud layer. White indicates areas with $|\mathcal{D}| < 10^{-6}s^{-1}$ (see section 4.3.3 about the threshold) or areas where divergence in the sub-cloud and cloud layers have the same sign (no dipole). The cloud field is also shown on top as grey shading, where the light shading indicates cloudy columns with a cloud base above 1 km, and darker shading is for cloudy columns with a cloud base below 1 km. The three examples include: 7 January at 22:00 LT (top row), when both UV-OFF and SC-OFF produce larger CC than the control ($CC_{\text{control}} = 0.26$, $CC_{\text{UV-OFF}} = 0.51$, $CC_{\text{SC-OFF}} = 0.55$); 17 January at 12:00 LT (middle row), when UV-OFF and SC-OFF both produce smaller CC than the control ($CC_{\text{control}} = 0.42$, $CC_{\text{UV-OFF}} = 0.19$, $CC_{\text{SC-OFF}} = 0.29$); and 11 February at 05:00 LT (bottom row), when $CC_{\text{control}} = 0.19$, $CC_{\text{UV-OFF}} = 0.17$, $CC_{\text{SC-OFF}} = 0.31$.

In all three experiments, SMOCs are prevalent, as in the observations (George et al., 2023),
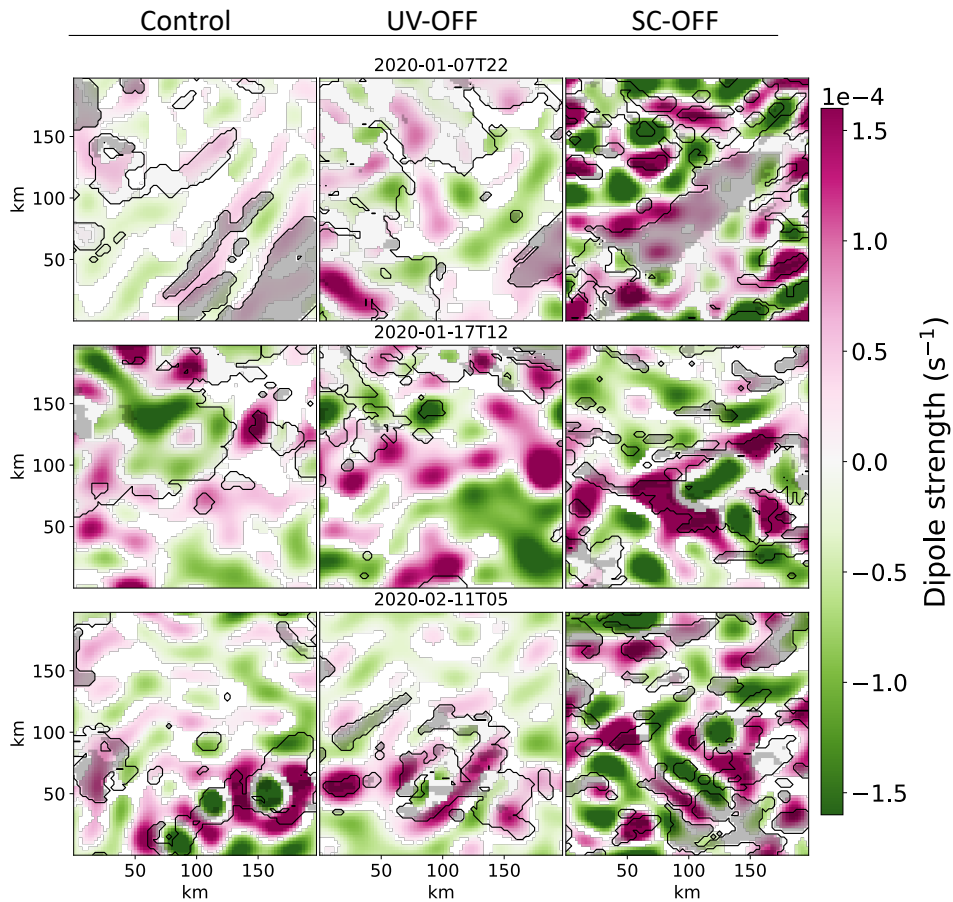
Figure 4.10: Instantaneous fields of dipole $\mathcal{D}'$ strength, defined as the delta between the sub-cloud and the cloud layer divergence $\mathcal{D}$. Positive (negative) values indicate sub-cloud layer convergence (divergence). The black contours and the grey shading indicate cloudy grids. Light (dark) shading is for grids with cloud base above (below) 1km. Each row refers to a date (7 January at 22:00 LT, 17 January at 12:00 LT, and 11 February at 05:00 LT), each column refers to an experiment.

with alternating (in space) converging and diverging branches of circulations. Convergence and divergence, and thus the dipole $\mathcal{D}'$, are generally stronger when convection is resolved *e.g.*, SC-OFF in the right column, which highlights the coupling between convection and mesoscale wind fields. Just from visual inspection, clouds in some scenes seem to favour regions of strong convergence/divergence (see the bottom row for control and UV-OFF), but even in regions without clouds, or where clouds are not rooted below 1 km, SMOCs are evident. We return to the relationship between cloudiness and circulations in section 4.8 below.

In Figure 4.11 we quantify the area covered by SMOCs in panel a), the strength of $\mathcal{D}'$ in b) and the horizontal-to-vertical aspect ratio of SMOCs in c). Removing parameterised transport from control to UV-OFF and then to SC-OFF incrementally increases the coverage and strength of SMOCs. The SMOC coverage increases from ~ 0.65 in the control to more than 0.7 in SC-OFF, with explicit convection strongly narrowing the distribution at the lower end (scenes without SMOCs become rare). The strength is about 0.5×10^{-4} in the control, 0.6×10^{-4} in UV-OFF, and 1×10^{-4} in SC-OFF. The increase in SMOC strength is in line with our analysis of EKE.
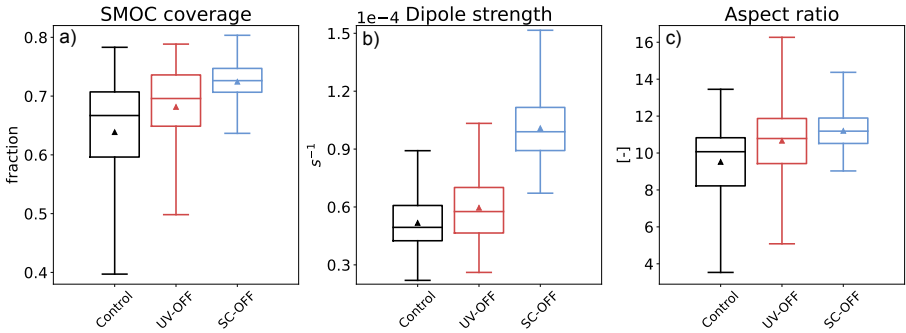
Figure 4.11: Panel a) shows the distribution of SMOC coverage, defined as the area fraction covered by SMOCs. Panel b) shows the SMOC strength, defined as the magnitude of the dipole $\mathcal{D}'$ of mesoscale horizontal wind divergence. Panel c) shows the non-dimensional aspect ratio of SMOCs, defined as the ratio between horizontal size and vertical extent. Box limits indicate the interquartile range, with a central line marking the median. The triangle indicates the mean, and the whiskers capture the range of the remaining data.

The aspect ratio in Figure 4.11 c) indicates how much wider than taller the SMOCs are. The mean boundary layer height that effectively sets the vertical extent of SMOCs (defined in section 4.3.3) is between 1 km and 1.5 km throughout the simulated period and does not differ much between the experiments. The mean horizontal size of SMOCs varies more, with most values between 10 km and 16 km, leading to a mean aspect ratio around 10. In the control (black) the aspect ratio ranges between 4 and 14, while for SC-OFF (blue) it is never lower than 8. In UV-OFF (red) the largest aspect ratios are found, up to 16, but a long tail towards low aspect ratios keeps the mean ratio small.

4.8 Relation between changes in cloudiness and circulations

Whether clouds drive mesoscale circulations or vice-versa is an ongoing topic of discussion in the community. According to George et al. (2023), SMOCs are not likely driven by radiation; instead, they are thought to be sustained or enhanced by moisture anomalies in the sub-cloud layer. Jansson et al. (2023) reveal how such moisture anomalies can grow from the initial (latent) heating perturbations produced by shallow cumulus convection. One of our questions is whether changes in the circulations between the control and other experiments help explain the overall changes in low cloud cover, in particular the increase in $CC_{z<1km}$ from the control to the SC-OFF experiment, and the small decrease in $CC_{z<1km}$ from the control to UV-OFF (Figure 4.5).

Figure 4.10 suggests that SMOCs are more ubiquitous than clouds, that is, not all converging SMOCs exhibit clouds. Figure 4.11 a) indeed shows that SMOCs cover a much larger fraction of the domain (~ 0.7) compared to the fraction covered by clouds below 1 km (~ 0.1) (Figure 4.5).
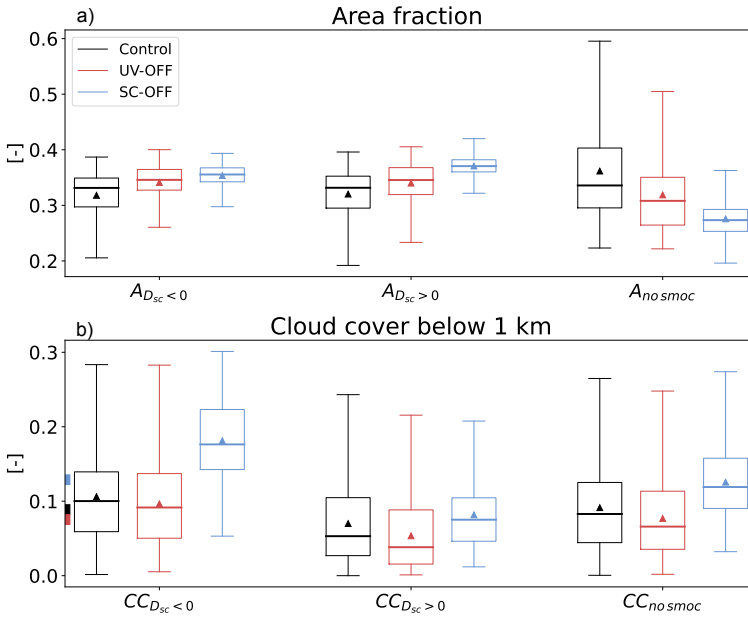
Figure 4.12: In a) the area covered by converging SMOCs, diverging SMOCs, and the area without SMOCs (*no smoc*) are shown for the control, UV-OFF, and SC-OFF. In b), cloud cover below 1km is shown, sampled on the area covered by converging SMOCs ($CC_{D_{sc}<0}$), the area covered by diverging SMOCs ($CC_{D_{sc}>0}$), and the area not on SMOCs ($CC_{no\,smoc}$). The square markers on the left y-axis are the mean CC below 1 km sampled on the entire domain as in Figure 4.5 ($CC_{z<1km}$).

To address whether clouds are favoured over converging SMOCs we divide the distribution of SMOC coverage in Figure 4.11 a) into areas of sub-cloud convergence, divergence or neither (*no smoc*), the sum of which equals 1. The increase in SMOC coverage in SC-OFF

and UV-OFF as seen in Figure 4.11 evidently comes from an increase in both converging and diverging branches, while areas with no SMOCs become rare.

In UV-OFF, changes in resolved updraft strength w^{UP} (Figure 4.3), in the heat flux, and thermodynamic profiles are marginal, so that we expect that changes in cloud statistics are produced through changes in the dynamics. In the absence of parameterised wind mixing between converging and diverging layers, stronger and more extensive SMOCs regions can be sustained. This condition suggests more stratiform cloudiness in a cloud layer confined by the trade-inversion, at times when SMOCs are promoted.

In Figure 4.12 b) we show CC below 1 km sampled over only the converging branches of SMOCs where $\mathcal{D}'_{sc} < 0$, or only the diverging branch where $\mathcal{D}_{sc} > 0$, and only over the areas with no meaningful SMOC dipole (*no smoc*). For completeness we also show, as square markers on the left y-axis, the mean cloud cover ($CC_{z<1km}$) over the entire domain, derived from Figure 4.5. Summing the product of area fraction times the cloud cover over these different categories would give the total (domain) cloud cover.

Clouds are found preferentially in areas of sub-cloud convergence. In all three experiments, $CC_{\mathcal{D}_{sc}<0}$ is higher than the overall CC, and higher than over areas with sub-cloud divergence or areas without SMOCs. The difference is most pronounced with fully explicit resolved convection in SC-OFF. Mean values for CC are around 0.1 for the control and UV-OFF, and 0.17 for SC-OFF over converging SMOCs. The lowest cloud cover is found over diverging SMOCs, where 50% of the time cloud cover is below 0.05 in the control and in the UV-OFF experiment. Regions where no SMOCs are detected have a CC distribution that represents well the domain average, with mean values around 0.08 for the control and UV-OFF, and 0.13 for SC-OFF. The results show that the enhanced cloudiness in SC-OFF is dominated by enhanced cloudiness above converging SMOCs, whereas the reduced cloudiness in UV-OFF is dominated by reduced cloudiness above diverging SMOCs and *no smoc* regions.

4.9 Conclusions

This study investigates the influence of parameterised and resolved shallow convective transport on the cloud field and on mesoscale circulations using the mesoscale model HARMONIE-AROME. The model experiments focus on the EUREC4A-MIP, simulating a large domain east of Barbados over the north Atlantic trade-wind region from 1 January to 29 February, 2020. Three model simulations are carried out: 1) a control simulation with an active SCP; 2) an experiment without parameterised momentum transport by shallow convection, UV-OFF; 3) an experiment with an inactive SCP, thus omitting all parameterised transport by shallow convection, SC-OFF. The goal is to shed light on the implications of parameterised shallow convection in kilometre-scale simulations and evaluate our conceptual understanding of mesoscale cloud organisation and circulations coupled to shallow convection.

In the UV-OFF and SC-OFF experiments, the missing parameterised transport of momentum in the sub-cloud layer is almost entirely compensated by an increase in momentum transport by the eddy-diffusivity scheme, in response to stronger wind shear developing. In the cloud layer, resolved convection only partially takes over the momentum transport. In

SC-OFF, the total heat and moisture fluxes increase, carried by much stronger convection now resolved at the grid-scale.

Inspired by (Honnert et al., 2011), we recently performed ten days of large-eddy simulations with 100 m grid spacing over a 150 km x 150 km domain for the same EUREC4A period (Savazzi et al., 2024) to study, among other things, the dependence of total turbulent flux on grid spacing. At a grid spacing of 2.5 km, the sub-grid heat and moisture flux should carry more than 60% of the total flux in the middle of the cloud layer. This is far from being the case for the SC-OFF experiment, where the resolved fluxes largely dominate the sub-grid fluxes from the ED scheme (Figure 4.7). In the control experiment, the partition between sub-grid and resolved fluxes is more similar to what is suggested by LES.

With a grid spacing of 2.5 km, the non-local transport of heat and moisture from the lower to the upper cloud layer is more efficient when done by resolved eddies in SC-OFF than by the parameterisation in the control. In contrast, the sub-cloud layer is less efficiently mixed by resolved eddies, highlighting the importance of the parameterised dry mass-flux transport. Removing sub-grid transport by SC effectively builds up instability in the lower layers and triggers strong resolved updrafts.

Compared to satellite infrared imagery (GOES16), the SC-OFF experiment, with stronger convection, degrades the structure and organisation of the projected cloud field. Clouds become too deep and are too small and numerous. They are also distributed too uniformly across the domain, reducing the fraction of open sky, and become more symmetric. The larger number of clouds increases cloud cover below 1 km. A few of these clouds rise deeper driven by strong updrafts, resulting in more precipitation. As convection is deeper and mixing is more efficient in the cloud layer, the inversion is weaker and widespread stratiform outflow layers below the inversion are less common, reducing cloud cover above 1 km. Radiosonde measurements further reveal that in the SC-OFF (and in UV-OFF) a too strong zonal wind jet develops near cloud base.

In SC-OFF, larger total heat fluxes driven by stronger resolved convection (leading to larger resolved eddy kinetic energy) strengthen and widen the areas with significant mesoscale convergence and divergence. While the increased wind shear works against convection (Helfer et al., 2020), changes in the thermodynamic environment outclass the shear effect and shallow meridional overturning circulations (George et al., 2023), or SMOCs, become more pronounced (Figure 4.13).

The UV-OFF experiment develops larger eddy kinetic energy in the cloud layer due to less sub-grid momentum mixing in this layer and thus more horizontal wind variance. SMOCs become somewhat stronger and wider. This is favourable for cloudiness that forms in the upper cloud layer, as UV-OFF produces larger clouds above 1 km, due to more or wider stratiform outflow layers (Figure 4.13).

The extent to which the ED scheme and the resolved flow can compensate for the missing transport by SCP is dependent on the model resolution. Interestingly, removing the SCP in a coarser model, like IFS (ECMWF, 2024) with ~9 km grid spacing, produces an opposite response from that in HARMONIE. In the IFS, SMOCs are hardly resolved and resolved motions do not effectively take over the parameterised transport by SC. This leads to a lack
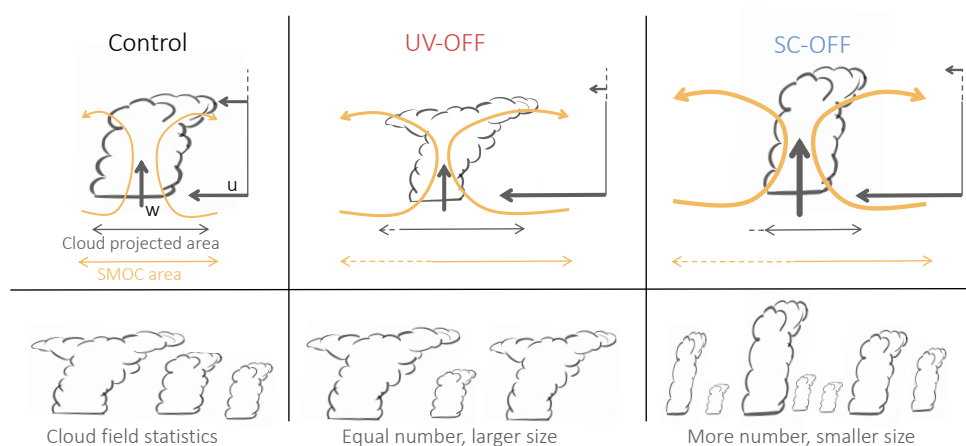
Figure 4.13: Sketch representing, for the three experiments, a typical resolved mesoscale circulation (top row) and a typical cloud field (bottom row).

of vertical mixing when removing the SCP in IFS, increasing the stability and strengthening the inversion (Bechtold et al., 2014a). Other components of the model, such as the cloud scheme, could also influence this response, although less pronouncedly as resolution refines. Despite the many pitfalls (Brown et al., 2006; Schlemmer et al., 2017; Xiao et al., 2023), our results demonstrate that even at a grid spacing of 2.5 km, a parameterisation for shallow convection may be needed.

4.10 Open Research

The data from the three HARMONIE-AROME experiments used in this study are publicly available at the following DOI: 10.4121/d61e2238-b969-45e1-8649-62197f30025a with CC BY-SA. All observational data used in this study are freely available and can be easily accessed via the EUREC4A-Intake catalog at https://github.com/eurec4a/eurec4a-intake as described at howto.eurec4a.eu.

5

THE GAP BETWEEN MEASURED AND PARAMETERISED CONVECTIVE MOMENTUM TRANSPORT

The Integrated Forecasting System (IFS) of the European Centre for Medium-Range Weather Forecasts (ECMWF) currently has a grid spacing of about 9 km and relies on separate schemes for the subgrid transport of boundary layer turbulence and shallow moist convection. These schemes have been extensively tested for the transport of heat and moisture, against field observations and large eddy simulation. Momentum transport has less often been the focus of such studies, or only for rather idealised cases with constant background winds. In the CMTRACE campaign we seek evidence of the mesoscale flows and the momentum fluxes they carry in complex convective atmospheres. Horizontal and vertical winds, measured by upward scanning and vertically pointing lidar, provide - for the first time - profiles of momentum fluxes up to 2 km at convection-permitting scales (minimum resolution 200 m - 500m). These are complemented with tower-based turbulence fluxes at heights below 200 m, which we here use to validate the IFS. We explore three weeks, between September 13th and October 3rd 2021, characterised by a multitude of shallow convective activity above the Cabauw supersite (Netherlands). At 180 m the CMTRACE measurements miss about 30% of the momentum flux due to the sampling resolution. A comparison with the IFS shows similar wind profiles, except for the presence of a known weak wind bias with a too pronounced westerly component. The known wind bias is here seen to extend across a much deeper layer than just near the surface: up to 800 m. The model significantly overestimates the momentum fluxes throughout the boundary layer, especially during times with more clouds. The shallow convection scheme and the eddy diffusivity component of the boundary layer schemes are unaffected by the addition of a dry mass-flux contribution in the momentum transport of the boundary layer scheme, suggesting that the bias is rooted in the cloud layer rather than in the subcloud layer.

5.1 Introduction

Turbulent flows occur across a wide range of spatial and temporal scales in the atmosphere. These range from millimetre-scale eddies near the surface to large synoptic weather systems spanning hundreds of kilometres, resulting in a continuous cascade of energy across different scales. Capturing this spectrum presents significant challenges for numerical models, which are inherently limited by their discretised grid. Models can only resolve flows larger than their grid spacing, while they must parameterise smaller eddies. Parameterisations attempt to represent the statistical effect of small-scale turbulence on the resolved flow.

The conventional approach for kilometre to hectometre model grid spacing is to distinguish two schemes for handling subgrid processes in the boundary layer (BL): the turbulence or boundary layer scheme and the convection scheme. With the turbulence scheme, modellers intend to represent smaller-scale, continuous motions driven by wind shear and surface stress. Most turbulence parameterisations are based on an eddy-diffusivity approach, which simply dissipates the local gradient. This estimates the flux $\overline{\phi' w'}$ of a quantity ϕ as the product of the local gradient of $\overline{\phi}$ and a coefficient K. Refinements to this basic formulation allow for counter-gradient transport (e.g. Brown and Grant, 1997), which is common at the top of a dry BL (Dixit et al., 2021; Schumann, 1987).

The convection scheme is typically intended for larger-scale, intermittent vertical motions driven by buoyancy and latent heat release, leading to cloud and precipitation formation (Arakawa, 2004). The basic concept of this scheme was developed to represent the effect of deep cumulus convection, which organises in coherent vertical plumes (Arakawa and Schubert, 1974; Yanai, 1964). The mass-flux approach (Arakawa, 2004) proved to be very effective at representing this non-local process, and the scheme was extended to include the effect of shallow cumuli.

Despite interesting developments of a unified boundary layer scheme, which combines eddy-diffusivity and mass-flux (EDMF) to represent large dry eddies (Siebesma et al., 2007; Siebesma, 2000; Soares et al., 2004), the need for improving subgrid boundary layer mixing is still high. A new generation of convection-permitting models, running at kilometre scale, challenges the mass-flux approach. The grid spacings of these models fall in the grey-zone of convection, where convection is partly resolved but some smaller buoyancy driven eddies remain subgrid. How to best represent the partition between subgrid and resolved convective transport is an ongoing topic of discussion (Honnert et al., 2011; Siebesma et al., 2003) .

In this discussion, momentum have often received less attention than conserved scalars, like heat and moisture (Holland and Rasmusson, 1973; Koning et al., 2022). The effect is that many findings on conserved scalars are arbitrarily applied to momentum transfer despite the fundamental differences described, for example, by Badlan et al. (2017) and Carr and Bretherton (2001). In this study we evaluate the sub-grid momentum fluxes in the most recent IFS cycle (49r1) against novel measurements of shallow convective boundary layers from the CMTRACE 2021 field campaign (Dias Neto et al., 2023). CMTRACE is the first campaign to measure wind profiles at convection-permitting resolutions and thus provide observed estimates of the momentum flux throughout the boundary layer. For

5

three weeks, collocated wind lidar and cloud radar retrieved seamless wind profiles from near the surface up to cloud tops above a flat grass field in Cabauw, Netherlands.

Large eddy simulations (LES) have often been used to overcome the lack of wind and momentum-flux measurements in the atmosphere. Such simple experiments greatly aid the evaluation of convection schemes for the transport of momentum. With a domain of only 6.4 x 6.4 km^2, Brown (1999) was among the first to recognise the dominant role of cross-cloud pressure gradients for the momentum budget of a shallow convective case. The standard mass-flux approach neglects such pressure gradient term and is also strongly limited by the challenges of determining correct values of mass-flux and in-cloud momentum at cloud base (Schlemmer et al., 2017). Using the Cloud-Layers Unified by Binormals framework (CLUBB; Golaz et al. (2002)), Larson et al. (2019) suggests a prognostic parameterisation of the subgrid momentum flux that overcomes such limits. This method is able of predicting counter-gradient momentum fluxes and closely adheres to the budget equation of momentum flux.

Despite the fundamental advancements possible with LES studies, some fundamental limits remain. The small LES domains often do not allow for a full development of convective cells (Helfer et al., 2020), and the arbitrary choices at the boundaries imply a strong dependency on the large scale forcing (Savazzi et al., 2024). With a large domain (200 x 100 km^2) and realistic boundary conditions, Dixit et al. (2021) found a counter-gradient flux layer that was twice as deep as that observed in idealised simulations. The dominant mechanism sustaining counter-gradient momentum flux was shown to be dependent on the domain size and the ability of the model to realistically simulate the mesoscale organisation in the winds, accompanying organisation in the clouds.

Our ability to design parameterisations is challenged by the wide range of scales at which convection occurs, and by the ever increasing model resolutions (Freitas et al., 2020; Satoh et al., 2018; Stevens et al., 2019; Wedi et al., 2020). These challenges require accurate measurements of atmospheric fluxes across scales. The recent understanding of mesoscale organisation in the wind further demonstrate the value of measuring momentum flux (George et al., 2021a; Savazzi et al., 2022; Vogel et al., 2022). The novel CMTRACE campaign offers an unprecedented opportunity to advance the development of models for subgrid momentum transport, as it directly measures shallow mesoscale circulations in a real environment.

After a description of the observational (section 5.2) and modelling (section 5.3) datasets we present an evaluation of the winds (section 5.4). In section 5.5 we analyse the momentum fluxes from observations and evaluate the CMTRACE flux measurements. A direct comparison of observed and modelled momentum fluxes is in section 5.6 and in section 5.7, where we subsample for periods with clear and cloudy conditions. In section 5.8 we investigate the role of parameterised dry plumes with a second model experiment. The results are summarised and discussed in section 5.9.

5.2 Observational dataset

The Cabauw Experimental Site for Atmospheric Research (CESAR) is located at Cabauw, the Netherlands, 0.7 m below sea level at 51° 58' N latitude and 4° 54' E longitude. It

features a 213-m high meteorological tower and a wide range of advanced ground-based remote-sensing facilities. The tower was built in 1972, and its capabilities have been continuously extended with new observational equipment. The site also functions as a testbed for new measurement techniques. In this study we use data from the CMTRACE campaign (Dias Neto et al., 2023), and from the sonic anemometers permanently mounted on the tower.

5.2.1 CMTRACE
The first field campaign from the Tracing Convective Momentum Transport in Complex Cloudy Atmospheres experiment project (CMTRACE) took place in Cabauw, between September 13th and October 3rd 2021 (Dias Neto et al., 2023). During this field campaign, two cloud radars and one wind lidar (Vaisala scanning WindCube 200s) operated with a similar scanning strategy to derive wind speed and direction profiles from near the surface up to cloud tops. The wind lidar provides information on the sub-cloud layer winds, while the cloud radars provide information on the cloud layer winds.

The detailed description of the setup is published in Dias Neto et al. (2023), here we present the data availability for level 2 of the dataset. The zonal u, meridional v, and vertical w wind components are available with a vertical resolution of 50 m, which we regrid to 100 m, and temporal resolution of 72 seconds, which we approximate and regrid to 1 minute. There is a 3-day data gap between the 17th and the 20th of September, and a 1-day data gap on the 2nd of October. Along the vertical axis the data is more easily retrieved in the lower 1 km, as the lidar relies on aerosol and the radars on cloud droplets for the backscatter. Figure 5.1 shows how the number of retrievals diminish rapidly above 1 km.

We apply Reynolds decomposition using time windows of 30 minutes and obtain wind anomalies (u', v', w') from which we compute the momentum fluxes $(\overline{u'w'}, \overline{v'w'},)$. Taylor's frozen hypothesis suggests that the wind speed can be used to translate turbulence measurements as a function of time to their corresponding measurements in space. Thus, for a wind speed of 5 ms^{-1} and IFS grid spacing of 9 km, one can compute wind anomalies against $(\frac{9\,\text{km}}{5\,\text{ms}^{-1}})$ 30 min time windows. This is equivalent to what would be the subgrid fluxes in IFS. The same reasoning shows that the size of the smallest eddy captured with a 1 min resolution is 300 m, if the wind speed is 5 ms^{-1}. The fluxes obtained with a fixed 30 minutes window are marginally different from using a varying time window every day based on the daily mean wind speed.
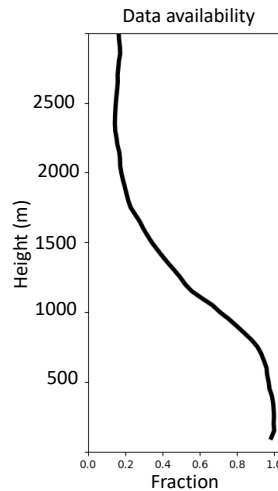
Other than calculating momentum fluxes directly at the native resolution of the dataset, we can also

Figure 5.1: Profile of data availability for CMTRACE level 2.

derive a mass-flux based momentum flux, whereby:

$$\overline{u'w'}^M = M_u(u_u - u_e) + M_d(u_d - u_e),$$ (5.1)

where only the zonal component is shown for brevity. The subscripts u and d denote the updraft and downdraft regions, the subscript e denotes the environment, and M is the mass-flux. The latter reads:

$$\begin{cases} M_u = \overline{\rho} A_u w_u, \\ M_d = \overline{\rho} A_d w_d, \end{cases}$$ (5.2)

where $\overline{\rho}$ is the air density, A_u (A_d) is the fraction of updraft (downdraft) regions, and w_u (w_d) is the vertical wind in the updraft (downdraft). For this estimate of the momentum fluxes we divide the time series in windows of 30 minutes and apply a threshold on the measured vertical velocity to identify updrafts and downdrafts. We use both a low and a high threshold (± 0.05 ms^{-1} and ± 0.2 ms^{-1}) to test the robustness of the method, within the range of thresholds employed by previous investigators (Zhang and Wu, 2003; Zhu, 2015).

5.2.2 Cabauw tower

The three wind components are measured at a frequency of 10 Hz by Gill R3 sonic anemometers installed at 5 m, 60 m, 100 m and 180 m height on beams pointing south east from the Cabauw tower. The eddy covariance technique allows to compute momentum fluxes from this dataset. The calculation is repeated with time windows ranging from 30 seconds (300 samples) to 30 minutes (18000 samples). The flux is thus partitioned between scales smaller and larger than the threshold time window as follows:

$$\overline{u'w'} = \overline{u''w''} + \overline{\widetilde{u}'\widetilde{w}'},$$ (5.3)

where the overline tilde is an average over the arbitrary time threshold, and the double prime is an anomaly with respect to this average. The first term on the rhs indicates the contribution from scales between 0.1 sec and the threshold, while the second term on the rhs indicates the contribution of scales between the threshold and 30 min. The fluxes $\widetilde{u}'\widetilde{w}'$ and $\widetilde{v}'\widetilde{w}'$, obtained with a threshold of 1 minute, are compared with the estimates from CMTRACE, and used to quantify the amount of flux missed with the 1 minute resolution of CMTRACE. At 180 we can also define a combined dataset, which we call CMTRACE+, where the CESAR fluxes for time scales < 1 min ($\overline{u''w''}$ and $\overline{v''w''}$) are added to CMTRACE.

For the purpose of this study we apply only a first order correction to the raw sonic measurements. We filter out all dates with missing values in the validated 10 minutes averaged dataset from CESAR. Then, we remove spikes where any of the three wind components is larger than ± 30 ms^{-1}. We also apply a 30 degrees rotation of the coordinate system around the vertical axis to compensate for the tilt of the instruments. This rotation is important to align the wind components (u and v) with the west-east and south-north directions. This geometric transformation has no impact on quantities like wind speed $U = (\overline{u}^2 + \overline{v}^2)^{0.5}$ and total flux $\tau = (\overline{u'w'}^2 + \overline{v'w'}^2)^{0.5}$

5.3 MODELLING DATASET

Figure 5.2 shows a schematic of how the subgrid fluxes are represented by the Integrated Forecasting System (IFS) of ECMWF. The model distinguishes between the boundary layer (BL) scheme and the shallow convection (SC) scheme. Their contribution to the total subgrid flux can be written as:

$$\overline{w'\phi'}^{\text{Subgrid}} = \overline{w'\phi'}^{\text{SC}} + \overline{w'\phi'}^{\text{BL}}, \tag{5.4}$$

where $\phi = [s, q_t, u, v]$ is a generic variable.
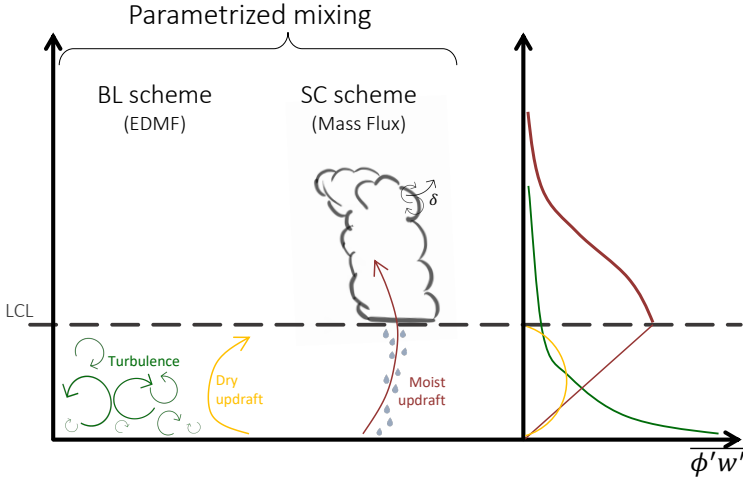
Figure 5.2: Sketch representing the partition of IFS subgrid fluxes into the boundary layer and shallow convection schemes. The profiles on the right resemble the flux shapes imposed by the parameterisations.

The shallow convection (SC) scheme (brown in Figure 5.2) is based on the bulk mass-flux approach (Tiedtke, 1989) with a moist updraft and a downdraft component. The flux contribution from the SC scheme can be written as:

$$\overline{w'\phi'}^{\text{SC}} = M_{\text{u}}^{\text{SC}}(\phi_{\text{u}}^{\text{SC}} - \overline{\phi}) + M_{\text{d}}^{\text{SC}}(\phi_{\text{d}}^{\text{SC}} - \overline{\phi}), \tag{5.5}$$

where M_{u} and M_{d} are the updraft and downdraft mass-fluxes respectively, and the overbar denotes the grid-box mean. The mass-fluxes are computed at cloud base through a moist static energy closure and their value is linearly extrapolated to zero at the surface as described in Bechtold et al. (2014b).

The boundary layer (BL) scheme is parameterised using the eddy diffusivity mass-flux (EDMF) framework (Siebesma, 2000). This combines a simple, downgradient eddy diffusivity term for the small scale turbulence (green in Figure 5.2), with a mass-flux term for the larger dry plumes (yellow in Figure 5.2). The latter term allows for counter gradient transport as dry plumes can mix non-local properties from near the surface to near cloud base. The flux contribution from the BL scheme can be written as:

$$\overline{w'\phi'}^{\text{BL}} = -K\frac{\partial\overline{\phi}}{\partial z} + M_{\text{u}}^{\text{BL}}(\phi_{\text{u}}^{\text{BL}} - \overline{\phi}), \tag{5.6}$$

where K is the eddy diffusivity.

Our modelling dataset comprises two simulations with cycle 49r1 of the IFS.

1. IFS-ctrl: The control run uses the operational setup, where the mass-flux term of the BL scheme only mixes heat and moisture, but not momentum. This reduces equation 5.6 to

$$\overline{w'\phi'}^{\text{BL}} = -K\frac{\partial\overline{\phi}}{\partial z} \qquad \text{for } \phi = [u,v]. \tag{5.7}$$

   The mass-flux term of the BL scheme remains active for heat and moisture, only when the SC scheme is not triggered.

2. IFS-dryMF: In this second experiment we modified the BL scheme so that its mass-flux component would also transport horizontal momentum rather than just heat and moisture.

For each of the runs, we extract hourly output for day 2 of the forecasts (lead time of 24 to 48 h) on an area of six by six grid boxes around the Cabauw site. The horizontal grid spacing is about 9 km at this latitude, which gives a domain of about 54 x 54 km^2. The hybrid vertical coordinate of 137 levels is projected onto a regular grid of geopotential height with spacing of 100 m. In this study we present only domain averages of the forecasts to obtain smoother wind and flux profiles and account for the possibility that the model misses the exact location of the eddies.

5.4 Modelled and measured winds

The three-week period of the field campaign is dominated by daytime shallow convective activity with different intensity. Figure 5.3 shows six MODIS-Terra scenes from NASA's Worldview[1]. The satellite's visible images are taken around 10:30 local time (LT) every day. Typical summertime cloud topped boundary layers were encountered, with cloud base around 600 m. The cloud top varies significantly, with some (deeper) shallow convection extending to 2 km towards the end of the campaign. On September 16th, 24th, and 28th (panels a,c,e respectively) the scenes are dominated by shallow cumuli of different size and intensity. September 21st (panel b) shows little moist convection under a layer of high cirrus clouds. September 27th (panel d) and October 2nd (panel f) are dominated by a stratocumulus deck.

We use the CESAR dataset here to validate the lidar measurements, which we can do at two heights: 100 m and 180 m. In Figure 5.4 a is the distribution of wind speed at 180 from CESAR and CMTRACE. This provides a first order estimate of the measurement uncertainties, showing no significant biases and a difference between the two observational datasets within 2 ms^{-1}. The temporal evolution in Figure 5.4 b shows that wind speed at 180 m ranges from few metres per second at the beginning of the campaign to a maximum of ~20 ms^{-1} on October 2nd, with an average of ~8 ms^{-1}. The winds from IFS-ctrl (red) are too weak, but follow the hourly and daily evolution of the observations. The difference between the two observational datasets is smaller than the difference between observations and the model.

---

[1]https://worldview.earthdata.nasa.gov/
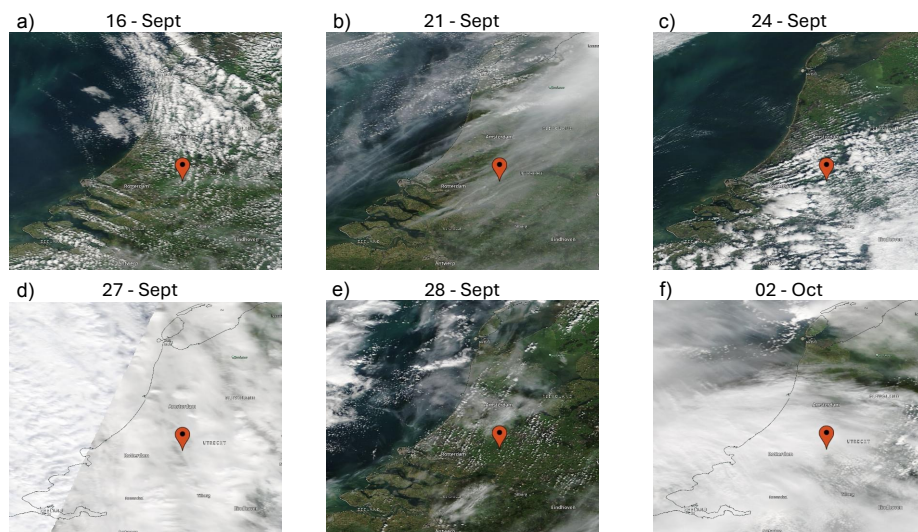
Figure 5.3: MODerate-resolution Imaging Spectroradiometer (MODIS) -Terra True Color corrected reflectance. The images cover the area 51.1N to 53.3N, and 3.3E to 5.8E. The red marker indicates Cabauw, Netherlands. The images correspond to time XX, on 16th September (a), 21st September (b), 24th September (c), 27th Septembe (d), 28th September (e), 2nd Ovtober (f).
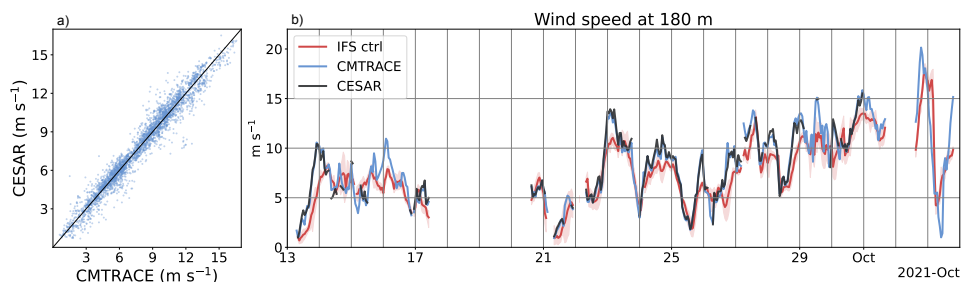
Figure 5.4: Wind speed at 180 m. In panel a is a scatter-plot for the two observational datasets, where the tower measurements are coarsened to 1 min resolution. In panel b is a time series with IFS-ctrl (red), CMTRACE (blue), and CESAR (brown) at 1 hour resolution. The red shading shows the 5th and 95th percentile of the 54 x 54 km^2 domain.

Figure 5.5 shows the IFS-ctrl and CMTRACE wind profiles from 100 m to 2 km. The profiles only consider the daytime hours, from 09:00 to 16:00 LT. The amount of retrievals from CMTRACE diminishes with height (see Figure 5.1). Thus, we mask out, at every height and time, the model output without a corresponding measurement. The red dashed lines in Figure 5.5 a, b, and c represent the unmasked IFS-ctrl wind profiles, while the solid lines have been masked with CMTRACE. Above 1.2 km the distance between the solid and dashed lines becomes increasingly large, suggesting that the few measurement points are not representative of the entire field campaign. For this reason, care is used in interpreting the results above 1.2 km and a grey shading is used to denote height where CMTRACE is

less reliable.
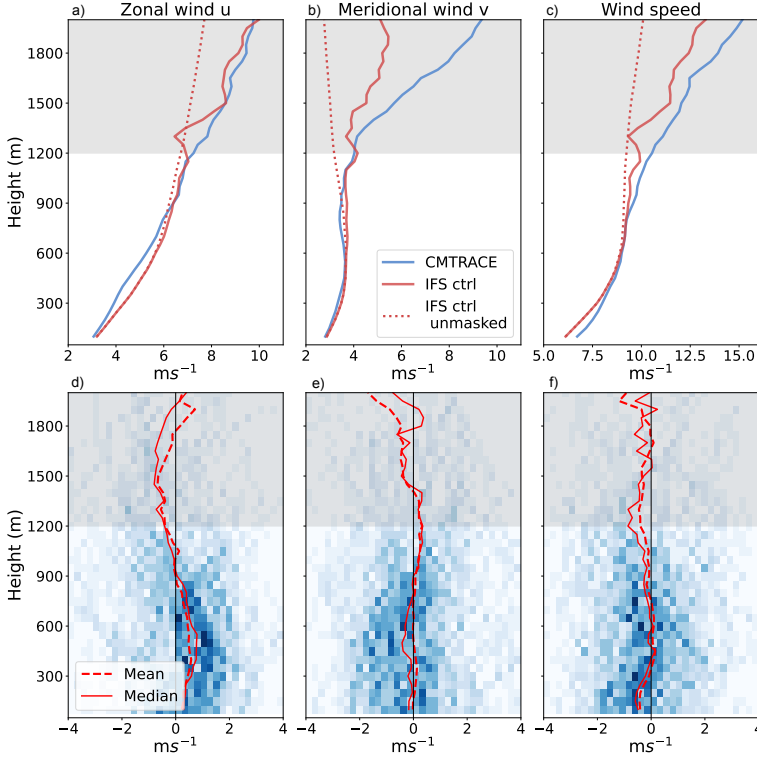
Figure 5.5: Mean wind profiles from CMTRACE and IFS-ctrl in the top row. Distribution of the wind errors (IFS-ctrl - CMTRACE) in the bottom row, where the blue colour indicates the density of the histogram, the solid red line indicates the median, and the dashed indicates the mean. The grey shading indicates where CMTRACE is less reliable due to a lack of measurements.

IFS-ctrl captures very well the mean winds, except for a mean overestimation of the zonal component between 100 m and 800 m, and an underestimation of the wind speed in the lowest 500 m. This is in line with known IFS biases of near-surface wind direction (Sandu et al., 2020) and wind speed (Thomas Haiden, 2024). The distributions of the wind errors (IFS-ctrl - CMTRACE) in Figure 5.5 d, e, and f show that the small mean biases are the result of compensating positive and negative errors of more than 2 ms^{-1} for both the zonal and meridional wind components.

5.5 Observed momentum fluxes

Our key interest is to compare modeled and observed momentum flux profiles, as driven by convection on scales of about 500 m and larger, and assess how these differences relate to wind biases. To achieve this, it is first essential to demonstrate the reliability of the momentum flux from the 1 minute CMTRACE measurements. We can estimate the contribution of scales smaller than 1 minute at 100 m and 180 m from the high-frequency

sonic anemometers mounted on the Cabauw tower. Referring to equation 5.3, in Figure 5.6 we show $1 - \frac{\overline{\widetilde{u'}\widetilde{w'}}}{\overline{u'w'}}$ in panel a, and $1 - \frac{\overline{\widetilde{v'}\widetilde{w'}}}{\overline{v'w'}}$ in panel b. The term $\frac{\overline{\widetilde{u'}\widetilde{w'}}}{\overline{u'w'}}$ (or $\frac{\overline{\widetilde{v'}\widetilde{w'}}}{\overline{v'w'}}$) indicates the magnitude of the coarsened flux with respect to the total flux, and 1 - this term indicates which fraction of the total flux is thus missed by not having information on time scales smaller than what used for the coarsening.

Figure 5.6: Fraction of the zonal (a) and meridional (b) momentum fluxes explained by fluctuations on scales smaller than the filter time shown on the xaixs. Each value is expressed as a fraction of the flux at the 30 minutes scale $\overline{u'w'}$. Data is taken from the tower where black refers to the measurements at 180 m, and grey for 100 m. Each box plot indicate the three quartiles: median, 25th and 75th percentiles.
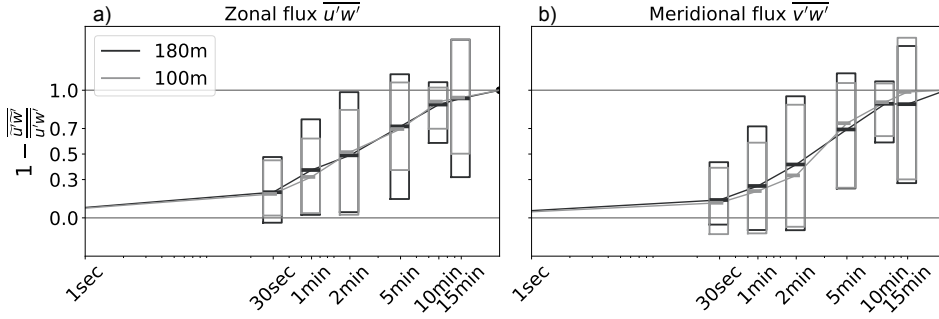
The fraction is calculated for daytime hours on windows of 30 minutes from the CESAR measurements, both at 100 m (grey) and at 180 m (black). This gives about 175 time windows (samples), where their interquartile ranges are shown by the boxplots and the medians are connected by a line. At 30 min there is no anomaly to be calculated and $\overline{\widetilde{u'}\widetilde{w'}} = 0$, thus the fraction of flux missed by such a coarse dataset is 1 at any time. On the other side of the spectra, at 0.1 sec, $\overline{\widetilde{u'}\widetilde{w'}} = \overline{u'w'}$ and the fraction goes to 0. About 30% of the zonal momentum flux is explained by scales smaller than 1 minute, while this is about 25% for the meridional momentum flux. In other words, the CMTRACE data misses between 25% and 30% of the momentum flux at 180 m.

Figure 5.6 suggests also that doubling the resolution from 1 minute to 30 seconds would only allow to measure a small additional fraction of the momentum flux. In fact, most of the flux from scales smaller than 1 minute is carried between 0.1 and 30 seconds. Fractions below 0 and above 1 indicate contributions of $\overline{\widetilde{u'}\widetilde{w'}}$ with an opposite sign to $\overline{u'w'}$. This is possible because of the close coexistence of positive and negative fluxes, which can partly compensate at scales of 30 minutes.

The interquartile range of the distributions in Figure 5.6 is large, indicating that the fraction carried by the different scales changes over time. Savazzi et al. (2024) suggests that the organisation of the eddies determines the evolution of this fraction with scales. In less organised convection, small scales tend to be dominating and the fraction increases quicker with larger time windows. The opposite is for well organised convective fields, where the momentum flux is dominated by longer time scales. An investigation of the spatial organisation of the flow field is insightful but beyond the scope of this study.

Earlier, we used the tower observations to compare against the winds measured by the wind lidar (Figure 5.4 a), showing good agreement at 1 min averages. We can also use the tower to validate the momentum fluxes. To do that, we take the tower observations, average it to exclude variations on time scales less than 1 minute ($\widetilde{u}$), and compute the tower-equivalent 30 min momentum flux ($\overline{\widetilde{u}'\widetilde{w}'}$ and $\overline{\widetilde{v}'\widetilde{w}'}$). With these fluxes we compute the quantity $\widetilde{\tau}$. In Figure 5.7, panel a refers to daytime only, here the solid distribution refers to the difference between CMTRACE τ and the raw CESAR τ, while the dashed distribution refers to the difference between CMTRACE τ and the coarsened CESAR $\widetilde{\tau}$. In panel b is the evolution of τ at 180 m from CMTRACE (blue), from the raw CESAR τ (solid black), and from the coarsened $\widetilde{\tau}$ (dashed black). This time series covers a subset of days, from September 20th to September 27th.
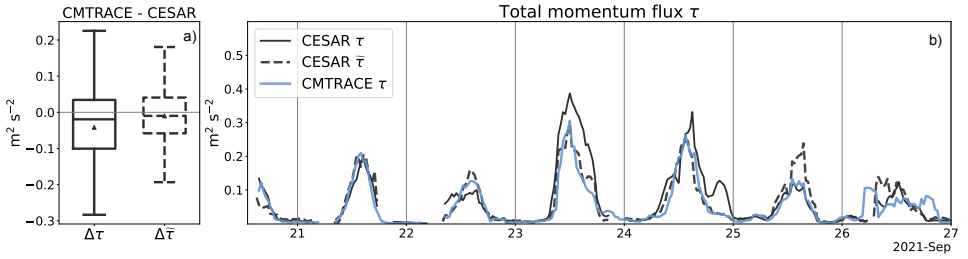
Figure 5.7: Total momentum flux τ at 180 m from CMTRACE (blue), CESAR τ at 0.1 second resolution (solid black), and CESAR $\widetilde{\tau}$ coarsened to 1 minute resolution (dashed black). In panel a is the distribution of the difference between CMTRACE and CESAR, for both temporal resolutions. In panel b is the evolution for a subset of days.

The peaks in momentum flux are captured by both datasets with similar temporal evolution. Despite some differences, the coarsened CESAR dataset (dashed black) better matches the flux from CMTRACE. The contribution of each scale to the total flux τ is not constant because the distance between the solid black and the dashed lines in Figure 5.7 b) changes significantly among days. On September 21st, for example, the contribution of scales smaller than 1 min is almost negligible; thus, the solid and the dashed black lines overlap. Instead, on September 23rd the small scales add an extra 0.05 m^2s^{-2} to the flux calculated with the coarsened winds.

The differences between the dashed and solid black lines show the amount of total flux τ carried by scales smaller than 1 minute. The solid distribution in Figure 5.7a shows that, on average, CMTRACE underestimates the total momentum flux by -0.03 m^2s^{-2}, with extremes of -0.3 m^2s^{-2} and +0.2 m^2s^{-2}. Instead, the difference between CMTRACE τ and the coarsened CESAR $\widetilde{\tau}$ (dashed), shows a Gaussian distribution around a mean of about zero, with the extremes at $\pm$ 0.2 m^2s^{-2}. This confirms that, when compared at the same temporal resolution, the two observational datasets measure the same flux, except for a small Gaussian noise.

5.6 Model and observations side by side

Models parameterise subgrid fluxes based on conceptual formulations of the physical processes. For example, the boundary layer scheme accounts for the local mixing by

turbulence; while, the shallow convection scheme takes care of the more organised and non-local turbulent mixing above the liquid condensation level. Such distinction is not captured by measurement of the wind flow in the real world, making any evaluation of the individual schemes non trivial.

In Figure 5.8 is the distribution of τ for day time hours at 180 m. The figure shows IFS-ctrl, where the subgrid (red) is divided into the two components from the BL (green) and SC (brown) schemes. From the observations, CESAR is shown in black, CMTRACE in solid blue, and CMTRACE+ in dashed dark blue. CMTRACE+ is defined in section 5.2.2 as the sum of CMTRACE and the CESAR flux for time scales < 1 min.
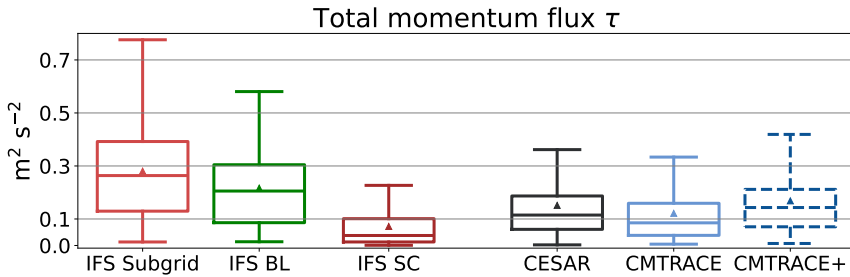
Figure 5.8: Distribution of total momentum flux τ at 180 m from IFS-ctrl subgrid (red), IFS-ctrl BL scheme (green), IFS-ctrl SC scheme (brown), CMTRACE (blue), CESAR (black).

At 180 m, the BL scheme gives the largest contribution to the parameterised momentum flux but the SC scheme still adds a non-negligible component. On average, about a third of the subgrid momentum flux at 180 m is carried by the SC scheme. This contribution is smaller than the flux measured by CMTRACE (solid blue), suggesting that at one minute resolution the instruments capture part of what the model considers turbulence and parameterises in the BL scheme. Neither CESAR nor CMTRACE+ produce as much momentum flux as the BL scheme, suggesting that this is too active in IFS-ctrl. Above 180 m the relative contribution of the SC and BL schemes changes in a way that is not possible to capture with CMTRACE. For this reason, in the rest of this section we compare only the total subgrid (SC+BL) momentum flux from IFS-ctrl with the observations.

With Figure 5.9 and Figure 5.10, we look for major discrepancies in how observed and modeled fluxes at convective scales behave. Figure 5.9 shows the temporal evolution of the zonal (a,b), meridional (c,d), and total τ (e,f) momentum fluxes for CMTRACE (a,c,e) and IFS-ctrl (b,d,f). A description of how these are estimated is in section 5.2.1 for CMTRACE and in section 5.3 for IFS. The temporal evolutions are accompanied by the corresponding winds at 180 m (solid black lines on the right y-axis). For CMTRACE we coarsened the dataset to 1 hour resolution for a fair comparison with the model; and for IFS-ctrl we use averages of the 6x6 grid boxes.

Both datasets reveal a clear diurnality in the magnitude of the fluxes. September 23rd and 24th have strong momentum fluxes at daytime with $\overline{u'w'}$ up to 0.2 m^{2}s^{-2} in the observations (panel a) and over 0.4 m^{2}s^{-2} in the model (panel b). On September 20th both datasets

Figure 5.9: Zonal (a,b), meridional (c,d), and total (e,f) momentum fluxes from CMTRACE (a,c,e) and IFS-ctrl (b,d,f) averaged to 1 hour resolution in the case of CMTRACE. The temporal evolution refers to a subset of days (from September 20th to September 27th), and the black line shows the wind at 180 m.

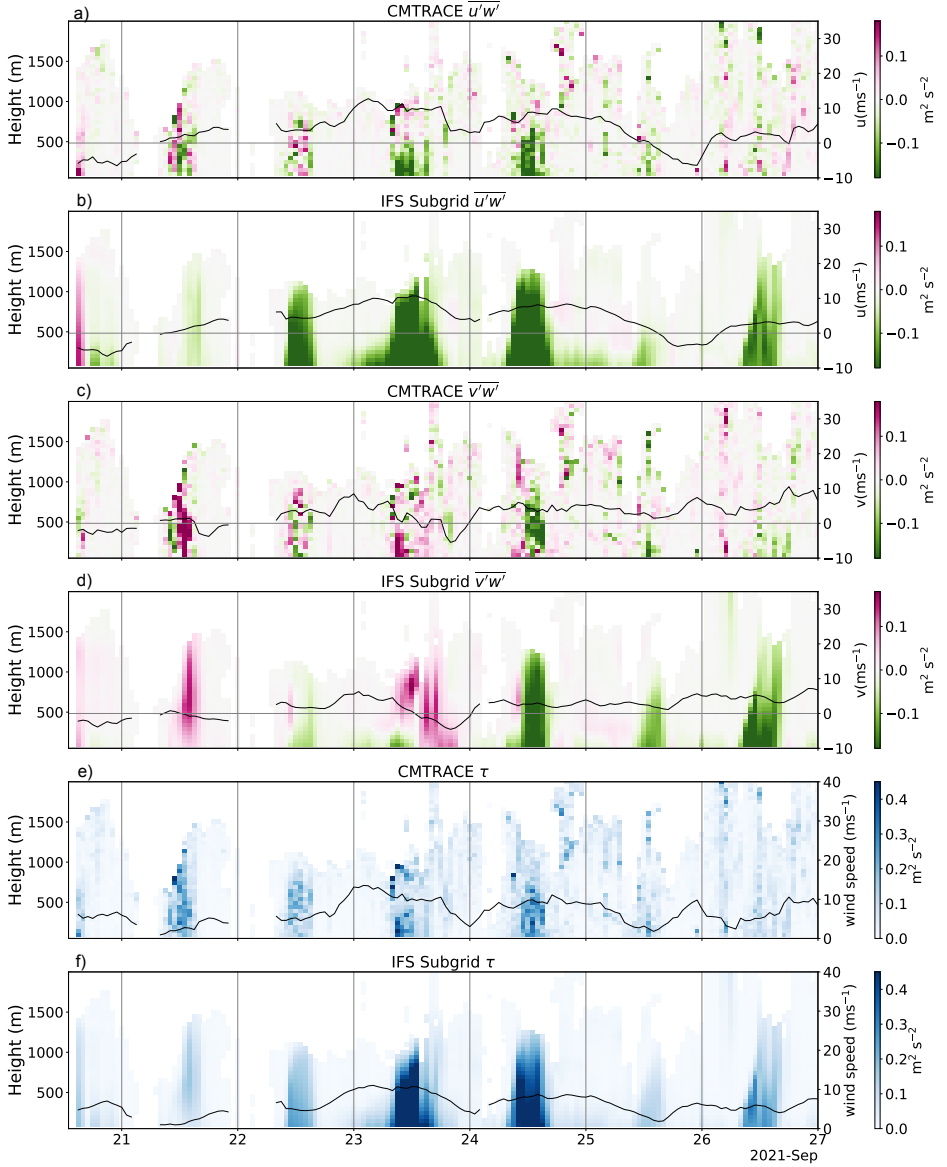capture positive zonal momentum fluxes near the surface in correspondence of a negative zonal wind. On other days, like September 27th, CMTRACE (panels a,c) shows alternating small positive and negative fluxes throughout the boundary layer, while IFS-ctrl (panels b,d) produces only strong negative fluxes both in the zonal and meridional directions. The significant variability observed in the sign of the momentum fluxes can not be explained solely by changes in the wind direction, and IFS-ctrl is not able to capture it.
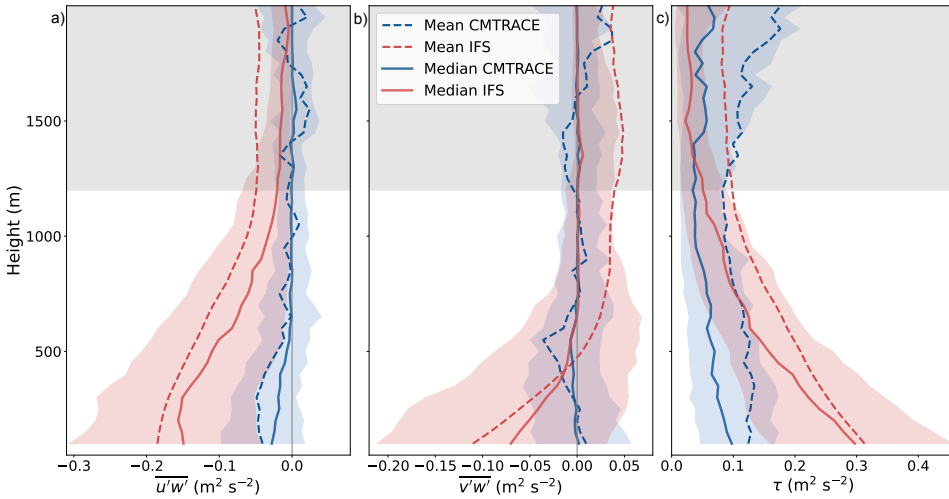
Figure 5.10: Zonal (a), meridional (b), and total (c) momentum fluxes from CMTRACE (blue) and IFS-ctrl (red). The profiles refer to daytime only (from 09:00 to 16:00) and show mean (dashed), median (solid), and interquartile range (shaded area).

From all days of the campaign, Figure 5.10 focuses on daytime only, and presents the distribution of $\overline{u'w'}$ (a), $\overline{v'w'}$ (b), and τ (c) for both CMTRACE (blue) and IFS-ctrl (red). The dashed lines refer to the mean, the solid lines to the median, and the shaded are to the interquartile range. The measured zonal momentum flux (blue in panel a) is stronger near the surface and reduces to about zero ($\pm$ 0.04 m^{2}s^{-2}) at 500 m, while for IFS-ctrl the flux is strictly negative, except there where the winds are coming from the east, and it approaches zero above 1 km. Negative values of $\overline{u'w'}$ indicate the upward (downward) transport of weak (strong) zonal wind. This correlation is stronger in IFS-ctrl than in CMTRACE, which only shows somewhat consistent $\overline{u'w'} < 0$ below 500 m. In the meridional direction (panel b) CMTRACE and IFS-ctrl have a more similar distribution, with both medians around zero above 500 m. Despite this, IFS-ctrl tends to have a few stronger events with $\overline{v'w'} > 0$, which skew the distribution and bring the mean to about 0.04 m^{2}s^{-2}.

The quantity τ, in Figure 5.10 c, allows to focus on the magnitude of the momentum flux, ignoring any error in the direction of the winds and sign of the flux. This indicates the strongest momentum fluxes below 500 m for both CMTRACE and IFS-ctrl. The total flux τ reduces with height and is largest near the surface, where shear- and buoyancy- driven wind fluctuations are present. Above 1.2 km, the lack of measurements produces statistics that are biased towards few strong events, thus the artefact of an increasing mean flux.

The distribution of τ is skewed both in IFS-ctrl and CMTRACE. In the latter dataset the mean is about 0.03 m^2s^{-2} larger than the median at all heights. This indicates that about 50% of the total flux is smaller than 0.1 m^2s^{-2} but, strong fluxes, up to 0.4 m^2s^{-2} are measured (as shown in Figure 5.9 e). The medians (solid) are often in better agreement than the means. Furthermore, the mean can produce unexpected behaviours where mean zonal and meridional fluxes of about 0 $m^2\ s^{-2}$ in CMTRACE are associated with a mean total momentum flux of about 0.1 $m^2\ s^{-2}$.

We expect the momentum fluxes to decrease away from the surface as shear-driven turbulence plays a smaller role when the profiles of wind are better mixed. However, there may be more reasons for the fairly small momentum fluxes in the observations. First, the nature of the measurements is such that sampling horizontal and vertical wind at a minute resolution can only capture fluctuations on scales of 500 m and larger, depending on the wind speed, as described in section 5.5. These smaller-scale collocated turbulent motions may be associated with much larger fluxes. The inability to capture small scales increases with height, as the volume scanned by the lidar to derive the horizontal wind increases. Second, it is evident that the momentum fluxes change sign frequently, which in the mean leads to a small turbulent flux (Figure 5.10), but at individual times fluxes exceed 0.1 m^2s^{-2} (Figure 5.9).

With the help of the high resolution tower data, we go deeper into the comparison of the fluxes at near-surface levels. Figure 5.11 shows the distribution (panels a, c, e) and the temporal evolution (panel b, d, f) of $\overline{u'w'}$, $\overline{v'w'}$, and τ at 180 m. We compare the subgrid (SC+BL) momentum flux from IFS-ctrl with both the 9 km equivalent fluxes from CESAR ($\overline{u'w'}$), and CMTRACE+. The boxplots on the left refer to daytime over the three week campaign period, while the evolutions on the right are for a subset of days. IFS-ctrl is in red, while blue and black are the observations.

The zonal momentum flux is largely overestimated by IFS-ctrl with a mean of -0.2 m^2s^{-2}, which is more than double in magnitude compared to CMTRACE+ and CESAR. The meridional momentum flux is, on average, better captured by IFS, with a mean around -0.08 m^2s^{-2}, but maxima and minima are larger than what observed. IFS-ctrl is overestimating flux profiles more on days where fluxes are generally larger and winds stronger, for example, September 23rd and 24th in Figure 5.11 f. The mean τ is around 0.29 m^2s^{-2} for IFS-ctrl, which is about 0.1 m^2s^{-2} larger than the observed ~0.18 m^2s^{-2}. The model tends to exaggerate the daytime peaks, for example on September 23rd and 24th. The night time hours are excluded from the distribution in panels a,c,e, nevertheless the evolution in panel f shows a too strong (turbulent) momentum flux also at night.
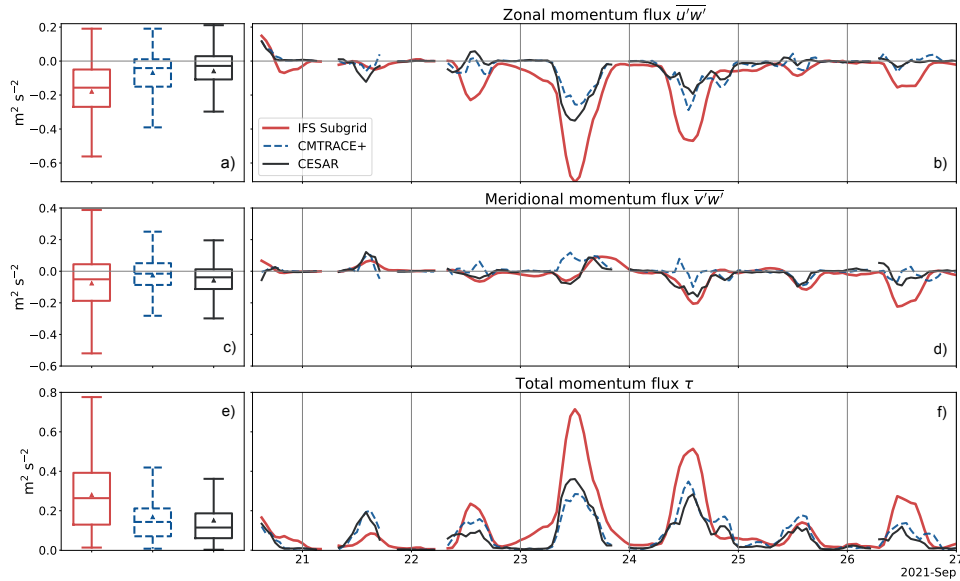
Figure 5.11: Distribution for daytime only (09:00 to 16:00) (a) and temporal evolution for a subset of days (b) of τ. IFS-ctrl subgrid (SC+BL) is in red, CMTRACE+ is in dashed blue, and CESAR is in solid black.

5.7 Clear sky and cloud topped boundary layers

CMTRACE provides a new and promising view into momentum flux profiles beyond the surface layer where we have tower observations. Here, we compare the vertical profiles with the IFS, accepting that CMTRACE does not capture the full range of turbulent scales. In Figure 5.12 we divide the dataset into hours with clear sky (a,b,c) and cloud topped boundary layer (d,e,f). The latter group, which we refer to as cloudy, is defined by hours with more than 5% of the CMTRACE profiles being cloudy, in accordance with Koning et al. (2021). A profile is considered cloudy if clouds are detected between 200 m and 2.5 km; all other profiles are defined as clear sky. Using daytime only, we classify about 59% of the hours as having a cloud topped BL, and 41% as clear sky.

Figure 5.12 shows the mean fluxes from CMTRACE (blue) and the subgrid fluxes from IFS-ctrl (red), which are divided into the contribution from the SC scheme (yellow) and the BL scheme (green). At 100 m and 180 m the grey dots show the fluxes measured by CESAR, down to scales of 0.1 seconds ($\overline{u'w'}, \overline{v'w'}, \tau$). The shaded blue areas indicate the momentum fluxes estimated with the mass-flux approach applied to the CMTRACE dataset (section 5.2.1), which we will review further in section 5.7.1.

Evidently, IFS-ctrl overestimates the momentum fluxes not just in the surface layer, but across the entire depth of the boundary layer, compared to both tower and lidar observations. The BL scheme alone produces more turbulent flux than what measured by the sonic anemometers on the tower. This overestimation is larger for the zonal momentum flux (a, d). The contribution from the BL scheme (green) is largest near the surface and reduces
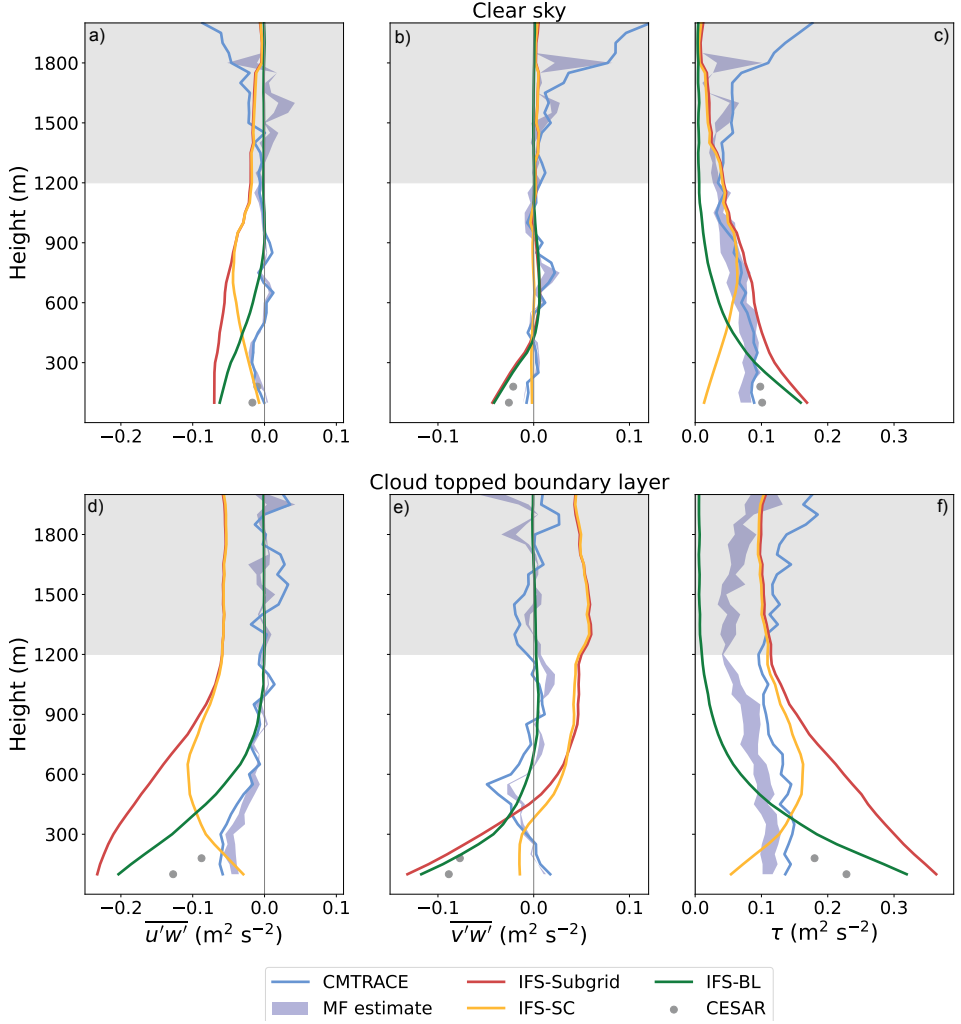
Figure 5.12: Mean profiles of zonal momentum flux (a,d), meridional momentum flux (b,e), and τ (c,f) for hours of less active (top row) and more active convection (bottom row). From IFS-ctrl, the subgrid flux (red) is divided into the SC scheme (yellow) and BL scheme (green). From CMTRACE the measured flux is in solid blue, and the flux estimated with the mass-flux approach is in shaded blue. From CESAR (grey dots) the flux is measured at 100 m and 180 m.

to zero around 900 m for the zonal component and around 500 m for the meridional component (panels b,e). The SC scheme (yellow) introduces fluxes which peak at cloud base, around 600 m in Figure 5.12 d. In the meridional direction (panels b,e), the fluxes from shallow convection are significantly smaller than in the zonal direction.

On average, the contributions from both the BL and SC schemes are smaller for clear sky (Figure 5.12 a,b,c) than for cloudy conditions (Figure 5.12 d,e,f). During hours of clear sky, the negative fluxes from the BL scheme reduce to ~0 m^2s^{-2} about 100 m below those observed during cloudy conditions. The different depth of this turbulent (frictional) layer, is also clearly visible in the total flux τ (panels c and f). Figure 5.12 a,c, shows that the SC scheme produces some momentum flux also on clear sky conditions. This is explained because our distinction into clear sky and cloudy conditions is based on CMTRACE and does not exclude the presence of clouds in IFS. For $\overline{u'w'}$ (panels a,d), the contribution of the SC scheme doubles from clear sky to cloudy, while for $\overline{v'w'}$ the contribution is about zero in clear sky (panel b). On cloudy conditions (panel e), $\overline{v'w'}$ by the SC scheme is negative (~-0.02 m^2s^{-2}) below 300 m, and positive above.

In panel c, between 600 m and 1.1 km, the total subgrid flux from IFS-ctrl is close to the observations, with about 0.1 m^2s^{-2} at 900 m. On the cloudy conditions, the observations show a marginally stronger mean momentum flux at 900 m (~ 0.12 m^2s^{-2}), but IFS-ctrl has a mean of 0.2 m^2s^{-2}, almost double as strong. We could add an estimated 30% extra flux to CMTRACE at higher levels, roughly based on Figure 5.6. This might be an overestimation if we assume that small-scale turbulence is largest near the surface and decreases upward, but could also be a good indication of the turbulent flux that is present by entrainment fluxes. However, this additional flux would still indicate a total momentum flux smaller than what IFS-ctrl produces.

The shape, not just the magnitude, of the momentum fluxes is also an important diagnostic for the transport of momentum. The momentum flux divergence, together with the sign of the wind, determine the wind tendency introduced by the flux. Figure 5.12 shows that, despite the differences in the magnitude of the momentum fluxes, the vertical rate of change of $\overline{u'w'}$ and $\overline{v'w'}$ is similar to what suggested by CESAR below 180 m and by CMTRACE above. For example, in Figure 5.12 b,e the decrease of $\overline{v'w'}$ from 100 m to 180 m is similar in IFS-ctrl and CESAR, despite the latter showing a weaker flux. This suggests that the tendencies appear more strongly constrained than the fluxes.

5.7.1 The mass-flux approach
The shaded blue profiles in Figure 5.12 represent observed momentum fluxes that are derived by mimicking a mass-flux approach. We take 30 min time windows and multiply the mean updraft (downdraft) velocity with the difference in updraft (downdraft) momentum and mean momentum. Essentially, this assumes that the overall momentum flux is a strong function of the total vertical mass flux and the mean anomalous momentum it carries. A lower and an upper vertical velocity threshold (±0.2 and ±0.5 ms^{-1}) is used to identify the updrafts and downdrafts, their difference is represented by the blue shading.

The mass-flux approach is a good representation of the measured momentum flux on hours with clear sky (Figure 5.12 a,b,c). For cloud topped boundary layers (panels d,e,f), the mass-

flux approach underestimates the zonal and total momentum flux by about 20% throughout the lowest 600 m. Above 1 km, there is also an underestimation of the meridional and total momentum flux, but here, we do not have as much representative data (see Figure 5.1).

The underestimation of the momentum flux by the mass-flux estimate can have two reasons: The momentum averaged over updrafts (or downdrafts) may not be representative of the diverse momentum fluctuations carried in individual updrafts. The fact that the direct momentum flux varies between positive and negative fluctuations (see Figure 5.9 a,c) is already evident of that. Another reason may be that fluctuations outside of stronger up- or downdrafts carry non-negligible momentum. Overall, the mass flux approach provides estimates broadly in line with the direct observed fluxes.

5.8 Influence of dry mass-flux of momentum

In the control simulation (IFS-ctrl) analysed so far, the BL scheme represents the transport of horizontal momentum solely through an eddy diffusivity approach, despite heat and moisture are treated with and EDMF approach (see section 5.3). In this section we show the effect of applying EDMF to horizontal momentum too, by adding a dry mass-flux component to the transport of u and v in the BL scheme. With this we aim at including the role of organised dry convection which are large enough to produce non local transport of momentum, but do not reach the liquid condensation level.
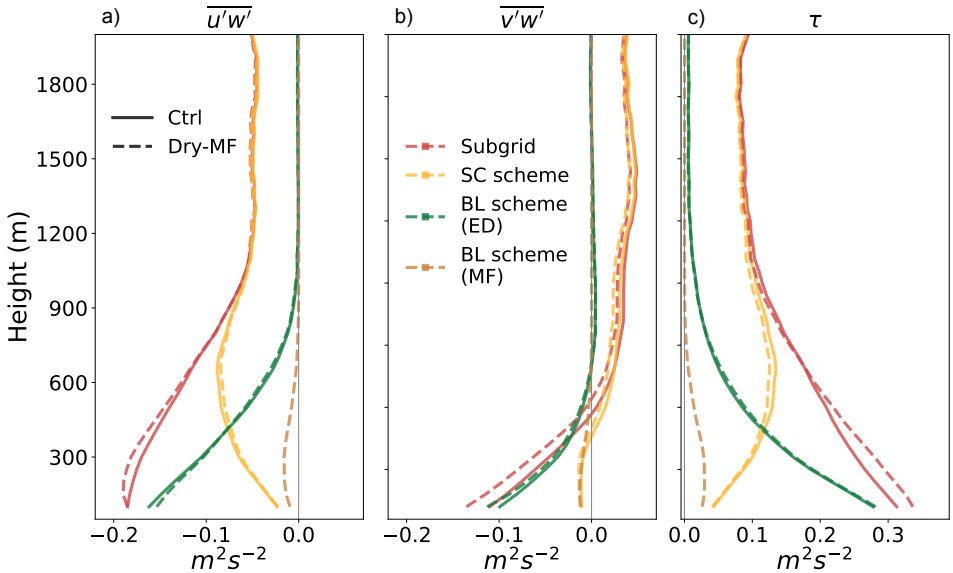
Figure 5.13: Mean profiles of zonal (a), meridional (b), and total (c) momentum flux for the two experiments: IFS-ctrl (solid) and IFS-dryMF (dashed). Red is for the combined subgrid fluxes, yellow for the SC scheme, green for the ED component of the BL scheme, brown for the MF component of the BL scheme.

One hypothesis for the too large sub-cloud layer momentum flux in the IFS is that the model misses some source of mixing. As a result, the model could maintain too large wind

shear. This is in line with the overestimation of zonal wind and larger sub-cloud layer wind shear in the lowest hundreds of meters (Figure 5.5). This would produce turbulent fluxes by the eddy-diffusivity scheme that are larger than observed.

Figure 5.13 shows the mean daytime momentum fluxes for the IFS-ctrl (solid) and for the IFS-dryMF, with active dry mass-flux (dashed). The MF component in the BL scheme (dashed brown) adds a small parabolic flux in the subcloud layer of the IFS-dryMF experiment. Such a flux profile would accelerate winds below 300 m, while decelerating winds between 300 m and cloud base. The magnitude of this additional flux is rather small, and hence, neither the SC scheme (yellow) nor the ED component of the BL scheme (green) change sensibly from IFS-ctrl (solid). The result is a net increase of the overall subgrid flux below 600 m, for both the zonal and meridional components. This brings the subgrid fluxes further away from observations, suggesting a deterioration of the flux forecast.

While the differences in fluxes are small, we do observe that the too strong westerly wind bias reduces in IFS-dryMF. At the same time, this makes the weak wind speed bias more pronounced in IFS-dryMF. This is shown in Figure 5.14 a and c, where red indicates the distribution of the wind bias for IFS-ctrl and blue for IFS-dryMF.
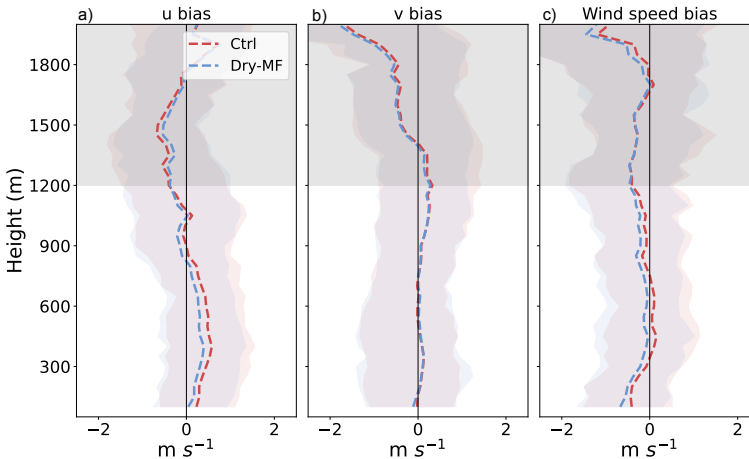
Figure 5.14: Distribution of the bias (IFS - CMTRACE) for zonal wind (a), meridional wind (b), and wind speed (c). The shaded area indicates the interquartile, while the dashed line indicates the mean. Red refers to the IFS-ctrl, blue refers to IFS-dryMF.

A possible explanation for the small difference between IFS-ctrl and IFS-dryMF is that the erroneous source of mixing is concentrated near the mixed layer top or near cloud base. Above 600 m, the dry mass-flux (brown dashed in Figure 5.13) does not add any flux, but between 600 m and 900 m, the moist MF (SC scheme) is causing too large zonal and meridional momentum fluxes (yellow lines in Figure 5.13). This creates a strong acceleration over the layer 0 to 600 m (negative flux increases with height), and strong deceleration between 600 and 900 m (negative flux decreases with height). To compensate for the acceleration in the lowest 600 m, the model can only create stronger turbulent flux

divergence (green lines in Figure 5.13).

5.9 Discussion and conclusions

This study is the first to make use of direct measurements of momentum flux profiles, from near-surface to cloud top, for an evaluation of the subgrid momentum transport in IFS. We find up to twice as much momentum flux in IFS than in the observations throughout the boundary layer, and we suggest that the root of the erroneous mixing lies near cloud base. This is supported by Figure 5.12, as errors increase when convection becomes more active. Observed momentum fluxes at scales between 500 m and 9 km are small above 600 m because the fluctuations u' and v' are not well correlated with w'. Instead, momentum fluxes from the moist mass-flux and eddy diffusivity of IFS are too strong.

A possible explanation for the weak observed momentum flux is that convective plumes are embedded in mesoscale circulations with converging winds in the ascending branches. This coupling with mesoscale circulations is important at convection-permitting resolutions (Vogel et al., 2022). Convective heating at cloud base drives upward flow, which drives a local pressure low, that can trigger horizontal inflow (Zhang and Cho, 1991). Because of this pressure gradient, momentum is not well conserved inside the plume. Thus, the additional mesoscale flow components could give the plume a less distinct momentum flux signature.

The CMTRACE dataset only partly addresses this hypothesis, as it misses the turbulent momentum flux at scales smaller than 500 m. This may be very pronounced near cloud top, in the entrainment zone (de Rooy et al., 2013). Such a flux reduces the vertical gradient of the turbulent momentum flux, which would then result in less flux divergence. Adding such a flux could bring the profiles of CMTRACE closer to IFS in Figure 5.10.

Despite this limitation CMTRACE, gives new insights on how momentum flux looks in a convective boundary layer. The CMTRACE field campaign (Dias Neto et al., 2023), which took place at Cabauw between September 13th and October 3rd 2021, used a novel scanning technique to retrieve high resolution (1 minute) wind profiles. A collocated wind cube lidar and two cloud radars were programmed to point vertically and retrieve one profile of vertical velocity at the end of every horizontal scan. The relatively high-frequency of the measurements allows to apply the eddy covariance method to the CMTRACE dataset similar to what is done with sonic anemometers.

During the campaign, daytime shallow convection dominates the vertical transport, but near-surface winds up to 20 ms^{-1} also drive significant small scale turbulent mixing, especially in the second half of the campaign. The horizontal winds are well captured by IFS, despite a weak wind bias of about 0.5 ms^{-1} in the lower 300 m, and a too westerly component between 100 m and 800 m. Both our observational datasets (CMTRACE and CESAR) agree well on the evolution and magnitude of the winds at 180 m.

For a comparison of the observational datasets, we coarsened CESAR to 1 minute and recomputed the eddy covariance. The mean distance between the momentum flux observed by CMTRACE τ and by the coarsened CESAR $\widetilde{\tau}$ is close to zero, with an interquartile range of ± 0.04 m^{2}s^{-2}. This gives confidence about the scanning technique capturing the right

correlation between horizontal and vertical wind anomalies with just a single vertical velocity profile per minute. With an increasingly coarser CESAR dataset we estimate how different scales contribute to the momentum fluxes over a 30 min time window (equivalent to the 9 km grid box of IFS). At 180 m, the flux captured with 1 minute resolution is about 70% and 75% of the total, for zonal and meridional momentum flux respectively.

IFS overestimates the momentum flux τ with differences between hours of clear sky and cloud topped boundary layer. On clear sky conditions the combined transport by the SC and BL schemes is in the same ballpark as the observations, with τ being about 0.1 m^2s^{-2} between 600 m and 1.1 km. During cloudy conditions, the SC scheme alone produces fluxes that exceed observed values, with twice as strong fluxes for the zonal component, at cloud base. The SC scheme of IFS is based on the mass-flux approach, which we evaluate applying the same method to the measured winds. The observational estimate of mass-flux captures most of the measured momentum flux on clear sky conditions, but misses about 10% at all levels when clouds are present.

With the IFS-dryMF experiment we aimed at improving the physical representation of dry organised plumes in the subcloud layer. We added a dry mass-flux component to the momentum transport in the BL scheme. The result is a larger subgrid flux, but no sensible compensating response from the SC scheme nor the eddy diffusivity component of the BL scheme. In the IFS-dryMF experiment the zonal wind bias reduces and halves below 800 m, while the total wind speed bias worsens.

With increasing resolutions and models operating in the grey zone of shallow convection, the correct partition between parameterised and resolved fluxes becomes crucial for accurate wind estimates. The spatial organisation of clouds is also bound to a realistic representation of the subgrid momentum fluxes. Previous studies (Vial et al., 2016; Vogel et al., 2022, e.g.) showed that the coupling between clouds and circulations is directly linked to parameterised fluxes.

Further improvements in measuring momentum fluxes are expected from a campaign with two collocated wind cube lidars: one scanning and retrieving u and v, while the second always vertically pointing to retrieve w at high resolution. Further insights are expected by complementing the set of data with large eddy simulations of the region around Cabauw. With a large enough domain, such simulations will allow to address the role of mesoscale flows on the momentum flux.

DATA AVAILABILITY
The observational data used in this study were gathered in the CMTRACE 2021 field campaign. We used Version 1.0.0 of the level 2 dataset, publicly available (Dias Neto, 2022). The raw sonic anemometer dataset is available on request, while the validated 10 minute resolution CESAR data is available at https://dataplatform.knmi.nl/dataset/cesar-tower-meteo-lb1-t10-v1-2 . The data for the IFS experiments are available on request.

6

Conclusions

"[…]
tra le rossastre nubi
stormi d'uccelli neri
com'esuli pensieri,
nel vespero migrar."
- Giosuè Carducci -

6

6.1 Research questions

This thesis is motivated by the recognition that shallow cumulus clouds are more than passive tracers and actively shape not only the heat and moisture profiles, but also the circulations (winds) that help set the structure of cloudiness and precipitation. The importance of shallow convection (SC) for its mixing effect of momentum has been recognised for many years (Siebesma and Cuijpers, 1995; Tiedtke, 1989). However, recent studies of convective momentum transport (CMT) in idealised simulations (Dixit et al., 2021; Helfer et al., 2021), raised questions on the dependence and influence of CMT on cloud organisation. Shallow convection at the mesoscales is rich and complex, characterised by cloud structures and organisations that cannot be captured by idealised simulations of simple cases (Nuijens and Siebesma, 2019).

The key question guiding this thesis is:

How does CMT influence and depend on organised shallow cumulus fields?

New observations from the EUREC4A and CMTRACE 2021 field campaigns provided insightful context for a hierarchy of simulations that we carried out to answer this question. EUREC4A took place between January and February 2020 over the North Atlantic Ocean, east of Barbados. Among its many contributions, it provided measurements of mesoscale convergence, which enabled retrieving mesoscale wind tendency profiles and constructing the observed momentum budget (Nuijens et al., 2022). This was achieved through the deployment of over 1,200 dropsondes along a circular flight pattern with a 220 km diameter: the EUREC4A circle (George et al., 2021b).

CMTRACE 2021 was conducted around Cabauw (The Netherlands), where a 200 m tower is equipped with sonic anemometers at 5 m, 60 m, 100 m and 180 m, measuring high frequency winds and momentum fluxes. For three weeks during the summer of 2021, a collocated wind lidar and two cloud radars provided, for the first time, direct measurements of the three wind components (u, v, w) throughout the boundary layer, with a minimum resolution of 1 minute (~500 m). This allowed us to compute momentum fluxes and study turbulent momentum transport across scales, from sub-kilometre to mesoscales.

The majority of the research presented in this thesis (Chapters 2, 3, and 4) focuses on EUREC4A, modelling the observed atmospheric state with LES and NWP models. The domain of interest is consistently centred on the EUREC4A circle. However, we use a hierarchy of models with different domain sizes, resolutions, and temporal extents, to meet the specific requirements of each study.

We quantified the tropospheric wind bias of the global Integrated Forecasting System (IFS) of the ECMWF during EUREC4A. We reproduced these complex atmospheric conditions with the Dutch Atmospheric Large Eddy Simulation (DALES), to reveal the relationship between cloud organisation and the contribution of different scales to the turbulent convective momentum flux. With the mesoscale model HARMONIE-AROME, we tested our ability to simulate shallow convection on the kilometre-scale, and we investigated the influence of SC and its transport, specifically that of momentum, on the mesoscale flow and cloud organisation. Lastly, we complement what we learned about CMT from EUREC4A with a study focusing on the CMTRACE campaign, where we directly compared

the sub-grid momentum fluxes in IFS with novel measurements of the momentum fluxes. This hierarchical model framework bridged the sub-kilometre scales and the mesoscales, capturing their interactions in various atmospheric regimes, from trade cumuli above the warm tropical North-Atlantic Ocean to summer convection over land in The Netherlands.

Below we summarise the methods and the research questions, while the key findings of the thesis are presented in section 6.2. In section 6.3, we offer a perspective into the future of parameterised momentum transport in shallow convective environments.

In **Chapter 2**, we used dropsondes, radiosondes, and lidar measurements from the EU-REC4A field campaign to assess the lower tropospheric wind bias in medium-range forecasts and reanalyses produced with the IFS. The origin of the wind bias was also explored using model experiments with two different versions of the moist convection parameterisation, and a model experiment with inactive momentum transport by parameterised SC. Previous studies (Sandu et al., 2020) showed a persistent wind bias at the surface but only hypothesised a link with the sub-grid momentum transport. We focused on EUREC4A and investigated wind profiles extending up to 5 km height. This study was the first to use observational vertical profiles of wind fields over ocean for such an extended period of time and from multiple instruments.

In Chapter 2 we addressed the following questions:

a) How can various wind profiling observations be combined to investigate the temporal variability of wind bias in operational ECMWF high-resolution deterministic forecasts (approximately 9 km at the Equator)?

b) How is the wind bias different between reanalyses, and forecasts?

c) To what extent does the assimilation of observations from EUREC4A improve the reanalyses and forecasts performed with the IFS?

d) How do different wind tendencies (sub-grid and resolved) play a role in the wind bias?

In **Chapter 3** we focused on a subdomain and a subset of days within EUREC4A. With the Dutch Atmospheric Large Eddy Simulation (DALES), we simulated an area spanning 150 x 150 km^2 for 9 days. The simulations we carried out here had realistically varying large-scale forcing and used a domain much larger than that of previous LES studies (e.g. Helfer et al., 2021), capturing multiple degrees of cloud organisation.

In Chapter 3 we addressed the following questions:

a) Which scales contribute to momentum fluxes throughout the boundary layer?

b) How do scale contributions change as the cloud field organises?

c) How are different scales contributing to the momentum flux divergence?

In **Chapter 4** we evaluated how the cloud field and the mesoscale circulations respond to either parameterised or explicit shallow convection and CMT in the mesoscale model HARMONIE-AROME. With a horizontal grid spacing of 2.5 km, we simulated an area of 3200 x 2025 km^2 that encompasses the domains studied in Chapter 2 and Chapter 3,

from 1 January to 29 February 2020. We performed three experiments with different representations of shallow convection: 1) one with a fully active SC parameterisation, 2) one without momentum flux by SC parameterisation, 3) one with a deactivated SC parameterisation. This allowed us to explore the extent to which, with a grid spacing of 2.5 km, shallow convective transport can be represented by the combination of just an eddy-diffusivity parameterisation and resolved dynamics.

More specifically, in Chapter 4 we addressed the following questions:

a) How do low-level cloudiness and mesoscale circulations depend on the presence (or absence) of parameterised transport of heat, moisture, and momentum by shallow convection?

b) Which experimental setup brings us closer to the observed cloud fields?

Lastly, in **Chapter 5** we used wind measurements from the CMTRACE 2021 field campaign. These measurements of momentum flux through the full boundary layer depth across three weeks of varying cloud fields, allowed us a first glance at how momentum flux behave in real nature, in the presence of complex cloud fields. We evaluated the sub-grid momentum fluxes in the most recent IFS cycle (49r1) and we assessed the role of parameterised dry convection in the sub-cloud layer.

In Chapter 5 we addressed the following questions:

a) What scales of momentum flux are captured by the wind lidar?

b) How does the profile of momentum flux vary during daytime and with wind speed?

c) What role does parameterised dry mass flux play in momentum transport within the sub-cloud layer?

6.2 Main conclusions

Before summarising the findings addressing the many questions explored throughout this thesis, we present a short answer to the key question: How does CMT influence and depend on organised shallow cumulus fields?

By strengthening mesoscale overturning circulations, CMT is crucial in modulating wind speed and direction throughout the lower troposphere, as well as in controlling cloud organisation. In particular, sub-kilometre scales are most responsible for CMT, but stronger mesoscale circulations translate to larger contributions from the mesoscales and more organised cloud fields.

Chapter 2 shows that the wind biases in the IFS forecast are not just at the surface, but extend throughout the troposphere, with the largest bias and RMSE in wind speed at 3 km, with an underestimation of about 1 m s^{-1} and RMSE of about 2 m s^{-1}. This mean bias is the result of large positive and negative errors, up to 4 m s^{-1} that can partly compensate over time. The wind bias in the sub-cloud layer exhibits a diurnal cycle just like the wind speed itself. Both forecast and reanalysis overestimate the amplitude of the diurnal cycle, but only the reanalysis captures the phase of the cycle. This diurnality is overestimated

by the IFS, with too weak winds during the day and too strong winds during the night, particularly in the forecasts.

The wind bias is not very sensitive to the assimilation of local wind information, and is well constrained through large-scale dynamics. Instead, the wind bias is explained by biases in the parameterised momentum tendencies, which were measured (as a residual) on the EUREC4A circle. Parameterised momentum tendencies in the model are active in the lowest 1.5 km in the zonal direction, where the parameterised diffusivity component appears too large, compensated by too strong resolved tendencies. Above 2 km, the parameterised tendencies in the IFS miss a significant acceleration of winds that translates to the weak-wind bias observed at that height. Large-scale dynamics, influenced by equatorial deep convection, also contribute to the bias, which reduces from the model cycle 47r2 to cycle 47r3.

In **Chapter 3** we find that momentum fluxes vary significantly on mesoscales, with compensating positive and negative values. This variability is observed on scales between 100 m and 150 km. The dominant scales contributing to the total momentum transport are larger in the cloud layer than in the sub-cloud layer, where small eddies carry most of the momentum flux. In the cloud layer, the contribution of mesoscales to heat and moisture fluxes is generally comparable to momentum fluxes. However, in the sub-cloud layer, this contribution is smaller for momentum than for heat and moisture fluxes, because turbulent wind stresses dominate.

The multitude of atmospheric conditions simulated in Chapter 3 show that the partitioning of the flux among scales is highly variable. For example, scales smaller than 2.5 km (the grid spacing of HARMONIE-AROME) account for between 20% and 90% of the total momentum flux, with an average of 80%. This variability cannot be explained by the boundary layer height, as suggested by Honnert et al. (2011). Instead, we suggest the importance of a system's horizontal scale, and demonstrate how cloud organisation explains the flux partitioning among scales. We quantify cloud organisation with the metric I_{org} (Weger et al., 1992) and show that the contribution of mesoscales to the momentum flux increases as the cloud field organises.

We find that deeper and more organised convection is associated with weaker winds near the surface and less shear in the cloud layer. These conditions are also more favourable for counter-gradient momentum transport, similar to what is known for deep convection (Moncrieff, 1981), as coherent structures generate stronger in-cloud pressure gradients. In organised cloud fields, the turbulent momentum flux is responsible for a significant acceleration of the zonal wind in the upper cloud layer, in line with what observed also in Chapter 2. This acceleration, missed by IFS, is mostly introduced by scales larger than 2 km, suggesting the potential role of mesoscale circulations or gravity waves.

Mesoscale circulations are clearly visible in our DALES simulations. These shallow mesoscale overturning circulations (SMOCs; George et al. (2021a)) are hypothesised to be internally driven by convection, whose heating anomalies drive ascent that helps aggregate moisture into already moist areas and drives the growth of convective areas to mesoscales (Bretherton and Blossey, 2017; Janssens et al., 2022). In other words, shallow cumuli, just like deep cumuli, are strongly coupled to accompanying horizontal circulations that have

scales several times the boundary layer depth. Principally, such circulations should be resolved by models with a grid spacing small enough to resolve cloud clusters with length scales of a few kilometres.

This is explored in **Chapter 4**, where we test the influence of the shallow convective parameterisation (SCP) on SMOCs and cloud organisation. The horizontal grid spacing of 2.5 km in HARMONIE-AROME is fine enough to resolve the larger shallow convection, but too coarse to represent smaller eddies, especially active in the sub-cloud layer. In this grey zone of shallow convection, we demonstrate that a SCP is still necessary, but it may be too strong in its current formulation (as shown in Chapter 5).

In Chapter 4 we show how SCP dampens mesoscale circulations in the km-scale storm-resolving model HARMONIE-AROME. Without SCP, there is more buoyancy available, which sustain more vigorous vertical velocities. This deepens the cloud layer, with few clouds showing higher cloud tops. As a result, clouds become more numerous, but smaller, and they organise less. The stronger mixing in the cloud layer introduced by more resolved SC (the experiment without SCP) weakens the trade-inversion, translating to larger cloud cover near cloud base, but smaller cloud cover near cloud top, as a weaker inversion reduces the amount of stratiform clouds.

When turning off only the momentum transport by parameterised SC, the thermodynamic environment is not significantly affected, but cloudiness below the inversion and wind variance at mesoscales increase. In this case, the missing parameterised CMT in the sub-cloud layer is compensated by the parameterised eddy diffusivity scheme, while in the cloud layer this compensation is done by the resolved dynamics. This results in larger and stronger SMOCs. Without parameterised momentum transport by SC, the zonal wind (the dominant component) accelerates near cloud base, while surface winds weaken. This response is similar in IFS (Chapter 2), where removing the momentum mixing by SCP reduces the surface wind bias but produces a too strong zonal wind jet near cloud base.

Using the LES results from Chapter 3, we also conclude that, in HARMONIE-AROME, the partitioning between resolved and sub-grid fluxes is unbalanced, when SCP is inactive. According to LES, a grid spacing of 2.5 km (as in HARMONIE-AROME) should resolve less than 40% of the total heat and moisture fluxes in the cloud layer. However, this percentage exceeds 80% when the SCP is inactive in HARMONIE-AROME.

Clearly, a parameterisation for SC is needed in HARMONIE-AROME (Chapter 4) and in IFS (**Chapter 5**), where the grid spacing is 9 km. In this grey-zone of shallow convection, models should be informed by observations or LES to determine which part of the flux should be parameterised and which should be resolved (Honnert, 2019). We address this with LES in Chapter 3 and with novel observations in Chapter 5, where we find that the current mass-flux formulation is too active and produces too much sub-grid momentum flux in the IFS.

The novel measurements of momentum flux profiles from the CMTRACE 2021 campaign capture scales of 500 m and larger. We compute the convective scale motions (up to ~ 9 km) by averaging over 10 minutes. At these scales, observed momentum fluxes can be both positive and negative, so that the average over several hours often reduces to

zero. A possible explanation for this is the development of a local low pressure in the ascending branch of the circulations. Because of this pressure gradient, momentum is not well conserved inside the plume.

Momentum fluxes from CMTRACE 2021 are in line with the (coarsened) turbulent fluxes from sonic anemometers at 100 m and 180 m. Although the measurements can reach up to ~2 km, there is only limited data above 1.2 km, restricting our analysis to below this level. The observations, despite their limitations, reveal excessive momentum fluxes in IFS. Errors increase as convection becomes more active, suggesting that the root of the erroneous mixing lies in the moist mass-flux contribution, particularly near the cloud base, where the strength of the convective updrafts is determined.

The dry mass-flux component is not transporting momentum by default in IFS, but even when activated, the model does not show a sensible compensating response in the moist mass-flux nor in the eddy diffusivity components. The effect of adding a dry mass-flux for momentum is a net increase in sub-grid momentum fluxes in the sub-cloud layer. This changes the shape of the momentum flux profiles, thus of the momentum tendencies. On average, with an active dry mass-flux for momentum, zonal winds weakens below 800 m.

6.3 RECOMMENDATIONS

This thesis, along with the wealth of recent studies exploring the interaction between shallow convection and circulations, has greatly benefited from novel observational datasets and advances in computational capabilities. Significant opportunities remain to leverage these resources further in understanding convective momentum transport. However, more sophisticated experimental modelling frameworks and new observations are still required before we can accurately represent momentum transport in the next generation of turbulence and convection parameterisations.

Some of the questions that remain to be answered are:

1. How does local scale momentum transport influence large-scale winds and circulations?

2. What sets the diurnal cycle of the wind speed and direction in the trades?

3. How should a parameterisation for CMT account for the pressure gradients developing within the convection?

4. How should a parameterisation of CMT account for the degree of spatial organisation?

The multi-model framework (IFS, HARMONIE, DALES) employed in this thesis has demonstrated significant advantages when combined with observations from the EUREC4A campaign. However, it has also provided valuable insights, revealing opportunities for improvement in future applications. For example, the recently implemented open boundary conditions in DALES offer several advantages in studying momentum transport (Liqui Lung et al., 2024). Open boundary conditions can enhance the realism of large-scale flow, aiding in understanding its influence on mesoscale and sub-mesoscale dynamics.

The sensitivity to external forcing remains a limit of LES as long as global domains remain unfeasible. Global kilometre-scale simulations are available (Stevens et al., 2019) but are still not enough to fully resolve shallow convection. Multi-day global LES with sub-kilometre resolution are still far from being available, but they would allow for a precise coupling of the small and the large-scales, thus assessing how shallow convection can feedback into the large-scale. Despite this, it is arguable whether such pharaonic simulations are needed.

Several pressing question around momentum transport can still be answered with cheaper, yet ambitious, experimental setups. For example, LES domains spanning the size of the Hadley cell in the latitude direction (0° N to 30° N) and covering both land and ocean in the longitude direction (70° W to 30° W), would allow to address the influence of equatorial deep convection on the trade-wind bias. One hypothesis is that the diurnal cycle of equatorial deep convection over land determines the diurnal cycle of the trade winds by establishing a large-scale pressure gradient.

Badlan et al. (2017) showed that the momentum budget in deep convective systems is sensitive to the development of local horizontal pressure gradients, which arise only when convection and the circulations associated with it are well resolved. LES with open boundaries and domains of a few hundreds of kilometres would be enough to allow the development of more pronounced horizontal circulations. This could shed light on the role of pressure gradients in the momentum budget of shallow convection. A hope is that such simulations could help explain the origin of the observed turbulent flux near cloud tops, perhaps by uncovering the presence of gravity waves generated by some of the deeper shallow convection.

Mesoscale models offer another valuable platform for further exploration of convective momentum transport without requiring substantial additional resources. Since developing the next generation of parameterisations for boundary layer transport may involve a degree of iterative refinement, mesoscale models provide an excellent framework for testing and optimising these formulations. In particular, as the role of dry and moist convection can be readily disentangled in HARMONIE-AROME, future investigations should consider experiments that disable momentum transport by moist mass-flux while retaining the dry mass-flux component. Such an approach would push the model towards resolving more shallow convection, as discussed in Chapter 4, while preserving some sub-grid non-local momentum transport within the sub-cloud layer.

Building on the findings of this thesis, which emphasise the critical role of cloud organisation in shaping momentum fluxes, the Royal Netherlands Meteorological Institute (KNMI) is exploring the use of vertical velocity as a scaling parameter for the intensity of parameterised fluxes by shallow convection. However, different proxies, like rain rate, should also be explored, as vertical velocity is poorly defined in models and it is difficult to constrain with observations. Stochastic convection schemes (Lin and Neelin, 2002) offer an additional promising approach to better inform the SCP regarding sub-grid variability.

Addressing the partitioning between the turbulence scheme and convection scheme is also becoming urgent, as mesoscale models operate at increasingly fine resolutions. Scale aware parameterisations (Tiedtke, 1989) offer a possible solution to modelling the atmosphere in the grey zone of shallow convection, under different degrees of organisation.

A combination of observations and LES often yield the best results in informing model development. Observations can be expensive to deploy over large areas, limited in spatial coverage, and sensitive to instrument errors or calibration. Nevertheless, they offer significant advantages over LES. Observations include all scales of motion present in the atmosphere reflecting the true interplay of processes like convection, turbulence, meso- and large- scale dynamics. Observation are also free from assumptions, such as the boundary conditions, and provide samples across realistic environments.

Measuring turbulent momentum fluxes has long been a challenging task. However, the CMTRACE 2021 field campaign enabled comprehensive measurements of these fluxes throughout the boundary layer. A follow-up to the CMTRACE 2021 field campaign, namely CMTRACE 2022, features wind measurements with temporal resolution finer than 1 minute. Two wind lidars, one vertically pointing and the other scanning, enhanced sampling of the vertical wind component w, thus making possible a more accurate computation of momentum fluxes at higher frequencies.

Some limits remain in this way of measuring momentum fluxes, where the scanning lidar draws an upside down cone. The tilt allows to measure horizontal wind components, but implies that the measurements are averaged over an area that increases with height. Furthermore, the resolution is constrained by the time it takes for the lidar to perform a scan, which will never allow to capture eddies smaller than a few hundred meters, even near the surface. A way of overcoming such limits is under evaluation as part of the STRINQS-ORCESTRA campaign, where a sonic anemometer was mounted on a drone to profile winds and fluxes at high resolution (~ 0.1 second).

6

Bibliography

References

Agee, E. M. (1987). Mesoscale cellular convection over the oceans. *Dynamics of Atmospheres and Oceans*, 10(4):317–341.

Agee, E. M., Chen, T. S., and Dowell, K. E. (1973). A review of mesoscale cellular convection. *Bulletin of the American Meteorological Society*, 54.

Arakawa, A. (1969). Parameterization of cumulus convection, Proc. WMO/IUGG symposium on Numerical Weather Prediction in Tokyo. *Japan Meteor. Agency*, 0:8–1, 8–6.

Arakawa, A. (2004). The Cumulus Parameterization Problem: Past, Present, and Future. *Journal of Climate*, 17(13):2493–2525. Publisher: American Meteorological Society Section: Journal of Climate.

Arakawa, A., Jung, J.-H., and Wu, C.-M. (2011). Toward unification of the multiscale modeling of the atmosphere. *Atmospheric Chemistry and Physics*, 11(8):3731–3742. Publisher: Copernicus GmbH.

Arakawa, A. and Schubert, W. H. (1974). Interaction of a Cumulus Cloud Ensemble with the Large-Scale Environment, Part I. *Journal of the Atmospheric Sciences*, 31(3):674–701. Publisher: American Meteorological Society Section: Journal of the Atmospheric Sciences.

Atkinson, B. W. and Wu Zhang, J. (1996). Mesoscale shallow convection in the atmosphere. *Reviews of Geophysics*, 34(4):403–431. _eprint: https://onlinelibrary.wiley.com/doi/pdf/10.1029/96RG02623.

Badlan, R. L., Lane, T. P., Moncrieff, M. W., and Jakob, C. (2017). Insights into convective momentum transport and its parametrization from idealized simulations of organized convection. *Quarterly Journal of the Royal Meteorological Society*, 143(708):2687–2702. _eprint: https://onlinelibrary.wiley.com/doi/pdf/10.1002/qj.3118.

Bechtold, P., Cuijpers, J. W. M., Mascart, P., and Trouilhet, P. (1995). Modeling of Trade Wind Cumuli with a Low-Order Turbulence Model: Toward a Unified Description of Cu and Se Clouds in Meteorological Models. *Journal of the Atmospheric Sciences*, 52.

Bechtold, P., Forbes, R., Sandu, I., Lang, S., and Ahlgrimm, M. (2020). A major moist physics upgrade for the IFS. Pages: 24-32 Section: Meteorology.

Bechtold, P., Sandu, I., Klocke, D., Semane, N., Ahlgrimm, M., Beljaars, A., Forbes, R., and Rodwell, M. (2014a). The role of shallow convection in ECMWF's integrated forecasting system. Number: 725 Pages: 27.

Bechtold, P., Semane, N., Lopez, P., Chaboureau, J.-P., Beljaars, A., and Bormann, N. (2014b). Representing Equilibrium and Nonequilibrium Convection in Large-Scale Models. *Journal of the Atmospheric Sciences*, 71(2).

Becker, T., Bechtold, P., and Sandu, I. (2021). Characteristics of convective precipitation over tropical Africa in storm-resolving global simulations. *Quarterly Journal of the Royal Meteorological Society*, 147(741):4388–4407. _eprint: https://onlinelibrary.wiley.com/doi/pdf/10.1002/qj.4185.

Belmonte Rivas, M. and Stoffelen, A. (2019). Characterizing ERA-Interim and ERA5 surface wind biases using ASCAT. *Ocean Science*, 15(3):831–852. Publisher: Copernicus GmbH.

Bengtsson, L., Andrae, U., Aspelien, T., Batrak, Y., Calvo, J., Rooy, W. d., Gleeson, E., Hansen-Sass, B., Homleid, M., Hortal, M., Ivarsson, K.-I., Lenderink, G., Niemelä, S., Nielsen, K. P., Onvlee, J., Rontu, L., Samuelsson, P., Muñoz, D. S., Subias, A., Tijm, S., Toll, V., Yang, X., and Koltzow, M. O. (2017). The HARMONIE AROME Model Configuration in the ALADIN HIRLAM NWP System. *Monthly Weather Review*, 145(5):1919–1935. Publisher: American Meteorological Society Section: Monthly Weather Review.

Bengtsson, L., Böttger, H., and Kanamitsu, M. (1982). Simulation of hurricane-type vortices in a general circulation model. *Tellus*, 34(5):440–457. _eprint: https://onlinelibrary.wiley.com/doi/pdf/10.1111/j.2153-3490.1982.tb01833.x.

Beucher, F., Couvreux, F., Bouniol, D., Faure, G., Favot, F., Dauhut, T., and Ayet, A. (2022). Process-oriented evaluation of the oversea AROME configuration: Focus on the representation of cloud organisation. *Quarterly Journal of the Royal Meteorological Society*, 148(749):3429–3447. _eprint: https://onlinelibrary.wiley.com/doi/pdf/10.1002/qj.4354.

Boing, S. J., Siebesma, A. P., Korpershoek, J. D., and Jonker, H. J. J. (2012). Detrainment in deep convection. *Geophysical Research Letters*, 39(20). _eprint: https://agupubs.onlinelibrary.wiley.com/doi/pdf/10.1029/2012GL053735.

Bony, S. and Dufresne, J.-L. (2005). Marine boundary layer clouds at the heart of tropical cloud feedback uncertainties in climate models. *Geophysical Research Letters*, 32(20). _eprint: https://onlinelibrary.wiley.com/doi/pdf/10.1029/2005GL023851.

Bony, S., Schulz, H., Vial, J., and Stevens, B. (2020a). Sugar, Gravel, Fish, and Flowers: Dependence of Mesoscale Patterns of Trade-Wind Clouds on Environmental Conditions. *Geophysical Research Letters*, 47(7):e2019GL085988. _eprint: https://onlinelibrary.wiley.com/doi/pdf/10.1029/2019GL085988.

Bony, S., Semie, A., Kramer, R. J., Soden, B., Tompkins, A. M., and Emanuel, K. A. (2020b). Observed Modulation of the Tropical Radiation Budget by Deep Convective Organization and Lower-Tropospheric Stability. *AGU Advances*, 1(3):e2019AV000155. _eprint: https://onlinelibrary.wiley.com/doi/pdf/10.1029/2019AV000155.

Bony, S., Stevens, B., Frierson, D. M. W., Jakob, C., Kageyama, M., Pincus, R., Shepherd, T. G., Sherwood, S. C., Siebesma, A. P., Sobel, A. H., Watanabe, M., and Webb, M. J. (2015). Clouds, circulation and climate sensitivity. *Nature Geoscience*,

8(4):261–268. Bandiera_abtest: a Cg_type: Nature Research Journals Number: 4 Primary_atype: Reviews Publisher: Nature Publishing Group Subject_term: Atmospheric dynamics;Climate change;Climate-change policy Subject_term_id: atmospheric-dynamics;climate-change;climate-change-policy.

Bougeault, P. (1981). Modeling the Trade-Wind Cumulus Boundary Layer. Part I: Testing the Ensemble Cloud Relations Against Numerical Data. *Journal of the Atmospheric Sciences*, 38.

Boutle, I. A., Eyre, J. E. J., and Lock, A. P. (2014). Seamless Stratocumulus Simulation across the Turbulent Gray Zone. *Monthly Weather Review*, 142(4):1655–1668. Publisher: American Meteorological Society Section: Monthly Weather Review.

Brast, M., Schemann, V., and Neggers, R. A. J. (2018). Investigating the Scale Adaptivity of a Size-Filtered Mass Flux Parameterization in the Gray Zone of Shallow Cumulus Convection. *Journal of the Atmospheric Sciences*, 75(4):1195–1214. Publisher: American Meteorological Society Section: Journal of the Atmospheric Sciences.

Bretherton, C. S. and Blossey, P. N. (2017). Understanding Mesoscale Aggregation of Shallow Cumulus Convection Using Large-Eddy Simulation. *Journal of Advances in Modeling Earth Systems*, 9(8):2798–2821. _eprint: https://onlinelibrary.wiley.com/doi/pdf/10.1002/2017MS000981.

Bretherton, C. S., Blossey, P. N., and Khairoutdinov, M. (2005). An Energy-Balance Analysis of Deep Convective Self-Aggregation above Uniform SST. *Journal of the Atmospheric Sciences*.

Brient, F., Schneider, T., Tan, Z., Bony, S., Qu, X., and Hall, A. (2016). Shallowness of tropical low clouds as a predictor of climate models' response to warming. *Climate Dynamics*, 47(1):433–449.

Brown, A. R. (1999). Large-Eddy Simulation and Parametrization of the Effects of Shear on Shallow Cumulus Convection. *Boundary-Layer Meteorology*, 91(1):65–80.

Brown, A. R., Beljaars, A. C. M., and Hersbach, H. (2006). Errors in parametrizations of convective boundary-layer turbulent momentum mixing. *Quarterly Journal of the Royal Meteorological Society*, 132(619):1859–1876. _eprint: https://rmets.onlinelibrary.wiley.com/doi/pdf/10.1256/qj.05.182.

Brown, A. R., Beljaars, A. C. M., Hersbach, H., Hollingsworth, A., Miller, M., and Vasiljevic, D. (2005). Wind turning across the marine atmospheric boundary layer. *Quarterly Journal of the Royal Meteorological Society*, 131(607):1233–1250. _eprint: https://rmets.onlinelibrary.wiley.com/doi/pdf/10.1256/qj.04.163.

Brown, A. R. and Grant, A. L. M. (1997). Non-local mixing of momentum in the convective boundary layer. *Boundary-Layer Meteorology*, 84(1):1–22.

Brueck, M., Nuijens, L., and Stevens, B. (2015). On the Seasonal and Synoptic Time-Scale Variability of the North Atlantic Trade Wind Region and Its Low-Level Clouds. *Journal of*

the Atmospheric Sciences, 72(4):1428–1446. Publisher: American Meteorological Society Section: Journal of the Atmospheric Sciences.

Bryan, G. H., Wyngaard, J. C., and Fritsch, J. M. (2003). Resolution Requirements for the Simulation of Deep Moist Convection. *Monthly Weather Review*, 131(10):2394–2416. Publisher: American Meteorological Society Section: Monthly Weather Review.

Brümmer, B., Augstein, E., and Riehl, H. (1974). On the low-level wind structure in the Atlantic trade. *Quarterly Journal of the Royal Meteorological Society*, 100(423):109–121. _eprint: https://rmets.onlinelibrary.wiley.com/doi/pdf/10.1002/qj.49710042310.

Carr, M. T. and Bretherton, C. S. (2001). Convective Momentum Transport over the Tropical Pacific: Budget Estimates. *Journal of the Atmospheric Sciences*, 58(13):1673–1693. Publisher: American Meteorological Society Section: Journal of the Atmospheric Sciences.

Charney, J., Arakawa, A., Baker, J., and Bolin, B. (1979). *Carbon Dioxide and Climate: A Scientific Assessment.* National Academies Press, Washington, D.C.

Chaudhuri, A. H., Ponte, R. M., Forget, G., and Heimbach, P. (2013). A Comparison of Atmospheric Reanalysis Surface Products over the Ocean and Implications for Uncertainties in Air–Sea Boundary Forcing. *Journal of Climate*, 26(1):153–170. Publisher: American Meteorological Society Section: Journal of Climate.

Chelton, D. B., Esbensen, S. K., Schlax, M. G., Thum, N., Freilich, M. H., Wentz, F. J., Gentemann, C. L., McPhaden, M. J., and Schopf, P. S. (2001). Observations of Coupling between Surface Wind Stress and Sea Surface Temperature in the Eastern Tropical Pacific. *Journal of Climate*.

Chelton, D. B. and Freilich, M. H. (2005). Scatterometer-Based Assessment of 10-m Wind Analyses from the Operational ECMWF and NCEP Numerical Weather Prediction Models. *Monthly Weather Review*, 133(2):409–429. Publisher: American Meteorological Society Section: Monthly Weather Review.

Chelton, D. B., Schlax, M. G., Freilich, M. H., and Milliff, R. F. (2004). Satellite Measurements Reveal Persistent Small-Scale Features in Ocean Winds. *Science*, 303(5660):978–983. Publisher: American Association for the Advancement of Science Section: Research Articles.

Craig, G. C. and Dornbrack, A. (2008). Entrainment in Cumulus Clouds: What Resolution is Cloud-Resolving? *Journal of the Atmospheric Sciences*, 65(12):3978–3988. Publisher: American Meteorological Society Section: Journal of the Atmospheric Sciences.

Dai, A. and Deser, C. (1999). Diurnal and semidiurnal variations in global surface wind and divergence fields. *Journal of Geophysical Research: Atmospheres*, 104(D24):31109–31125. _eprint: https://agupubs.onlinelibrary.wiley.com/doi/pdf/10.1029/1999JD900927.

Dauhut, T., Couvreux, F., Bouniol, D., Beucher, F., Volkmer, L., Pörtge, V., Schäfer, M., Ayet, A., Brilouet, P.-E., Jacob, M., and Wirth, M. (2023). Flower trade-wind clouds are shallow

mesoscale convective systems. *Quarterly Journal of the Royal Meteorological Society*, 149(750):325–347. _eprint: https://onlinelibrary.wiley.com/doi/pdf/10.1002/qj.4409.

de Rooy, W. C., Bechtold, P., Frohlich, K., Hohenegger, C., Jonker, H., Mironov, D., Pier Siebesma, A., Teixeira, J., and Yano, J.-I. (2013). Entrainment and detrainment in cumulus convection: an overview. *Quarterly Journal of the Royal Meteorological Society*, 139(670):1–19. _eprint: https://onlinelibrary.wiley.com/doi/pdf/10.1002/qj.1959.

de Rooy, W. C. and Siebesma, A. (2010). Analytical expressions for entrainment and detrainment in cumulus convection. *Quarterly Journal of the Royal Meteorological Society*, 136(650):1216–1227. _eprint: https://onlinelibrary.wiley.com/doi/pdf/10.1002/qj.640.

de Rooy, W. C. and Siebesma, A. P. (2008). A Simple Parameterization for Detrainment in Shallow Cumulus. *Monthly Weather Review*, 136(2):560–576. Publisher: American Meteorological Society Section: Monthly Weather Review.

de Rooy, W. C., Siebesma, P., Baas, P., Lenderink, G., de Roode, S. R., de Vries, H., van Meijgaard, E., Meirink, J. F., Tijm, S., and van 't Veen, B. (2022). Model development in practice: a comprehensive update to the boundary layer schemes in HARMONIE-AROME cycle 40. *Geoscientific Model Development*, 15(4):1513–1543. Publisher: Copernicus GmbH.

Deardorff, J. W. (1980). Stratocumulus-capped mixed layers derived from a three-dimensional model. *Boundary-Layer Meteorology*, 18(4):495–527.

Dee, D. P., Uppala, S. M., Simmons, A. J., Berrisford, P., Poli, P., Kobayashi, S., Andrae, U., Balmaseda, M. A., Balsamo, G., Bauer, P., Bechtold, P., Beljaars, A. C. M., Berg, L. v. d., Bidlot, J., Bormann, N., Delsol, C., Dragani, R., Fuentes, M., Geer, A. J., Haimberger, L., Healy, S. B., Hersbach, H., Hólm, E. V., Isaksen, L., Kållberg, P., Köhler, M., Matricardi, M., McNally, A. P., Monge-Sanz, B. M., Morcrette, J.-J., Park, B.-K., Peubey, C., Rosnay, P. d., Tavolato, C., Thépaut, J.-N., and Vitart, F. (2011). The ERA-Interim reanalysis: configuration and performance of the data assimilation system. *Quarterly Journal of the Royal Meteorological Society*, 137(656):553–597. _eprint: https://rmets.onlinelibrary.wiley.com/doi/pdf/10.1002/qj.828.

Dias Neto, J. (2022). The tracing convective momentum transport in complex cloudy atmospheres experiment - level 2.

Dias Neto, J., Nuijens, L., Unal, C., and Knoop, S. (2023). Combined wind lidar and cloud radar for high-resolution wind profiling. *Earth System Science Data*, 15(2):769–789. Publisher: Copernicus GmbH.

Dixit, V., Nuijens, L., and Helfer, K. C. (2021). Counter-Gradient Momentum Transport Through Subtropical Shallow Convection in ICON-LEM Simulations. *Journal of Advances in Modeling Earth Systems*, 13(6):e2020MS002352. _eprint: https://agupubs.onlinelibrary.wiley.com/doi/pdf/10.1029/2020MS002352.

Dorrestijn, J., Crommelin, D. T., Siebesma, A. P., and Jonker, H. J. J. (2013). Stochastic parameterization of shallow cumulus convection estimated from high-resolution model data. *Theoretical and Computational Fluid Dynamics*, 27(1):133–148.

ECMWF (2024). IFS Documentation. Cycles 47r3 to 48r1.

Foley, A. M., Leahy, P. G., Marvuglia, A., and McKeogh, E. J. (2012). Current methods and advances in forecasting of wind power generation. *Renewable Energy*, 37(1):1–8.

Forbes, R., Laloyaux, P., and Rodwell, M. (2021). IFS upgrade improves moist physics and use of satellite observations. *ECMWF Newsletter*, 169:17–24. Type: 10.21957/m3805gf17r.

Freitas, S. R., Putman, W. M., Arnold, N. P., Adams, D. K., and Grell, G. A. (2020). Cascading Toward a Kilometer-Scale GCM: Impacts of a Scale-Aware Convection Parameterization in the Goddard Earth Observing System GCM. *Geophysical Research Letters*, 47(17):e2020GL087682. _eprint: https://onlinelibrary.wiley.com/doi/pdf/10.1029/2020GL087682.

Frisch, U. (1995). *Turbulence: The Legacy of A. N. Kolmogorov*. Cambridge: Cambridge University Press. ISBN: 9781139170666 Publisher: Cambridge University Press.

George, G., Stevens, B., Bony, S., Klingebiel, M., and Vogel, R. (2021a). Observed Impact of Mesoscale Vertical Motion on Cloudiness. *Journal of the Atmospheric Sciences*, 78(8):2413–2427. Publisher: American Meteorological Society Section: Journal of the Atmospheric Sciences.

George, G., Stevens, B., Bony, S., Pincus, R., Fairall, C., Schulz, H., Kölling, T., Kalen, Q. T., Klingebiel, M., Konow, H., Lundry, A., Prange, M., and Radtke, J. (2021b). JOANNE : Joint dropsonde Observations of the Atmosphere in tropical North atlaNtic meso-scale Environments. *Earth System Science Data Discussions*, pages 1–33. Publisher: Copernicus GmbH.

George, G., Stevens, B., Bony, S., Vogel, R., and Naumann, A. K. (2023). Widespread shallow mesoscale circulations observed in the trades. *Nature Geoscience*, 16(7):584–589. Number: 7 Publisher: Nature Publishing Group.

Gerard, L. (2007). An integrated package for subgrid convection, clouds and precipitation compatible with meso-gamma scales. *Quarterly Journal of the Royal Meteorological Society*, 133(624):711–730. _eprint: https://onlinelibrary.wiley.com/doi/pdf/10.1002/qj.58.

Gille, S. T. (2005). Statistical Characterization of Zonal and Meridional Ocean Wind Stress. *Journal of Atmospheric and Oceanic Technology*, 22(9):1353–1372. Publisher: American Meteorological Society Section: Journal of Atmospheric and Oceanic Technology.

Golaz, J.-C., Larson, V. E., and Cotton, W. R. (2002). A PDF-Based Model for Boundary Layer Clouds. Part I: Method and Model Description. *Journal of the Atmospheric Sciences*, 59.

Gottschall, J., Catalano, E., Dörenkämper, M., and Witha, B. (2018). The NEWA Ferry Lidar Experiment: Measuring Mesoscale Winds in the Southern Baltic Sea. *Remote Sensing*, 10(10):1620. Number: 10 Publisher: Multidisciplinary Digital Publishing Institute.

Grant, L. D., Moncrieff, M. W., Lane, T. P., and van den Heever, S. C. (2020). Shear-Parallel Tropical Convective Systems: Importance of Cold Pools and Wind Shear. *Geophysical Research Letters*, 47(12):e2020GL087720. _eprint: https://onlinelibrary.wiley.com/doi/pdf/10.1029/2020GL087720.

Hadley, G. (1735). VI. Concerning the cause of the general trade-winds. *Philosophical Transactions of the Royal Society of London*, 39(437):58–62. Publisher: Royal Society.

Hartmann, D. L., Ockert-Bell, M. E., and Michelsen, M. L. (1992). The Effect of Cloud Type on Earth's Energy Balance: Global Analysis. *Journal of Climate*.

Helfer, K. C., Nuijens, L., and Dixit, V. V. (2021). The role of shallow convection in the momentum budget of the trades from large-eddy-simulation hindcasts. *Quarterly Journal of the Royal Meteorological Society*, n/a(n/a). _eprint: https://rmets.onlinelibrary.wiley.com/doi/pdf/10.1002/qj.4035.

Helfer, K. C., Nuijens, L., Roode, S. R. D., and Siebesma, P. (2020). How wind shear affects trade-wind cumulus convection. Archive Location: world Publisher: Earth and Space Science Open Archive Section: Atmospheric Sciences.

Hersbach, H., Bell, B., Berrisford, P., Hirahara, S., Horányi, A., Munoz-Sabater, J., Nicolas, J., Peubey, C., Radu, R., Schepers, D., Simmons, A., Soci, C., Abdalla, S., Abellan, X., Balsamo, G., Bechtold, P., Biavati, G., Bidlot, J., Bonavita, M., Chiara, G. D., Dahlgren, P., Dee, D., Diamantakis, M., Dragani, R., Flemming, J., Forbes, R., Fuentes, M., Geer, A., Haimberger, L., Healy, S., Hogan, R. J., Hólm, E., Janisková, M., Keeley, S., Laloyaux, P., Lopez, P., Lupu, C., Radnoti, G., Rosnay, P. d., Rozum, I., Vamborg, F., Villaume, S., and Thepaut, J.-N. (2020). The ERA5 global reanalysis. *Quarterly Journal of the Royal Meteorological Society*, 146(730):1999–2049. _eprint: https://rmets.onlinelibrary.wiley.com/doi/pdf/10.1002/qj.3803.

Heus, T., van Heerwaarden, C. C., Jonker, H. J. J., Pier Siebesma, A., Axelsen, S., van den Dries, K., Geoffroy, O., Moene, A. F., Pino, D., de Roode, S. R., and Vilà-Guerau de Arellano, J. (2010). Formulation of the Dutch Atmospheric Large-Eddy Simulation (DALES) and overview of its applications. *Geoscientific Model Development*, 3(2):415–444. Publisher: Copernicus GmbH.

Hogan, T. F. and Pauley, R. L. (2007). The Impact of Convective Momentum Transport on Tropical Cyclone Track Forecasts Using the Emanuel Cumulus Parameterization. *Monthly Weather Review*.

Holland, J. Z. and Rasmusson, E. M. (1973). Measurements of the Atmospheric Mass, Energy, and Momentum Budgets Over a 500-Kilometer Square of Tropical Ocean. *Monthly Weather Review*, 101(1):44–55. Publisher: American Meteorological Society Section: Monthly Weather Review.

Hollingsworth, A. (1994). Validation and diagnosis of atmospheric models. *Dynamics of Atmospheres and Oceans*, 20(3):227–246.

Honnert, R. (2019). Grey-Zone Turbulence in the Neutral Atmospheric Boundary Layer. *Boundary-Layer Meteorology*, 170(2):191–204.

Honnert, R., Masson, V., and Couvreux, F. (2011). A Diagnostic for Evaluating the Representation of Turbulence in Atmospheric Models at the Kilometric Scale. *Journal of the Atmospheric Sciences*, 68(12):3112–3131. Publisher: American Meteorological Society Section: Journal of the Atmospheric Sciences.

Houchi, K., Stoffelen, A., Marseille, G. J., and De Kloe, J. (2010). Comparison of wind and wind shear climatologies derived from high-resolution radiosondes and the ECMWF model. *Journal of Geophysical Research*, 115(D22):D22123.

Hwang, Y.-T. and Frierson, D. M. W. (2013). Link between the double-Intertropical Convergence Zone problem and cloud biases over the Southern Ocean. *Proceedings of the National Academy of Sciences*, 110(13):4935–4940. Publisher: Proceedings of the National Academy of Sciences.

IPCC (2023). *Climate Change 2021 – The Physical Science Basis: Working Group I Contribution to the Sixth Assessment Report of the Intergovernmental Panel on Climate Change*. Cambridge University Press, Cambridge.

Janssens, M., Arellano, J. V.-G. d., Heerwaarden, C. C. v., Roode, S. R. d., Siebesma, A. P., and Glassmeier, F. (2022). Non-Precipitating Shallow Cumulus Convection is Intrinsically Unstable to Length-Scale Growth. *Journal of the Atmospheric Sciences*, -1(aop). Publisher: American Meteorological Society Section: Journal of the Atmospheric Sciences.

Janssens, M., Arellano, J. V.-G. d., Scheffer, M., Antonissen, C., Siebesma, A. P., and Glassmeier, F. (2021). Cloud Patterns in the Trades Have Four Interpretable Dimensions. *Geophysical Research Letters*, 48(5):e2020GL091001. _eprint: https://agupubs.onlinelibrary.wiley.com/doi/pdf/10.1029/2020GL091001.

Jansson, F., Janssens, M., Gronqvist, J. H., Siebesma, A. P., Glassmeier, F., Attema, J., Azizi, V., Satoh, M., Sato, Y., Schulz, H., and Kolling, T. (2023). Cloud Botany: Shallow Cumulus Clouds in an Ensemble of Idealized Large-Domain Large-Eddy Simulations of the Trades. *Journal of Advances in Modeling Earth Systems*, 15(11):e2023MS003796. _eprint: https://onlinelibrary.wiley.com/doi/pdf/10.1029/2023MS003796.

Jonker, H. J., Verzijlbergh, R. A., Heus, T., and Siebesma, A. P. (2006). The Influence of the Sub-Cloud Moisture Field on Cloud Size Distributions and the Consequences for Entrainment. *17th Symposium on Boundary Layers and Turbulence, 27th Conference on Agricultural and Forest Meteorology, 17th Conference on Biometeorology and Aerobiology.*

Kershaw, R. and Gregory, D. (1997). Parametrization of momentum transport by convection. I: Theory and cloud modelling results. *Quarterly Journal of the Royal Meteorological Society*, 123(541):1133–1151. _eprint: https://onlinelibrary.wiley.com/doi/pdf/10.1002/qj.49712354102.

Khairoutdinov, M. and Kogan, Y. (2000). A New Cloud Physics Parameterization in a Large-Eddy Simulation Model of Marine Stratocumulus. *Monthly Weather Review*, 128(1):229–243.

Koning, A. M., Nuijens, L., Bosveld, F. C., Siebesma, A. P., van Dorp, P. A., and Jonker, H. J. J. (2021). Surface-Layer Wind Shear and Momentum Transport From Clear-Sky to Cloudy Weather Regimes Over Land. *Journal of Geophysical Research: Atmospheres*, 126(21):e2021JD035087. _eprint: https://onlinelibrary.wiley.com/doi/pdf/10.1029/2021JD035087.

Koning, A. M., Nuijens, L., and Mallaun, C. (2022). Momentum fluxes from airborne wind measurements in three cumulus cases over land. *Atmospheric Chemistry and Physics*, 22(11):7373–7388. Publisher: Copernicus GmbH.

Kurowski, M. J., Paris, A., and Teixeira, J. (2024). The Unique Behavior of Vertical Velocity in Developing Deep Convection. *Geophysical Research Letters*, 51(20):e2024GL110425. _eprint: https://onlinelibrary.wiley.com/doi/pdf/10.1029/2024GL110425.

Lamaakel, O. and Matheou, G. (2022). Organization Development in Precipitating Shallow Cumulus Convection: Evolution of Turbulence Characteristics. *Journal of the Atmospheric Sciences*.

Lancz, D., Szintai, B., and Honnert, R. (2018). Modification of a Parametrization of Shallow Convection in the Grey Zone Using a Mesoscale Model. *Boundary-Layer Meteorology*, 169(3):483–503.

Lappen, C.-L. and Randall, D. A. (2001). Toward a Unified Parameterization of the Boundary Layer and Moist Convection. Part I: A New Type of Mass-Flux Model. *Journal of the Atmospheric Sciences*, 58(15).

Larson, V. E., Domke, S., and Griffin, B. M. (2019). Momentum Transport in Shallow Cumulus Clouds and Its Parameterization by Higher-Order Closure. *Journal of Advances in Modeling Earth Systems*, 11(11):3419–3442. _eprint: https://agupubs.onlinelibrary.wiley.com/doi/pdf/10.1029/2019MS001743.

LeMone, M. A. (1983). Momentum Transport by a Line of Cumulonimbus. *Journal of the Atmospheric Sciences*, 40(7):1815–1834. Publisher: American Meteorological Society Section: Journal of the Atmospheric Sciences.

LeMone, M. A., Barnes, G. M., and Zipser, E. J. (1984). Momentum Flux by Lines of Cumulonimbus over the Tropical Oceans. *Journal of the Atmospheric Sciences*, 41(12):1914–1932. Publisher: American Meteorological Society Section: Journal of the Atmospheric Sciences.

LeMone, M. A. and Moncrieff, M. W. (1994). Momentum and Mass Transport by Convective Bands: Comparison of Highly Idealized Dynamical Models to Observations. *Journal of the Atmospheric Sciences*, 51(2):281–305. Publisher: American Meteorological Society Section: Journal of the Atmospheric Sciences.

LeMone, M. A. and Pennell, W. T. (1976). The Relationship of Trade Wind Cumulus Distribution to Subcloud Layer Fluxes and Structure. *Monthly Weather Review*.

Lenderink, G. and Holtslag, A. a. M. (2004). An updated length-scale formulation for turbulent mixing in clear and cloudy boundary layers. *Quarterly Journal of the Royal Meteorological Society*, 130(604):3405–3427. _eprint: https://onlinelibrary.wiley.com/doi/pdf/10.1256/qj.03.117.

Li, D. and Bou-Zeid, E. (2011). Coherent Structures and the Dissimilarity of Turbulent Transport of Momentum and Scalars in the Unstable Atmospheric Surface Layer. *Boundary-Layer Meteorology*, 140(2):243–262.

Lin, J.-L., Mapes, B. E., and Han, W. (2008). What Are the Sources of Mechanical Damping in Matsuno–Gill-Type Models? *Journal of Climate*, 21(2):165–179. Publisher: American Meteorological Society Section: Journal of Climate.

Lin, J. W.-B. and Neelin, J. D. (2002). Considerations for Stochastic Convective Parameterization. *Journal of the Atmospheric Sciences*, 59(5).

Liqui Lung, F., Jakob, C., Siebesma, A. P., and Jansson, F. (2024). Open boundary conditions for atmospheric large-eddy simulations and their implementation in DALES4.4. *Geoscientific Model Development*, 17(9):4053–4076. Publisher: Copernicus GmbH.

Malkus, J. S. and Riehl, H. (1964). Cloud structure and distributions over the tropical Pacific Ocean1. *Tellus*, 16(3):275–287. _eprint: https://onlinelibrary.wiley.com/doi/pdf/10.1111/j.2153-3490.1964.tb00167.x.

Marchand, R., Ackerman, T., Smyth, M., and Rossow, W. B. (2010). A review of cloud top height and optical depth histograms from MISR, ISCCP, and MODIS. *Journal of Geophysical Research: Atmospheres*, 115(D16). _eprint: https://onlinelibrary.wiley.com/doi/pdf/10.1029/2009JD013422.

Moeng, C.-H., Dudhia, J., Klemp, J., and Sullivan, P. (2007). Examining Two-Way Grid Nesting for Large Eddy Simulation of the PBL Using the WRF Model. *Monthly Weather Review*.

Moncrieff, M. W. (1981). A theory of organized steady convection and its transport properties. *Quarterly Journal of the Royal Meteorological Society*, 107(451):29–50. _eprint: https://onlinelibrary.wiley.com/doi/pdf/10.1002/qj.49710745103.

Moncrieff, M. W. (1992). Organized Convective Systems: Archetypal Dynamical Models, Mass and Momentum Flux Theory, and Parametrization. *Quarterly Journal of the Royal Meteorological Society*, 118(507):819–850. _eprint: https://onlinelibrary.wiley.com/doi/pdf/10.1002/qj.49711850703.

Moncrieff, M. W. (2019). Toward a Dynamical Foundation for Organized Convection Parameterization in GCMs. *Geophysical Research Letters*, 46(23):14103–14108. _eprint: https://onlinelibrary.wiley.com/doi/pdf/10.1029/2019GL085316.

Myers, T. A., Scott, R. C., Zelinka, M. D., Klein, S. A., Norris, J. R., and Caldwell, P. M. (2021). Observational constraints on low cloud feedback reduce uncertainty of climate sensitivity. *Nature Climate Change*, 11(6):501–507. Number: 6 Publisher: Nature Publishing Group.

Neggers, R. A. J. (2009). A Dual Mass Flux Framework for Boundary Layer Convection. Part II: Clouds. *Journal of the Atmospheric Sciences*, 66(6):1489–1506. Publisher: American Meteorological Society Section: Journal of the Atmospheric Sciences.

Neggers, R. A. J., Neelin, J. D., and Stevens, B. (2007). Impact Mechanisms of Shallow Cumulus Convection on Tropical Climate Dynamics. *Journal of Climate*, 20(11):2623–2642. Publisher: American Meteorological Society Section: Journal of Climate.

NOAA (2020). GOES-R Series Data Book.

Nuijens, L., Savazzi, A., de Boer, G., Brilouet, P.-E., George, G., Lothon, M., and Zhang, D. (2022). The frictional layer in the observed momentum budget of the trades. *Quarterly Journal of the Royal Meteorological Society*, 148(748):3343–3365. _eprint: https://onlinelibrary.wiley.com/doi/pdf/10.1002/qj.4364.

Nuijens, L., Serikov, I., Hirsch, L., Lonitz, K., and Stevens, B. (2014). The distribution and variability of low-level cloud in the North Atlantic trades. *Quarterly Journal of the Royal Meteorological Society*, 140(684):2364–2374. _eprint: https://rmets.onlinelibrary.wiley.com/doi/pdf/10.1002/qj.2307.

Nuijens, L. and Siebesma, A. P. (2019). Boundary Layer Clouds and Convection over Subtropical Oceans in our Current and in a Warmer Climate. *Current Climate Change Reports*, 5(2):80–94.

Nuijens, L. and Stevens, B. (2012). The Influence of Wind Speed on Shallow Marine Cumulus Convection. *Journal of the Atmospheric Sciences*, 69(1):168–184. Publisher: American Meteorological Society Section: Journal of the Atmospheric Sciences.

Nuijens, L., Stevens, B., and Siebesma, A. P. (2009). The Environment of Precipitating Shallow Cumulus Convection. *Journal of the Atmospheric Sciences*, 66(7).

Ooyama, K. (1971). A Theory on Parameterization of Cumulus Convection. *Journal of the Meteorological Society of Japan. Ser. II*, 49A:744–756.

Petch, J. C., Brown, A. R., and Gray, M. E. B. (2002). The impact of horizontal resolution on the simulations of convective development over land. *Quarterly Journal of the Royal Meteorological Society*, 128(584):2031–2044. _eprint: https://onlinelibrary.wiley.com/doi/pdf/10.1256/003590002320603511.

Phillips, N. A. (1956). The general circulation of the atmosphere: A numerical experiment. *Quarterly Journal of the Royal Meteorological Society*, 82(352):123–164. _eprint: https://onlinelibrary.wiley.com/doi/pdf/10.1002/qj.49708235202.

Radtke, J., Naumann, A. K., Hagen, M., and Ament, F. (2022). The relationship between precipitation and its spatial pattern in the trades observed during EUREC4A. *Quarterly Journal of the Royal Meteorological Society*, 148(745):1913–1928. _eprint: https://onlinelibrary.wiley.com/doi/pdf/10.1002/qj.4284.

Rasp, S., Schulz, H., Bony, S., and Stevens, B. (2020). Combining Crowdsourcing and Deep Learning to Explore the Mesoscale Organization of Shallow Convection. *Bulletin of the American Meteorological Society*, 101.

Rauber, R. M., Stevens, B., Ochs, H. T., Knight, C., Albrecht, B. A., Blyth, A. M., Fairall, C. W., Jensen, J. B., Lasher-Trapp, S. G., Mayol-Bracero, O. L., Vali, G., Anderson, J. R., Baker, B. A., Bandy, A. R., Burnet, E., Brenguier, J.-L., Brewer, W. A., Brown, P. R. A., Chuang, R., Cotton, W. R., Girolamo, L. D., Geerts, B., Gerber, H., Göke, S., Gomes, L., Heikes, B. G., Hudson, J. G., Kollias, P., Lawson, R. R., Krueger, S. K., Lenschow, D. H., Nuijens, L., O'Sullivan, D. W., Rilling, R. A., Rogers, D. C., Siebesma, A. P., Snodgrass, E., Stith, J. L., Thornton, D. C., Tucker, S., Twohy, C. H., and Zuidema, P. (2007). Rain in Shallow Cumulus Over the Ocean: The RICO Campaign. *Bulletin of the American Meteorological Society*, 88(12):1912–1928. Publisher: American Meteorological Society Section: Bulletin of the American Meteorological Society.

Redelsperger, J.-L. (1997). The Mesoscale Organization of Deep Convection. In Smith, R. K., editor, *The Physics and Parameterization of Moist Atmospheric Convection*, pages 59–98. Springer Netherlands, Dordrecht.

Rennie, M. P., Isaksen, L., Weiler, F., Kloe, J. d., Kanitz, T., and Reitebuch, O. (2021). The impact of Aeolus wind retrievals on ECMWF global weather forecasts. *Quarterly Journal of the Royal Meteorological Society*, n/a(n/a). _eprint: https://rmets.onlinelibrary.wiley.com/doi/pdf/10.1002/qj.4142.

Retsch, M. H., Jakob, C., and Singh, M. S. (2020). Assessing Convective Organization in Tropical Radar Observations. *Journal of Geophysical Research: Atmospheres*, 125(7):e2019JD031801. _eprint: https://agupubs.onlinelibrary.wiley.com/doi/pdf/10.1029/2019JD031801.

Richter, J. H. and Rasch, P. J. (2008). Effects of Convective Momentum Transport on the Atmospheric Circulation in the Community Atmosphere Model, Version 3. *Journal of Climate*.

Riehl, H., Yeh, T. C., Malkus, J. S., and Seur, N. E. l. (1951). The north-east trade of the Pacific Ocean. *Quarterly Journal of the Royal Meteorological Society*, 77(334):598–626. _eprint: https://rmets.onlinelibrary.wiley.com/doi/pdf/10.1002/qj.49707733405.

Rio, C. and Hourdin, F. (2008). A Thermal Plume Model for the Convective Boundary Layer: Representation of Cumulus Clouds. *Journal of the Atmospheric Sciences*, 65(2):407–425. Publisher: American Meteorological Society Section: Journal of the Atmospheric Sciences.

Risien, C. M. and Chelton, D. B. (2008). A Global Climatology of Surface Wind and Wind Stress Fields from Eight Years of QuikSCAT Scatterometer Data. *Journal of Physical Oceanography*, 38(11):2379–2413. Publisher: American Meteorological Society Section: Journal of Physical Oceanography.

Roode, S. R. d., Duynkerke, P. G., and Jonker, H. J. J. (2004). Large-Eddy Simulation: How Large is Large Enough? *Journal of the Atmospheric Sciences*, 61(4):403–421. Publisher: American Meteorological Society Section: Journal of the Atmospheric Sciences.

Saggiorato, B., Nuijens, L., Siebesma, A. P., de Roode, S., Sandu, I., and Papritz, L. (2020). The Influence of Convective Momentum Transport and Vertical Wind Shear on the Evolution of a Cold Air Outbreak. *Journal of Advances in Modeling Earth Systems*, 12(6):e2019MS001991. _eprint: https://onlinelibrary.wiley.com/doi/pdf/10.1029/2019MS001991.

Salesky, S. T., Chamecki, M., and Bou-Zeid, E. (2017). On the Nature of the Transition Between Roll and Cellular Organization in the Convective Boundary Layer. *Boundary-Layer Meteorology*, 163(1):41–68.

Sandu, I., Bechtold, P., Nuijens, L., Beljaars, A., and Brown, A. (2020). On the causes of systematic forecast biases in near-surface wind direction over the oceans. *ECMWF Technical Memorandum*, 866. Publisher: ECMWF.

Sandu, I., Beljaars, A., Bechtold, P., Mauritsen, T., and Balsamo, G. (2013). Why is it so difficult to represent stably stratified conditions in numerical weather prediction (NWP) models? *Journal of Advances in Modeling Earth Systems*, 5(2):117–133. _eprint: https://agupubs.onlinelibrary.wiley.com/doi/pdf/10.1002/jame.20013.

Satoh, M., Noda, A. T., Seiki, T., Chen, Y.-W., Kodama, C., Yamada, Y., Kuba, N., and Sato, Y. (2018). Toward reduction of the uncertainties in climate sensitivity due to cloud processes using a global non-hydrostatic atmospheric model. *Progress in Earth and Planetary Science*, 5(1):67.

Savazzi, A., Nuijens, L., Rooy, W. d., Janssens, M., and Siebesma, A. P. (2024). Momentum Transport in Organized Shallow Cumulus Convection. *Journal of the Atmospheric Sciences*, 81(2):279–296. Publisher: American Meteorological Society Section: Journal of the Atmospheric Sciences.

Savazzi, A., Nuijens, L., Sandu, I., George, G., and Bechtold, P. (2022). The representation of the trade winds in ECMWF forecasts and reanalyses during EUREC[4]A. *Atmospheric Chemistry and Physics*, 22(19):13049–13066. Publisher: Copernicus GmbH.

Schlemmer, L., Bechtold, P., Sandu, I., and Ahlgrimm, M. (2017). Uncertainties related to the representation of momentum transport in shallow convection. *Journal of Advances in Modeling Earth Systems*, 9(2):1269–1291. _eprint: https://agupubs.onlinelibrary.wiley.com/doi/pdf/10.1002/2017MS000915.

Schneider, E. K. and Lindzen, R. S. (1976). A discussion of the parameterization of momentum exchange by cumulus convection. *Journal of Geophysical Research (1896-1977)*, 81(18):3158–3160. _eprint: https://onlinelibrary.wiley.com/doi/pdf/10.1029/JC081i018p03158.

Schneider, T., Teixeira, J., Bretherton, C. S., Brient, F., Pressel, K. G., Schar, C., and Siebesma, A. P. (2017). Climate goals and computing the future of clouds. *Nature Climate Change*, 7(1):3–5. Number: 1 Publisher: Nature Publishing Group.

Schulz, H. (2022). C[3]ONTEXT: a Common Consensus on Convective OrgaNizaTion during the EUREC[4]A eXperimenT. *Earth System Science Data*, 14(3):1233–1256. Publisher: Copernicus GmbH.

Schulz, H., Eastman, R., and Stevens, B. (2021). Characterization and Evolution of Organized Shallow Convection in the Downstream North Atlantic Trades. *Journal of Geophysical Research: Atmospheres*, 126(17):e2021JD034575. _eprint: https://onlinelibrary.wiley.com/doi/pdf/10.1029/2021JD034575.

Schumann, U. (1987). The countergradient heat flux in turbulent stratified flows. *Nuclear Engineering and Design*, 100(3):255–262.

Sentic, S., Bechtold, P., Fuchs-Stone, Z., Rodwell, M., and Raymond, D. J. (2022). On the impact of dropsondes on the ECMWF Integrated Forecasting System model (CY47R1) analysis of convection during the OTREC (Organization of Tropical East Pacific Convection) field campaign. *Geoscientific Model Development*, 15(8):3371–3385. Publisher: Copernicus GmbH.

Sherwood, S. C., Bony, S., and Dufresne, J.-L. (2014). Spread in model climate sensitivity traced to atmospheric convective mixing. *Nature*, 505(7481):37–42. Publisher: Nature Publishing Group.

Siebesma, A. P., Bretherton, C. S., Brown, A., Chlond, A., Cuxart, J., Duynkerke, P. G., Jiang, H., Khairoutdinov, M., Lewellen, D., Moeng, C.-H., Sanchez, E., Stevens, B., and Stevens, D. E. (2003). A Large Eddy Simulation Intercomparison Study of Shallow Cumulus Convection. *Journal of the Atmospheric Sciences*, 60(10):1201–1219. Publisher: American Meteorological Society Section: Journal of the Atmospheric Sciences.

Siebesma, A. P. and Cuijpers, J. W. M. (1995). Evaluation of Parametric Assumptions for Shallow Cumulus Convection. *Journal of the Atmospheric Sciences*, 52(6).

Siebesma, A. P., Soares, P. M. M., and Teixeira, J. (2007). A Combined Eddy-Diffusivity Mass-Flux Approach for the Convective Boundary Layer. *Journal of the Atmospheric Sciences*, 64(4):1230–1248. Publisher: American Meteorological Society Section: Journal of the Atmospheric Sciences.

Siebesma, Teixeira, A. P. (2000). An Advection-Diffusion scheme for the convective boundary layer: description and 1d-results.

Slingo, A. and Slingo, J. M. (1988). The response of a general circulation model to cloud longwave radiative forcing. I: Introduction and initial experiments. *Quarterly Journal of the Royal Meteorological Society*, 114(482):1027–1062. _eprint: https://onlinelibrary.wiley.com/doi/pdf/10.1002/qj.49711448209.

Soares, P. M. M., Miranda, P. M. A., Siebesma, A. P., and Teixeira, J. (2004). An eddy-diffusivity/mass-flux parametrization for dry and shallow cumulus convection. *Quarterly Journal of the Royal Meteorological Society*, 130(604):3365–3383. _eprint: https://onlinelibrary.wiley.com/doi/pdf/10.1256/qj.03.223.

Sommeria, G. and Deardorff, J. W. (1977). Subgrid-Scale Condensation in Models of Nonprecipitating Clouds. *Journal of the Atmospheric Sciences*, 34.

Stephan, C. C., Schnitt, S., Schulz, H., Bellenger, H., de Szoeke, S. P., Acquistapace, C., Baier, K., Dauhut, T., Laxenaire, R., Morfa-Avalos, Y., Person, R., Quiñones Meléndez, E., Bagheri, G., Böck, T., Daley, A., Güttler, J., Helfer, K. C., Los, S. A., Neuberger, A., Röttenbacher, J., Raeke, A., Ringel, M., Ritschel, M., Sadoulet, P., Schirmacher, I., Stolla, M. K., Wright, E., Charpentier, B., Doerenbecher, A., Wilson, R., Jansen, F., Kinne, S., Reverdin, G., Speich, S., Bony, S., and Stevens, B. (2021). Ship- and island-based atmospheric soundings from the 2020 EUREC^{4}A field campaign. *Earth System Science Data*, 13(2):491–514. Publisher: Copernicus GmbH.

Stevens, B., Bony, S., Brogniez, H., Hentgen, L., Hohenegger, C., Kiemle, C., L'Ecuyer, T. S., Naumann, A. K., Schulz, H., Siebesma, P. A., Vial, J., Winker, D. M., and Zuidema, P. (2020). Sugar, gravel, fish and flowers: Mesoscale cloud patterns in the trade winds. *Quarterly Journal of the Royal Meteorological Society*, 146(726):141–152. _eprint: https://onlinelibrary.wiley.com/doi/pdf/10.1002/qj.3662.

Stevens, B., Bony, S., Farrell, D., Ament, F., Blyth, A., Fairall, C., Karstensen, J., Quinn, P. K., Speich, S., Acquistapace, C., Aemisegger, F., Albright, A. L., Bellenger, H., Bodenschatz, E., Caesar, K.-A., Chewitt-Lucas, R., de Boer, G., Delanoë, J., Denby, L., Ewald, F., Fildier, B., Forde, M., George, G., Gross, S., Hagen, M., Hausold, A., Heywood, K. J., Hirsch, L., Jacob, M., Jansen, F., Kinne, S., Klocke, D., Kölling, T., Konow, H., Lothon, M., Mohr, W., Naumann, A. K., Nuijens, L., Olivier, L., Pincus, R., Pöhlker, M., Reverdin, G., Roberts, G., Schnitt, S., Schulz, H., Siebesma, A. P., Stephan, C. C., Sullivan, P., Touzé-Peiffer, L., Vial, J., Vogel, R., Zuidema, P., Alexander, N., Alves, L., Arixi, S., Asmath, H., Bagheri, G., Baier, K., Bailey, A., Baranowski, D., Baron, A., Barrau, S., Barrett, P. A., Batier, F., Behrendt, A., Bendinger, A., Beucher, F., Bigorre, S., Blades, E., Blossey, P., Bock, O., Böing, S., Bosser, P., Bourras, D., Bouruet-Aubertot, P., Bower, K., Branellec, P., Branger, H., Brennek, M., Brewer, A., Brilouet, P.-E., Brügmann, B., Buehler, S. A., Burke, E., Burton, R., Calmer, R., Canonici, J.-C., Carton, X., Cato Jr., G., Charles, J. A., Chazette, P., Chen, Y., Chilinski, M. T., Choularton, T., Chuang, P., Clarke, S., Coe, H., Cornet, C., Coutris, P., Couvreux, F., Crewell, S., Cronin, T., Cui, Z., Cuypers, Y., Daley, A., Damerell, G. M., Dauhut, T., Deneke, H., Desbios, J.-P., Dörner, S., Donner, S., Douet, V., Drushka, K., Dütsch, M., Ehrlich, A., Emanuel, K., Emmanouilidis, A., Etienne, J.-C., Etienne-Leblanc, S., Faure, G., Feingold, G., Ferrero, L., Fix, A., Flamant, C., Flatau, P. J., Foltz, G. R., Forster, L., Furtuna, I., Gadian, A., Galewsky, J., Gallagher, M., Gallimore, P., Gaston, C., Gentemann, C., Geyskens, N., Giez, A., Gollop, J., Gouirand, I., Gourbeyre, C., de Graaf, D., de Groot, G. E., Grosz, R., Güttler, J., Gutleben, M., Hall, K., Harris, G., Helfer, K. C., Henze, D., Herbert, C., Holanda, B., Ibanez-Landeta, A., Intrieri, J., Iyer, S., Julien, F., Kalesse, H., Kazil, J., Kellman, A., Kidane, A. T., Kirchner, U., Klingebiel, M., Körner, M., Kremper, L. A., Kretzschmar, J., Krüger, O., Kumala, W., Kurz, A., L'Hégaret, P., Labaste, M., Lachlan-Cope, T., Laing, A., Landschützer, P., Lang, T., Lange, D., Lange, I., Laplace, C., Lavik, G., Laxenaire, R., Le Bihan, C., Leandro, M., Lefevre, N., Lena, M., Lenschow, D., Li, Q., Lloyd, G., Los, S., Losi, N., Lovell, O., Luneau, C., Makuch, P., Malinowski, S., Manta, G., Marinou, E., Marsden, N., Masson, S., Maury, N., Mayer, B., Mayers-Als, M., Mazel, C., McGeary, W., McWilliams, J. C., Mech, M., Mehlmann, M., Meroni, A. N., Mieslinger, T., Minikin, A., Minnett, P., Möller, G., Morfa Avalos, Y., Muller, C., Musat, I., Napoli, A., Neuberger, A., Noisel, C., Noone, D., Nordsiek, F., Nowak, J. L., Oswald,

L., Parker, D. J., Peck, C., Person, R., Philippi, M., Plueddemann, A., Pöhlker, C., Pörtge, V., Pöschl, U., Pologne, L., Posyniak, M., Prange, M., Quiñones Meléndez, E., Radtke, J., Ramage, K., Reimann, J., Renault, L., Reus, K., Reyes, A., Ribbe, J., Ringel, M., Ritschel, M., Rocha, C. B., Rochetin, N., Röttenbacher, J., Rollo, C., Royer, H., Sadoulet, P., Saffin, L., Sandiford, S., Sandu, I., Schäfer, M., Schemann, V., Schirmacher, I., Schlenczek, O., Schmidt, J., Schröder, M., Schwarzenboeck, A., Sealy, A., Senff, C. J., Serikov, I., Shohan, S., Siddle, E., Smirnov, A., Späth, F., Spooner, B., Stolla, M. K., Szkółka, W., de Szoeke, S. P., Tarot, S., Tetoni, E., Thompson, E., Thomson, J., Tomassini, L., Totems, J., Ubele, A. A., Villiger, L., von Arx, J., Wagner, T., Walther, A., Webber, B., Wendisch, M., Whitehall, S., Wiltshire, A., Wing, A. A., Wirth, M., Wiskandt, J., Wolf, K., Worbes, L., Wright, E., Wulfmeyer, V., Young, S., Zhang, C., Zhang, D., Ziemen, F., Zinner, T., and Zoger, M. (2021). EUREC4A. *Earth System Science Data*, 13(8):4067–4119.

Stevens, B., Farrell, D., Hirsch, L., Jansen, F., Nuijens, L., Serikov, I., Brügmann, B., Forde, M., Linne, H., Lonitz, K., and Prospero, J. M. (2016). The Barbados Cloud Observatory: Anchoring Investigations of Clouds and Circulation on the Edge of the ITCZ. *Bulletin of the American Meteorological Society*, 97(5):787–801. Publisher: American Meteorological Society Section: Bulletin of the American Meteorological Society.

Stevens, B., Satoh, M., Auger, L., Biercamp, J., Bretherton, C. S., Chen, X., Düben, P., Judt, F., Khairoutdinov, M., Klocke, D., Kodama, C., Kornblueh, L., Lin, S.-J., Neumann, P., Putman, W. M., Röber, N., Shibuya, R., Vanniere, B., Vidale, P. L., Wedi, N., and Zhou, L. (2019). DYAMOND: the DYnamics of the Atmospheric general circulation Modeled On Non-hydrostatic Domains. *Progress in Earth and Planetary Science*, 6(1):61.

Stevens, D. E. (1979). Vorticity, Momentum and Divergence Budgets of Synoptic-Scale Wave Disturbances in the Tropical Eastern Atlantic. *Monthly Weather Review*, 107(5):535–550. Publisher: American Meteorological Society Section: Monthly Weather Review.

Stoffelen, A., Pailleux, J., Källén, E., Vaughan, J. M., Isaksen, L., Flamant, P., Wergen, W., Andersson, E., Schyberg, H., Culoma, A., Meynart, R., Endemann, M., and Ingmann, P. (2005). The Atmospheric Dynamics Mission for Global Wind Field Measurement. *Bulletin of the American Meteorological Society*, 86(1):73–88. Publisher: American Meteorological Society Section: Bulletin of the American Meteorological Society.

Suselj, K., Kurowski, M. J., and Teixeira, J. (2019a). On the Factors Controlling the Development of Shallow Convection in Eddy-Diffusivity/Mass-Flux Models. *Journal of the Atmospheric Sciences*, 76.

Suselj, K., Kurowski, M. J., and Teixeira, J. (2019b). A Unified Eddy-Diffusivity/Mass-Flux Approach for Modeling Atmospheric Convection. *Journal of the Atmospheric Sciences*, 76(8).

Tan, Z., Kaul, C. M., Pressel, K. G., Cohen, Y., Schneider, T., and Teixeira, J. (2018). An Extended Eddy-Diffusivity Mass-Flux Scheme for Unified Representation of Subgrid-Scale Turbulence and Convection. *Journal of Advances in Modeling Earth Systems*, 10(3):770–800. _eprint: https://onlinelibrary.wiley.com/doi/pdf/10.1002/2017MS001162.

Thomas Haiden, M. J. (2024). Evaluation of ECMWF forecasts.

Tiedtke, M. (1989). A Comprehensive Mass Flux Scheme for Cumulus Parameterization in Large-Scale Models. *Monthly Weather Review*, 117(8):1779–1800. Publisher: American Meteorological Society Section: Monthly Weather Review.

Tompkins, A. M. and Semie, A. G. (2017). Organization of tropical convection in low vertical wind shears: Role of updraft entrainment. *Journal of Advances in Modeling Earth Systems*, 9(2):1046–1068. _eprint: https://onlinelibrary.wiley.com/doi/pdf/10.1002/2016MS000802.

Tung, W.-W. and Yanai, M. (2002a). Convective Momentum Transport Observed during the TOGA COARE IOP. Part I: General Features. *Journal of the Atmospheric Sciences*, 59(11):1857–1871. Publisher: American Meteorological Society Section: Journal of the Atmospheric Sciences.

Tung, W.-W. and Yanai, M. (2002b). Convective Momentum Transport Observed during the TOGA COARE IOP. Part II: Case Studies. *Journal of the Atmospheric Sciences*, 59(17):2535–2549. Publisher: American Meteorological Society Section: Journal of the Atmospheric Sciences.

Ueyama, R. and Deser, C. (2008). A Climatology of Diurnal and Semidiurnal Surface Wind Variations over the Tropical Pacific Ocean Based on the Tropical Atmosphere Ocean Moored Buoy Array. *Journal of Climate*, 21(4):593–607. Publisher: American Meteorological Society Section: Journal of Climate.

Vial, J., Bony, S., Dufresne, J.-L., and Roehrig, R. (2016). Coupling between lower-tropospheric convective mixing and low-level clouds: Physical mechanisms and dependence on convection scheme. *Journal of Advances in Modeling Earth Systems*, 8(4):1892–1911. _eprint: https://onlinelibrary.wiley.com/doi/pdf/10.1002/2016MS000740.

Vial, J., Bony, S., Stevens, B., and Vogel, R. (2017). Mechanisms and Model Diversity of Trade-Wind Shallow Cumulus Cloud Feedbacks: A Review. *Surveys in Geophysics*, 38(6):1331–1353.

Vial, J., Vogel, R., Bony, S., Stevens, B., Winker, D. M., Cai, X., Hohenegger, C., Naumann, A. K., and Brogniez, H. (2019). A New Look at the Daily Cycle of Trade Wind Cumuli. *Journal of Advances in Modeling Earth Systems*, 11(10):3148–3166. _eprint: https://agupubs.onlinelibrary.wiley.com/doi/pdf/10.1029/2019MS001746.

Vial, J., Vogel, R., and Schulz, H. (2021). On the daily cycle of mesoscale cloud organization in the winter trades. *Quarterly Journal of the Royal Meteorological Society*, 147(738):2850–2873. _eprint: https://onlinelibrary.wiley.com/doi/pdf/10.1002/qj.4103.

Vogel, R., Albright, A. L., Vial, J., George, G., Stevens, B., and Bony, S. (2022). Strong cloud circulation coupling explains weak trade cumulus feedback. *Nature*, 612(7941):696–700. Number: 7941 Publisher: Nature Publishing Group.

Vogel, R., Konow, H., Schulz, H., and Zuidema, P. (2021). A climatology of trade-wind cumulus cold pools and their link to mesoscale cloud organization. *Atmospheric Chemistry and Physics*, 21(21):16609–16630. Publisher: Copernicus GmbH.

Vogel, R., Nuijens, L., and Stevens, B. (2020). Influence of deepening and mesoscale or-
    ganization of shallow convection on stratiform cloudiness in the downstream trades.
    Quarterly Journal of the Royal Meteorological Society, 146(726):174–185. _eprint:
    https://onlinelibrary.wiley.com/doi/pdf/10.1002/qj.3664.

Wedi, N. P., Polichtchouk, I., Dueben, P., Anantharaj, V. G., Bauer, P., Boussetta, S.,
    Browne, P., Deconinck, W., Gaudin, W., Hadade, I., Hatfield, S., Iffrig, O., Lopez,
    P., Maciel, P., Mueller, A., Saarinen, S., Sandu, I., Quintino, T., and Vitart, F.
    (2020). A Baseline for Global Weather and Climate Simulations at 1 km Resolu-
    tion. *Journal of Advances in Modeling Earth Systems*, 12(11):e2020MS002192. _eprint:
    https://onlinelibrary.wiley.com/doi/pdf/10.1029/2020MS002192.

Weger, R. C., Lee, J., Zhu, T., and Welch, R. M. (1992). Clustering, random-
    ness and regularity in cloud fields: 1. Theoretical considerations. *Jour-
    nal of Geophysical Research: Atmospheres*, 97(D18):20519–20536. _eprint:
    https://onlinelibrary.wiley.com/doi/pdf/10.1029/92JD02038.

Wicker, L. J. and Skamarock, W. C. (2002). Time-Splitting Methods for Elastic Models
    Using Forward Time Schemes. *Monthly Weather Review*, 130(8):2088–2097. Publisher:
    American Meteorological Society Section: Monthly Weather Review.

Wing, A. A. and Emanuel, K. A. (2014). Physical mechanisms controlling
    self-aggregation of convection in idealized numerical modeling simula-
    tions. *Journal of Advances in Modeling Earth Systems*, 6(1):59–74. _eprint:
    https://onlinelibrary.wiley.com/doi/pdf/10.1002/2013MS000269.

Witschas, B., Lemmerz, C., Geiß, A., Lux, O., Marksteiner, U., Rahm, S., Reitebuch, O., and
    Weiler, F. (2020). First validation of Aeolus wind observations by airborne Doppler wind
    lidar measurements. *Atmospheric Measurement Techniques*, 13(5):2381–2396. Publisher:
    Copernicus GmbH.

Wolken-Möhlmann, G., Gottschall, J., and Lange, B. (2014). First Verification Test and Wake
    Measurement Results Using a SHIP-LIDAR System. *Energy Procedia*, 53:146–155.

Wood, R., Köhler, M., Bennartz, R., and O'Dell, C. (2009). The diurnal cycle of surface
    divergence over the global oceans. *Quarterly Journal of the Royal Meteorological Society*,
    135(643):1484–1493. _eprint: https://onlinelibrary.wiley.com/doi/pdf/10.1002/qj.451.

Wu, X., Deng, L., Song, X., and Zhang, G. J. (2007). Coupling of Convective Momentum
    Transport with Convective Heating in Global Climate Simulations. *Journal of the Atmo-
    spheric Sciences*, 64(4):1334–1349. Publisher: American Meteorological Society Section:
    Journal of the Atmospheric Sciences.

Wu, X. and Yanai, M. (1994). Effects of Vertical Wind Shear on the Cumulus Transport of
    Momentum: Observations and Parameterization. *Journal of the Atmospheric Sciences*,
    51(12):1640–1660. Publisher: American Meteorological Society Section: Journal of the
    Atmospheric Sciences.

Wyngaard, J. C. (2004). Toward Numerical Modeling in the Terra Incognita. *Journal of the Atmospheric Sciences*, 61(14):1816–1826. Publisher: American Meteorological Society Section: Journal of the Atmospheric Sciences.

Xiao, H., Ovchinnikov, M., Berg, L. K., and Mülmenstädt, J. (2023). Evaluating Shallow Convection Parameterization Assumptions With a q–w Quadrant Analysis. *Journal of Advances in Modeling Earth Systems*, 15(8):e2022MS003526. _eprint: https://onlinelibrary.wiley.com/doi/pdf/10.1029/2022MS003526.

Yanai, M. (1964). Formation of tropical cyclones. *Reviews of Geophysics*, 2(2):367–414. _eprint: https://onlinelibrary.wiley.com/doi/pdf/10.1029/RG002i002p00367.

Yu, X. and Lee, T.-Y. (2010). Role of convective parameterization in simulations of a convection band at grey-zone resolutions. *Tellus A*, 62(5):617–632. _eprint: https://onlinelibrary.wiley.com/doi/pdf/10.1111/j.1600-0870.2010.00470.x.

Zhang, G. J. and Cho, H.-R. (1991). Parameterization of the Vertical Transport of Momentum by Cumulus Clouds. Part II: Application. *Journal of the Atmospheric Sciences*, 48(22):2448–2457. Publisher: American Meteorological Society Section: Journal of the Atmospheric Sciences.

Zhang, G. J. and Wu, X. (2003). Convective Momentum Transport and Perturbation Pressure Field from a Cloud-Resolving Model Simulation. *Journal of the Atmospheric Sciences*, 60(9):1120–1139. Publisher: American Meteorological Society Section: Journal of the Atmospheric Sciences.

Zhao, G. and Di Girolamo, L. (2006). Cloud fraction errors for trade wind cumuli from EOS-Terra instruments. *Geophysical Research Letters*, 33(20). _eprint: https://onlinelibrary.wiley.com/doi/pdf/10.1029/2006GL027088.

Zhu, P. (2015). On the Mass-Flux Representation of Vertical Transport in Moist Convection. *Journal of the Atmospheric Sciences*, 72(12):4445–4468. Publisher: American Meteorological Society Section: Journal of the Atmospheric Sciences.

Zuidema, P., Torri, G., Muller, C., and Chandra, A. (2017). A Survey of Precipitation-Induced Atmospheric Cold Pools over Oceans and Their Interactions with the Larger-Scale Environment. *Surveys in Geophysics*, 38(6):1283–1305.

Curriculum Vitae

Alessandro C. M. Savazzi

2020 - 2025 **Delft University of Technology, The Netherlands**
PhD Candidate
Including research visits at:

- Meteo-France
- Max-Planck-Institute for Meteorology (MPI-Meteo)
- European Centre for Medium-Range Weather Forecasts (ECMWF)

2020 **Delft University of Technology, The Netherlands**
Researcher

2017 - 2019 **Delft University of Technology, The Netherlands**
M.Sc cum laude in Environmental Engineering
Thesis: "Convective Mass-Flux From Long Term Radar Reflectivities Over Darwin, Australia"

2014 - 2017 **Politecnico di Milano, Italy**
B.Sc in Environmental and Land Planning Engineering
Thesis: "Biogas from organic waste"

04 June 1995 **Born in Milan, Italy**

List of Publications

Savazzi, A.C.M., Jakob, C., Siebesma, A. P. (2021): Convective mass-flux from long term radar reflectivities over Darwin, Australia. *Journal of Geophysical Research: Atmospheres, 126, e2021JD034910.* https://doi.org/10.1029/2021JD034910

Savazzi, A.C.M., Nuijens, L., Sandu, I., George, G., Bechtold, P. (2022): The representation of the trade winds in ECMWF forecasts and reanalyses during EUREC4A. *Atmospheric Chemistry and Physics, 22, 13049–13066*, https://doi.org/10.5194/acp-22-13049-2022

Nuijens, L., **Savazzi, A.C.M.**, de Boer, G., Brilouet, P.-E., George, G., Lothon, M., et al. (2022): The frictional layer in the observed momentum budget of the trades. *Quarterly Journal of the Royal Meteorological Society, 148(748) 3315–3337.* https://doi.org/10.1002/qj.4364

Savazzi, A.C.M., Nuijens, L., de Rooy, W., Janssens, M., Siebesma, A.P. (2024): Momentum Transport in Organized Shallow Cumulus Convection. *Journal of the Atmospheric Sciences, 81, 279–296,* https://doi-org.tudelft.idm.oclc.org/10.1175/JAS-D-23-0098.1

Savazzi, A.C.M., Nuijens, L., de Rooy, W., Siebesma, A. P. (2025): The Influence of Parameterized Shallow Convection on Trade-Wind Clouds and Circulations in the HARMONIE-AROME Mesoscale Model. Journal of Advances in Modeling Earth Systems. *Journal of Advances in Modeling Earth Systems*, http://dx.doi.org/10.1029/2024MS004538

Included in this thesis.

Conference contributions

20 October 2021   **BBOS Autumn Symposium, Utrecht, The Netherlands**
Poster presentation

16 May 2022   **2rd Workshop on Cloud Organisation (WCO2), Utrecht, The Netherlands**
Poster presentation

25 May 2022   **EGU, Vienna, Austria**
Oral presentation

25 July 2022   **3rd Pan-GASS Meeting, Monterey, California**
Poster presentation

5 September 2022   **NAC , Utrecht, The Netherlands**
Poster presentation

21 October 2022   **BBOS Autumn Symposium, Oranjewoud, The Netherlands**
Oral presentation

9 July 2023   **CFMIP-GASS meeting, Paris, France**
Poster presentation

4 September 2023   **3rd Workshop on Cloud Organisation and Precipitation Extremes (WCO3), Trieste, Italy**
Oral presentation

16 April 2024   **EGU, Vienna, Austria**
Oral presentation

10 September 2024   **Workshop on Diagnostics for Global Weather Prediction, Reading, United Kingdom**
Oral presentation

Acknowledgments

"Rare sono le persone che usano la mente,
poche coloro che usano il cuore e
uniche coloro che usano entrambi."
- Rita Levi Montalcini -

While working on this dissertation, I was fortunate to meet and learn from remarkable people —those who skilfully combine both intellect and heart. I wish to express my deep gratitude to these inspiring people and to everyone who supported me in reaching this long-cherished milestone.

I am especially thankful to Louise Nuijens, who guided me step by step, from a broad introduction to meteorology during my Master's program to the detailed exploration of convective momentum transport that forms the core of this dissertation. She welcomed me into her team, providing me with the time and space to explore my research interests. I am grateful for the opportunity she offered me, as well as for her generous support in terms of resources, time, and honest guidance. Louise followed all my ups and downs, she knew how and when to encourage me, making sure I would work at the best of my ability and always with motivation. Beyond her exceptional scientific expertise, I greatly admire her communication style and professionalism, which serve as my guiding principles.

My deepest gratitude also goes to Pier Siebesma. I am honoured to have worked with him, as his wise feedback guided me towards ambitious goals and meaningful projects. His broad perspective and deep understanding of convection have been invaluable in framing my research within its wider scientific context. Pier has been incredibly supportive whenever I questioned the significance of my work or I had difficulty articulating its impact on advancing scientific understanding. I am especially grateful for the long discussions that left no question unanswered and for the confidence I felt knowing he was my supervisor.

A number of other unofficial mentors have played a crucial role in shaping my ideas and scientific identity. Thank you to Christian Jakob for his incredible wisdom and kindness. During my time at Monash University he offered attentive, thoughtful supervision without judgment, and made atmospheric convection utterly fascinating. Thank you to Irina Sandu for her unwavering enthusiasm. She kept me motivated and engaged with science during the challenging times of COVID. I look back on our Zoom meetings with a smile, in a time when human interactions were rare. Her dedication is truly inspiring. Thank you to Wim de Rooy who patiently answered all my questions about the HARMONIE model and its parameterisations. He created a comfortable atmosphere where no question felt too

simple to ask, which helped me learn a great deal. He also never missed a chance to offer encouragement, making sure I recognised progress, even when it felt slow. Thank you to Peter Bechtold for dedicating his time to teaching me about the IFS model. He welcomed me at ECMWF and has always been generous with his vast experience and knowledge of convection parameterisation, and much more. I feel privileged to have learned, and to keep learning, from him. While acknowledging my mentors, I also recognise the key role of my high-school teacher Grazia Merigioli, who first made me curious about science. She taught me to recognise the fragility of many natural equilibria, lightning purpose and motivation for what is now my career path.

I first worked on the CloudBreak project in 2020, where I was warmly welcomed into the "Wind Whispers" group by Beatrice, Mariska, Kevin, and Vishal. They were not only brilliant but also incredibly supportive, always happy to share their knowledge of atmospheric momentum transport. Thanks to them, I got a real glimpse of what life as a young researcher would look like a few years down the line. I'm truly grateful for everything they taught me. At the end of 2020, I joined the CMTRACE project, where Jose made studying winds great fun. He has this way of turning complex topics into something engaging and approachable. More than that, he was a fantastic colleague, always checking in to see how things were going and making sure I never felt lost.

Many more people played an important role in developing my ideas and directly improve this thesis. I am extremely grateful for the fruitful exchanges at foreign institutes where I was always welcomed greatly. Thank you to Marius and Raphaela, you made my visit to Hamburg a real pleasure and an explosion of ideas. Thank you to Thibaut, with just a short visit to MeteoFrance I benefitted from so many feedback which gave new understanding to my results. Thank you to Richard, Tobias and the rest of the Physical Processes team at ECMWF. I felt welcomed like a member of the team since the beginning of my visit and I learned a lot joining your Friday meetings.

Within the GRS department, I benefitted greatly from frequent interactions with Frans, Fredrik, Geet, Martin, Pouriya, and Stephan. Your sharp and challenging questions often brought fresh perspectives, helping me refine my work and produce more comprehensive studies. I truly appreciated your presence, which made the working environment not only stimulating but also highly enjoyable. Thank you to all the friendly people at the GRS department —the PhD candidates, postdocs, secretaries, and staff— who work hard to make the department an ever more pleasant place, from organising coffee breaks to social events. Please keep up your positive efforts in fostering an inclusive and safe community.

With Ben, Max, Philip, and Yan, I had the pleasure of building a friendship that extended beyond work. Despite our different research focuses, we shared experiences and emotions throughout our PhD journey. Your support was invaluable, making me feel understood at every stage. Thanks to you, I also met Elisa and Julia, and together we formed The Pandas. I am deeply grateful to this special group for helping me find a balance between work and leisure.

Thank you to all those friends that don't know and don't ask about the details of my job. Filipe and Tomás are the most joyful people I know. Their Portuguese spirit has been a warm spark during the long and cold Dutch winters. Thank you for the fun evenings,

the genuine laughs, and the warm hugs. Alessandra, Andrea, and Simone, companions in adventures around the globe. We shared every aspect of our lives for many years, from laughter to tears. Thank you for such an intense and irreplaceable friendship. Thank you Alberto, Filippo, Matteo and Sebastiano as you regularly remind me that my courage to moving abroad comes from having a safety net: a network of great friends in Milan that are always ready to welcome me back, at any time, after many years.

Thank you to Camille, Fabian B., Fabian S., Manuel, and Pooja, whom I met when I first moved to Delft. We shared the experience of being international students, and you remained important friends throughout my PhD. Though we have since followed different paths, scattered across the world, you helped me realise how unique and personal each journey is: there is no standard, no constraint. You taught me the value of searching and working towards my own dreams.

To Bas, thank you for your unwavering support, encouragement, and kindness. Your presence has made the past year lighter and more meaningful.

A profound word of thanks goes to what has been my family outside of Italy. I have been fortunate to share my home with wonderful people —Arianna, Jonathan, Ombretta, Pietro, and Stefano— who created a welcoming space, making Delft truly feel like home.

Finally, my deepest gratitude goes to my family in Milan. My parents and my brothers, you have shaped my ethics, values, and ambitions, providing the foundation upon which I have built everything. Grazie, for your love and for supporting my decisions with everything you had to give.

Thanks to all of you, the PhD journey has been fun, rewarding, and inspiring.